

DESIGNING NANOSCALE CONSTRUCTS FROM ATOMIC THIN SHEETS OF
GRAPHENE, BORON NITRIDE AND GOLD NANOPARTICLES FOR ADVANCED
MATERIAL APPLICATIONS

by

KABEER JASUJA

B.S., Indian Institute of Technology, Kharagpur, 2007

AN ABSTRACT OF A DISSERTATION

submitted in partial fulfillment of the requirements for the degree

DOCTOR OF PHILOSOPHY

Department of Chemical Engineering
College of Engineering

KANSAS STATE UNIVERSITY
Manhattan, Kansas

2011

Abstract

Nanoscale materials invite immense interest from diverse scientific disciplines as these provide access to precisely understand the physical world at their most fundamental atomic level. In concert with this aim of enhancing our understanding of the fundamental behavior at nanoscale, this dissertation presents research on three nanomaterials: Gold nanoparticles (GNPs), Graphene and ultra-thin Boron Nitride sheets (UTBNSs). The three-fold goals which drive this research are: incorporating mobility in nanoparticle based single-electron junction constructs, developing effective strategies to functionalize graphene with nano-forms of metal, and exfoliating ultrathin sheets of Boron Nitride.

Gold nanoparticle based electronic constructs can achieve a new degree of operational freedom if nanoscale mobility is incorporated in their design. We achieved such a nano-electromechanical construct by incorporating elastic polymer molecules between GNPs to form 2-dimensional (2-D) molecular junctions which show a nanoscale reversible motion on applying macro scale forces. This GNP-polymer assembly works like a molecular spring opening avenues to maneuver nano components and store energy at nano-scale.

Graphene is the first isolated nanomaterial that displays single-atom thickness. It exhibits quantum confinement that enables it to possess a unique combination of fascinating electronic, optical, and mechanical properties. Modifying the surface of graphene is extremely significant to enable its incorporation into applications of interest. We demonstrated the ability of chemically modified graphene sheets to act as GNP stabilizing templates in solution, and utilized this to process GNP composites of graphene. We discovered that GNPs synthesized by chemical or microwave reduction stabilize on graphene-oxide sheets to form snow-flake morphologies and bare-surfaces respectively. These hybrid nano constructs were extensively studied to understand the effect and nature of GNPs' interaction with graphene, and applied to address the challenge of dispersing bare-surfaced GNPs for efficient liquid-phase catalysis. We also revisited the functionalization of graphene and present a non-invasive surface introduction of interfaceable moieties.

Isostructural to graphene, **ultrathin BN sheet** is another atomic-thick nanomaterial possessing a highly diverse set of properties inconceivable from graphene. Exfoliating UTBNs has been challenging due to their exceptional intersheet-bonding and chemical-inertness. To develop applications of BN monolayers and evolve research, a facile lab-scale approach was desired that can produce processable dispersions of BN monolayers. We demonstrated a novel chlorosulfonic acid based treatment that resulted in protonation assisted layer-by-layer exfoliation of BN monolayers with highest reported yields till date. Further, the BN monolayers exhibited extensively protonated N centers, which are utilized for chemically interfacing GNPs, demonstrating their ability to act as excellent nano-templates.

The scientific details obtained from the research shown here will significantly support current research activities and greatly impact their future applications. Our research findings have been published in **ACS Nano, Small, Journal of Physical Chemistry Letters, MRS Proceedings** and have gathered >45 citations.

DESIGNING NANOSCALE CONSTRUCTS FROM ATOMIC THIN SHEETS OF
GRAPHENE, BORON NITRIDE AND GOLD NANOPARTICLES FOR ADVANCED
MATERIAL APPLICATIONS

by

KABEER JASUJA

B.S., Indian Institute of Technology, Kharagpur, 2007

A DISSERTATION

submitted in partial fulfillment of the requirements for the degree

DOCTOR OF PHILOSOPHY

Department of Chemical Engineering
College of Engineering

KANSAS STATE UNIVERSITY
Manhattan, Kansas
2011

Approved by:

Major Professor
Vikas Berry

Copyright

KABEER JASUJA

2011

Abstract

Nanoscale materials invite immense interest from diverse scientific disciplines as these provide access to precisely understand the physical world at their most fundamental atomic level. In concert with this aim of enhancing our understanding of the fundamental behavior at nanoscale, this dissertation presents research on three nanomaterials: Gold nanoparticles (GNPs), Graphene and ultra-thin Boron Nitride sheets (UTBNSs). The three-fold goals which drive this research are: incorporating mobility in nanoparticle based single-electron junction constructs, developing effective strategies to functionalize graphene with nano-forms of metal, and exfoliating ultrathin sheets of Boron Nitride.

Gold nanoparticle based electronic constructs can achieve a new degree of operational freedom if nanoscale mobility is incorporated in their design. We achieved such a nano-electromechanical construct by incorporating elastic polymer molecules between GNPs to form 2-dimensional (2-D) molecular junctions which show a nanoscale reversible motion on applying macro scale forces. This GNP-polymer assembly works like a molecular spring opening avenues to maneuver nano components and store energy at nano-scale.

Graphene is the first isolated nanomaterial that displays single-atom thickness. It exhibits quantum confinement that enables it to possess a unique combination of fascinating electronic, optical, and mechanical properties. Modifying the surface of graphene is extremely significant to enable its incorporation into applications of interest. We demonstrated the ability of chemically modified graphene sheets to act as GNP stabilizing templates in solution, and utilized this to process GNP composites of graphene. We discovered that GNPs synthesized by chemical or microwave reduction stabilize on graphene-oxide sheets to form snow-flake morphologies and bare-surfaces respectively. These hybrid nano constructs were extensively studied to understand the effect and nature of GNPs' interaction with graphene, and applied to address the challenge of dispersing bare-surfaced GNPs for efficient liquid-phase catalysis. We also revisited the functionalization of graphene and present a non-invasive surface introduction of interfaceable moieties.

Isostructural to graphene, **ultrathin BN sheet** is another atomic-thick nanomaterial possessing a highly diverse set of properties inconceivable from graphene. Exfoliating UTBNs has been challenging due to their exceptional intersheet-bonding and chemical-inertness. To develop applications of BN monolayers and evolve research, a facile lab-scale approach was desired that can produce processable dispersions of BN monolayers. We demonstrated a novel chlorosulfonic acid based treatment that resulted in protonation assisted layer-by-layer exfoliation of BN monolayers with highest reported yields till date. Further, the BN monolayers exhibited extensively protonated N centers, which are utilized for chemically interfacing GNPs, demonstrating their ability to act as excellent nano-templates.

The scientific details obtained from the research shown here will significantly support current research activities and greatly impact their future applications. Our research findings have been published in **ACS Nano, Small, Journal of Physical Chemistry Letters, MRS Proceedings** and have gathered >45 citations.

Table of Contents

List of Figures	xii
List of Tables	xxii
Acknowledgements	xxiii
Dedication	xxv
1 Introduction	1
1.1 Gold Nanoparticles and their electronic constructs	2
1.1.1 Single electron tunneling junctions.....	2
1.1.2 Nanoparticle junction science developed in this thesis	4
1.2 Graphene.....	4
1.2.1 The Excitement about graphene.....	5
1.2.2 Graphene science developed in this thesis	6
1.3 2-dimensional form of hexagonal Boron Nitride (<i>h</i> -BN)	8
1.3.1 Ultrathin sheets of h-BN: Analog of graphene.....	8
1.3.2 2-D Boron Nitride science developed in this thesis.....	8
1.4 Overview of Dissertation.....	9
1.5 References	10
2 Reversibly Compressible and Stretchable spring like Polymeric Nanojunctions between Gold nanoparticles	14
2.1 Overview.....	14
2.2 Introduction.....	15
2.3 Experimental Section.....	16
2.3.1 Diffusional electrostatic assembly process	16
2.3.2 Estimation of compression–stretching	17
2.3.3 Estimation of the difference in tunneling distances $d_{HP}-d_{LP}$	17
2.3.4 Relationship between compression forces and the electric field	18
2.4 Results and Discussion	20
2.5 Summary	29

2.6	References	29
3	Implantation and Growth of Dendritic Gold nanostructures on Graphene derivatives:	
	Electrical Property Tailoring and Raman Enhancement	34
3.1	Overview.....	34
3.2	Introduction.....	34
3.3	Experimental Section.....	36
3.3.1	Preparation of Graphene-Oxide	36
3.3.2	Synthesis of GO-SFGN Hybrids.....	36
3.3.3	Immobilizing the GO-SFGN Hybrids on silica surface	36
3.3.4	TEM and SAED.....	37
3.3.5	FESEM and EDS	37
3.3.6	Electrical Studies	37
3.3.7	Raman Spectroscopic Measurements	37
3.4	Results and Discussion	38
3.5	Summary.....	50
3.6	References	50
4	Microwave reduced Uncapped Metal Nanoparticles on Graphene: Tuning Catalytic.	
	Electrical and Raman Properties	54
4.1	Overview.....	54
4.2	Introduction.....	54
4.3	Experimental Section.....	57
4.3.1	Preparation of Bare surfaced gold nanostructures on graphene.....	57
4.3.2	TEM and SAED.....	57
4.3.3	FESEM.....	57
4.3.4	Electrical Conductivity and Gating Measurements	57
4.3.5	Raman Spectroscopic Measurements	57
4.3.6	Catalytic Measurements	58
4.4	Results and Discussion	58
4.5	Summary.....	69

4.6	References	70
5	Exfoliation of Boron Nitride	74
5.1	Overview.....	74
5.2	Introduction.....	74
5.3	Experimental section	76
5.3.1	Synthesis of UTBNs	76
5.3.2	Transfer to aqueous phase	77
5.3.3	XPS analysis	77
5.3.4	FESEM Imaging and EDS.....	78
5.3.5	TEM Imaging and SAED studies	78
5.3.6	Zeta Potential Measurement.....	78
5.3.7	Synthesis of citrate capped GNPs and templating on UTBNs.....	78
5.4	Results and Discussion	78
5.5	Summary	87
5.6	References	88
6	Conclusion and Future Work	94
6.1	Summary of contributions.....	94
6.2	Future work on detecting mechanical motion in a molecule using graphene-platform	
	96	
6.2.1	Introduction	96
6.2.2	Experimental Section	97
6.2.3	Preliminary Results.....	98
6.2.4	Intellectual Merit	99
6.3	Future work on a novel scheme to non-invasively functionalize graphene	100
6.3.1	Introduction	100
6.3.2	Experimental Section	102
6.3.3	Preliminary Results.....	102
6.3.4	Intellectual merit.....	102
6.4	Closing Remarks	104

Appendix A Appendix for the work on reversibly compressible and stretchable spring-like polymeric junctions in between metal nanoparticles.....	105
Appendix B . Appendix for the work on implantation and growth of dendritic gold nanostructures on graphene derivatives	119
Appendix C Appendix for the work on microwave assisted growth of nanoparticles on graphene	136
Appendix D Appendix for the work on synthesizing ultra thin sheets of Boron Nitride using chlorosulfonic acid	146
Appendix E Personal Publication List	165

List of Figures

Figure 1.1 The first class of nanosystem explored in the thesis comprises of a percolating assembly of gold nanoparticles cross-linked with elastic polymer molecules. It is shown to present a unique construct within which the phenomenon of molecular spring could be realized.....	3
Figure 1.2 The second class of nanosystem explored in this thesis is Graphene. a) An artistic rendition of the single-layer thick graphene layer. b) Graphene can be obtained by a simple mechanical exfoliation of graphite <i>via</i> repeated cleavage using a Scotch tape. c) Optical image of a chemically modified form of graphene sheet immobilized on a silica substrate with pre-deposited gold electrodes.	6
Figure 1.3 The third class of nanosystem explored in this thesis is the atomic thin sheet of Boron Nitride. a) An artistic rendition of the single-layer thick boron nitride layer. It can be obtained by a similar mechanical scotch tape exfoliation process. b) Optical image of a chemically modified form of boron nitride sheet on a lacey carbon grid. These are obtained by a method developed in this thesis.	9
Figure 2.1 Fabrication and functioning of GNP–cPAH device. a) Field-emission scanning electron microscopy (FESEM) images of 30-nm GNPs deposited on ~50-nm-thick cPAH film, which show an increase in GNP density with deposition time. Conduction–percolation is achieved at 120 min. b) FESEM images of typical HP and LP devices with deposition times of 8 and 24 hours, respectively. c) FESEM image of a typical LP device between gold electrodes connected to a power supply. d) Schematic representation of compression and stretching of cPAH junctions between GNPs. Upon application of a high electric field, the GNPs undergo charge polarization leading to mutual attraction, which compresses the cPAH junction. Upon application of centrifugal force, the GNPs move apart causing the cPAH junctions to stretch. Scale bars: 100nm for (a, b) and 500nm for (c).	16

Figure 2.2 Conductivities of HP and LP devices. The inter nanoparticle distance was controlled by varying the time of deposition of nanoparticles. Two kinds of devices are presented, namely HP and LP devices with deposition times of ~8 h and ~24 h to get higher and lower inter-GNP cPAH thickness, respectively, which in turn affects the native conductivity as shown. The difference in the inter particle distance for these devices can be calculated using the force balance and electron tunneling equations: 19

Figure 2.3 Compression of elastic cPAH junctions. a) Electric-field-induced ($4 \times 10^4 \text{ V cm}^{-1}$) cPAH junction compression for LP and HP devices over 10 min, where compression increases with time before reaching a steady-state value of 0.2 and 0.05 nm for the HP and LP devices, respectively. The data fit well with the spring-in-viscous-media equation (dashed line). Inset: native conductivity states for the devices. b) Steady-state junction compression in an HP device as a function of electric field applied for 10 min. The solid line is the fit for compression due to electric-field-induced polarization. Inset: AFM image of an HP device. 21

Figure 2.4 Relaxation of the cPAH junctions. a) Compressed molecules upon release of electric-field-induced forces relax back to their native state with the rate of relaxation governed by the magnitude of compression. An LP device compressed by ≈ 2.3 , 4.3, and 6.3 pm relaxes back to its precompressed state in ≈ 0.5 , 2, and 6 min, respectively. The relaxation data fit well with the spring-in-viscous-media equation (solid line). b) Compression-relaxation cycle of an HP device with two conductivity states. The compressed state (0.2 nm compressed) with conductivity higher by two orders of magnitude is achieved by application of an electric field of 40 kV cm^{-1} for 20 min and the native state is restored after ≈ 1200 min. 24

Figure 2.5 Proof of compression mechanism. a) The conductivity of an HP device increases upon successive applications of electric fields of equal magnitude in the positive ($+6 \times 10^4 \text{ V cm}^{-1}$) and negative ($-6 \times 10^4 \text{ V cm}^{-1}$) directions. Inset: the increase in average junction compression. b) In a crosswire configuration of electrodes, upon application of a $4 \times 10^4 \text{ V cm}^{-1}$ electric field in the x direction, a molecular compression of ≈ 4.2 pm along the x axis results in molecular stretching of ≈ 1.8 pm along the y axis. Top inset: optical micrograph of

the crosswire configuration of electrodes. Bottom inset: schematic of expansion in the y direction induced by compression in the x direction. (a) and (b) together show that the change in conductivity in LP and HP devices is exclusively a result of molecular compression and not charge trapping. Scale bar: 10 μm 26

Figure 2.6 Molecular stretching. a) Centrifugation-induced stretching is achieved by spinning an LP device under a centrifugal field of 90 g , which results in an increase in the junction stretching with time. Steady-state stretching of 2.7 μm is achieved in 30 s. The data fit well with the spring-in-viscous-media equation (solid line). The inset shows the increase in stretching with an increase in centrifugal field applied for 30 s. After a threshold centrifugal field of 45 g , cPAH junction stretching was found to increase linearly (solid line) with centrifugal field. b) The transient relaxation of another LP device is shown. The device relaxes from its stretched state of 12 μm to its prestretched state in ≈ 60 min. Inset: schematic of the setup for a device chip on a centrifuge. c) Solvent-induced rearrangement. An LP device annealed with alternate exposures to a vacuum and 40% humidity leads to a decrease in conductivity. After the fourth cycle, an irreversible decrease in conductivity of 13% is achieved, which corresponds to ≈ 6 μm expansion of the molecular junctions. The observed expansion is expected to be a result of release of internal stress in the GNP–cPAH structure, which was estimated to be 2.36×10^{-14} N per junction. 28

Figure 3.1 Formation mechanism of snowflake shaped gold nanostructures on graphene-oxide. (a) Interfacing the $-\text{COOH}$ and $-\text{OH}$ groups on GO sheets with a freshly prepared solution of gold nuclei, formed during hydroxyl-amine-assisted reduction of gold salt, results in nuclei attachment and seed-mediated formation of snowflake-shaped gold nanostructures (SFGNs) on the GO surface. (b) Right: FESEM of SFGNs templated on GO lying on silica surface. The SFGNs appearing darker (labeled D) are on the rear surface, while the SFGNs appearing brighter (labeled B) are on the front surface of the immobilized GO sheet (scale bar = 500 nm). Center: Higher magnification transmission electron microscopy (TEM) image showing the detailed characteristics and the structural parameters of SFGN exhibiting a dendritic morphology. Scale bar = 100 nm. Left: FESEM image showing wrinkles (labeled W) on GO associated with a darker SFGN. Scale bar = 200 nm. 39

Figure 3.2 “Snowflake”-shaped dendritic morphology of the gold nanostructures and AFM scan of GO–SFGN hybrid. (a) FESEM images of individual SFGNs with 5 and 6 primary branches (N_p), respectively, showing a distinct secondary branching (scale bar = 100 nm). Bottom insets show binary edge-resolved images for these SFGNs used for determining the circularity parameter ($\lambda = 4\pi \cdot \text{area}/\text{perimeter}^2$). Values smaller than unity indicate a high degree of corrugated edges. (b) Raman Spectra for GO–SFGN and GO showing the presence of SFGNs on GO enhances the intensity of D and G bands by ~250% and ~800% suggesting chemical enhancement, and hence a chemical-bond formation between SFGNs and GO, (c) atomic force microscopy scan of GO sheets templated with SFGNs with ~44 nm height as shown in the bottom line scan (scale bar = 500 nm). The height of a characteristic wrinkle (W) is ~8 nm. Inset shows AFM image for an individual SFGN (scale bar = 100 nm).

..... 41

Figure 3.3 Absorption spectra of SFGNs templated on graphene–oxide: (a) spectra of gold salt and GO display no significant peak in the visible region; (b) spectra of a freshly prepared solution of GO, gold salt, and hydroxyl-amine display an absorption peak at ~580 nm. Higher magnification FESEM micrographs (insets) for a bare GO sheet and of a GO sheet templated with SFGNs immobilized on silica substrates are shown. Scale bar equals 1 μm for the right inset and 5 μm for the left inset..... 43

Figure 3.4 Growth mechanism of SFGNs on GO sheets and their structural dependence on the synthesis temperature. (a) Schematic showing the elementary steps involved in the seeding growth of SFGNs on GO template. Au ions diffuse from the bulk to the GO sheet where they are catalytically reduced and incorporated in the growing Au nuclei. Bottom inset shows seed particles on GO that were prepared by sodium borohydride-assisted reduction of gold salt in the presence of sodium citrate and GO. Scale bar = 10 nm. (b) The morphology and density of the synthesized GNs sensitively depends on the reaction temperature. GNs synthesized at room temperature (25 °C) exhibit dendritic “snowflake” morphology with a high coverage on GO. At low temperature (4 °C), the GNs assume a spherical morphology with less coverage, and at higher temperatures (75 °C), GNs exhibit a random cluster formation with very dense coverage. Scale bars = 500 nm. Inset shows the

variation of surface coverage index for GO–gold hybrids synthesized at these three temperatures. 45

Figure 3.5 Structural variation in the morphology of SFGNs and diffraction pattern studies. (a) TEM images of SFGNs with 4, 5, 6, and 7 primary branches. Scale bar = 100 nm. (b) Bar graph showing the distribution of primary branches in the SFGNs synthesized at 25 °C. The analysis is for a total of 120 SFGNs deposited on GO. (c) FESEM images for gold-nanostructure-templated GO sheets that were synthesized at 70 °C showing high surface coverage densities and excellent selectivity of gold on GO. Scale bar= 5 μm. (d) Selected area electron diffraction (SAED) pattern for an SFGN with $N_p = 5$ (inset) shows that SFGNs have several defects and multiple crystal domains. Scale bar = 100 nm. 47

Figure 3.6 Electrical properties of graphene-templated with SFGNs. (a) The conductivity of a GO–SFGN sheet ($9.49 \times 10^{-2} \mu S$) increases ~102-fold after reduction with hydrazine. Inset shows a GO sheet templated with SFGNs incorporated between electrodes. Scale bar = 2 μm. (b) Conductivity of a bare GO sheet increases 103 folds after hydrazine reduction. Top inset: Optical micrograph of a bare GO sheet between gold electrodes. Scale bar = 5 μm. (c) GO–SFGN hybrid exhibits a semiconducting behavior showing an exponential dependence of conductivity on temperature ($\sigma \propto \exp(-E_g/(2kBT))$). Bottom left inset shows a similar temperature-response for a G–SFGN device. Top inset shows the I – V response for a GO–SFGN device over a temperature range of 273–345 K showing a gradual increase in conductivity. (d) Schottky fit for a G–SFGN device from which the Schottky barrier height is calculated to be ~39 meV. Top inset shows the variable range hopping fit for G–SFGN, which describes the data equally well. 48

Figure 4.1 Microwave (MW)-assisted in situ synthesis of multiple shaped bare-surfaced gold nanoparticles (BSGNs) on graphene oxide (GO). (a) An aqueous solution of gold salt, when microwaved for ~2 min, results in the formation of gold nuclei which agglomerate to form clusters (i). However, when the solution mixture also contains GO, the gold nanostructures get templated on the GO sheets (ii). This is attributed to the oxy-functional groups present on GO sheets, which stabilize the Au nuclei. (b) FESEM image of a BSGN-templated GO sheet on a silica substrate. The BSGNs acquire several shapes, such as triangular,

truncated-corner triangular, and hexagonal (as shown in the inset). (c) TEM image of a dendritic GNP encapsulated by a GO sheet. These GO-coated NPs are formed via MW exposure on the solution maintained at a lower ambient temperature.....59

Figure 4.2 Before the MW exposure, a solution of GO and gold salt does not exhibit a significant peak in the visible region. After the MW exposure, a wide absorption peak centered at ~575 nm appears in the spectrum. The top left inset shows the change in the color of the reactant mixture as it is exposed to MW irradiations. The GNS-decorated GO sheets (top right inset) are immobilized on a Si substrate for FESEM imaging, and the presence of BSGNs results in localized deformation of GO sheets, leading to the formation of wrinkles, the nodes of which are formed by the BSGNs (bottom right inset).....61

Figure 4.3 (a) FESEM image of a GO sheet decorated with BSGNs, exhibiting dark and bright contrast. The darker BSGNs are templated on the rear surface of the GO sheet, and the brighter BSGNs are templated on the exposed surface of the GO sheet. (b) FESEM image of a GO sheet that was immobilized ~72 h after being incubated in the microwave gold salt solution, exhibiting a high surface coverage index ($\eta = 0.79$). (c) TEM image of a GO sheet exhibiting dendritic and polyhedral GNS. (d) TEM image of an individual dendritic-shaped GNS wrapped with a GO sheet prepared by MW exposure to the solution of GO and gold salt maintained at a lower ambient temperature.63

Figure 4.4 (a) The presence of BSGNs enhances the native Raman spectra of GO sheets by 300%, characteristic for a chemical enhancement, suggesting that the BSGNs chemically attach to the oxy-functional groups on GO. The inset shows the Lorentzian fit to the 2D band of the Raman spectra of GO and GO-BSGN sheets showing the presence of two components, which suggests a characteristic of few-layered graphene. (b) BSGNs stabilized on GO sheets were studied for their catalytic activity for NaBH₄-induced reduction of 4-nitroaniline (4-NA) . The reaction time can be evaluated by monitoring the successive decrease of the band at 380 nm for 4-NA and the corresponding increase in the band at 238 nm for *p*-phenylene diamine. Complete reduction of 4-NA in the presence of BSGNs stabilized on GO takes ~8 min. The insets show the first-order exponential fits for the

reaction catalyzed by GO–gold seeds and 5 nm citrate-capped GNPs. The rate constants are found to be 0.243 and 0.094 min⁻¹ respectively..... 65

Figure 4.5 (a) BSGNs enhance the average conductance of GO sheets by an order of magnitude.

The top inset shows the FESEM image of the surface-immobilized GO–BSGN composite, and the bottom inset shows the optical image of a GO sheet in between gold electrodes. (b) The effect of BSGNs on the nature of charge carriers in GO is determined by comparing the gating behaviour of GO and GO–BSGN at a constant source–drain voltage (*V*_{DS}) of 5 V. The top inset shows the gating behaviour of GO, which exhibits a p-type semiconducting behaviour; the Dirac neutrality point is situated at 18 V. In the presence of BSGNs, the Dirac neutrality point shift towards negative voltages, making GO–BSGN an n-type semiconductor. The bottom inset shows the schematic for the gating setup. 69

Figure 5.1 Chlorosulfonic Acid (CA) exfoliation of Ultrathin Boron Nitride Sheets (UTBNSs) The

AA' stacked α -BN sheets when suspended in CA undergo protonation at the N centre of the slightly polar B-N bonds which results in surface chemical modification of the intermittent layers. The presence of a high density of positive surface charges lead to intersheet repulsions that overcome the interlayer binding forces, resulting in layer-by-layer exfoliation of UTBNSs which remain suspended in CA due to electrostatic stabilization. Bottom left inset shows the optical image of UTBNSs on a silica substrate. The immobilized sheets exhibit surface wrinkles (labeled W) and raised regions (labeled R), which arise from the multiple-point electrostatic attachment. 76

Figure 5.2 Optical Properties of UTBNSs and Band-gap determination a) Tyndall effect as

observed in UTBNSs dispersed in a CA solution. The path of laser beam is clearly distinguishable in the CA solution containing UTBNSs as compared to the bare CA solution. b, Ultraviolet-visible absorption spectra of UTBNSs suspended in water at room temperature. The aqueous solution is obtained by transferring the CA containing exfoliated UTBNSs in water (as explained in Experimental section and Appendix section D.2). Inset shows the Tauc plot generated from the absorption spectra for UTBNSs. The linear regime is extrapolated to obtain gap wavelength λ_0 =216 nm and corresponding optical band gap E_g =5.74 eV. 80

Figure 5.3 XPS studies to determine the chemical functionalization of UTBNSs a, B1s and N1s core level spectra from the XPS analysis of the α -BN flakes. The spectra fitted with Gaussian distributions exhibit peaks at 190.8eV and 398.4eV respectively, which correspond to the conjugated BN structures shown in the top right inset (=B- and =N-). b, B1s and N1s spectra of UTBNSs (obtained from an UTBNS film, cross-sectional FESEM image shown in middle inset) exhibit extended shoulders at higher binding energies in addition to the primary peaks at 190.8eV and 398.4eV respectively. The N1s spectra in the UTBNSs exhibits secondary shoulders at (1)400.1 eV, (2)401.1 eV, (3)401.6 eV and (4)402.2 eV attributed to N atoms protonated in four distinct manners as represented in the bottom right inset. This indicates functionalization of UTBNSs post CA treatment. 81

Figure 5.4 Presence of functionalized N centers on UTBNSs and stability of UTBNSs in aqueous phase. a, Confocal Image of a UTBNS covalently tagged with FITC molecules suggesting a uniform presence of functionalized N atoms on its surface. The bottom right inset shows the optical image of the corresponding UTBNS. b, UTBNSs, when dispersed in water exhibit positively charged surface due to the presence of protonated N atoms. This leads to their electrostatic stabilization enabling a colloidal formation. c, The net energy of water dispersed UTBNSs can be modeled using DLVO theory. The graph shows the net energy evaluated per unit surface area for an UTBNS exhibiting a zeta potential value $\zeta=+25$ mV. Top inset shows the size distribution of UTBNSs dispersed in water determined using laser light scattering. The average diameter of sheets is ~ 24.5 μm . Bottom Inset shows the zeta-potential for UTBNSs dispersed in water as a function of the solution pH. The blue region ($\zeta > 2.4$ mV) denote pH regimes in which UTBNS dispersion is stable. The red region ($\zeta < 2.4$ mV) denote an instability in the colloidal dispersion [This analysis is for sheets with surface areas $>1\mu\text{m}^2$]. 83

Figure 5.5 Figure 5| Electron Microscopy Imaging of UTBNSs. a, FESEM image of UTBNSs obtained from α -BN flakes and immobilized on 300 nm thick silica substrate. The absence of any wrinkled relief-features on the deposited sheet is attributed to electrostatically stretched UTBNS configuration within the aqueous dispersion. b, TEM image of large-

<p>sized and small-sized UTBNSs on lacey carbon grid. The larger sheets exhibit crevices on their surface which contribute to a high density of dangling bonds.</p> <p>Figure 5.6 Raman spectroscopic study of UTBNSs and self-assembly of gold nanoparticles. a Raman spectrum of the UTBNS shown in panel a (red), compared with the Raman spectrum of α-BN flake (blue) from which it was exfoliated; exhibiting peaks at 1384cm^{-1} and 1366cm^{-1} respectively. The samples were excited by a 633 nm laser. These peaks correspond to the characteristic E_{2g} vibrational phonon mode of α-BN shown in top left inset. Top right inset shows the transverse phonon mode spectra ($\sim 1050\text{cm}^{-1}$) obtained from UTBNS representing the presence of sp^3 defect sites. The curves are fitted using Lorentzian distributions b, FESEM Image of an UTBNS templated with gold nanoparticles. Citrate capped gold nanoparticles (GNPs) can be templated on UTBNSs <i>via</i> a solution-phase electrostatic self-assembly process. The GNPs deposit uniformly on the sheet featuring a high surface coverage.</p> <p>Figure 6.1 Schematic illustration of an amino azo-benzene molecule functionalized graphene sheet. The azo-benzene molecule can be reversibly switched between its <i>cis</i> and <i>trans</i> conformational states on irradiations with UV (365 nm) and blue (420 nm) lights. The conformational change is associated with a molecular motion of the electron rich benzene moiety bringing it closer to the Graphene base by a distance of $2.1 \text{ \AA} - 0.7 \text{ \AA} = 1.4 \text{ \AA}$. The sensitive graphene base is utilized for electrically detecting this sub-nano scale molecular motion.</p> <p>Figure 6.2 Controlled conductance switching in an azo-functionalized graphene device can be achieved by irradiations with UV and blue lights. A <i>trans</i> to <i>cis</i> isomerization of the azo molecule on UV application switches the azo-functionalized graphene to a higher conductive state that reverts close to its original state upon <i>cis</i> to <i>trans</i> isomerization. This electrical response of graphene is measured at temperatures of 273 K and 300 K. Temperature acts as an external factor to regulate the memory of this optoelectronic switch.</p> <p>Figure 6.3 Chromium carbonyl functionalization of graphene <i>via</i> formation of metal-aromatic η^6 coordination bond.</p>	<p>85</p> <p>86</p> <p>97</p> <p>99</p> <p>101</p>
--	--

Figure 6.4 : Chromium carbonyl functionalization of an arene molecule *via* metal-aromatic η^6 coordination bond. Transfer of electrons in a bond formation and π - π Interactions among the non-bonding orbitals which increase the electron density at the arene center has an electron accepting tendency..... 101

Figure 6.5 Preliminary Results (confirmation of bonding on graphene): (a) XPS analysis of pristine graphene sample before and after treatment with the chromium hexacarbonyl solution at a temperature of 80 °C and 2 atm. Functionalization of $\text{Cr}(\text{CO})_3$ on graphene is evidenced by the appearance of 3 new peaks post treatment: 578.4 eV & 587.7 eV (Cr 2p spectra) and 45.4 eV (Cr 3p spectra). The formation of coordination bond between the metal atom and aromatic ring alters the electron density of the conjugated C atoms on graphene and is reflected in the C1s spectra in the form of a shift of 0.5 eV. (b) The average conductance of graphene decreases by an order of magnitude post functionalization, and (c) Average carrier mobility enhances by 42.8% post functionalization 103

List of Tables

Table 1 Structural Parameters (number of primary branches, their average length, average width and the angle of emergence range) shown for different SFGNs	123
--	-----

Acknowledgements

The path to earning my doctoral degree has been the best learning phase of my life so far and I am indebted for this to my research advisor, Dr. Vikas Berry. He has had the greatest influence on my development as an academician and a person. He is an amazing scientist and the best mentor a student can ask for. His inspiring words always motivated me and built in me the confidence to develop an independent thinking and pursue research with a distinctive vision and direction. I have been blessed to work under his supportive guidance and sincerely hope to carry forward and share the vision he has imparted within me. I am also very grateful to Namrita Berry for her kind support throughout my stay at Manhattan.

I would like to express my heart-felt gratitude to Dr. James Edgar, Dr. Keith Hohn and Dr. Gurpreet Singh for serving in my advisory committee and for their guidance. They have always been very supportive of my endeavors and allowed me to use their lab facilities whenever I needed. I am very thankful for their valuable suggestions which have helped me immensely in shaping up my research work. I also thank Dr. Viktor Chikan for serving as Outside Chair representative from the Graduate School.

For the work in this thesis, I must give special thanks to Heather Shinogle and Dr. David Moore in the Microscopy and Analytical Laboratory at the University of Kansas. They taught me electron microscopy and always shared their skills and resourcefulness which helped me a lot in generating miniscule details on the nanosystems we explored. I am also grateful to Dr. Qiang Charles Ye, Department of Bioengineering, University of Kansas for teaching me Raman Spectroscopy that we extensively applied to understand our nanomaterials.

I am immensely thankful to the former and present members of our lab: Arthur Thompson, Ashvin Nagaraja, Steven Melton, Jose Armesto, Joshua Linn, Cody Fager, Christina Davis, Kayum Ayinde, Nihar Mohanty and Phong Nguyen; they played a very big role in helping me put the scientific ideas into practice. It is because of this group of people all this work has been made possible. I will be ever grateful to them for their continued assistance in my experimental work. I acknowledge the immense help I have received from all the graduate students in our Department. I would also like to thank Dr. Dan Boyle, Dr. Hongwang Wang, Dr.

Stefan Bossmann, Dr. Sreeram Cingarapu and Dr. Kenneth Klabunde at K-state for allowing me to use their laboratory facilities.

I would like to acknowledge all Faculty members and Staff in the Chemical Engineering Department for providing a thriving environment to work in. I specially thank Florence Sperman, Lauren Muse and Cindy Barnhart for their generous help in administrative works.

Lastly I want to thank my family to whom I dedicate this thesis: my brother Varun, my mother Kiran and my father Om Prakash, for all their love, support and motivation. It is their kind blessings and hard work of years that gave me the valuable opportunity to explore science at this level. I have also been blessed to meet Aisha Rasool while here at K-state; she has been and will always be a great source of inspiration to me.

The completion of this thesis draws to end a memorable phase of my life at K-state during which I made scientific and personal discoveries and developed life long relationships. I will carry along the valuable lessons learnt and the vision that I have obtained into the next phase of life which waits with open arms.

Dedication

To my Family

1 Introduction

Atomic, molecular and nano sciences have made great progress in the past thirty years and have brought about a radical revolution in several fields of fundamental and applied research. These branches of science are motivated by the quest for a deep and precise understanding of the physical world as these provide opportunities to probe matter down to its most ultimate fundamental form. The underlying concept which grasps the entirety of nano sciences is, that at nano dimensional scale, the every day material starts behaving in extraordinary ways. This central concept has enabled immense possibilities that will revolutionize several key applications, including medical diagnosis¹, drug delivery^{2,4}, miniaturization of semiconductors⁴, environmental friendly chemical ingredients⁵, and clean energy generation⁶; and these emerging technologies promise to deliver even more applications in the future.

Understanding the behavior of nanomaterials, which forms the heart of nano sciences research, is often an intricate enterprise. The ability to observe, control, and hence understand the molecular and nano processes has taken extraordinarily strides in the past few years^{7,8}. Now we have reached a point in the development of state-of-the-art techniques where we have tools to tackle the challenges offered by the emerging frontiers of these sciences. It is now conceivable to manipulate and even sculpt materials at their ultimate tiniest scale to a level at which, in essence, a full-fledged miniaturized analytical laboratory can be realized on a single hand-held chip⁹.

In addition to the emergence of new technologies, the development of nano sciences is distinguished by an entirely new class of low dimensional systems, namely: the 0-dimensional class of quantum dots & nanoparticles¹⁰; 1-dimensional class of nanotubes & nanowires¹¹; and 2-dimensional class of graphene and atomically thin materials¹². **Each of these classes offers a set of unexplored physico-chemical properties and provides avenues to peek into their small world and hence understand their fundamental behavior at nanoscale. This underlying viewpoint is what forms the central theme of the thesis work presented here.**

The research work presented here attempts to understand the science of nano scale processes that were realized on three distinct nanosystems: **gold nanoparticles** (which belong to the class of zero-dimensional nanomaterials); and atomic thin sheets of **graphene** and **boron nitride** (which belong to the class of 2-dimensional nanomaterials).

The three important questions which we have tackled in this thesis are:

(1) Can a controlled nanoscale motion be incorporated in a gold nanoparticle based single electron tunneling construct?;

(2) Can the atomic thin sheets of graphene be interfaced with nano forms of metal and if this interfacing is achievable, can this be utilized to address some of the challenges offered by the developing sciences of graphene and metal nanoparticles (such as modulating graphene conductivity and bare-surface stabilization of nanoparticles) ?;

(3) Can atomic thin sheets of boron nitride be synthesized in processable yields by a method which mends the deficiencies available in current methods?

As explained ahead in the ensuing sections, these questions play a crucial role in developing our understanding of these nanosystems. The research work presented here comprehensively addresses these questions by examining some intriguing concepts and systematically developing the related theoretical concepts. The following sections provide overview perspectives on the three aforementioned nanosystems that will equip the readers to visualize the merit of the posed questions.

1.1 Gold Nanoparticles and their electronic constructs

A percolating assembly of gold nanoparticles cross linked with elastic polymer molecules (**Figure 1.1**) is the first nanosystem explored in the thesis. The ensuing sub sections present a brief account of the fundamental knowledge and the findings we have obtained about this nanosystem.

1.1.1 Single electron tunneling junctions

Percolating assemblies of metal nanoparticles form a special category of electronic construct, in which the electric current flows at the single electron level as opposed to the

continuous charge flow that takes place in conventional electronic devices¹³. When configured in a percolating fashion, the assembly of metal nanoparticles effectuates the formation of small metallic islands connected to each other *via* tunnel barriers which have a resistance exceeding the quantum resistance (h/e^2), which enables the electrons to effectively tunnel through the junctions.¹⁴ With the existing fabrication techniques, it is possible to fabricate tunnel junctions of increasingly smaller dimensions facilitating an access to the nano regime space formed in between the nanoparticles.

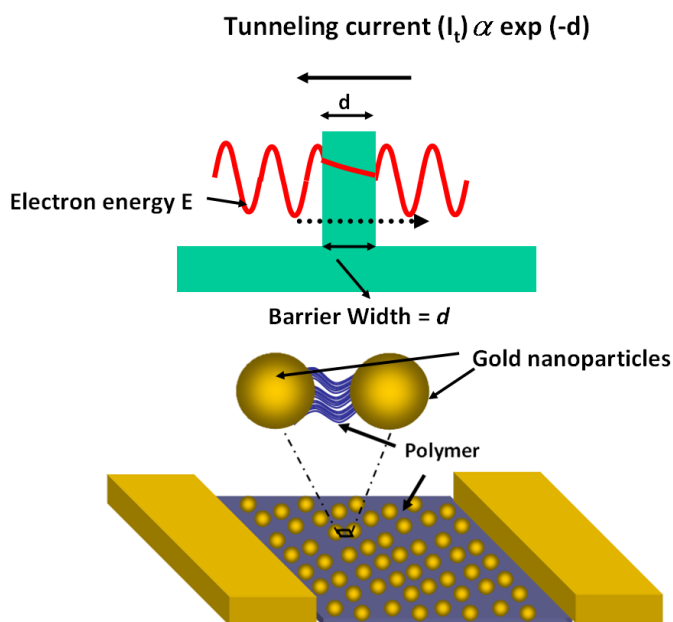


Figure 1.1 The first class of nanosystem explored in the thesis comprises of a percolating assembly of gold nanoparticles cross-linked with elastic polymer molecules. It is shown to present a unique construct within which the phenomenon of molecular spring could be realized.

What makes such single electron tunneling devices appealing is their **ability to combine the characteristics of classical effects with the quantum effects**. These open the realm of physics to study a wide range of novel phenomena at the nanoscale. Here, we have focused on the study of a system of percolating gold nanoparticles which has been cross-linked with elastic polymer molecules. The next sub-section provides a succinct view of the '*molecular spring*' phenomena which we were able to realize in this nano construct reasserting the capability that lies with the single electron junction devices.

1.1.2 Nanoparticle junction science developed in this thesis

The electronic construct of elastic polymer molecules sandwiched in between gold nanoparticles enabled integration of molecular elasticity with nanoelectronics and investigation of the nano dynamics. Confined nano forces were generated in this construct by exercising externally derived macro scale forces of electronic and mechanical origins. As explained in detail in Chapter 2, the gold nanoparticles were utilized as movable connectors for applying nano level forces and as nano electrodes to measure the nano scale deformations *via* change in the electron tunneling conductivity. The knowledge obtained from this work adds to the present capabilities of integrating and maneuvering electronic devices at the molecular scale.

1.2 Graphene

Graphene is a single layer of carbon atoms arranged in a hexagonal lattice structure. It is the first two-dimensional crystalline material to be isolated, and owing to its single atom thick nature, is of immense scientific and applied interest. This is the second nanosystem we have explored in this thesis.

“Carbon has this genius of making a chemically stable two-dimensional, one atom thick membrane in a three dimensional world. And that, I believe, is going to be very important in future of chemistry and technology in general.”

This statement was quoted by Richard Smalley in his address of receiving Nobel Prize for the discovery of fullerenes in 1996.¹⁵ Not much later, in 2004, this concept was experimentally realized by Konstantin Novoselov and Andre Geim in one of their thought experiments that appeared as a seminal paper in *Science*, which led to the discovery of graphene and went on to win the Nobel Prize in 2010.¹²

It was well established that graphite consists of stacked hexagonal carbon sheets, but it was believed that a single sheet was thermodynamically unstable and hence couldn't be isolated from this stack. Novoselov and Geim succeeded in isolating large individual sheets by repeated mechanical exfoliation of graphite with scotch tape (**Figure 1.2**). They were the first to verify the 2-dimensional properties of graphene and to open up a new class of materials by

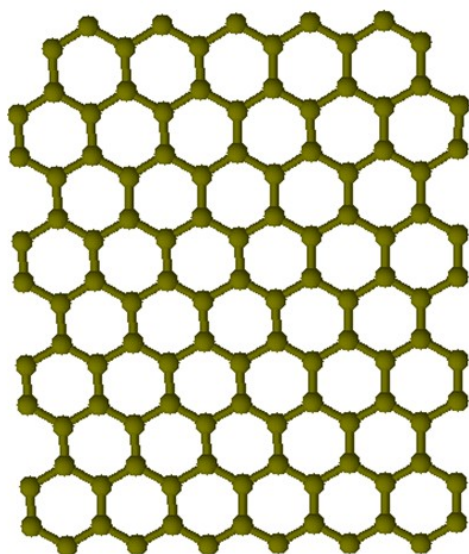
utilizing the same exfoliation scheme to produce single layers of boron nitride and molybdenum disulfide.

1.2.1 The Excitement about graphene

Single-atom thickness is the minimum possible dimension that will ever be achieved in a material; it endows the class of graphenic structures with properties at the extremes of all known materials: exceptional electron mobility at room temperature ($200,000 \text{ cm}^2\text{V}^{-1}\text{s}^{-1}$)^{16, 17}, high thermal conductivity ($5000 \text{ Wm}^{-1}\text{K}^{-1}$)¹⁸, high Young's modulus ($\sim 1.0 \text{ T Pa}$)¹⁹ and utmost impermeability (doesn't permeate even the smallest possible He gas atoms). Moreover, the quantum confinement in graphene leads to a linear dispersion relation of electrons and holes that gives interesting analogies between graphene and particle physics. This provides physicists opportunities to study and apply several physico-chemical phenomena that couldn't have been realized earlier.^{20, 21} This excellent merger of scientifically significant and industrially applicable properties in the graphenic systems draws equal interests from scientists and engineers.

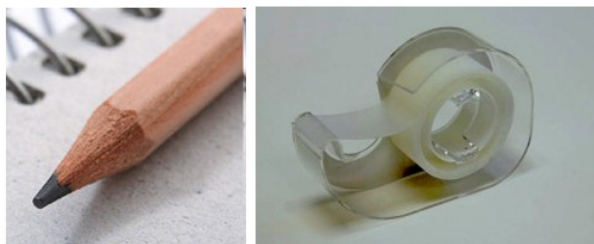
The properties of graphene suggest several exciting electronic applications including high-frequency oscillators, field effect transistors, transparent flexible touch screens, and solar energy processing panels^{6, 22,23}. Potential advanced material applications include mechanically robust and yet light-weight material applications including hydrogen visualization templates for TEM, components of satellites and aircraft technology.²⁴

a.



● Carbon

b.



c.

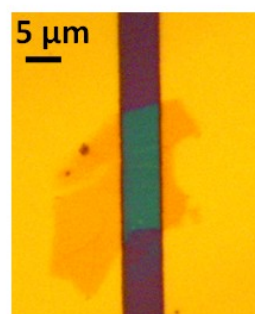


Figure 1.2 The second class of nanosystem explored in this thesis is Graphene. a) An artistic rendition of the single-layer thick graphene layer. b) Graphene can be obtained by a simple mechanical exfoliation of graphite *via* repeated cleavage using a Scotch tape. c) Optical image of a chemically modified form of graphene sheet immobilized on a silica substrate with pre-deposited gold electrodes.

The carbon backbone of graphene provides a plethora of possibilities for surface chemical modification. This aspect of graphene was thoroughly investigated and exploited by building advanced composites of graphene.

1.2.2 Graphene science developed in this thesis

In this thesis, the chemical science of graphene was developed. Chemically modified graphene sheets (CMGs) were interfaced with electron rich metal-nanoparticles. This is a subject of immense fundamental and applied interest, as integrating the 2-D nanostructures with entities that have useful properties, enables the formation of hybrid composites, which can

potentially address the pertinent research and industrial challenges.²⁵ Integrating graphene with gold nanoparticles (GNPs) can form a hetero-structure that displays, not only the useful properties of both its parent materials, but also the novel nanoscale properties that emerge from their unique interfacing.²⁵

We comprehensively studied the interfacing of graphene-oxide sheets with gold nanostructures that are produced *in-situ* by controlled diffusion and catalytic-reduction of gold ions. The mechanism which enables this interfacing within this unique nanosystem was characterized and the ability of graphene-oxide sheets to act as GNP-stabilizing templates in solution was established. Such a provision led to the formation of dendritic ‘snow-flake-shaped’ gold-nanostructures (SFGNs) on the surface of GO sheets. We then characterized these graphene-sheets templated with gold nanostructures for their structural properties, electrical characteristics and Raman scattering; and were able to demonstrate that the chemiophysical forces within this system can be regulated to control the morphology, coverage density and stability in solution-dispersion and that the presence of gold nanostructures can sensitively tailor the native properties of graphene. These studies form Chapter 3 of this thesis.

We carried forward this discovery to address a major challenge in liquid phase catalysis by synthesizing stable liquid-dispersions of “uncapped” supported metal nanoparticles with enhanced density of accessible catalytic sites. These novel “uncapped” metal nanoparticles were realized by leveraging the high-density of accessible and bondable oxy-functional groups on graphene oxide (GO) sheets and the high steric-hindrance offered by their micron-scale area. With a large-density of active sites facilitated by their uncapped surface, these unique solvent-dispersed, supported gold-nanostructures exhibited several-fold enhancements in their catalytic activity as compared to similarly shaped surfactant-capped gold nanoparticles. Chapter 4 describes this work in detail.

Two prospective studies on graphene science were also initiated and are currently underway; one showcased the ability of graphene to detect the sub-nano scale mechanical motion of a molecule and the other revisited the functionalization of graphene by demonstrating a novel non-invasive functionalization scheme. These works are in their incipient stages and are proposed as future works in Chapter 6.

1.3 2-dimensional form of hexagonal Boron Nitride (*h*-BN)

The experimental isolation of graphene had opened up the possibility of extracting and isolating 2-dimensional forms of crystals composed of elements other than carbon. Novoselov and Geim reported that micromechanical cleavage technique can also be applied to obtain thin sheets of *h*-BN.^{26, 27} This is the third class of nanomaterial explored in the thesis.

1.3.1 Ultrathin sheets of *h*-BN: *Analog of graphene*

An atomic thick sheet of boron nitride is isostructural to graphene (**Figure 1.3**), and it offers a unique set of properties which can't be realized in graphene system: such as large band-gap, high optical-transparency, tunable photoluminescence²⁸, high mechanical strength²⁹, high thermal conductivity, UV cathodoluminescence³⁰, and atom-thick electron-tunneling-barrier. Its pronounced thermo-chemical stability (stable up to 1000°C in air and up to 1800°C in inert atmosphere) makes it a superior candidate for high-temperature applications and in chemically-hazardous environment.³¹ In spite of these rich properties, the 2-D form of BN doesn't yet share the immense progress relished by graphene. This is because the chemically-passive nature and strong intersheet *lip-lip* bonding in *h*-BN makes its exfoliation in its single-atom thick form challenging. This is the challenge that we have addressed in our work and have developed a chemical exfoliation route that results in the highest ever reported yields of atomic thin sheets.

1.3.2 2-D Boron Nitride science developed in this thesis

The current processes of exfoliating thin BN sheets are based on sonicating BN crystals in the presence of intercalating solvents. However, the yields obtained in these processes are extremely low. Moreover, the Ultra-thin boron nitride sheets (UTBNSs) obtained in these processes exhibit small sizes.³² In this thesis we have investigated the first fundamental study on protonation of the chemically-impervious BN crystal lattice and utilized it for a layer-by-layer exfoliation of ultra thin BN sheets which could be dispersed in solvents. This also led to the transformation of the chemically-passive BN lattice to its chemically-active form enabling its interfacing with dye-molecules and GNPs. This work has several potential applications similar to the ones that have been realized from graphene suspensions.³³

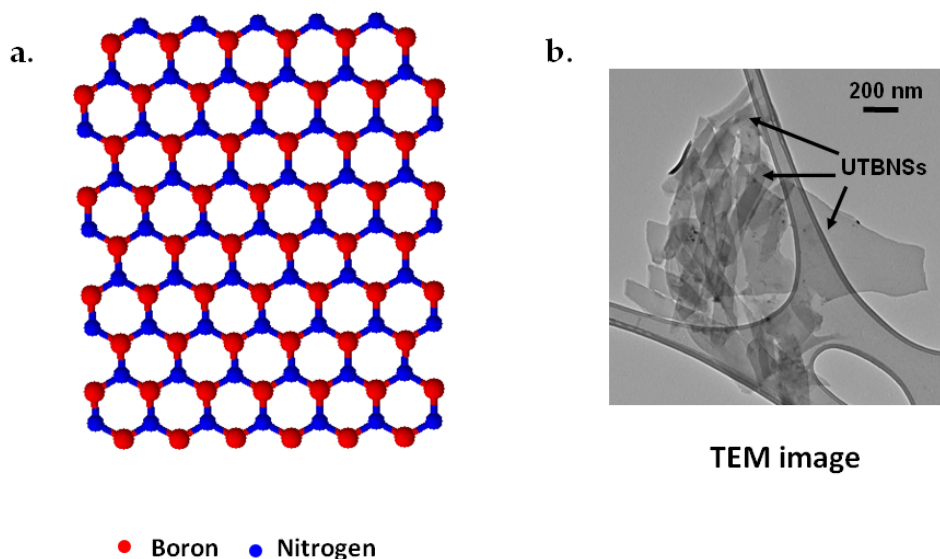


Figure 1.3 The third class of nanosystem explored in this thesis is the atomic thin sheet of Boron Nitride. a) An artistic rendition of the single-layer thick boron nitride layer. It can be obtained by a similar mechanical scotch tape exfoliation process. b) TEM image of a chemically modified form of boron nitride sheet on a lacey carbon grid. These are obtained by a method developed in this thesis.

1.4 Overview of Dissertation

Chapter 1 introduces the current state of knowledge available on low-dimensional nanomaterials and presents an overview of the experimental projects that are discussed ahead in Chapters 2-5.

Chapter 2 presents a detailed study on the introduction of nanomechanical motion in an electronic construct designed from gold nanoparticles and elastic polymer molecules. This work utilizes the nanoscale phenomenon of electron tunneling to detect nano scale motion. The work presented in this chapter has appeared as an article in *Small*.

In **Chapter 3**, we study and demonstrate the capability of chemically modified graphene sheets to act as swimming macromolecular templates in solution and utilize this to decorate

these sheets with gold nanoparticles synthesized *in-situ* by a seeding method.. This work has appeared as an article in *ACS Nano*.

The work presented in **Chapter 4** builds on the important insights developed in Chapter 3 and utilize these to overcome a major challenge in liquid-phase catalysis of dispersing naked nanoparticles with active catalytic sites. This work has been published as an article in the *Journal of Physical Chemistry Letters*.

In **Chapter 5**, a new chemical synthetic route is presented that exfoliates atomic thin sheets of boron nitride from its bulk form. This comprise the first fundamental study on protonation of chemically impervious boron nitride crystal lattice The sheets produced are studied in detail in terms of their structural features and utilized as templates. This work is currently under review by *Nature Communications*.

At the end, **Chapter 6** summarizes the key contributions this research has provided towards the field of nanotechnology and presents two potential works on graphene for future research directions.

The **Appendices** at the end of the dissertation contain reference materials cited within the text, such as important mathematical derivations, fundamental concepts and supplementary details. As a whole, this dissertation describes classes of novel experiments on nanosystems and provides both a theoretical and experimental framework of carrying out such detailed measurements in future.

1.5 References

1. Ajima, K.; Murakami, T.; Mizoguchi, Y.; Tsuchida, K.; Ichihashi, T.; Iijima, S.; Yudasaka, M.; Enhancement of In Vivo Anticancer Effects of Cisplatin by Incorporation Inside Single-Wall Carbon Nanohorns. *ACS Nano* **2008**, 2, 2057-2064.

2. Ciofani, G.; Raffa, V.; Menciassi, A.; Cuschieri, A.; Folate Functionalized Boron Nitride Nanotubes and their Selective Uptake by Glioblastoma Multiforme Cells: Implications for their Use as Boron Carriers in Clinical Boron Neutron Capture Therapy. *Nanoscale Res. Lett.* **2009**, 4, 113-121.

3. Ciofani, G.; Raffa, V.; Menciassi, A.; Cuschieri, A. Boron nitride nanotubes: An innovative tool for nanomedicine. *Nano Today* **2009**, 4, 8-10.

4. Radisavljevic B.; Radenovic A.; Brivio J.; Giacometti V.; Kis A. Single-layer MoS₂ transistors. *Nat Nano* **2011**, 6, 147-150.
5. Patchkovskii, S.; Tse, J. S.; Yurchenko, S. N.; Zhechkov, L.; Heine, T.; Seifert, G. Graphene nanostructures as tunable storage media for molecular hydrogen. *Proceedings of the National Academy of Sciences of the United States of America* **2005**, 102, 10439-10444.
6. Guo, C. X.; Guai, G. H.; Li, C. M. Graphene Based Materials: Enhancing Solar Energy Harvesting. *Adv. Energy Mater.* **2011**, n/a-n/a.
7. Schedin, F.; Geim, A. K.; Morozov, S. V.; Hill, E. W.; Blake, P.; Katsnelson, M. I.; Novoselov, K. S. Detection of individual gas molecules adsorbed on graphene. **2007**, 6, 655.
8. Novoselov, K. S.; Jiang, Z.; Zhang, Y.; Morozov, S. V.; Stormer, H. L.; Zeitler, U.; Maan, J. C.; Boebinger, G. S.; Kim, P.; Geim, A. K. Room-Temperature Quantum Hall Effect in Graphene. *Science* **2007**, 315, 1379-1379.
9. Daw, R.; Finkelstein, J. Lab on a chip. *Nature* **2006**, 442, 367-367.
10. Tyagi, P.; Cooney, R. R.; Sewall, S. L.; Sagar, D. M.; Saari, J. I.; Kambhampati, P. Controlling Piezoelectric Response in Semiconductor Quantum Dots via Impulsive Charge Localization. *Nano Letters* **2010**, 10, 3062-3067.
11. Chopra, N. G.; Luyken, R. J.; Cherrey, K.; Crespi, V. H.; Cohen, M. L.; Louie, S. G.; Zettl, A. Boron-Nitride Nanotubes. *Science* **1995**, 269, 966-967.
12. Novoselov, K. S.; Geim, A. K.; Morozov, S. V.; Jiang, D.; Zhang, Y.; Dubonos, S. V.; Grigorieva, I. V.; Firsov, A. A. Electric Field Effect in Atomically Thin Carbon Films. *Science* **2004**, 306, 666-669.
13. Müller, K. -.; Herrmann, J.; Raguse, B.; Baxter, G.; Reda, T. Percolation model for electron conduction in films of metal nanoparticles linked by organic molecules. *Phys. Rev. B* **2002**, 66, 075417.
14. Wang, W.; Lee, T.; Reed, M. A. Elastic and Inelastic Electron Tunneling in Alkane Self-Assembled Monolayers. *The Journal of Physical Chemistry B* **2004**, 108, 18398-18407.
15. Smalley, R. E. Discovering the fullerenes. *Rev. Mod. Phys.* **1997**, 69, 723.

16. Bolotin, K. I.; Sikes, K. J.; Jiang, Z.; Klima, M.; Fudenberg, G.; Hone, J.; Kim, P.; Stormer, H. L. Ultrahigh electron mobility in suspended graphene. *Solid State Commun.* **2008**, *146*, 351-355.
17. Morozov, S. V.; Novoselov, K. S.; Katsnelson, M. I.; Schedin, F.; Elias, D. C.; Jaszczak, J. A.; Geim, A. K. Giant Intrinsic Carrier Mobilities in Graphene and Its Bilayer. *Phys. Rev. Lett.* **2008**, *100*, 016602.
18. Balandin, A. A.; Ghosh, S.; Bao, W.; Calizo, I.; Teweldebrhan, D.; Miao, F.; Lau, C. N. Superior Thermal Conductivity of Single-Layer Graphene. *Nano Letters* **2008**, *8*, 902-907.
19. Lee, C.; Wei, X.; Kysar, J. W.; Hone, J. Measurement of the Elastic Properties and Intrinsic Strength of Monolayer Graphene. *Science* **2008**, *321*, 385-388.
20. Novoselov, K. S.; Jiang, Z.; Zhang, Y.; Morozov, S. V.; Stormer, H. L.; Zeitler, U.; Maan, J. C.; Boebinger, G. S.; Kim, P.; Geim, A. K. Room-Temperature Quantum Hall Effect in Graphene. *Science* **2007**, *315*, 1379-1379.
21. Novoselov, K. S.; Geim, A. K.; Morozov, S. V.; Jiang, D.; Katsnelson, M. I.; Grigorieva, I. V.; Dubonos, S. V.; Firsov, A. A. Two-dimensional gas of massless Dirac fermions in graphene. *Nature* **2005**, *438*, 197-200.
22. Berger, C.; Song, Z.; Li, T.; Li, X.; Ogbazghi, A. Y.; Feng, R.; Dai, Z.; Marchenkov, A. N.; Conrad, E. H.; First, P. N.; de Heer, W. A. Ultrathin Epitaxial Graphite: 2D Electron Gas Properties and a Route toward Graphene-based Nanoelectronics. *The Journal of Physical Chemistry B* **2004**, *108*, 19912-19916.
23. Watcharotone, S.; Dikin, D. A.; Stankovich, S.; Piner, R.; Jung, I.; Dommett, G. H. B.; Evmenenko, G.; Wu, S.; Chen, S.; Liu, C.; Nguyen, S. T.; Ruoff, R. S. Graphene/Silica Composite Thin Films as Transparent Conductors. *Nano Letters* **2007**, *7*, 1888-1892.
24. Stankovich, S.; Dikin, D. A.; Dommett, G. H. B.; Kohlhaas, K. M.; Zimney, E. J.; Stach, E. A.; Piner, R. D.; Nguyen, S. T.; Ruoff, R. S. Graphene-based composite materials. *Nature* **2006**, *442*, 282-286.

25. Wu, Q.; Xu, Y.; Yao, Z.; Liu, A.; Shi, G. Supercapacitors Based on Flexible Graphene/Polyaniline Nanofiber Composite Films. *ACS Nano* **2010**, *4*, 1963-1970.
26. Coleman, J. N.; Lotya, M.; O'Neill, A.; Bergin, S. D.; King, P. J.; Khan, U.; Young, K.; Gaucher, A.; De, S.; Smith, R. J.; Shvets, I. V.; Arora, S. K.; Stanton, G.; Kim, H.; Lee, K.; Kim, G. T.; Duesberg, G. S.; Hallam, T.; Boland, J. J.; Wang, J. J.; Donegan, J. F.; Grunlan, J. C.; Moriarty, G.; Shmeliov, A.; Nicholls, R. J.; Perkins, J. M.; Grievson, E. M.; Theuwissen, K.; McComb, D. W.; Nellist, P. D.; Nicolosi, V. Two-Dimensional Nanosheets Produced by Liquid Exfoliation of Layered Materials. *Science* **2011**, *331*, 568-571.
27. Withers, N. 2D nanostructures: Inorganic graphene. *Nat Chem* **2010**.
28. Museur, L.; Kanaev, A. Near band-gap photoluminescence properties of hexagonal boron nitride. *Journal of Applied Physics* **2008**, *103*, 103520-103520-7.
29. et, C. L. Thickness-dependent bending modulus of hexagonal boron nitride nanosheets. *Nanotechnology* **2009**, *20*, 385707.
30. Watanabe, K.; Taniguchi, T.; Niiyama, T.; Miya, K.; Taniguchi, M. Far-ultraviolet plane-emission handheld device based on hexagonal boron nitride. *Nat Photon* **2009**, *3*, 591-594.
31. Chen, Y.; Zou, J.; Campbell, S. J.; Le Caer, G. Boron nitride nanotubes: Pronounced resistance to oxidation. *Appl. Phys. Lett.* **2004**, *84*, 2430-2432.
32. Coleman, J. N.; Lotya, M.; O'Neill, A.; Bergin, S. D.; King, P. J.; Khan, U.; Young, K.; Gaucher, A.; De, S.; Smith, R. J.; Shvets, I. V.; Arora, S. K.; Stanton, G.; Kim, H.; Lee, K.; Kim, G. T.; Duesberg, G. S.; Hallam, T.; Boland, J. J.; Wang, J. J.; Donegan, J. F.; Grunlan, J. C.; Moriarty, G.; Shmeliov, A.; Nicholls, R. J.; Perkins, J. M.; Grievson, E. M.; Theuwissen, K.; McComb, D. W.; Nellist, P. D.; Nicolosi, V. Two-Dimensional Nanosheets Produced by Liquid Exfoliation of Layered Materials. *Science* **2011**, *331*, 568-571.
33. Li, D.; Muller, M. B.; Gilje, S.; Kaner, R. B.; Wallace, G. G. Processable aqueous dispersions of graphene nanosheets. *Nat Nano* **2008**, *3*, 101-105.

2 Reversibly Compressible and Stretchable spring like Polymeric Nanojunctions between Gold nanoparticles

2.1 Overview

The question this chapter sets out to address is whether or not it is possible to incorporate controlled dynamics within an electronic construct designed from metallic nanoparticles. Integrating molecular dynamics into nanoelectronics has the potential to enable the development of nano electromechanical systems like energy storage devices, molecular timers and molecular actuators, which could be integrated to build self-sustaining molecular machines. The major challenges in building such a system are: **(a)** providing mechanism for application of confined forces acting on or generated by the molecular-junction, **(b)** fabrication of strong chemically-bonded molecular-junctions, which will not fail upon mechanical deformation, and **(c)** having a nano-scale mechanically mobile system to achieve unrestrained mechanics. Such molecular mechanics cannot be achieved in a device construct where molecular junctions are incorporated between 'rigid' electrodes.

We demonstrate here the fabrication and operation of a "molecular-spring" nanodevice which can store compression and stretching energy under the application of controllable and confined forces. The system is built by covalently/electrostatically incorporating cross-linked polyelectrolyte (cPE) molecules in between gold nanoparticles (GNPs). This leads to a sandwiched structure of cPE molecules in between gold nanoparticles. The molecular-junctions are reversibly compressed and stretched by applying electrically and centrifugally induced forces respectively, while GNPs play a dual role of: **(a)** movable connectors to apply forces, and **(b)** nano electrodes to measure molecular deformation via change in electron tunneling conductivity. These 'molecular-spring' junctions can thus be compressed and stretched by high electrical field and centrifugal field respectively, and can subsequently apply forces on the nanoparticles to bring them back to their native state. We show here a study on the dynamics of these junctions.

2.2 Introduction

The ability to control the electronic properties and manipulate the surface chemistries of zero- (0D), one- (1D), and two-dimensional (2D) nanostructures has led to the development of novel nanoscale constructs with a wide range of applications. Over the last decade, molecules with actuating mechanics and unique structural properties have been incorporated between electrode junctions^{1,2} to develop memory switches,³ shuttles,⁴⁻⁶ and rectifiers.^{7,8} In addition, 0D nanoparticles have been used for plasmonic devices,⁹ gas detection,¹⁰ and biodevices,¹¹ 1D nanowires for nanogenerators^{12,13} and biosensors,¹⁴ and 2D graphene nanostructures in solar cells¹⁵ and gas sensors.¹⁶ Furthermore, the mobility of nanocomponents has recently brought a new degree of freedom in nanodevice operations using novel nanoelectromechanical systems, such as carbon-nanotube switches,¹⁷ biodevices,¹⁸ gas detectors,¹⁰ touch sensors,¹⁹ elastic membranes,²⁰ and mechanical gauges.²¹ Integrating such mobility of nanoparticles with the elasticity of polymers can produce next-generation spring like electromechanical nanodevices and molecular machines. Herein, we present a study of the electromechanics of an array of gold nanoparticles (GNPs) with spring like nanoscale polymeric junctions incorporated between them.

Integration of the elasticity of polymeric junctions into a device construct requires: **(1)** sustained forces applied to the junction from opposite directions, **(2)** a structurally well integrated polymeric junction, and **(3)** a nonrigid system with reasonable mobility to achieve unrestrained motion. Herein, we consider a device with cross linked poly(allylamine hydrochloride) (cPAH) molecules sandwiched between 30-nm GNPs (**Figure 2.1**). Metal nanoparticles, with their low mass and electronic properties that are sensitively dependent on organic capping²²⁻²⁴ and interparticle distance,^{10,18,19,25,26} are great candidates for both applying confined forces and measuring molecular deformation, while the cPAH provides the elastic polymeric junction. The GNP-cPAH structure is fabricated by a diffusional electrostatic assembly process, in which the thickness of the inter nanoparticle polymeric junctions can be controlled by the duration of nanoparticle deposition and the degree of cross linking of cPAH (as shown ahead)

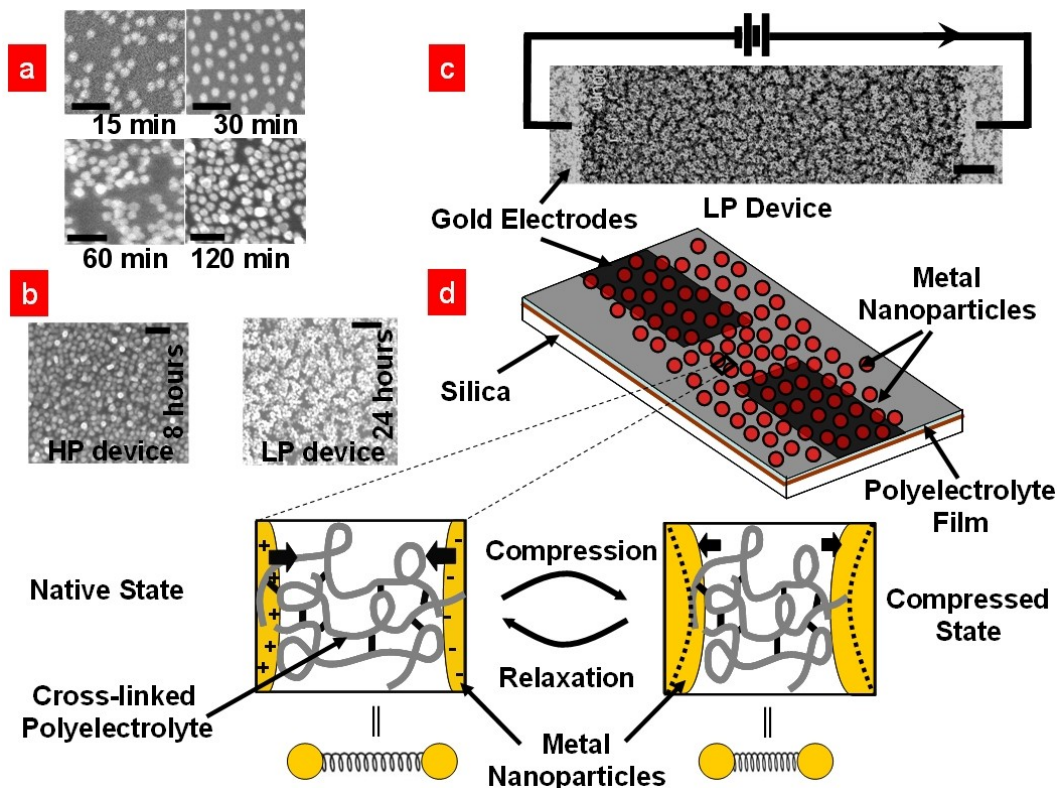


Figure 2.1 Fabrication and functioning of GNP-cPAH device. **a)** Field-emission scanning electron microscopy (FESEM) images of 30-nm GNPs deposited on ~50-nm-thick cPAH film, which show an increase in GNP density with deposition time. Conduction-percolation is achieved at 120 min. **b)** FESEM images of typical HP and LP devices with deposition times of 8 and 24 hours, respectively. **c)** FESEM image of a typical LP device between gold electrodes connected to a power supply. **d)** Schematic representation of compression and stretching of cPAH junctions between GNPs. Upon application of a high electric field, the GNPs undergo charge polarization leading to mutual attraction, which compresses the cPAH junction. Upon application of centrifugal force, the GNPs move apart causing the cPAH junctions to stretch. Scale bars: 100nm for (a, b) and 500nm for (c).

2.3 Experimental Section

2.3.1 Diffusional electrostatic assembly process

The devices were prepared on a 1- μ m-thick silica substrate with gold electrodes 300nm thick, 5 μ m apart, and 0.7mm wide (see Appendix A, Figure A.1) by a diffusional electrostatic

assembly process. The silica substrate was treated with an oxygen plasma (600 mTorr, 100 W, 120 s) to clean the surface and to introduce hydrophilic groups. Positively charged polyelectrolyte, PAH solution (5%), was spin-coated (3000 rpm, 30 s) on the clean silica substrate. The film was then baked in oxygen at 140 °C for 18 h to partially crosslink the PAH and to attach it to silica,³⁸ whereby increasing the baking time and temperature increased the degree of cross-linking. The excess PAH not bound to the substrate was removed by placing the substrate in deionized water for 1 min and drying in nitrogen. The prepared substrate was then suspended in negatively charged GNP solution to deposit GNPs on the cPAH film, followed by washing with water and drying. GNP deposition led to further cross-linking of the cPAH film.

2.3.2 *Estimation of compression–stretching*

All the measurements of average compression and stretching of the junctions were conducted by the Simmons model for electron tunneling.¹⁸ The low barrier height (≈ 0.4 eV) calculated from the Fowler–Nordheim fit suggests that the Simmons model is a more appropriate fit for our case. Fitting the data with the Simmons model gave a barrier height of (0.8156 ± 0.0091) eV for the LP device and (0.8335 ± 0.0064) eV for the HP device. The compression Δd was calculated from the Simmons model by taking the ratio between the final and initial conductivities at low bias (0.2 V):

$$\frac{J}{J_o} = \exp\left(-2 \frac{\sqrt{2m\phi}}{\eta} \Delta d\right) \quad \text{Equation 2.1}$$

where J is the current density, Δd is the compression of tunneling distance, m is the electron mass, ϕ is the barrier height, and h ($=2\pi\hbar$) is Planck's constant. This expression is similar to direct tunneling. The change in the barrier height due to rearrangement of molecules is expected to be low [39] and was not included in the analysis.

2.3.3 *Estimation of the difference in tunneling distances $d_{HP}-d_{LP}$*

The difference between the average initial cPAH thicknesses for LP and HP devices was calculated by manipulating the Simmons model to factor out the barrier thickness from the pre exponential term (details in the Appendix). For both HP and LP devices, conductivities were

measured at $V_1 = 0.01$ V ($V \ll \phi / e$) and $V_2 = 1$ V ($V \ll \phi / e$) and the following expression was used to calculate the difference in the thickness between LP and HP polymeric junctions:

$$\frac{(J_1^2/J_2)_{HP}}{(J_1^2/J_2)_{LP}} = \exp\left(-\frac{\sqrt{m\phi}}{\eta}(4-\sqrt{2})(d_{HP}-d_{LP})\right) \quad \text{Equation 2.2}$$

The difference in the junction thickness ($d_{HP}-d_{LP}$) was found to be 0.81 nm. Devices with high cPAH (HP) or low (LP) cPAH junction thickness were fabricated with a GNP deposition time of about 8 hours and 24 hours, respectively (**Figure 2.1a,b**). The GNP deposition time determined the deposition density of the GNPs and in turn the thickness of the polymeric junctions (see Appendix A, Figure A.2). Nanoparticles formed a generally 2D percolating network between gold electrodes (**Figure 2.1c**). HP devices were observed to have conductivity an order of magnitude lower than that of LP devices ($d_{HP} > d_{LP}$, **Figure 2.2**).

2.3.4 Relationship between compression forces and the electric field

The electric-field-induced forces generated between the nanoparticles are attributed to electric-field-induced polarization of the GNPs. The polarization charges induced would be directly proportional to the total electric field minus the fraction used to generate currents:

$$q_{\text{polarization}} \propto (E - \alpha IE) \quad \text{Equation 2.3}$$

where E is the applied electric field, I is the current flowing through the systems, and α is the proportionality constant, which is dependent on the fraction of time tunneling takes place. Since the force of attraction between the nanoparticles is caused by these induced charges, the term expressing this force would be:

$$F \propto \frac{(E - \alpha IE)^2}{(d_o - \Delta d)^2} \quad \text{Equation 2.4}$$

where F is the force, d_o is the initial average junction thickness, and Δd is the final compression. Further, we know that at equilibrium²⁰

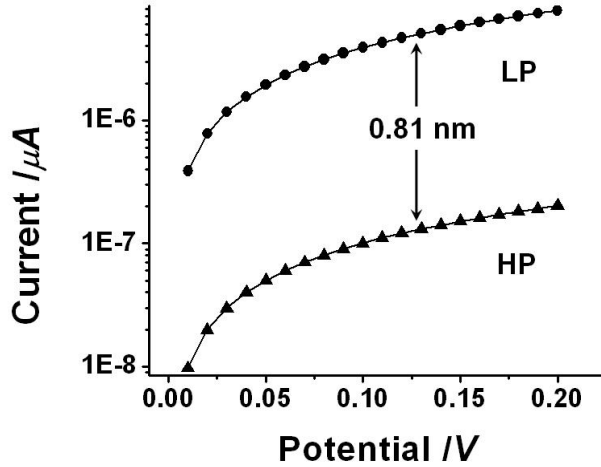


Figure 2.2 Conductivities of HP and LP devices. The inter nanoparticle distance was controlled by varying the time of deposition of nanoparticles. Two kinds of devices are presented, namely HP and LP devices with deposition times of ~8 h and ~24 h to get higher and lower inter-GNP cPAH thickness, respectively, which in turn affects the native conductivity as shown. The difference in the inter particle distance for these devices can be calculated using the force balance and electron tunneling equations:

$$F \propto (\Delta d) \quad \text{Equation 2.5}$$

$$I \propto \exp\left(-2 \frac{\sqrt{2m\phi}}{\eta} \Delta d\right) = \exp(2.304 \Delta d) \quad \text{Equation 2.6}$$

Combining these equations we get:

$$E \propto \frac{(\Delta d)^{1/2} \left(1 - \left(\Delta d / d_o\right)\right)}{(1 - B \exp(2.304 \Delta d))} \quad \text{Equation 2.7}$$

This expression fits the data well with a regression of 99.76%. From this analysis the initial thickness of the HP device was found to be 2.34 nm. Thermal studies on similar devices¹⁸ have shown that the mode of electron transfer between nanoparticles is electron tunneling^{18,27} (direct tunneling at low voltages and Fowler–Nordheim tunneling at higher voltages; Appendix A, Figure A.3). From the Fowler–Nordheim fit to the current–voltage (I–V) curves, the barrier height was calculated to be low (≈ 0.4 eV) when compared to the band gap of most polymers (6–

8 eV), thus invalidating the Fowler–Nordheim fit based on a square barrier.²⁸ Therefore, in our case, the Fermi level of the metal nanoparticle is close to either the highest occupied molecular orbital (HOMO) or lowest unoccupied molecular orbital (LUMO) level, for which the Simmons model,^{29,30} which is based on a triangular barrier, is a more appropriate fit.²⁸ The barrier heights estimated from the Simmons fit are (0.8335 ± 0.0064) and (0.8156 ± 0.0091) eV for the HP and LP devices, respectively. Further, the difference in the average junction thicknesses of the HP and LP devices is estimated from the Simmons model to be $d_{\text{HP}} - d_{\text{LP}} = (0.81 \pm 0.007)$ nm (see Experimental Section; error = 0.858%). All the measurements of compression and stretching of junctions reported herein are made by the Simmons model fit, where the conductivity is inverse exponentially proportional to the barrier width (junction thickness), thus making it sensitively dependent on the junction thickness and giving an accurate estimate of junction compression and stretching.

2.4 Results and Discussion

Presented are the mechanics of compression and stretching of GNP–cPAH junctions induced by application of a high electric field and a radial centrifugal field, respectively (**Figure 2.1d**). To induce compression, a high electric field is applied which polarizes the metal nanoparticles, thus causing a mutual attraction between them.²⁵ For stretching the junctions, a centrifugal field is applied to induce the nanoparticles to move apart. Further, a solvent-induced GNP rearrangement process is also demonstrated that releases internal stresses in GNP–cPAH structures.

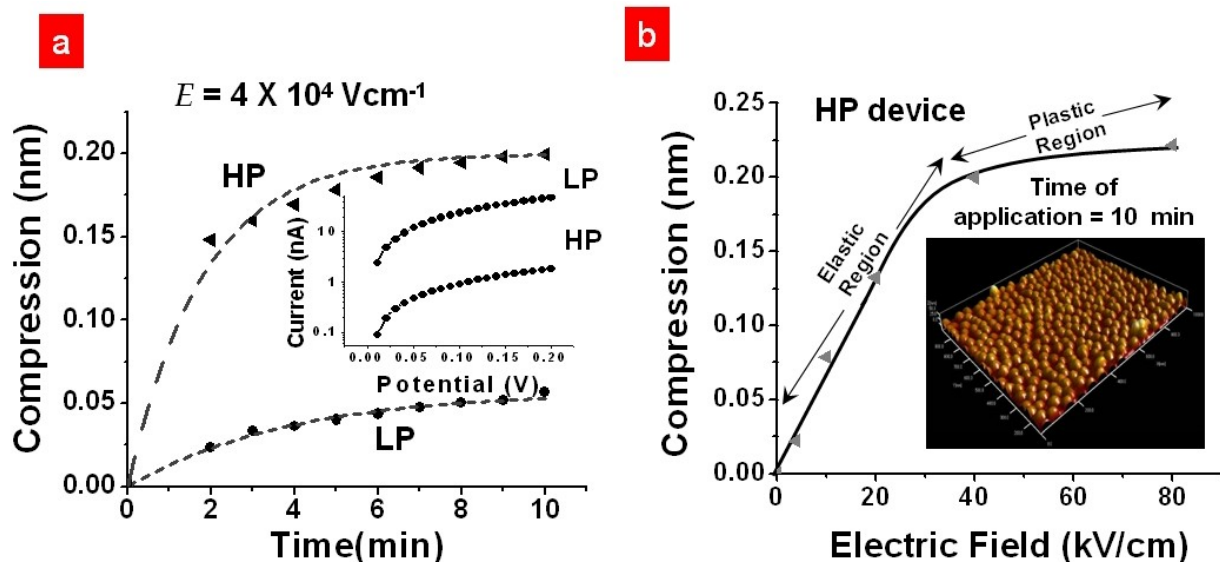


Figure 2.3 Compression of elastic cPAH junctions. **a)** Electric-field-induced ($4 \times 10^4 \text{ V cm}^{-1}$) cPAH junction compression for LP and HP devices over 10 min, where compression increases with time before reaching a steady-state value of 0.2 and 0.05 nm for the HP and LP devices, respectively. The data fit well with the spring-in-viscous-media equation (dashed line). Inset: native conductivity states for the devices. **b)** Steady-state junction compression in an HP device as a function of electric field applied for 10 min. The solid line is the fit for compression due to electric-field-induced polarization. Inset: AFM image of an HP device.

During the electric-field-induced compression process, the electron-tunneling events were found to produce a current of approximately $0.1 \mu\text{A}$ per nanoparticle or a minimum electron-transport time of $\approx 10^{-12} \text{ s}$ per nanoparticle. Since a tunneling event has a timescale of the order of 10^{-15} s ,³¹ during $\approx 99.9\%$ of the time there is no tunneling and nanoparticles undergo charge polarization which produces the inter particle force. These forces are responsible for the compression process.

Upon application of a $4 \times 10^4 \text{ V cm}^{-1}$ electric field for 10 min, the LP and HP devices undergo junction compression that increases with time and reaches a steady-state value of ≈ 0.05 and $\approx 0.2 \text{ nm}$, respectively (**Figure 2.3a**; see Experimental Section). The rate of molecular compression was found to decrease with time (Appendix A, Figure A.5), thus indicating an increase in opposing force, which is characteristic of a spring (junction). An LP device with

lower junction thickness undergoes a lesser compression than an HP device with higher junction thickness ($d_{\text{HP}} - d_{\text{LP}} = 0.81 \text{ nm}$; **inset of Figure 2.3a**). The average forces per nanoparticle generated by an electric field of $4 \times 10^4 \text{ V cm}^{-1}$ were calculated indirectly using the spring constants determined by the centrifugal experiments (shown later). The estimated forces were found to be $1.972 \times 10^{13} \text{ N}$ per junction for the LP device and $6.143 \times 10^{14} \text{ N}$ per junction for the HP device. These values are comparable to the reported force generated by an azo polymer ($2.6 \times 10^{14} \text{ N}$ per molecule), where the force from the conformational change of the azo groups led to a 0.22-nm displacement of an attached atomic force microscopy (AFM) tip.³²

The compression–time curve was found to follow the equation of the spring in viscous media (shown as a dashed line in **Figure 2.3a**):

$$\frac{\partial^2 \Delta d}{\partial t^2} \alpha \left(F_{\text{external}} - A \frac{\partial \Delta d}{\partial t} - k \Delta d \right) \quad \text{Equation 2.8}$$

From this fit, the ratio of the spring constants of the LP and HP devices ($k_{\text{LP}}/k_{\text{HP}}$) was found to be 12.32, which is consistent with that calculated from the centrifugal field study (13.18, shown later). This high ratio ($k_{\text{LP}}/k_{\text{HP}}$) is expected because the spring constant for axial elongation of a freely jointed chain of a polymer is given by equation , where h is the extended length of the polymer and α and β ($\beta > 2$) are polymer-specific constants.³³

$$k \alpha \left(\frac{\alpha k T}{h^\beta} \right) \quad \text{Equation 2.9}$$

The steady-state junction compression was found to increase with the magnitude of the applied electric-field-induced force (Figure 2.3b). A simple model for the polarization-induced force on the nanoparticles relates the compression to the electric field:

$$E \alpha \frac{(\Delta d)^{1/2} \left(1 - \left(\Delta d / d_o \right) \right)}{(1 - B \exp(2.304 \Delta d))} \quad \text{Equation 2.10}$$

where E is the electric field, Δd is the compression, d_o is the initial average thickness, and B is a constant proportional to the fraction of time tunneling occurs (explained in the Experimental Section). This model fits well with the data (solid line in Figure 2.3b) with regression of 99.76%.

The value of d_{HP} from this fit is (2.34 ± 0.12) nm, which gives a value of $d_{LP} = (1.53 \pm 0.12)$ nm (and $d_{HP}-d_{LP} = 0.81$ nm).

After removing the electric field, the compressed molecules were observed to relax by exerting a force that moves the nanoparticles back to their native positions. To reduce the timescale of operation, an LP device was initially compressed to a fixed base level, followed by a further compression of ≈ 2.3 pm, which decompressed to the base level in ≈ 0.5 min (**Figure 2.4a**). A similar compression by ≈ 4.3 and 6.3 pm led to decompression to the base level in ≈ 2 and 6 min, respectively (**Figure 2.4a**). The average rate of decompression depends on the thickness of the native junction (Appendix A, Figure A.7) and the magnitude of the induced compression. The rate of decompression followed the spring-in-viscous-media equation (solid line in **Figure 2.4a**; see the discussion on device dynamics in Appendix A, section A.8). A complete compression–decompression cycle and the associated two orders of magnitude change in conductivity for the electric-field-induced force on an HP device is shown in **Figure 2.4b**, where molecules compressed by 0.2 nm relax back to their native state in ≈ 1200 min.

Furthermore, since the nanomechanical response of the polymeric junctions depends on the mobility of the GNPs, changing the restraint on the GNPs by anchoring them with different polyelectrolyte thicknesses changes the device performance (Appendix A, Figure A.8). It was determined that for the system to exhibit a reversible compression, the poly electrolyte thickness cannot be too small (i.e., monolayer) or too large (>100 nm in thickness). For example, devices fabricated through layer-by-layer assembly of (PAH–GNP)¹⁰, with a monolayer of PAH between the GNPs and the substrate, did not exhibit compression. This finding is attributed to the complete restraining of the GNPs because they are closely bound to the surface. On the other hand, devices fabricated with a much larger polyelectrolyte thickness (>100 nm) exhibited partial relaxation in their initial compression runs (Appendix A, Figure A.9)

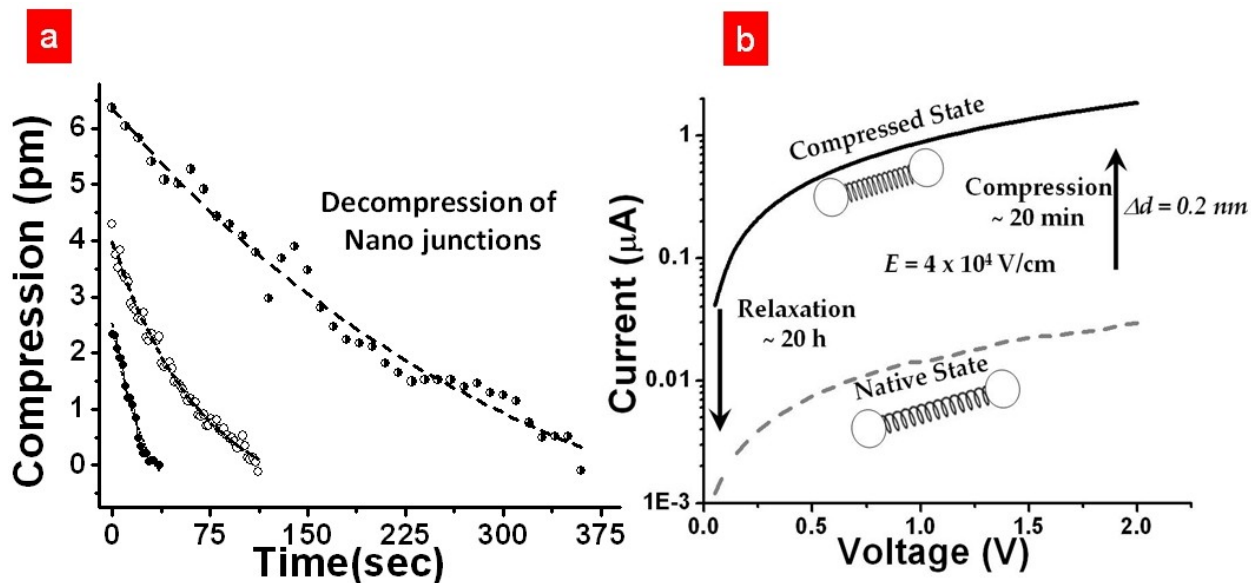


Figure 2.4 Relaxation of the cPAH junctions. a) Compressed molecules upon release of electric-field-induced forces relax back to their native state with the rate of relaxation governed by the magnitude of compression. An LP device compressed by ≈ 2.3 , 4.3 , and 6.3 pm relaxes back to its precompressed state in ≈ 0.5 , 2 , and 6 min, respectively. The relaxation data fit well with the spring-in-viscous-media equation (solid line). b) Compression–relaxation cycle of an HP device with two conductivity states. The compressed state (0.2 nm compressed) with conductivity higher by two orders of magnitude is achieved by application of an electric field of 40 kV cm^{-1} for 20 min and the native state is restored after $\approx 1200 \text{ min}$.

This result is attributed to an irreversible relocation of GNPs into the larger polyelectrolyte network. Finally, the devices with a $\approx 50\text{-nm}$ -thick polyelectrolyte layer and 30-nm GNPs show completely reversible compression (**Figure 2.4b**). Here, the GNPs exhibit a relatively unrestrained mobility without undergoing irreversible relocation. This unrestrained motion also compensates for the collective compression of the junctions .

It was established that an electric-field-induced increase in conductivity is a consequence of junction compression and not of charge trapping or ionic conductivity, as explained by the following points. (1) An LP device subjected to successive applications of positive and negative electric fields of $6 \times 10^4 \text{ V cm}^{-1}$ for 5 min exhibited a continued increase in conductivity, which indicates a polarization-induced compression (**Figure 2.5a**), unlike

charge trapping where an increase is expected to be followed by a decrease in conductivity for charging and discharging of the junction. **(2)** Typically, a two orders of magnitude higher electric field is required for charge trapping than the electric fields used in this study.³⁴ **(3)** The conductivity change due to charge trapping occurs at a timescale of micro- to nanoseconds³⁵ as a result of fast charge transfer, whereas in this study the timescales are in minutes. **(4)** There is no diodic behavior or hysteresis for high-voltage I–V runs (Appendix A, Figure A.6).

Compression of the molecular junction was confirmed by studying the electromechanical response of a device on a crosswire electrode arrangement (**Figure 2.5b, inset**). A $4 \times 10^4 \text{ V cm}^{-1}$ electric-field-induced compression of 4.3 pm along the x axis resulted in molecular stretching of 1.6 pm in the y direction, which indicates transverse-compression-induced longitudinal stretching (**Figure 2.5b**).

This gives a Poisson's ratio for the GNP–cPAH structure of 0.37, which is comparable to the 0.33 to 0.5 for polyelectrolyte multilayers.^{36,37} Since both an increase and a decrease in conductivity are observed instantaneously on the same device, this observation also confirms that the change in conductivity is not a result of the change in contact resistance. Additionally, the conductivity change is not thermally induced since any heat generated due to current flux should dissipate in much smaller timescales; however, in many cases decompression took as long as ≈ 1000 min. Ionic conductivity was also eliminated as a mode of conduction, since vacuum application led to an increase in conductivity, which is contrary to ionic conductivity.

To induce stretching of the polymeric junctions, a centrifugal field was applied to the GNP–cPAH devices. As expected, all devices under the centrifugal field showed an increase in molecular stretching with time before reaching the steady state (**Figure 2.6a**). An LP device placed in a centrifugal field of 90 g [$\approx 1.065 \times 10^{-14} \text{ N}$ per junction, calculated by using Equation 2.11] shows a steady-state molecular stretching of $\approx 2.7 \text{ pm}$ ($\approx 35.61 \text{ pm}$ for the HP device; see Appendix A, Figure A.10).

$$F_{\text{centrifugal field}} = (2\pi R \Delta R t \rho_{\text{GNP-cPAH}}) \omega^2 \Delta R$$

Equation 2.11

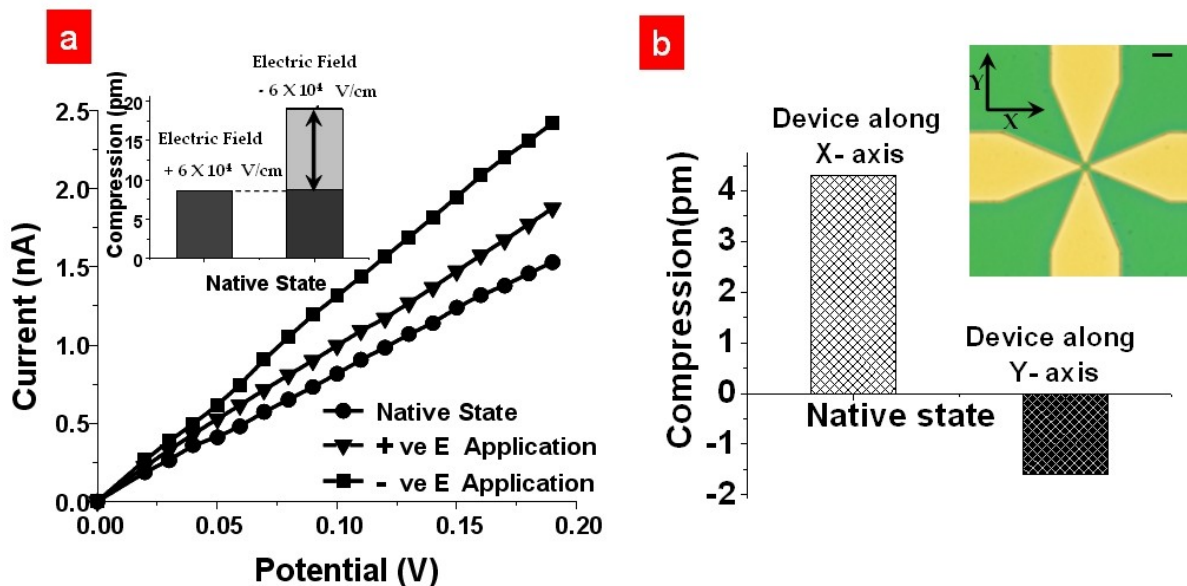


Figure 2.5 Proof of compression mechanism. a) The conductivity of an HP device increases upon successive applications of electric fields of equal magnitude in the positive ($+6 \times 10^4$ V cm^{-1}) and negative (-6×10^4 V cm^{-1}) directions. Inset: the increase in average junction compression. b) In a crosswire configuration of electrodes, upon application of a 4×10^4 V cm^{-1} electric field in the x direction, a molecular compression of ≈ 4.2 pm along the x axis results in molecular stretching of ≈ 1.8 pm along the y axis. Top inset: optical micrograph of the crosswire configuration of electrodes. Bottom inset: schematic of expansion in the y direction induced by compression in the x direction. (a) and (b) together show that the change in conductivity in LP and HP devices is exclusively a result of molecular compression and not charge trapping. Scale bar: 10 μm .

Here, R is the position of the device from the center of the centrifuge, ΔR is the distance between GNPs, ρ and t are the density and thickness of the GNP-PAH film, and ω is the angular velocity. As in the case of electric-field-induced compression, the spring-in-viscous-media equation fits well for the centrifugation-induced stretching (solid line in **Figure 2.6a**). No cPAH stretching is observed below a threshold centrifugal field of 45 g, which corresponds to the static frictional barrier to move nanoparticles (probably due to bonds with the substrate surface). A linear junction stretching is observed above 45 g.

A direct measurement of the spring constant (or stiffness) for the HP and LP devices was made by steady-state measurement of stretching at different forces. The spring constant for the HP device was estimated to be $k_{HP} = 2.99 \times 10^{-4} \text{ N m}^{-1}$ and for the LP device was $k_{LP} = 3.94 \times 10^{-3} \text{ N m}^{-1}$. The higher spring constant for the LP device is expected, as explained earlier. These values are comparable to the spring constants estimated for lateral compression of polyelectrolyte film ($k = 2.76 \times 10^{-3} \text{ N m}^{-1}$).³⁶ The typical transient relaxation behavior of a device is shown in **Figure 2.6b**, where a pre-stretched LP device, when further stretched by 12 pm, relaxes back to the pre-stretched level in ≈ 60 min. The data fit well with the spring-inviscous-media equation (solid line in **Figure 2.6b**). The inset in **Figure 2.6b** shows the centrifugation setup. Further, since the deformation of the junctions (electrically measured) is purely mechanically induced by centrifugal force, these results confirm the mechanical characteristics of the junction-deformation model of **Figure 2.1d**. However, further microscopic studies will be required to completely understand the mechanism of deformation.

In another experiment, to release the internal stresses in the nanoparticle array, the GNP-cPAH devices were subjected to multiple annealing cycles of removal and addition of water adsorbed on cPAH junction molecules. An annealing cycle consisted of a 3 min exposure to a vacuum (1 mTorr) to remove the adsorbed water and a 5 min exposure to $\approx 40\%$ humidity to allow readsorption. A typical response to annealing is shown in **Figure 2.6c**, where for an LP device an irreversible increase in average inter nanoparticle distances of ≈ 6 pm (corresponding to a decrease in conductivity of the device) was observed after four annealing cycles. This phenomenon is attributed to the release of the internal stresses in the nanoparticle array created during fabrication. While adsorption of water causes cPAH to become charged, mobile, and swollen, desorption of water causes the junction to contract. Repeated cycles of adsorption-desorption allow stabilization and readjustment of the nanoparticles, which causes the release of internal stresses. From our calculations of the spring constant for the LP device, we estimate the internal stresses per nanoparticle due to fabrication to be $2.36 \times 10^{-14} \text{ N}$ per junction by using Equation 2.12:

$$F|_{\text{expansion}}/\text{Area} = (k_{LP}x)/(\pi d_{GNP}^2/4)$$

$$\text{Equation 2.12}$$

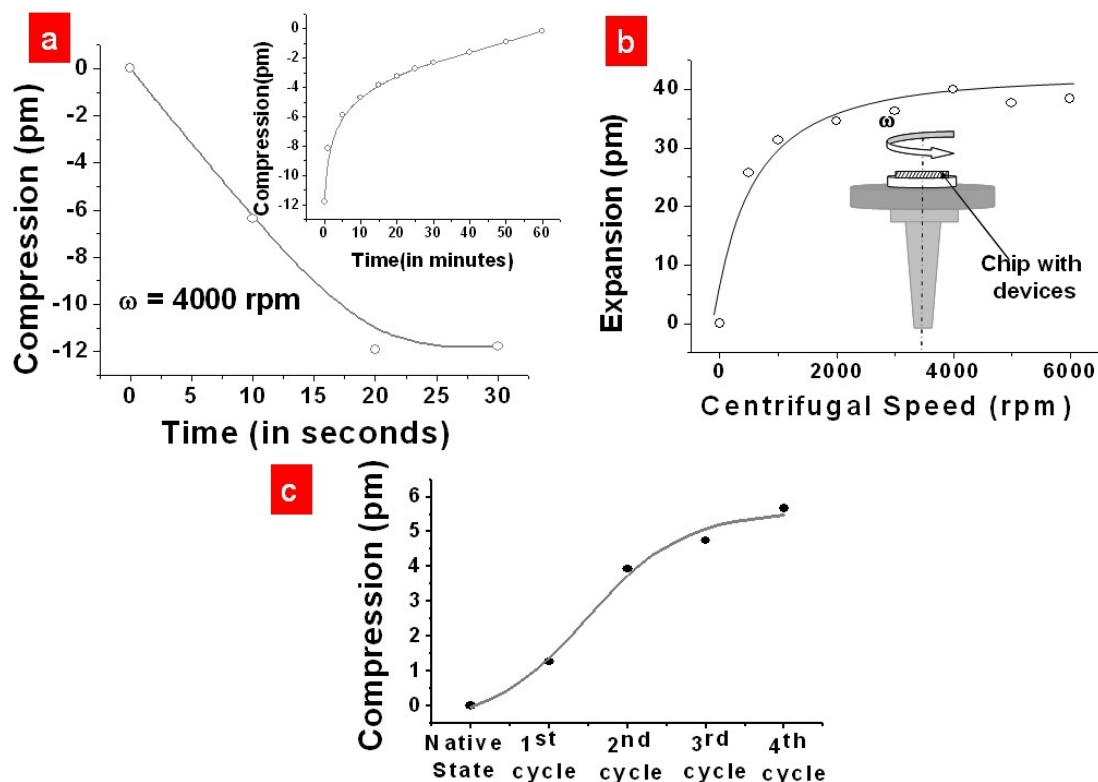


Figure 2.6 Molecular stretching. a) Centrifugation-induced stretching is achieved by spinning an LP device under a centrifugal field of 90 g, which results in an increase in the junction stretching with time. Steady-state stretching of 2.7 pm is achieved in 30 s. The data fit well with the spring-in-viscous-media equation (solid line). The inset shows the increase in stretching with an increase in centrifugal field applied for 30 s. After a threshold centrifugal field of 45 g, cPAH junction stretching was found to increase linearly (solid line) with centrifugal field. b) The transient relaxation of another LP device is shown. The device relaxes from its stretched state of 12 pm to its prestretched state in ≈ 60 min. Inset: schematic of the setup for a device chip on a centrifuge. c) Solvent-induced rearrangement. An LP device annealed with alternate exposures to a vacuum and 40% humidity leads to a decrease in conductivity. After the fourth cycle, an irreversible decrease in conductivity of 13% is achieved, which corresponds to ≈ 6 pm expansion of the molecular junctions. The observed expansion is expected to be a result of release of internal stress in the GNP–cPAH structure, which was estimated to be 2.36×10^{-14} N per junction.

Finally, it is important to note that the compression–stretching values measured here are the average for the cPAH junctions through which conduction occurs, which in turn are the smallest cPAH layer thicknesses, since conduction occurs through the least-resistant paths. Also, because we used a different set of LP and HP devices on the same chip for electrically induced compression, centrifugally induced stretching, and annealing, we add a further $\approx 10\%$ error in calculation of the spring constants and forces.

2.5 Summary

In conclusion, we have demonstrated a working system in which the spring like mechanics of cross linked molecular junctions have been incorporated as an active element of an electromechanical nanodevice, where forces (per junction) in the range of 10^{-15} to 10^{-13} N were found to produce 2.7 pm to 0.2 nm reversible compression or stretching of the junctions. The compression and stretching mechanics were found to be sensitively dependent on the junction properties and followed the spring-in-viscous-media model. The spring constants for the junctions were found to be 3.944×10^3 and 2.99×10^4 Nm^{-1} for devices with average junction thicknesses of 1.55 and 2.34 nm, respectively. We envision that this system will provide a solid step forward towards controlled electromechanics of nanoparticle devices. The integration of spring like molecular mechanics within nanodevices, as demonstrated here, can potentially be applied to build next-generation molecular systems, such as molecular-manipulation tools, electromechanical switches, and molecular-energy storage systems, and will add to the evolution of molecular machines and functional nanoelectronics.

2.6 References

1. L. Venkataraman, J. E. Klare, C. Nuckolls, M. S. Hybertsen, M. L. Steigerwald, Dependence of Single-molecule junction conductance on molecular conformation. *Nature* **2006**, 442, 904–907.
2. T. Dadoosh, Y. Gordin, R. Krahne, I. Khivrich, D. Mahalu, V. Frydman, J. Sperling, A. Yacoby, I. Bar-Joseph, Measurement of the conductance of single conjugate molecules *Nature* **2005**, 436, 677–680.

3. D. Dulic, S. J. van der Molen, T. Kudernac, H. T. Jonkman, J. J. D. De Jong, T. N. Bowden, J. van Esch, B. L. Feringa, B. J. van Wees, One way optoelectronic switching of photochromic molecules on gold *Phys. Rev. Lett.* **2003**, 91, 207402.
4. J. E. Green, J. W. Choi, A. Boukai, Y. Bunimovich, E. Johnston-Halperin, E. DeIonno, Y. Luo, B. A. Sheriff, K. Xu, Y. S. Shin, H. R. Tseng, J. F. Stoddart, J. R. Heath, A 160-kilobit molecular electronic memory patterned at 10^{11} bits per square centimetre *Nature* **2007**, 445, 414–417.
5. A. M. Brouwer, C. Frochot, F. G. Gatti, D. A. Leigh, L. Mottier, F. Paolucci, S. Roffia, G. W. Worpel, Photoinduction of Fast, Reversible Translational Motion in a Hydrogen-Bonded Molecular Shuttle *Science* **2001**, 291, 2124–2128.
6. N. Koumura, R. W. J. Zijlstra, R. A. van Delden, N. Harada, B. L. Feringa, Light-driven monodirectional molecular rotor *Nature* **1999**, 401, 152–155.
7. A. Aviram, M. A. Ratner, Molecular Rectifiers *Chem. Phys. Lett.* **1974**, 29, 277.
8. S. Yasuda, T. Nakamura, M. Matsumoto, H. Shigekawa, Phase Switching of a Single Isomeric Molecule and Associated Characteristic Rectification *J. Am. Chem. Soc.* **2003**, 125, 16430–16433.
9. J. K. Tang, H. L. Rong, X. C. Li, B. S. Zou, J. R. Li, The Photoelectric Response of Gold-Nanoparticle Monolayers *ChemPhysChem.* **2007**, 8, 1611–1614.
10. F. P. Zamborini, M. C. Leopold, J. F. Hicks, P. J. Kulesza, M. A. Malik, R. W. Murray, Electron Hopping Conductivity and Vapor Sensing Properties of Flexible Network Polymer Films of Metal Nanoparticles *J. Am. Chem. Soc.* **2002**, 124, 8958–8964.
11. S. J. Park, T. A. Taton, C. A. Mirkin, A Group-IV Ferromagnetic Semiconductor: $\text{Mn}_x\text{Ge}_{1-x}$ *Science* **2002**, 295, 1503–1506.
12. Y. F. Lin, J. Song, Y. Ding, S. Y. Lu, Z. L. Wang, Piezoelectric nanogenerator using CdS nanowires *Appl. Phys. Lett.* **2008**, 92, 022105.
13. J. H. Song, X. D. Wang, J. Liu, H. B. Liu, Y. L. Li, Z. L. Wang, Piezoelectric Potential Output from ZnO Nanowire Functionalized with p-Type Oligomer *Nano Lett.* **2008**, 8, 203–207.

14. Y. Cui, Q. Q. Wei, H. K. Park, C. M. Lieber, Nanowire Nanosensors for Highly Sensitive and Selective Detection of Biological and Chemical Species *Science* **2001**, 293,1289–1292.
15. X. Wang, L. J. Zhi, K. Mullen, Transparent, Conductive Graphene Electrodes for Dye-Sensitized Solar Cells *Nano Lett.* **2008**, 8, 323–327.
16. F. Schedin, A. K. Geim, S. V. Morozov, E. W. Hill, P. Blake, M. I. Katsnelson, K. S. Novoselov, Detection of individual gas molecules adsorbed on graphene *Nat. Mater.* **2007**, 6, 652–655.
17. J. E. Jang, S. N. Cha, Y. J. Choi, D. J. Kang, T. P. Butler, D. G. Hasko, J. E. Jung, J. M. Kim, G. A. J. Amaratunga, Nanoscale memory cell based on a nanoelectromechanical switched capacitor *Nat. Nanotechnol.* **2008**, 3, 26–30.
18. V. Berry, R. F. Saraf, Self-Assembly of Nanoparticles on Live Bacterium: An Avenue to Fabricate Electronic Devices *Angew. Chem.* **2005**, 117, 6626–6631.
19. V. Maheshwari, R. F. Saraf, High-Resolution Thin-Film Device to Sense Texture by Touch *Science* **2006**, 312, 1501–1504.
20. K. E. Mueggenburg, X. M. Lin, R. H. Goldsmith, H. M. Jaeger, Elastic membranes of close-packed nanoparticle arrays *Nat. Mater.* **2007**, 6, 656–660.
21. J. Herrmann, K. H. Muller, T. Reda, G. R. Baxter, B. Raguse, G. J. J. B. de Groot, R. Chai, M. Roberts, L. Wiczorek, Nanoparticle films as sensitive strain gauges *Appl. Phys. Lett.* **2007**, 91, 183105.
22. H. Cai, C. Xu, P. G. He, Y. Z. Fang, Colloid Au-enhanced DNA immobilization for the electrochemical detection of sequence-specific DNA *J. Electroanal. Chem.* **2001**, 510, 78–85.
23. A. S. Blum, Cowpea Mosaic Virus as a Scaffold for 3-D Patterning of Gold Nanoparticles *Nano Lett.* **2004**, 4, 867–870.
24. R. P. Andres, J. D. Bielefeld, J. I. Henderson, D. B. Janes, V. R. Kolagunta, C. P. Kubiak, W. J. Mahoney, R. G. Osifchin, Self-Assembly of a Two-Dimensional Superlattice of Molecularly Linked Metal Clusters *Science* **1996**, 273, 1690–1693.
25. V. Berry, S. Rangaswamy, R. F. Saraf, Highly Selective, Electrically Conductive Monolayer of Nanoparticles on Live Bacteria *Nano Lett.* **2004**, 4, 939–942.

26. H. Wohltjen, A. W. Snow, Colloidal Metal–Insulator–Metal Ensemble Chemiresistor Sensor *Anal. Chem.* **1998**, 70, 2856–2859.
27. K. H. Müller, J. Hermann, B. Raguse, G. R. Baxter, T. Reda, Percolation model for electron conduction in films of metal nanoparticles linked by organic molecules *Phys. Rev.B.* **2008**, 66, 075417.
28. W. Y. Wang, T. Lee, M. A. Reed, Elastic and Inelastic Electron Tunneling in Alkane Self-Assembled Monolayers *J. Phys. Chem. B* **2004**, 108, 18398– 18407.
29. J. G. Simmons, Generalized Formula for the Electric Tunnel Effect between Similar Electrodes Separated by a Thin Insulating Film *J. Appl. Phys.* **1963**, 34, 1793–1803.
30. J. G. Simmons, Generalized Thermal J-V Characteristic for the Electric Tunnel Effect *J. Appl. Phys.* **1964**, 35, 2655–2658.
31. K. K. Likharev, Single electron devices and their applications *Proc. IEEE* **1999**, 87, 606–632.
32. T. Hugel, N. B. Holland, A. Cattani, L. Moroder, M. Seitz, H. E. Gaub, Single molecule optomechanical cycle *Science* **2002**, 296, 1103–1106.
33. G. W. Slater, Y. Gratton, M. Kenward, L. McCormick, F. Tessier, Deformation, Stretching and Relaxation of single polymer chains: Fundamentals and Examples *Soft Mater.* **2004**, 2, 155–182.
34. J.-S. Lee, J. Cho, C. Lee, I. Kim, J. Park, Y.-M. Kim, H. Shin, J. Lee, F. Caruso, Layer-by-layer assembled charge-trap memory devices with adjustable electronic properties *Nat. Nanotechnol.* **2007**, 2, 790–795.
35. C. Bauer, G. Boschloo, E. Mukhtar, A. Hagfeldt, Ultrafast relaxation dynamics of charge carriers relaxation in ZnO nanocrystalline thin films *Chem. Phys. Lett.* **2004**, 387, 176–181.
36. L. Richert, A. J. Engler, D. E. Discher, C. Picart, Elasticity of Native and Cross-linked polyelectrolyte multilayer films *Biomacromolecules* **2004**, 5, 1908–1916.
37. A. J. Nolte, M. F. Rubner, R. E. Cohen, Determining the Young modulus of polyelectrolyte multilayer films via stress induced mechanical buckling instabilities *Macromolecules* **2005**, 38, 5367–5370.

38. G. A. C. M. Spierings, J. Haisma, F. J. H. M. Vanderkruis, Direct bonding of organic polymeric materials *Philips J. Res.* **1995**, 49, 139–149.
39. M. Del Valle, R. Gutierrez, C. Tejedor, G. Cuniberti, Tuning the conductance of a molecular switch *Nat. Nanotechnol.* **2007**, 2, 176–179.

3 Implantation and Growth of Dendritic Gold nanostructures on Graphene derivatives: Electrical Property Tailoring and Raman Enhancement

3.1 Overview

This chapter presents the science of forming gold nanoparticle composites of graphene sheets. Interfacing electron-rich metal nanoparticles with graphene derivatives can sensitively regulate the properties of the resultant hybrid with potential applications in metal-doped graphene field-effect transistors (FETs), surface-enhanced Raman spectroscopy, and catalysis. Here, we show that by controlling the rate of diffusion and catalytic reduction of gold ions on graphene oxide (GO), dendritic “snowflake-shaped” gold nanostructures (SFGNs) can be templated on graphene. The structural features of the SFGNs and their interfacing mechanism with GO were characterized by microscopic analysis and Raman-scattering. We demonstrate that (a) SFGNs grow on GO-surface via diffusion limited aggregation; (b) SFGN’s morphology (dendritic to globular), size (diameter of 150-500 nm and a height of 45-55 nm), coverage density, and dispersion stability can be controlled by regulating the chemiophysical forces; (c) SFGNs enhance the Raman signal by 2.5 folds; and (d) SFGNs act as anti-reduction resist during GO-SFGN’s chemical reduction. Further, the SFGNs interfacing with graphene reduces the apparent band gap (from 320 to 173 meV) and the Schottky barrier height (from 126 to 56 meV) of the corresponding FET.

3.2 Introduction

Graphene’s unique electrical,^{1, 2} mechanical³ and interfacial⁴ properties, such as **(a)** high carrier mobility with ballistic transport,^{1, 2} **(b)** mechanically strong carbon-carbon sp²-bonded honeycomb lattice,⁵ **(c)** confined carrier transport in truly two-dimensional space,⁶ **(d)** adjustable surface chemistry via chemical⁷⁻⁹ or plasma¹⁰ processes and **(e)** sensitive response to surface doping,^{11, 12} have led to the development of ultrafast electronic devices,^{1, 2, 13, 14} molecular

resolution sensors,¹² biodevices,⁴ polymer composites,¹⁵ liquid-crystal devices,¹⁶ electromechanical systems,¹⁷ and magnetoresistive/quantum-Hall devices.¹⁸⁻²⁰ Currently, there is a great interest in functionalization⁷⁻⁹ and doping^{11, 12} of graphene to manipulate its electrical,^{7-9, 11} structural,⁴ and interfacial⁴ properties to enhance its performance. Although, chemical functionalization of graphene results in the formation of scattering sites that reduce its carrier mobility, the thus produced graphene chemical derivatives (GCDs) are appropriate for interfacing with other systems⁴ and for room-temperature electronic applications as they exhibit a suitable band gap/conductivity. Metal functionalization on graphene however needs to be controlled and its effect studied in detail. For this purpose, solution-based gold functionalization of graphene is shown here.

Being structurally distinct from 0D molecules and 1D polymers, solvent-dispersed GCDs with quasi-2D structure and tethered chemical groups show novel physiochemical properties. We demonstrate that GCDs function as excellent in-solution substrates for metal nuclei seeding and their subsequent growth into nano dendritic structures. This process, occurring on GO sheets, is governed by diffusion limited transport²¹ of the gold ions with anisotropic lattice incorporation of gold atoms during the seeding growth and is controlled by the mass-transfer rates (shown later) (**Figure 3.1a**). Here, since the SFGNs are grown on GO, this process is fundamentally different from spherical nanoparticle interfacing^{7, 22-24} with graphene, via adsorption, electrochemical, or chemical routes. The highly anisotropic SFGNs, templated on GO sheets 1–4 nm thick (1–5 layers) and 25–200 μm^2 in area, have predominantly five primary branches with several sharp-edged secondary branches. The SFGNs interfacing on GO leads to **(a)** increase in conductivity by two folds, and **(b)** 2-fold enhancement of the Raman signals from GO. Further, the GO–SFGN sheets reduced to graphene-SFGN hybrid exhibits an apparent band gap of 164.24 meV and a Schottky barrier height of 38.98 meV. We envision that the graphene-metal interfacing will open avenues for next-generation graphene applications in areas including electronics, where the semiconductor properties of graphene could be modulated and integrated with other GCD systems to make graphene logic devices; bioimaging/diagnostic systems, where the surface-enhanced Raman spectroscopy (SERS) from SFGNs could be used for sensing biocomponents and bioprocesses; optoelectronics, where the

optical properties of SFGNs could be integrated with the electrical sensitivity of graphene to build solar cells, optical sensors, etc.; nanoheaters, where the IR absorption by anisotropic gold nanostructures could be used to generate thermal energy; and nanocatalysts.²⁴

3.3 Experimental Section

3.3.1 Preparation of Graphene-Oxide

To prepare the GO sheets, 5 g of Mesh 7-graphite flakes were mixed with 33 mL of 68% nitric acid + 200 mL of 96% sulfuric acid and stirred continuously for 40 min in an ice bath; 30 grams of potassium permanganate was then added into the solution, while the temperature was slowly increased to 40 °C, and kept at 40 °C for 30 min. Subsequently, the excess potassium permanganate was removed by treatment with 10% hydrogen peroxide. Finally, the GO sheets were obtained by centrifuging this solution at 15000 rpm for 30 min followed by repeated washing with DI water. The sample was then dialyzed (MWCO 2000D) for 24 h and the subsequently stored as a suspension in DI water at room temperature. All the chemicals used in this process were obtained from Fisher Scientific.

3.3.2 Synthesis of GO-SFGN Hybrids

The GO-SFGN hybrids were synthesized by mixing 1.3 μ L of (50% w/v) hydroxyl-amine (Sigma Aldrich) to 50 mL of 0.275 mM gold chloride trihydrate (Fisher Scientific) followed by an addition of 100 μ L of graphene-oxide suspension (80 mM carboxylic acid, quantified by titration). The mixture is kept under constant agitation (100 rpm) at room temperature for 1 h which results in the formation of SFGNs on GO sheets that can be immobilized on an amine-functionalized silica substrate.

3.3.3 Immobilizing the GO-SFGN Hybrids on silica surface

The GO sheets functionalized with metal nanostructures were immobilized via electrostatic interactions on a heavily doped n-type silicon substrate with a 300 nm thick thermally grown silica layer. Briefly the substrate is first exposed to oxygen plasma (100 W, 2 mbar, 2 min) followed by treatment with 3-amino propyl triethoxy silane (Gelest) that makes

the surface positively charged. This amine-functionalized substrate is then baked for 4 min at 120 °C and then momentarily exposed (~2 min) to the aqueous dispersion of GO, hydroxyl amine, and gold salt. The substrate is then thoroughly washed with deionized (DI) water that facilitates electrostatic and selective deposition of GO-SFGN hybrids on silica.

3.3.4 TEM and SAED

TEM images and SAED patterns were obtained with a Philips CM 100 transmission electron microscope operated at 100 kV. The GO-SFGN hybrids were deposited from solution on to 300 mesh size copper TEM specimen grids (Electron Microscopy Sciences) having a carbon support film.

3.3.5 FESEM and EDS

FESEM Images and EDS data were obtained with a Leo field emission scanning electron microscope operated at 10-15 kV

3.3.6 Electrical Studies

The electrical measurements for determining the effect of hydrazine reduction on GO and GO-SFGN hybrids were taken at room temperature, under a steady nitrogen environment, using a Keithley 2612 dual-channel system source meter connected to a computer *via* a GPIB/IEEE-488 interface card. The temperature studies for determining the band gap and Schottky barrier height were carried out in a Janes cryostat, the temperature of which can be externally controlled by a Lake Shore 331 temperature controller.

3.3.7 Raman Spectroscopic Measurements

The Raman spectra of GO and GO-SFGN sheets were determined by using a LabRAM ARAMIS Raman spectrometer located at the University of Kansas, Bioengineering Research Center, Lawrence, KS. The instrument was manufactured by HORIBA Jobin Yvon (Edison, New Jersey), and a HeNe laser ($\lambda = 633$ nm, a laser power of 17mW) was used as one of the excitation sources for the samples. The instrument conditions were a 200 μm confocal hole, 150 μm wide

entrance slit, 600 gr/mm grating, and 100 \times objective Olympus lens. Data processing was performed using LabSPEC 5 (HORIBA Jobin Yvon). The samples were mounted in a computer-controlled, high-precision x-y stage.

3.4 Results and Discussion

In this work, Hummers method ^{8, 25} is used to prepare graphene oxide (GO), having oxy-functional groups such as carboxyl ($-\text{COOH}$), hydroxyl ($-\text{OH}$), and epoxy groups (4) on its surface. In GO suspension, these oxy-functional groups are leveraged to stabilize gold nuclei, synthesized in situ by hydroxyl-amine assisted reduction of gold salt. The gold nuclei are subsequently grown via the seeding growth mechanism (**Figure 3.1a**) to synthesize the GO-SFGN hybrid by mixing 1.3 μL of hydroxylamine (NH_2OH , 50% w/v) to 50 mL of 0.275 mM gold salt ($\text{HAuCl}_4 \cdot 3\text{H}_2\text{O}$) followed by an addition of 100 μL of graphene oxide (GO) suspension (80 mM carboxylic acid, quantified by titration). After constant agitation at room temperature for 1 h, the resultant GO-SFGN hybrid sheets are immobilized on an amine-silanized silica substrate (see Appendix B, Figure B.1). Field emission scanning electron microscopy (FESEM) (**Figure 3.1b, right**) indicated excellent templating of SFGNs on GO. The SFGNs appearing darker under FESEM (labeled as “D”) are probably a result of their attachment on the rear GO surface (facing silica), which shields the SFGNs giving lesser average surface-electron-density. The brighter SFGNs (labeled as “B”) are templated on the exposed GO-surface. This is expected since SFGNs will nucleate on both sides of the GO-sheets exposed to the solution. This is further evidenced by the wrinkles emanating on the GO sheets from darker SFGNs (beneath the GO sheet) (**Figure 3.1b left**, see Appendix Figure B.2), which are expected to raise, stretch, and therefore wrinkle the GO-sheets around them.

Figure 3.2a shows FESEM micrographs of SFGNs with five and six primary branches (N_p) and several secondary or side branches. The presence of these secondary branches makes the SFGNs fundamentally different from multipod and star-shaped gold nanostructures.⁽²⁶⁻²⁹⁾ TEM (Figure 3.1b, center) of an SFGN with five primary branches ($N_p = 5$), shows an average primary branch length (L_p) of 260 nm and an average width (W_p) (the maximum thickness of the primary branch at the nodal point) of 120 nm. Each primary branch backbone structure

emanates parallel secondary or side branches with the same angles of emergence (Θ_e) (the angle between a side branch and its primary branch backbone) which vary from 35° to 90° from branch to branch. Θ_e for side branches labeled S-1 and S-2 is 60° while that for the side branches

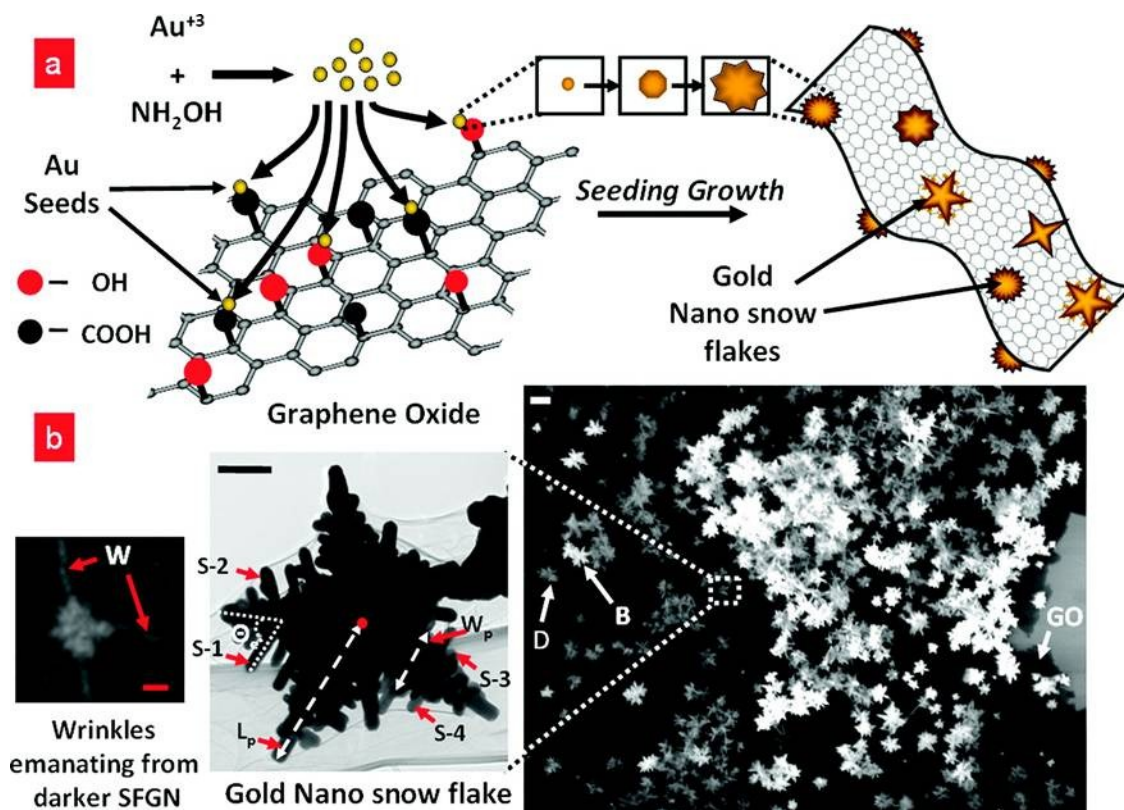


Figure 3.1 Formation mechanism of snowflake shaped gold nanostructures on graphene-oxide. (a) Interfacing the -COOH and -OH groups on GO sheets with a freshly prepared solution of gold nuclei, formed during hydroxyl-amine-assisted reduction of gold salt, results in nuclei attachment and seed-mediated formation of snowflake-shaped gold nanostructures (SFGNs) on the GO surface. (b) Right: FESEM of SFGNs templated on GO lying on silica surface. The SFGNs appearing darker (labeled D) are on the rear surface, while the SFGNs appearing brighter (labeled B) are on the front surface of the immobilized GO sheet (scale bar = 500 nm). Center: Higher magnification transmission electron microscopy (TEM) image showing the detailed characteristics and the structural parameters of SFGN exhibiting a dendritic morphology. Scale bar = 100 nm. Left: FESEM image showing wrinkles (labeled W) on GO associated with a darker SFGN. Scale bar = 200 nm.

labeled S-3 and S-4 is 80° (**Figure 3.1b, center**). This indicates that the secondary-branch's growth-direction is influenced by the crystal-lattice of their common primary branch rather than a random nucleation process. The longer secondary branches closer to the center than those near the tip, indicate that near-center secondary branches are exposed to the growth mixture for a longer time, implying a progressive growth of the primary branches from nuclei. Also, as shown later, a more pronounced secondary branching and instances of ternary branches in SFGNs can be obtained by increasing the concentration of gold ions in solution. Further characterization for more SFGNs is summarized in Appendix B, Table B1. Anisotropy as evaluated by circularity parameter ($\lambda = 4\pi \cdot \text{area} / \text{perimeter}^2$), as expected showed $\lambda < 1$, characteristic for branched structures (**Figure 3.2a, bottom insets**).

The effect of interaction of SFGNs with the GO-surface was probed by Raman scattering signal analysis for bare GO and GO-SFGN sheets (**Figure 3.2b**). Raman spectrum for a GO sheet exhibits the regular two peaks, corresponding to the D-band line (1340 cm⁻¹) and the G-band line (1590 cm⁻¹). SFGN-interfacing on GO enhanced the intensity of these bands by >250% (**Figure 3.2b**). Surface enhancement of Raman signals can be via electromagnetic enhancement (excitation of localized surface plasmons involving physical interaction) or chemical enhancement (formation of charge-transfer complexes involving chemical interaction) with enhancement factors of 10¹² and 10 to 100, respectively.^{30, 31} The low enhancement factor for GO-SFGN hybrid indicates the presence of a chemical interaction or bond between SFGNs and GO. The Raman signal enhancement is similar to the SERS effects previously reported in metal nanoparticle composites of carbon nanotubes.³² As shown later, a Raman enhancement factor of 800% is achieved by increasing the density of gold nanostructures on GO sheets by changing the synthesis temperature to 75 °C (**Figure 3.2b**).

Atomic force microscopy (AFM) scans on the GO-SFGN hybrids (**Figure 3.2c**) shows three regions: (i) large peaks corresponding to the SFGNs, (ii) small peaks corresponding to the

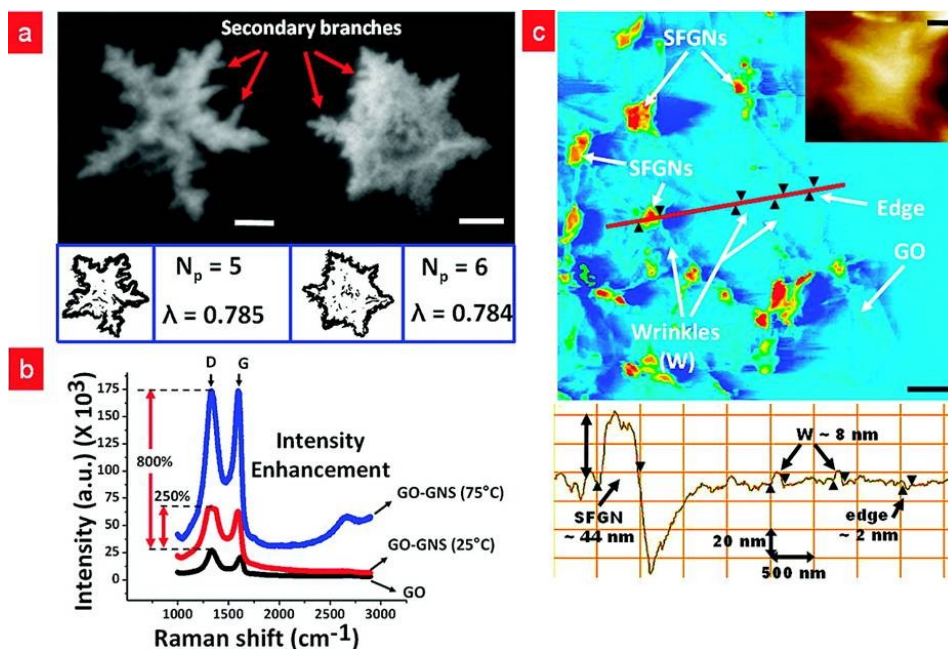


Figure 3.2 “Snowflake”-shaped dendritic morphology of the gold nanostructures and AFM scan of GO-SFGN hybrid. (a) FESEM images of individual SFGNs with 5 and 6 primary branches (N_p), respectively, showing a distinct secondary branching (scale bar = 100 nm). Bottom insets show binary edge-resolved images for these SFGNs used for determining the circularity parameter ($\lambda = 4\pi \cdot \text{area} / \text{perimeter}^2$). Values smaller than unity indicate a high degree of corrugated edges. (b) Raman Spectra for GO-SFGN and GO showing the presence of SFGNs on GO enhances the intensity of D and G bands by ~250% and ~800% suggesting chemical enhancement, and hence a chemical-bond formation between SFGNs and GO, (c) atomic force microscopy scan of GO sheets templated with SFGNs with ~44 nm height as shown in the bottom line scan (scale bar = 500 nm). The height of a characteristic wrinkle (W) is ~8 nm. Inset shows AFM image for an individual SFGN (scale bar = 100 nm).

wrinkles on GO, and (iii) small dips corresponding to the edge of the GO sheets (shown in the bottom panel). The height of the SFGN structure was 44 nm and varies between 45 and 55 nm (see Appendix B, Figure B.3), while the GO wrinkles were 8 nm high. AFM-tip curvature and low contrast of the thick SFGN structures hid the details of the primary and secondary branches of individual SFGN (**Figure 3.2c, top inset**). Further, the SFGNs from which wrinkles are emanating are expected to be underneath the GO sheet, as shown in **Figure 3.1b**.

The lower height of the SFGNs than their width and their flat surface being level with the GO sheets suggest that the SFGNs growth direction is more favored laterally than vertically to the GO surface. This indicates that the GO sheets functions as an in-solution substrate for particle growth. However, more studies are required to confirm this. In the absence of GO, the seeding solution (NH_2OH and gold salt) results in the formation of large irregular aggregates, which eventually settle down. This further signifies the role of GO sheets as stabilizing agents for controlled growth of SFGNs. SFGN-GO solutions were stable for >20 days. Absorption spectrum for a freshly prepared solution of SFGN-GO exhibits a broad peak at ~580 nm (**Figure 3.3**) suggesting the presence of colloidal aggregates in solution as well. Further, the SFGNs grown on GO for 20 days were higher in number but with a size and shape distribution similar to that for freshly prepared SFGNs.

The dendritic shape of SFGNs resemble: **(i)** the morphology of naturally occurring snowflakes, where the dendritic structures are generated from water molecules condensing via diffusion-limited mechanism on supercooled water droplets (snow nuclei), and **(ii)** the morphologies proposed for dendritic growth patterns due to molecular anisotropy.³³ These structures follow an adapted diffusion limited growth pattern model, where particles moving in random walk trajectories stick on a lattice containing a seed particle anisotropically (due to microscopic irregularities on the surface) with the seed tips growing preferentially. A modified two-step model is proposed here for the mechanism of formation of SFGNs. The first step involves the formation of gold nuclei on GO via NH_2OH -assisted reduction of gold salt and their stabilization via attachment with the negatively charged -COO^- and -OH^- groups on GO. We confirmed this step by growing gold nuclei on GO by sodium borohydride reduction of gold salt in the presence of sodium citrate as shown in Figure 4a, bottom inset (and Appendix B, Figure B.4). Since the SFGN formation is an aqueous phase process and unmodified graphene cannot be dispersed in water without surface modification or surfactants, achieving the SFGN formation on graphene (without the -COO^- and -OH^- groups) is challenging. Further, it is also difficult to control the density of -COO^- / OH^- groups on GO, since during the exfoliation process, the degree of oxidation of sheets is expected to be higher for sheets exfoliating early and thus exposed to the oxidizing media for longer time. Therefore, in a single batch, different

GO sheets will have different oxy-group densities, making it challenging to study the effect of oxy-groups on SFGN deposition characteristics.

The second step involves seeding growth of the gold nucleus induced by hydroxylamine assisted Au (III) reduction, catalyzed by the gold surface³⁴ of the nuclei. The dendritic morphology of these gold nanostructures (GNs) is attributed to the diffusion limited kinetics during the seeding growth. The seeding growth of gold nuclei on GO has further two elementary processes (**Figure 3.4a**): (a) external diffusion of Au (III) ions from bulk solution to the nuclei and; (b) particle incorporation of the Au atoms into the crystal structure by hydroxylamine-induced catalysis. The heat of SFGNs formation at nanoscale is removed by the

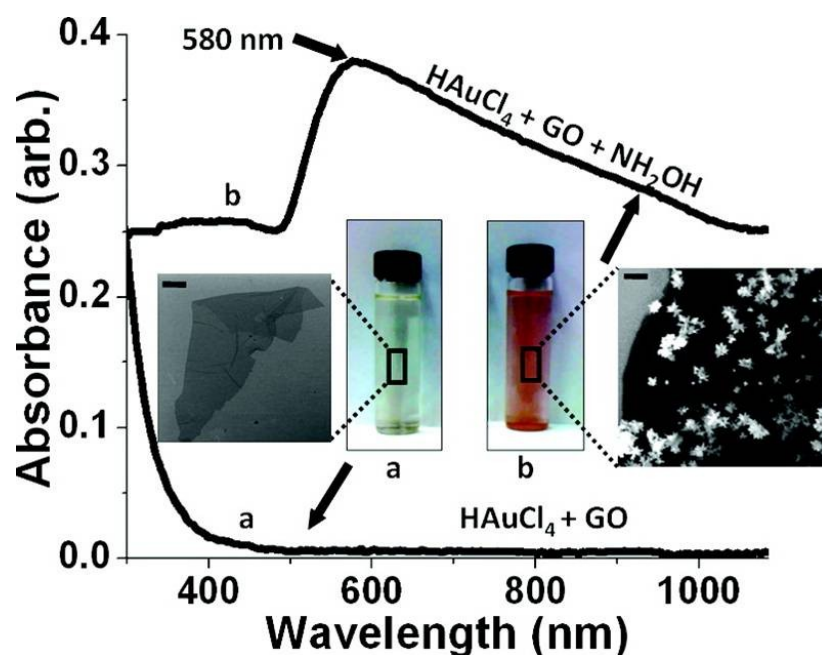


Figure 3.3 Absorption spectra of SFGNs templated on graphene-oxide: (a) spectra of gold salt and GO display no significant peak in the visible region; (b) spectra of a freshly prepared solution of GO, gold salt, and hydroxyl-amine display an absorption peak at ~580 nm. Higher magnification FESEM micrographs (insets) for a bare GO sheet and of a GO sheet templated with SFGNs immobilized on silica substrates are shown. Scale bar equals 1 μm for the right inset and 5 μm for the left inset.

surrounding water. The net resistance to SFGNs growth is thus a combination of resistances from these elemental steps:

$$k_F^{-1} = k_D^{-1} + k_G^{-1}$$

Equation 3.1

where k_F is the rate-constant for SFGN formation, k_D is the rate-constant for diffusion of Au ions from the bulk solution on to the GO surface, and k_G is the rate- constant of Au incorporation in the growing SFGN structure. Since particle incorporation step is catalytic, k_G is expected to be high, making external diffusion the rate determining step. This is further evidenced by the SFGN's structural dependence on the temperature of synthesis (**Figure 3.4b**) as studied by comparing the FESEM images of nanostructures synthesized at 4, 25, and 75 °C. The SFGNs are produced only at 25 °C, while the dendritic morphologies are not produced at low (4°C) or at high (75°C) temperatures. The size and density of the nanoparticles were found to increase with an increase in the temperature. The surface density of Gold Nanostructures was quantified by evaluating the surface coverage index η (η = fraction of GO surface covered by gold nanostructures). η for low, moderate, and high temperatures were calculated to be 0.06, 0.24, and 0.41, respectively, as shown in **Figure 3.4b inset**.

Since the diffusive resistance, $k_D^{-1} \propto T^{-1.5}$, and particle incorporation resistance, $k_G^{-1} \propto \exp(E_A/(RT))$ is higher for low temperature, smaller particles are formed with low density. Here, the particle-incorporation resistance is expected to be higher than that due to diffusion. At moderate temperature of 25°C, the diffusive resistance is thought to increase more than the particle-incorporation resistance leading to SFGNs formation. The anisotropic particle growth on the SFGN surface is a result of the difference in the surface chemical potential (μ) induced by small deformations. Irregular surfaces with high μ grow more preferentially than blunt surfaces with low μ [$\mu (R = \infty) < \mu (R = \text{constant})$] (Mullins-Sekerka instability).^{35, 36} The average rate of gold influx for the formation of an SFGN ($N_p = 5$) is estimated to be 0.1346 g cm⁻² h⁻¹ at 25 °C (see Appendix B, Figure B.5). At higher temperature (75 °C), the mass- transfer rates and the chemical potentials increase leading to a fast and thus unordered cluster formation with high surface coverage densities (**Figure 3.5c**) (see also Appendix B, Figure B.6). The high selectivity of deposition further confirms the role of GO's functional groups in gold nucleation. The GO-Au nanostructure hybrid synthesized at 75 °C was compared with the GO-SFGN hybrid synthesized at 25 °C for its SERS signals.

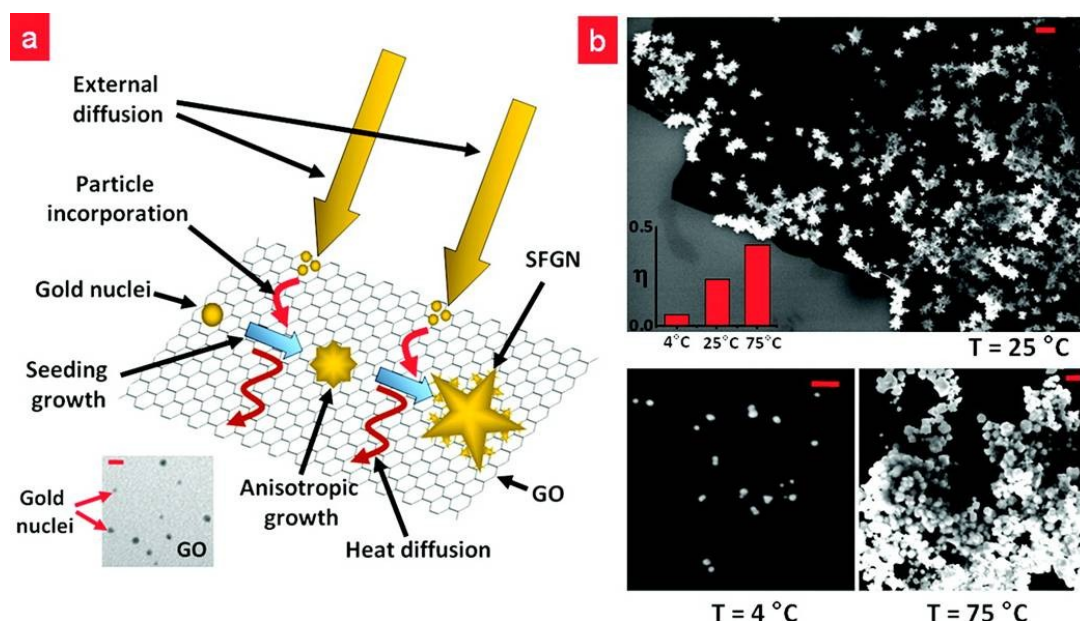


Figure 3.4 Growth mechanism of SFGNs on GO sheets and their structural dependence on the synthesis temperature. (a) Schematic showing the elementary steps involved in the seeding growth of SFGNs on GO template. Au ions diffuse from the bulk to the GO sheet where they are catalytically reduced and incorporated in the growing Au nuclei. Bottom inset shows seed particles on GO that were prepared by sodium borohydride-assisted reduction of gold salt in the presence of sodium citrate and GO. Scale bar = 10 nm. (b) The morphology and density of the synthesized GNs sensitively depends on the reaction temperature. GNs synthesized at room temperature (25 °C) exhibit dendritic “snowflake” morphology with a high coverage on GO. At low temperature (4 °C), the GNs assume a spherical morphology with less coverage, and at higher temperatures (75 °C), GNs exhibit a random cluster formation with very dense coverage. Scale bars = 500 nm. Inset shows the variation of surface coverage index for GO–gold hybrids synthesized at these three temperatures.

While the enhancement factors for GO–Au nanostructures synthesized at 25 °C was 250%, the GO–Au nanostructures synthesized at 75 °C exhibited a higher enhancement factor of 800% (**Figure 3.2b** and Appendix B, Figure B.7). The observed higher enhancement factor is expected since more metal is deposited at a higher temperature. Further, it was found that by

increasing the concentration of gold ions in the solution, a more pronounced growth of secondary branches can be achieved, which in some cases emanate ternary branches (see Appendix B, Figure B.8). The pronounced secondary growth can be explained by the higher concentration of gold ions that are available for particle incorporation during seeding growth. Interestingly, carboxyl/hydroxyl-functionalized silica substrate placed in the seeding solution did not form the SFGNs at 25 °C, indicating the importance of segregation of solution by GO.

Figure 3.5a,b shows the TEMs for SFGNs (synthesized at 25 °C) with $N_p = 4, 5, 6$, and 7 and the distribution of N_p for SFGNs synthesized at 25 °C, respectively. While, N_p ranges from 4 to 12, several SFGNs (49.2%) have $N_p = 5$ or 6, with a relatively small number of SFGNs having $N_p \geq 8$ (11.8%). The selected area electron diffraction (SAED) pattern (Figure 3.5d) of an SFGN with $N_p = 5$ (Figure 3.5d-inset) exhibited a mixed diffraction pattern, suggesting the presence of defects and multiple crystal domains in the SFGNs. Furthermore, the crystal defects were lesser for SFGNs with incompletely formed secondary branches (Appendix B, Figure B.9). The similar angle of emergence of the secondary branches suggests that similar crystal defects cause the secondary branching on a primary branch.

Electrical measurements on an SFGN–GO sheet and a bare-GO sheet immobilized on separate silica substrates with predeposited electrodes were conducted by immobilizing the sheet from solution on amine-functionalized silica substrates with 300 nm thick silica and gold electrodes 5 μm apart (insets, Figure 3.6a,b). The conductivity of GO–SFGN sheet was an order of magnitude higher than that for GO, attributed to the formation of low-resistance, gold-doped islands on GO. Next, the GO regions in both GO–SFGN and bare-GO devices were chemically reduced to graphene (G) by treatment with hydrazine vapors(8) ($R_G \ll R_{GO}$). After GO–SFGN to G–SFGN reduction (Figure 3.6a), the conductivity increased by 2 orders of magnitude; while for GO to G reduction (Figure 3.6b) it increased by 3 orders of magnitude. The lesser conductivity-change observed in GO–SFGN (100-fold) versus GO (1000-fold) post reduction is attributed to the presence of SFGNs, which shield the underlying GO against hydrazine treatment, resulting in a net smaller region of GO being reduced to G ($R_G < R_{SFGN/GO}$).

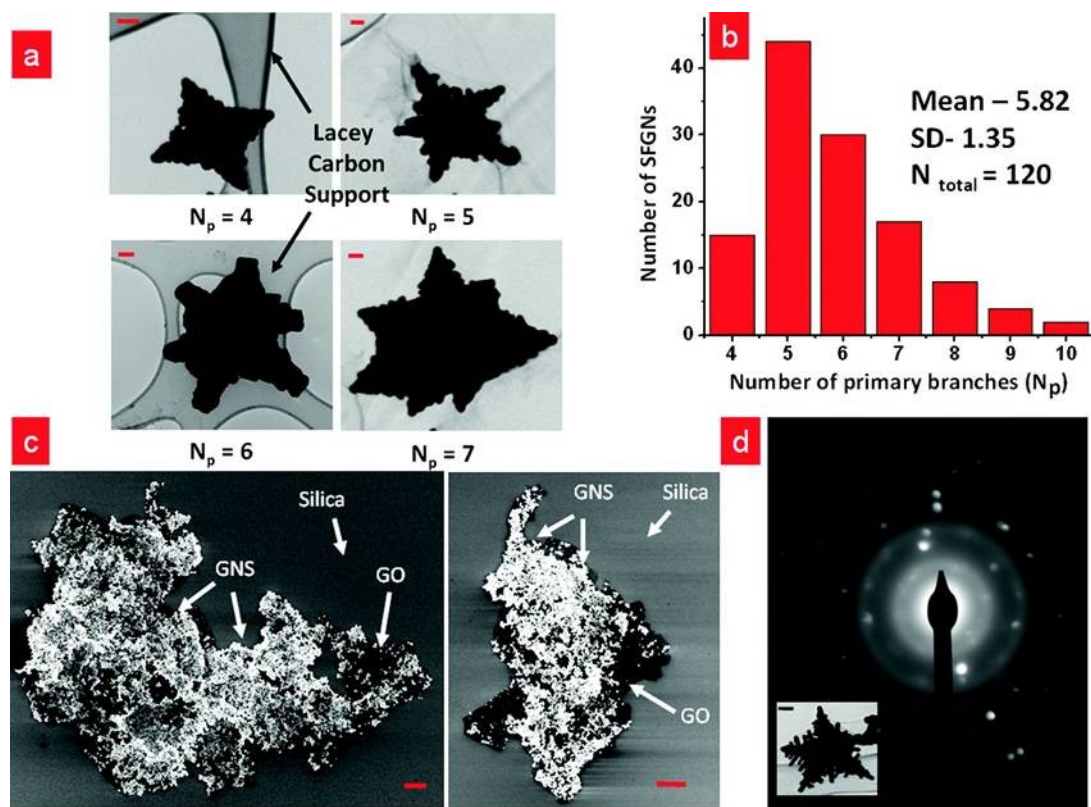


Figure 3.5 Structural variation in the morphology of SFGNs and diffraction pattern studies. (a) TEM images of SFGNs with 4, 5, 6, and 7 primary branches. Scale bar = 100 nm. (b) Bar graph showing the distribution of primary branches in the SFGNs synthesized at 25 °C. The analysis is for a total of 120 SFGNs deposited on GO. (c) FESEM images for gold-nanostructure-templated GO sheets that were synthesized at 70 °C showing high surface coverage densities and excellent selectivity of gold on GO. Scale bar= 5 μm . (d) Selected area electron diffraction (SAED) pattern for an SFGN with $N_p = 5$ (inset) shows that SFGNs have several defects and multiple crystal domains. Scale bar = 100 nm.

The SFGN shielding of GO against hydrazine treatment is further verified by comparing the band gap (E_g) values of GO-SFGN and G-SFGN hybrids obtained by measuring the temperature dependence of their conductivities. **Figure 3.6c** shows an exponential temperature-dependence [$\sigma \propto \exp(-E_g/(2k_B T))$] for the conductivity of a GO-SFGN and GO devices, from the slope of which their apparent band gap values are calculated to be $E_{g/\text{GO-SFGN}} = 173.85 \pm 0.01$ meV and $E_{g/\text{GO}} = 320.05 \pm 0.01$ meV, respectively (Appendix B, Figure B.10).

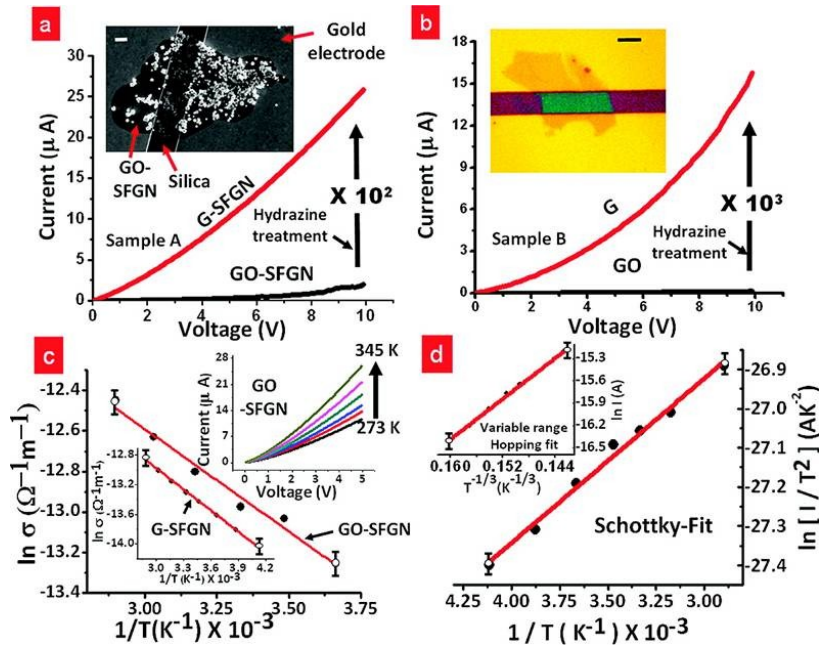


Figure 3.6 Electrical properties of graphene-templated with SFGNs. (a) The conductivity of a GO-SFGN sheet ($9.49 \times 10^{-2} \mu\text{S}$) increases ~ 102 -fold after reduction with hydrazine. Inset shows a GO sheet templated with SFGNs incorporated between electrodes. Scale bar = $2 \mu\text{m}$. (b) Conductivity of a bare GO sheet increases 103 folds after hydrazine reduction. Top inset: Optical micrograph of a bare GO sheet between gold electrodes. Scale bar = $5 \mu\text{m}$. (c) GO-SFGN hybrid exhibits a semiconducting behavior showing an exponential dependence of conductivity on temperature ($\sigma \propto \exp(-E_g/(2kBT))$). Bottom left inset shows a similar temperature-response for a G-SFGN device. Top inset shows the I - V response for a GO-SFGN device over a temperature range of 273–345 K showing a gradual increase in conductivity. (d) Schottky fit for a G-SFGN device from which the Schottky barrier height is calculated to be ~ 39 meV. Top inset shows the variable range hopping fit for G-SFGN, which describes the data equally well.

The decreased band gap in GO-SFGN explains its higher conductivity than GO as observed earlier. The conductivity of a G-SFGN device exhibits a similar temperature dependence (Figure 3.6c, bottom left inset) with a band gap of $E_g/\text{G-SFGN} = 164.24 \pm 0.003$ meV comparable to $E_g/\text{G} = 156.64 \pm 0.01$ meV for graphene (chemically reduced GO) (Appendix B,

Figure B.10). The band gap of G-SFGN and G being nonzero is attributed to the partial reduction of GO on the unexposed side-facing silica surface³⁷ and defects.

The higher band-gap value for G-SFGN as compared to G ($E_g/G < E_g/G\text{-SFGN}$) results from the presence of unreduced GO regions in the G-SFGN hybrid making G-SFGN less metallic than G. Therefore it can be inferred that the expected band gap values for GO-Au hybrids synthesized at 75 °C should be higher due to the high density of gold nanostructures, which shield larger GO regions against reduction. Further, the G-SFGN and GO-SFGN hybrids can be modeled as several back-to-back semiconductor-metal interfaces (Schottky contacts), the current through which at a forward bias V is described by

$$I = A^* \times a \times T^2 \times \exp\left(\frac{-q(\phi_B - V)}{k_B T}\right) \quad \text{Equation 3.2}$$

where A^* is the modified Richardson constant, a is the cross sectional area, ϕ_B is the Schottky barrier height, k_B is the Boltzmann constant and T is the absolute temperature. Figure 3.6d shows the plot of $\ln(I/T^2)$ versus $1/T$ data for a G-SFGN device exhibiting a linear dependence which is consistent with the equation 3.2. The Schottky barrier height (SBH) for G-SFGN hybrid as calculated from the slope of this curve (see Appendix B, section B.14) is 38.98 ± 0.06 meV. Similarly the SBHs for GO, GO-SFGN, and G (chemically reduced GO) were calculated to be 125.98 ± 0.27 , 52.63 ± 0.20 , and 37.36 ± 0.08 meV, respectively, indicating that the SBH in GO decreases as it forms a composite with the SFGNs. This holds similarity to the observed decrease of SBH in silicon carbide-Ti Schottky contacts after deposition of gold nanoparticles.⁽³⁸⁾ Further, the experimental data for the I-V scans of GO, G, GO-SFGN, and G-SFGN also fits the variable range hopping (VRH) mechanism ($\ln I \propto T^{-1/3}$), which involves consecutive inelastic tunneling. **Figure 3.6d** inset shows the VRH fit for a G-SFGN device (VRH fits for GO, G, and GO-SFGN are shown in Figure B.11, Appendix B). However, Schottky limited charge transport should be the preferred mode of charge transport as evidenced by a nonlinearity in the I-V curves shown in **Figure 3.6a,b**. VRH in graphene has been shown to produce linear I-V.³⁹ Further, the formation of Schottky contacts at the interface between metal electrode and graphene sheet is expected since the graphene sheet is contacted via a bottom gold-electrode configuration, which introduces significant Schottky barrier at the electrode

edges producing a nonlinear I-V behavior.³⁹ However, more experiments are required to analyze the individual roles of VRH and Schottky limited charge transport in graphene-gold devices.

3.5 Summary

We have demonstrated the electrical, structural, interfacial, and dendritic properties of controlled interfacing of graphene with gold nanostructures, its electrical properties, and Raman signal can be sensitively controlled. With continued interest in graphene technology, its metal-interfacing will be an important process both for its incorporation into other systems and for controlling its electrical properties by doping. Here, we leverage the molecular-functionality of GO in dispersion to grow and stabilize gold nanostructures with morphology controlled by manipulating the chemical and physical forces (diffusion and surface-potential). A 2-fold Raman enhancement and a control on the band gap and Schottky barrier was demonstrated. Since, metal nanostructures can sensitively tailor graphene's electrical and Raman properties, we envision that the research community will leverage the process shown here to build novel graphene applications in the areas of nanoelectronics, sensors, bioimaging, electro-optics, catalysis, logic-devices, etc. The study will also motivate further developments in this field by incorporating graphene's fermionic-confinement, spintronics effects, magnetic effects, and carrier collimation to develop next-generation conjugated devices with new functionalities.

3.6 References

1. Novoselov, K. S.; Geim, A. K.; Morozov, S. V.; Jiang, D.; Zhang, Y.; Dubonos, S. V.; Grigorieva, I. V.; Firsov, A. A. Electric Field Effect in Atomically Thin Carbon Films. *Science* **2004**, *306*, 666–669.
2. Novoselov, K. S.; Geim, A. K.; Morozov, S. V.; Jiang, D.; Katsnelson, M. I.; Grigorieva, I. V.; Dubonos, S. V.; Firsov, A. A. Two-Dimensional Gas of Massless Dirac Fermions in Graphene. *Nature* **2005**, *438*, 197–200.
3. Lee, C.; Wei, X. D.; Kysar, J. W.; Hone, J. Measurement of the Elastic Properties and Intrinsic Strength of Monolayer Graphene. *Science* **2008**, *321*, 385–388.

4. Mohanty, N.; Berry, V. Graphene-Based Single-Bacterium Resolution Biodevice and DNA Transistor: Interfacing Graphene Derivatives with Nanoscale and Microscale Biocomponents. *Nano Lett.* **2008**, *8*, 4469–4476.
5. Geim, A. K.; Novoselov, K. S. The Rise of Graphene. *Nat. Mater.* **2007**, *6*, 183–191.
6. Novoselov, K. S.; Jiang, D.; Schedin, F.; Booth, T. J.; Khotkevich, V. V.; Morozov, S. V.; Geim, A. K. Two- Dimensional Atomic Crystals. *Proc. Natl. Acad. Sci. U.S.A.* **2005**, *102*, 10451–10453.
7. Sundaram, R. S.; Gomez-Navarro, C.; Balasubranianian, K.; Burghard, M.; Kern, K. Electrochemical Modification of Graphene. *Adv. Mater.* **2008**, *20*, 3050–3053.
8. Stankovich, S.; Dikin, D. A.; Piner, R. D.; Kohlhaas, K. A.; Kleinhammes, A.; Jia, Y.; Wu, Y.; Nguyen, S. T.; Ruoff, R. S. Synthesis of Graphene-Based Nanosheets *via* Chemical Reduction of Exfoliated Graphite Oxide. *Carbon* **2007**, *45*, 1558–1565.
9. Ryu, S.; Han, M. Y.; Maultzsch, J.; Heinz, T. F.; Kim, P.; Steigerwald, M. L.; Brus, L. E. Reversible Basal Plane Hydrogenation of Graphene. *Nano Lett.* **2008**, *8*, 4597–4602.
10. Elias, D. C.; Nair, R. R.; Mohiuddin, T. M. G.; Morozov, S. V.; Blake, P.; Halsall, M. P.; Ferrari, A. C.; Boukhvalov, D. W.; Katsnelson, M. I.; Geim, A. K.; Novoselov, K. S. Control of Graphene's Properties by Reversible Hydrogenation: Evidence for Graphane. *Science* **2009**, *323*, 610–613.
11. Wehling, T. O.; Novoselov, K. S.; Morozov, S. V.; Vdovin, E. E.; Katsnelson, M. I.; Geim, A. K.; Lichtenstein, A. I. Molecular Doping of Graphene. *Nano Lett* **2008**, *8*, 173–177.
12. Schedin, F.; Geim, A. K.; Morozov, S. V.; Hill, E. W.; Blake, P.; Katsnelson, M. I.; Novoselov, K. S. Detection of Individual Gas Molecules Adsorbed on Graphene. *Nat. Mater.* **2007**, *6*, 652–655.
13. Novoselov, K. S.; McCann, E.; Morozov, S. V.; Fal'ko, V. I.; Katsnelson, M. I.; Zeitler, U.; Jiang, D.; Schedin, F.; Geim, A. K. Unconventional Quantum Hall Effect and Berry'S Phase of Bilayer Graphene. *Nat. Phys.* **2006**, *2*, 177–180.
14. Novoselov, K. S.; Jiang, Z.; Zhang, Y.; Morozov, S. V.; Stormer, H. L.; Zeitler, U.; Maan, J. C.; Boebinger, G. S.; Kim, P.; Geim, A. K. Room-Temperature Quantum Hall Effect in Graphene. *Science* **2007**, *315*, 1379.

15. Stankovich, S.; Dikin, D. A.; Dommett, G. H. B.; Kohlhaas, K. M.; Zimney, E. J.; Stach, E. A.; Piner, R. D.; Nguyen, S. T.; Ruoff, R. S. Graphene-Based Composite Materials. *Nature* **2006**, *442*, 282–286.
16. Blake, P.; Brimicombe, P. D.; Nair, R. R.; Booth, T. J.; Jiang, D.; Schedin, F.; Ponomarenko, L. A.; Morozov, S. V.; Gleeson, H. F.; Hill, E. W.; Geim, A. K.; Novoselov, K. S. Graphene-Based Liquid Crystal Device. *Nano Lett.* **2008**, *8*, 1704–1708.
17. Bunch, J. S.; van der Zande, A. M.; Verbridge, S. S.; Frank, I. W.; Tanenbaum, D. M.; Parpia, J. M.; Craighead, H. G.; McEuen, P. L. Electromechanical Resonators from Graphene Sheets. *Science* **2007**, *315*, 490–493.
18. Abanin, D. A.; Novoselov, K. S.; Zeitler, U.; Lee, P. A.; Geim, A. K.; Levitov, L. S. Dissipative Quantum Hall Effect in Graphene near the Dirac Point. *Phys. Rev. Lett.* **2007**, *98*.
19. Hill, E. W.; Geim, A. K.; Novoselov, K.; Schedin, F.; Blake, P. Graphene Spin Valve Devices. *IEEE Trans. Magn.* **2006**, *42*, 2694–2696.
20. Zhang, Y. B.; Tan, Y. W.; Stormer, H. L.; Kim, P. Experimental Observation of the Quantum Hall Effect and Berry's Phase in Graphene. *Nature* **2005**, *438*, 201–204.
21. Witten, T. A.; Sander, L. M. Diffusion-Limited Aggregation. *Phys. Rev. B* **1983**, *27*, 5686–5697.
22. Williaris, G.; Seger, B.; Kamat, P. V. TiO₂ Graphene Nanocomposites. UV-Assisted Photocatalytic Reduction of Graphene Oxide. *ACS Nano* **2008**, *2*, 1487–1491.
23. Muszynski, R.; Seger, B.; Kamat, P. V. Decorating Graphene Sheets with Gold Nanoparticles. *J. Phys. Chem. C* **2008**, *112*, 5263–5266.
24. Si, Y. C.; Samulski, E. T. Exfoliated Graphene Separated by Platinum Nanoparticles. *Chem. Mater.* **2008**, *20*, 6792–6797.
25. Hummers, W. S.; Offeman, R. E. Preparation of Graphitic Oxide. *J. Am. Chem. Soc.* **1958**, *80*, 1339.
26. Gole, A.; Murphy, C. J. Seed-Mediated Synthesis of Gold Nanorods: Role of the Size and Nature of the Seed. *Chem. Mater.* **2004**, *16*, 3633–3640.
27. Gou, L. F.; Murphy, C. J. Fine Tuning the Shape of Gold Nanorods. *Chem. Mater.* **2005**, *17*, 3668–3672.

28. Jana, N. R.; Gearheart, L.; Murphy, C. J. Seeding Growth for Size Control of 5–40 nm Diameter Gold Nanoparticles. *Langmuir* **2001**, *17*, 6782–6786.
29. Murphy, C. J.; San, T. K.; Gole, A. M.; Orendorff, C. J.; Gao, J. X.; Gou, L.; Hunyadi, S. E.; Li, T. Anisotropic Metal Nanoparticles: Synthesis, Assembly, And Optical Applications. *J. Phys. Chem. B* **2005**, *109*, 13857–13870.
30. Ko, H.; Singamaneni, S.; Tsukruk, V. V. Nanostructured Surfaces and Assemblies as SERS Media. *Small* **2008**, *4*, 1576–1599.
31. Campion, A.; Ivaneky, J. E.; Child, C. M.; Foster, M. On the Mechanism of Chemical Enhancement in Surface- Enhanced Raman-Scattering. *J. Am. Chem. Soc.* **1995**, *117*, 11807–11808.
32. Tong, L. M.; Li, Z. P.; Zhu, T.; Xu, H. X.; Liu, Z. F. Single Gold-Nanoparticle-Enhanced Raman Scattering of Individual Single-Walled Carbon Nanotubes *via* Atomic Force Microscope Manipulation. *J. Phys. Chem. C* **2008**, *112*, 7119–7123.

4 Microwave reduced Uncapped Metal Nanoparticles on Graphene: Tuning Catalytic, Electrical and Raman Properties

4.1 Overview

This chapter builds on the work presented in Chapter 3 and carries it forward to address a major challenge in liquid-phase catalysis of dispersing “uncapped” metal nanoparticles (NPs) with enhanced density of accessible catalytic sites in solution. We demonstrate that graphene oxide’s (GO's) high density of accessible and bondable oxy-functional groups and the high steric hindrance from its micrometer-scale area covalently implant, stabilize, and support bare-surfaced gold nanoparticles (BSGNs) produced in situ by a unique microwave reduction process. Comparing the efficiency of catalytic reduction of *p*-nitroaniline (*p*-NA) by BSGNs and similar sized surfactant-capped gold NPs showed that the uncapped surface on GO-supported NPs, **(a)** opens up 258% more active sites, and **(b)** enhances the catalytic reduction of *p*-NA by 10–100 fold. Further, BSGN implantation on GO, **(a)** amplifies the Raman signal of bare GO by ~ 3 fold, and **(b)** increases the conductivity of native p-type GO by >10 fold via injection of 1.328×10^{12} electrons/cm², consequently transforming it into an n-type semiconductor.

4.2 Introduction

Recently, single-atom thick, quasi-planar graphene sheets with sp² bound carbon atoms arranged in a honeycomb lattice have generated tremendous research interest owing to their fascinating electronic,¹⁻³ optical,⁴⁻⁶ and mechanical⁷ properties. Functionalized graphene sheets with arguably the largest surface area per volume, high density of interfactable chemical groups, and preserved semiconducting properties at room temperature are being leveraged for unique applications such as biosensing,⁸⁻¹⁰ chemical sensing,¹¹ field emission,¹² membrane fabrication,¹³ and nanocomposite fabrication.^{14, 15} These systems were realized by converting a fraction of the sp² graphenic carbons to oxygenated sp³ carbons, which covalently bind with polymers,^{14, 15} chemicals,^{16, 17} biomolecules,⁸⁻¹⁰ and micro/nanostructures.¹⁸⁻²¹ Of these, graphene nanoparticle composites are gaining great attention owing to the resultant multifunctional and unified

properties.¹⁸⁻²⁰ For example, GO-TiO₂ sheets can transfer electrons from a photo-excited TiO₂ nanoparticle to another site on GO for catalysis; graphene-palladium nanoparticle sheets can selectively detect hydrogen; graphene-platinum, graphene-palladium, and graphene-platinum-ruthenium nanocomposites exhibit enhanced catalytic activities; and gold nanostructures grown on GO can control its electrical properties and enhance its Raman scattering signal (our earlier work).¹⁹

Catalytic activity directly scales with the available active sites. Recently, surface-capped gold nanoparticle (GNP) deposition on graphene sheets has been an important research topic;^{18, 19, 21} however, the active sites on GNPs (solution phase) have so far been blocked by the stabilizing molecules.^{22,23} Here, we demonstrate that the local dielectric heating from microwave (MW) exposure of a metal salt solution results in nucleation of reactive naked NPs, which instantaneously implant on the GO sheets in a single step. The oxy-functional groups (carboxylic, epoxy, carbonyl, phenol, lactone, quinone, and hydroxyl groups) on GO chemically bond and stabilize these metal nuclei, thus eliminating the need to cap the catalytically active sites on GNPs. Since one face of the GNPs implant on the GO, the other exposed face is naked with the bare atomic sites. The present study illustrates and characterizes, for the first time, catalytic properties of solvent-dispersed bare-surfaced gold nanoparticles (BSGNs) and compares their efficiency with similar shaped surfactant-capped gold nanoparticles. We also show the structural, Raman, and electrical characterization of BSGNs implanted on GO. The key results demonstrated are that, **(a)** the structure of BSGNs on GO can be controlled by microwave exposure, **(b)** BSGNs exhibit 10–100-fold enhancement in catalytic reduction of *p*-nitroaniline as compared to that of surface-capped or non-naked GNPs with an increase in the effective catalytic site density by 258%, **(c)** BSGNs amplify the Raman signal of GO by ~3 fold, and **(d)** BSGNs inject $\sim 1.328 \times 10^{12}$ electrons/cm² in GO, consequently transforming it to an n-type semiconductor. We also demonstrate that GO can be applied to produce bare-surfaced monodisperse GNPs without microwave exposure.

The interaction of the electromagnetic waves with the high dielectric solvent molecules results in a space-confined uniform heating ($E \propto f\epsilon'(\tan \delta)P^2$, where P is the microwave power, f is the frequency of the microwave, ϵ' is the dielectric constant of the solvent, and δ is the loss

factor). The resultant local temperature rise has been employed to enhance the kinetics of organic reactions²⁴⁻²⁶ by utilizing the additional electronic kinetic energy to cross the reaction activation barrier. Similarly, the MW exposure on metal salts significantly reduces the barrier to reduction, nucleation, and ion incorporation, leading to formation of NPs which, due to a higher crystallization rate, have sharper edges than those formed by conventional heating.²⁷ However, so far, MW-nucleated NPs have been synthesized in the presence of reducing agents and stabilizing molecules such as chitosan, alkyltrimethyl ammonium bromide, and sodium citrate.²⁷⁻³³ In this study, we have demonstrated that the MW has a self-sufficient ability to induce nucleation of aqueous gold salt even in the absence of chemical reductants, and the nucleated GNPs thus formed can covalently bind (implant) on the GO sheets and become stabilized in solution. This is facilitated by the MW-induced dielectric heating via rapid dipolar rotations of the polarized water molecules that create local high-pressure regions in the salt water system. Near the critical range (150–300 °C), water is known to exhibit a 3-fold higher dissociation constant, hence functioning both as an acid and a base. We therefore attribute the chemical-free reduction of gold salt to the enhanced dissociation of water caused by local and confined dielectric heating effects from MW.³⁴ As expected, the GNPs exhibit sharp triangular, truncated triangular, hexagonal, globular, and dendritic morphologies, making them immensely useful for catalytic applications.³⁵ In the absence of GO, the MW-nucleated GNPs become unstable and aggregate. Therefore, the GO sheets act as swimming substrates on which GNPs imbed and which keep the NPs dispersed (**Figure 4.1a**). Further, the stability of the GNPs is unaffected if the GO sheets are added during or immediately after the MW exposure, which indicates that the covalent binding between the GO and GNPs is not MW-actuated. However, when the GO sheets are also present during the MW exposure, they are expected to undergo a partial reduction as prolonged MW exposure (~10 min) has been shown to result in a mild thermal reduction of GO sheets.³⁶ We also controlled the size distribution of naked GNPs imbedded on GO by a simple, non-MW-based reduction process (shown later). Recently, naked nanoparticles have been implanted on a graphene backbone by substrate-based electrochemical reactions.¹¹ However, it is challenging to solution-disperse these composites for liquid-phase reactions at high throughput.²¹

4.3 Experimental Section

4.3.1 *Preparation of Bare surfaced gold nanostructures on graphene*

The GO-BSGN nanocomposite was synthesized by MW exposure (1.05 kW, 2450 MHz) on an aqueous solution of GO (100 μ L, 20 mM carboxylic acid quantified by titration) and gold salt, $\text{HAuCl}_4 \cdot 3 \text{H}_2\text{O}$ (10 mL, 0.275 mM) for a time interval between 60 and 300 s with intermittent cooling after every 10 s. The mixture was allowed to stand for ~ 24 h, which resulted in the formation of BSGNs with triangular, hexagonal, and dendritic morphologies, which either assemble on or get wrapped with the GO sheets, depending on the MW exposure time.

4.3.2 *TEM and SAED*

TEM images and SAED patterns were obtained with a Philips CM 100 transmission electron microscope operated at 100 kV by depositing the GO-AGN hybrids from solution onto a 300 mesh size copper grid.

4.3.3 *FESEM*

FESEM Images were obtained with a Leo field emission scanning electron microscope operated at 10-15 kV.

4.3.4 *Electrical Conductivity and Gating Measurements*

All electrical measurements were taken at room temperature under a steady nitrogen environment using a Keithley 2612 dual channel system source meter connected to a computer via a GPIB/IEEE-488 interface card.

4.3.5 *Raman Spectroscopic Measurements*

The Raman spectra of GO and GO-BSGN sheets were determined by using a LabRAM ARAMIS Raman spectrometer located at the University of Kansas, Bioengineering Research Center, Lawrence, KS. The instrument was manufactured by HORIBA Jobin Yvon (Edison, New Jersey), and a HeNe laser ($\lambda = 633$ nm, a laser power of 17mW) was used as one of the excitation sources for the samples. The instrument conditions were a 200 μ m confocal hole, 150 μ m wide

entrance slit, 600 gr/mm grating, and 100 \times objective Olympus lens. Data processing was performed using LabSPEC 5 (HORIBA Jobin Yvon). The samples were mounted in a computer-controlled, high-precision x-y stage.

4.3.6 Catalytic Measurements

For the catalytic reaction, 600 μ L of a 10 $^{-3}$ M 4-NA solution was mixed with 4 mL of DI water followed by an addition of 600 μ L of 0.1 M NaBH₄; 600 μ L of the as prepared solution of GO-BSGN was added to study the catalytic activity of these nanostructures. Assuming a complete conversion of gold salt into NPs, the average concentration of BSGNs was calculated to be \sim 1013/ml. For catalytic activity comparison experiments, citrate-capped NPs with the same concentration were used.

4.4 Results and Discussion

The GO-BSGN nanocomposites were synthesized by MW exposure (1.05 kW, 2450 MHz) on an aqueous solution of gold salt, HAuCl₄·3H₂O (10 mL, 0.275 mM) and GO (prepared by Hummer's method, 100 μ L, 20 mM carboxylic acid quantified by titration) for a time interval between 60 and 300 s with intermittent cooling after every 10 s. The mixture was then allowed to stand for \sim 24 h, resulting in the formation of anisotropic BSGNs, which assembled on GO sheets (**Figure 4.1**). Upon carrying out the MW exposure in a lower ambient temperature (by placing the mixture in an ice bath), we observed the formation of a small incidence of dendritic GNPs, some of which were wrapped with GO sheets, presumably smaller in sizes (**Figure 4.1c**). The formation of dendritic nanostructures is explained later.

For structural characterization, the BSGN templated GO sheets were immobilized on an amine-silanized silica surface via electrostatic interfacing (see Appendix C, Figure C.1), which facilitates a selective deposition of only the GO-BSGN sheets separating them from the BSGNs that have not yet interfaced with GO sheets. **Figure 4.1b** shows an FESEM image of the immobilized GO-BSGN composite. The majority of the BSGNs exhibit polyhedral shapes with a broad size distribution from 50 to 350 nm, while there is a small fraction of spherical nanoparticles. The broad size and shape distribution is attributed to the absence of growth

termination from stabilizing molecules. Later, we show a mechanism to deposit monodisperse bare-surfaced nanoparticles on GO. Since the smaller GNPs are more in number (n) and have a higher surface potential, μ_{GNPs} , and thus higher free energy, they are expected to coagulate and grow to form larger nanoparticles³⁷ ($\sum_{i=1}^n (\mu_{\text{GNPs}} N_{\text{GNPs}}) > \sum_{i=1}^m (\mu_{\text{GNP,L}} N_{\text{GNP,L}})$, $n > m$, where $\mu_{\text{GNP,L}}$ is the surface potential of larger nanoparticles). Since diffusion and nucleation barriers

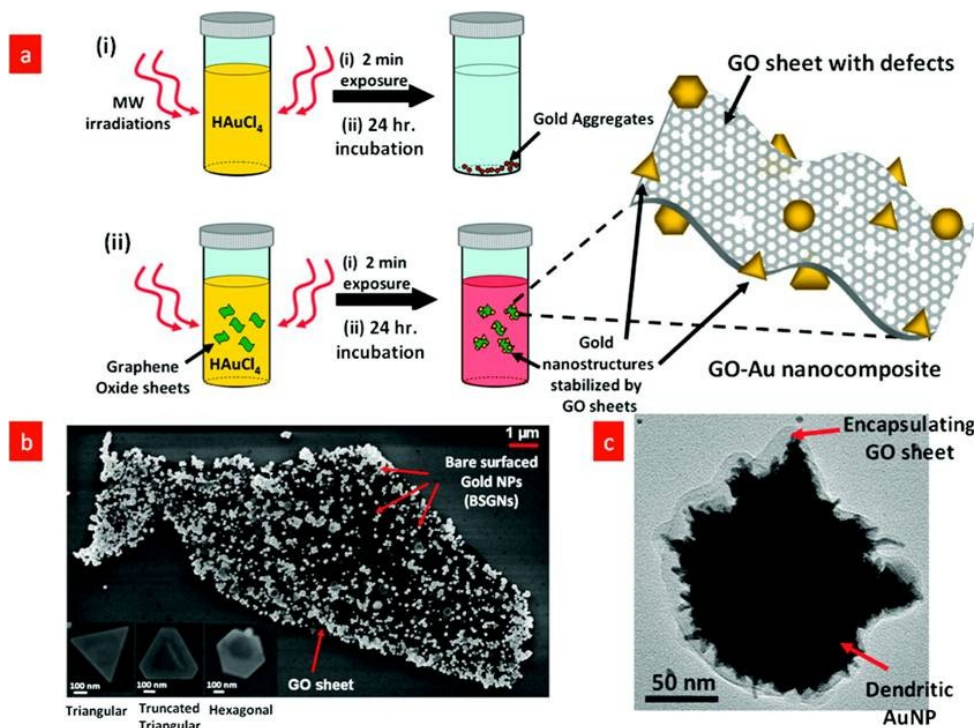


Figure 4.1 Microwave (MW)-assisted in situ synthesis of multiple shaped bare-surfaced gold nanoparticles (BSGNs) on graphene oxide (GO). (a) An aqueous solution of gold salt, when microwaved for ~2 min, results in the formation of gold nuclei which agglomerate to form clusters (i). However, when the solution mixture also contains GO, the gold nanostructures get templated on the GO sheets (ii). This is attributed to the oxy-functional groups present on GO sheets, which stabilize the Au nuclei. (b) FESEM image of a BSGN-templated GO sheet on a silica substrate. The BSGNs acquire several shapes, such as triangular, truncated-corner triangular, and hexagonal (as shown in the inset). (c) TEM image of a dendritic GNP encapsulated by a GO sheet. These GO-coated NPs are formed via MW exposure on the solution maintained at a lower ambient temperature.

are temperature- and concentration-dependent (explained later), this process could be further controlled by adjusting the MW power and salt concentrations.

BSGNs assemble homogeneously on the GO sheets with a high coverage index, η , of 0.31 ($\eta \equiv$ fraction of GO surface covered by BSGNs), which is attributed to the high density of oxy-functional groups on the surface of GO.³⁸ Also, the BSGNs are implanted on both sides of the GO sheets. This is evident in the FESEM images of the immobilized BSGN–GO sheets that show a contrast between the BSGNs present on different sides of the GO sheets. The BSGNs on the substrate-facing side of the GO appear darker since they get screened by the GO sheet, while those on the surface of GO sheet directly exposed to the electron beam appear brighter (**Figure 4.3a**). The substrate-facing BSGNs also raise and stretch the GO sheets during immobilization, which creates wrinkles (**Figure 4.2, right bottom inset**, and Appendix C, Figure C.2).

The absorption spectra of a freshly prepared solution of GO–BSGN composite (**Figure 4.2**) exhibits a broad peak centered at ~575 nm, confirming the wide size distribution of gold NPs. Absorption spectra of a non microwaved solution mixture of GO and gold salt kept for >7 days did not display any significant peak in the visible region nor result in the formation of any gold nanostructures, signifying that GO does not reduce the NPs. This along with the observation that the formation of BSGNs is independent of the order in which the GO sheets are introduced during synthesis (before or after MW exposure) suggests that the local dielectric heating from MW induces reduction of gold ions that results in the spontaneous formation of BSGNs. Selected-area electron diffraction (SAED) patterns of BSGNs (see Appendix C, Figure C.3) indicate mono crystallinity, which also supports the spontaneous formation of these NPs during the short MW exposure. The formation of BSGNs during the MW exposure is proposed to occur in two steps, **(1)** an instantaneous gold nucleation event, which might attach some gold nuclei on the GO sheets, and **(2)** the growth of nuclei on GO and in solution. The net rate of BSGN formation during the MW exposure (r_t) can thus be modeled as:

$$r_f = r_n + r_g \quad \text{Equation 4.1}$$

where r_n and r_g denote the rates for gold nucleation and growth of the nuclei, respectively. The process of nucleation takes place in an instantaneous burst during the MW exposure and hence is expected to have a very high rate constant. On the other hand, the rate of

nuclei growth is dependent on the internal solution diffusion of smaller gold nuclei ($k_d \propto T^{1.5}$) and their self-incorporation to form NPs ($k_i \propto \exp(-E_a/RT)$). At the high temperature facilitated by the MW, k_d and k_i assume large values, enabling a high nuclei growth rate that is expected to form regular sharp-edged gold nanostructures, as we observed.²⁷

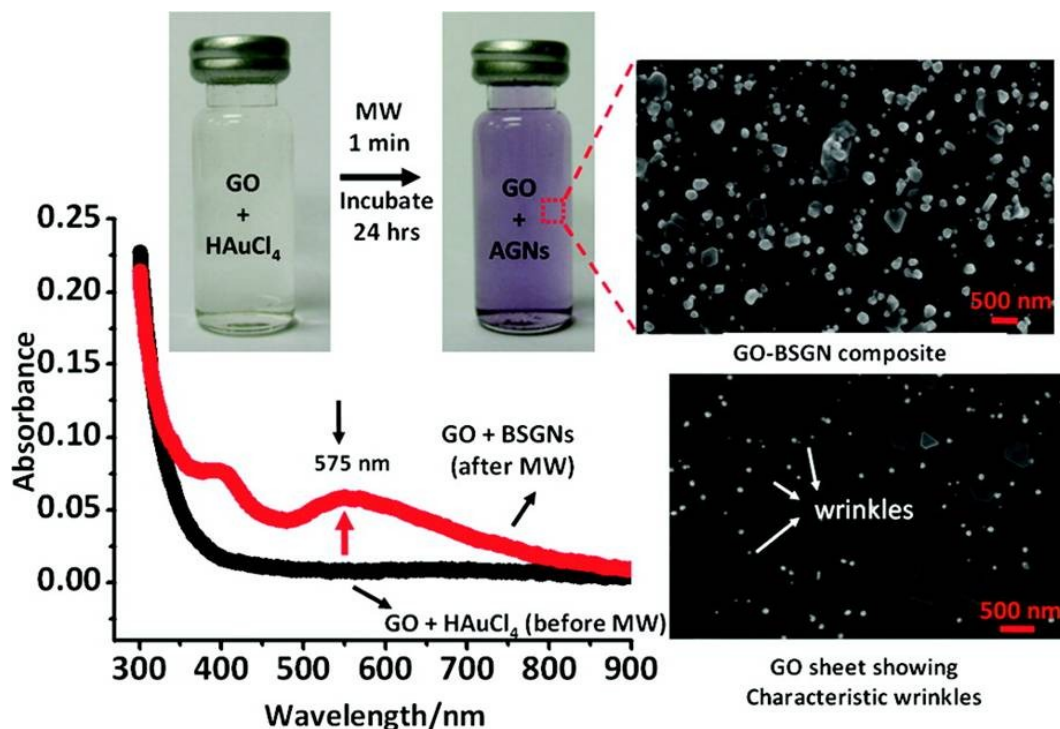


Figure 4.2 Before the MW exposure, a solution of GO and gold salt does not exhibit a significant peak in the visible region. After the MW exposure, a wide absorption peak centered at ~575 nm appears in the spectrum. The top left inset shows the change in the color of the reactant mixture as it is exposed to MW irradiations. The GNS-decorated GO sheets (top right inset) are immobilized on a Si substrate for FESEM imaging, and the presence of BSGNs results in localized deformation of GO sheets, leading to the formation of wrinkles, the nodes of which are formed by the BSGNs (bottom right inset).

The presence of floating NP-stabilizing templates in solution (facilitated by GO sheets) enabled us to determine key factors which govern the formation of NPs during MW exposure.

This was achieved by changing the ambient reaction temperature and observing its effect on the morphology of thus-formed NPs. When the ambient temperature of the reaction mixture was decreased (by placing the solution in an ice bath during microwave exposure), a small incidence of BSGNs were found to exhibit dendritic morphologies (**Figures 4.1c and 4.3c** and Appendix C, Figure C.5). At lower temperature, the resistances offered to the internal diffusion ($k_d^{-1} \propto T^{-1.5}$) and particle self-incorporation ($k_i^{-1} \propto \exp(E_a/RT)$) increased, making the growth of nuclei partly diffusion-limited. A diffusion-limited growth in the presence of molecular anisotropy results in the formation of dendritic structures.³⁹ The observed dendritic morphologies can be attributed to diffusion-limited hierarchical fusion of smaller gold nuclei, followed by anisotropic preferential growth on the sharp surfaces which exhibit higher chemical potentials [$\mu(R=\text{constant}) > \mu(R=\infty)$, Mullins–Sekereka instability⁴⁰]. Only a small incidence of NPs assumes dendritic shapes as it is difficult to lower the solution temperature homogeneously during MW exposure.

For a prolonged MW exposure duration (~3 min), some dendritic gold nanostructures suspended in solution also get wrapped/encapsulated within the GO sheets. (**Figure 4.3d**; also see Appendix C, Figure C.6). The encapsulation of NPs by GO sheets is driven by the covalent interaction forces between their surfaces; however, the complete mechanism needs more studies. Encapsulation of in-situ-formed Ag nanoparticles by GO sheets was reported earlier, where an optimal thickness (0.5 nm) and size ($\sim 1.5 \times 10^{-3} \mu\text{m}^2$) of the GO sheet was considered essential for the event of GO wrapping.⁴¹ Here, since the NP formation during the short MW exposure precedes their implantation on GO and several GO sheets exhibit large surface areas ($>1000 \mu\text{m}^2$) with multiple-layer thickness ($>1.5 \text{ nm}$), we observe a larger percentage of NP implants on GO sheets as compared to NPs wrapped with GO.

The absence of a chemical reducing agent makes this process fundamentally different from other solution-based GO–metal NP fabrication routes.^{27–30} The solution of BSGN-decorated GO sheets was stable for at least 60 days. In addition to the oxy-functional groups, the excellent stabilizing ability of GO sheets can also be ascribed to their micrometer-size surface area, which keeps the nuclei segregated in solution and reduces their coagulation probability.

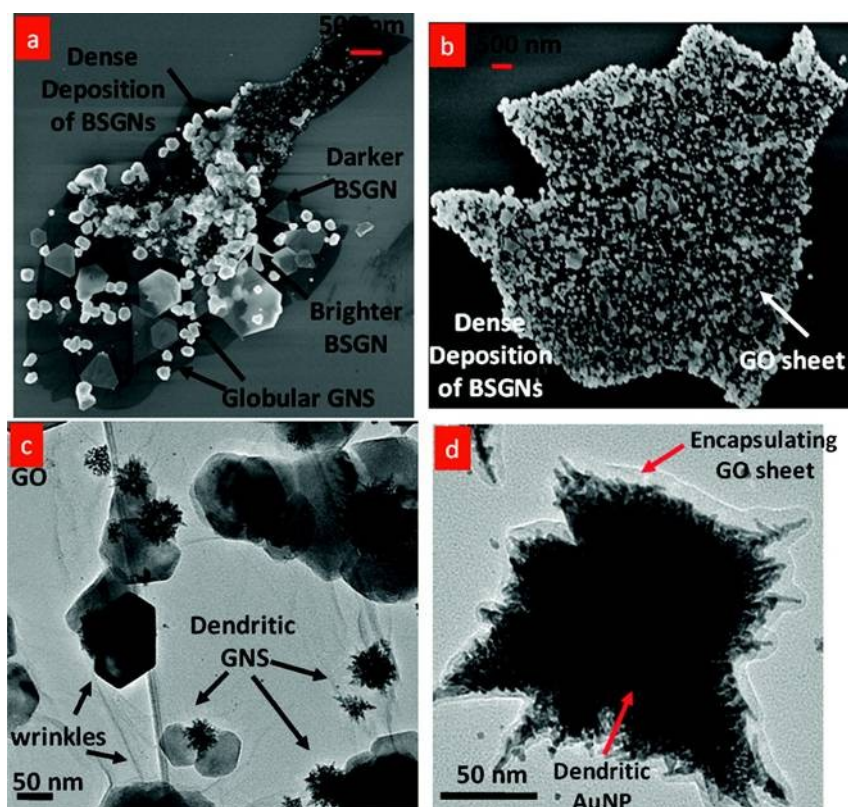


Figure 4.3 (a) FESEM image of a GO sheet decorated with BSGNs, exhibiting dark and bright contrast. The darker BSGNs are templated on the rear surface of the GO sheet, and the brighter BSGNs are templated on the exposed surface of the GO sheet. (b) FESEM image of a GO sheet that was immobilized ~ 72 h after being incubated in the microwave gold salt solution, exhibiting a high surface coverage index ($\eta = 0.79$). (c) TEM image of a GO sheet exhibiting dendritic and polyhedral GNS. (d) TEM image of an individual dendritic-shaped GNS wrapped with a GO sheet prepared by MW exposure to the solution of GO and gold salt maintained at a lower ambient temperature.

The dispersion density of BSGNs on GO can be enhanced by increasing the time of interaction between the microwaved gold salt solution and the GO sheets. **Figure 4.3b** shows a BSGN-GO sheet that was incubated for ~ 72 h before immobilizing on the silica substrate. This GO sheet exhibits a higher surface coverage index ($\eta = 0.79$) (see also Appendix C, Figure C.4) than the GO sheet incubated for ~ 24 h ($\eta = 0.31$). This observation suggests that BSGN implantation on GO is a diffusion-limited process. Thus, by increasing the time of interaction

between the microwaved gold salt solution and GO sheets, it is possible to significantly decrease the number of unassembled/unwrapped BSGNs and obtain a GO-BSGN composite dominant solution.

To probe the nature of interaction between the BSGNs and the GO surface, the GO-BSGN composites were analyzed for their Raman spectra. The D band line (1340 cm^{-1}) and G band line (1590 cm^{-1}) observed in the Raman spectrum of the GO sheet were found to be enhanced by $\sim 300\%$ by the presence of BSGNs (**Figure 4.4a**). This observed Raman signal enhancement is similar to the SERS effects that we reported earlier for metal nanoparticle composites of GO and suggests a chemical interaction between BSGNs and oxy-functional groups on GO.¹⁹



Here, we report the catalytic properties of the solution-dispersed GO-BSGN sheets for the GNP-catalyzed reduction of 4-nitroaniline (4-NA) to *p*-phenylene diamine (*p*-PDA) in the presence of NaBH_4 . The reaction rate is monitored by successive UV-vis absorbance measurements of the reaction solution ($4\text{-NA} + \text{NaBH}_4 \rightarrow \textit{p}\text{-PDA}$) as 4-NA and *p*-PDA exhibit distinct peaks at 380 and 238 nm, respectively. With the progress of reaction, the light-yellowish-colored 4-NA solution gradually turns colorless with the formation of *p*-PDA. In the presence of BSGNs-GO, the average reaction time (t_r) was ~ 8 min (**Figure 4.4b**). This reaction with the GO-supported BSGNs as catalysts is ~ 10 -fold faster than that reported in the literature for reduction using gold NPs as catalysts ($t_r = 86$ min) and ~ 100 -fold faster than the reduction using copper NP catalysts ($t_r = 8\text{--}12$ h) under identical conditions.^{42, 43}

Motivated by this excellent catalytic ability of BSGNs on GO and the fact that the catalytic rate constant of the GNPs increases with a decrease in the NP size, we synthesized GO-supported smaller GNP seeds (5–20 nm) by an in situ NaBH_4 reduction of gold salt (see Experimental Section). These smaller-sized spherical GNPs stabilized on GO are utilized to correlate the presence of a bare surface in the GO-supported gold seeds with the catalytic efficiency by comparing their catalytic activities with 5 nm citrate-capped gold nanoparticles. It

is pertinent to mention that establishing this correlation by utilizing the BSGNs synthesized by the MW method is challenging as they exhibit multiple shapes and hence cannot be directly compared for their catalytic activities with the citrate-stabilized spherical GNPs. The concentration of gold seeds/NPs in both solutions is made equivalent to $\sim 10^{13}$ /ML. The complete reduction of 4-NA takes ~ 6 min in the presence of GO-gold seeds and ~ 8 min in the presence of

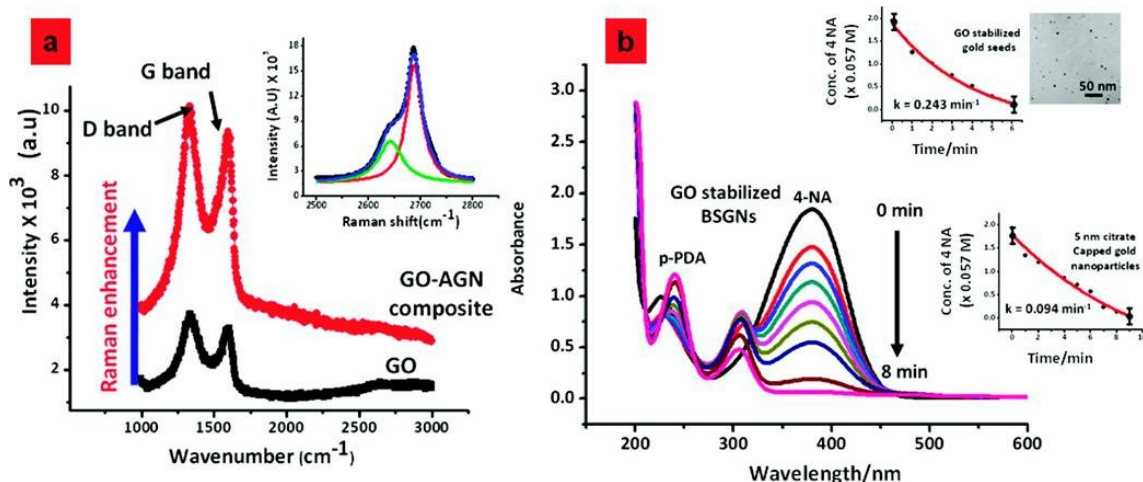


Figure 4.4 (a) The presence of BSGNs enhances the native Raman spectra of GO sheets by 300%, characteristic for a chemical enhancement, suggesting that the BSGNs chemically attach to the oxy-functional groups on GO. The inset shows the Lorentzian fit to the 2D band of the Raman spectra of GO and GO-BSGN sheets showing the presence of two components, which suggests a characteristic of few-layered graphene. (b) BSGNs stabilized on GO sheets were studied for their catalytic activity for NaBH_4 -induced reduction of 4-nitroaniline (4-NA). The reaction time can be evaluated by monitoring the successive decrease of the band at 380 nm for 4-NA and the corresponding increase in the band at 238 nm for *p*-phenylene diamine. Complete reduction of 4-NA in the presence of BSGNs stabilized on GO takes ~ 8 min. The insets show the first-order exponential fits for the reaction catalyzed by GO-gold seeds and 5 nm citrate-capped GNPs. The rate constants are found to be 0.243 and 0.094 min^{-1} respectively.

5 nm citrate-capped GNPs, with their first-order rate constants calculated to be $k_{\text{GO-gold seeds}} = 0.243 \text{ min}^{-1}$ and $k_{5 \text{ nm GNPs}} = 0.094 \text{ min}^{-1}$, respectively (**Figure 4.4b insets**), suggesting that the gold

seeds stabilized on GO have a higher catalytic activity than similar-shaped surfactant-coated gold nanoparticles.

Since the activity can be assumed to be directly proportional to the reaction rate constant, the active gold sites due to the naked surface on GO-gold seeds increase by a factor of $I_{\text{obs}} = k_{\text{GO-gold seeds}}/k_{5 \text{ nm GNP}} = 258\%$. The theoretical increase in the active gold sites (I_{theo}) on GO-gold seeds due to their naked surface (without including the effect of steric hindrance) can be given by:

$$I_{\text{theo}} = \frac{f \times A_{\text{gn}}}{f \times A_{\text{cp}}} \quad \text{Equation 4.2}$$

where, f is the fraction of catalytically active sites that are available per unit area on the bare surface of a spherical gold nanoparticle, A_{gn} is the bare area on the exposed semisurface of the GO-stabilized gold seed, and A_{cp} denotes the bare area on the citrate-capped GNP. We assume the rear-implanted semisurface of the GO-gold seed to be unavailable for catalytic participation. For a GNP/GO-gold seed with radius r , $A_{\text{gn}} = 2\pi r^2$ and $A_{\text{cp}} = 4\pi r^2 \times (1 - \partial)$, where ∂ is the fraction of the GNP surface area covered by the surfactant molecules. For N surfactant molecules adsorbed on a GNP with the projected area of the surfactant molecule = a_s ,

$$\partial = \frac{N \times a_s}{4\pi r^2} \quad \text{Equation 4.3}$$

For an equimolar concentration of gold salt and sodium tricitrate, N and a_s can be calculated as follows:

$$N = \frac{N_A \times \rho_{\text{gold}} \times \left(\frac{4\pi r^3}{3}\right)}{MW_{\text{goldsalt}}} \quad \text{Equation 4.4}$$

$$a_s = \pi r_o^2 \quad \text{Equation 4.5}$$

Here, a_s is approximated as the projected surface area of the carboxylic oxygen (radius = r_o) through which the citrate molecule binds to the GNP surface. For N_A (Avogadro's constant) = 6.023×10^{23} , $r = 5 \text{ nm}$, $r_o = 66 \text{ pm}$, $\rho_{\text{gold}} = 19.3 \text{ g/cm}^3$, and $MW_{\text{gold}} = 393.8$, N is calculated to be $1.54 \times$

10^4 , and δ is calculated to be 0.671. Substituting N and δ in equation 4.3, I_{theo} is calculated to be $\sim 152\%$, comparable to the value of $I_{\text{obs}} = 258\%$. Since the I_{theo} estimation does not consider the effect of steric hindrance from the surfactant molecules in the citrate-capped GNPs, the number of active sites on citrate-capped GNPs is overestimated. Hence, I_{theo} represents a lower bound of the increase in catalytically active sites due to the naked surface on the GO-gold seed. Clearly, the naked gold surface also benefits from the loss of steric hindrance as well.

We envision that the catalytic applications of the GO-BSGN composite will further benefit from the following facts: (1) GNPs catalyze a wide range of reactions with high selectivity, the kinetics of which can be significantly improved by substituting the stabilizing-agent-capped GNPs with GO-supported BSGNs; (2) the ability of the graphene platform to store and transfer electrons enhances the access paths available for electron transfer during the course of reaction, making it an ideal support material for the catalytic NPs; (3) (studied here) the GO-BSGN sheets can be suspended in several organic solvents, such as tetrahydrofuran, *N*-methyl-2-pyrrolidone, *N,N*-dimethylformamide, and ethylene glycol; (4) the GO-BSGN composite films on metal electrodes (such as Pt) can be used for electrocatalytic applications; and (5) the strong covalent interfacing of GNPs with GO would reduce catalyst poisoning.

For electrical characterization, GO and GO-BSGN composite sheets were immobilized on an amine-silanized silica on an n^{++} silicon substrate with prepatterned interdigitated gold electrodes. The **Figure 4.5a** insets show the FESEM and optical images of GO-BSGN and GO sheets deposited in between gold electrodes. Both devices had multilayered GO and GO-BSGN sheets (>5), as inferred by the Lorentzian analysis of the 2D band in their Raman spectra that comprises two components, which is characteristic of few-layer graphene (**Figure 4.5 a** inset). Figure 4.5 a compares the conductance of GO and GO-BSGN averaged over multiple samples. The average conductance of the GO-BSGN device ($27.02 \mu\text{S}$) was found to be $\sim 700\%$ higher than that of the GO devices ($0.387 \mu\text{S}$). This is attributed to the high density of gold islands on the GO surface, which offer a lower resistance to the carrier flow. The GO-BSGN ensemble can be modeled as an assembly of percolating BSGNs configured in parallel to the underlying GO surface, such that

$$R_{GO-BSGN} = \frac{R_{GO} \times R_{BSGN}}{R_{GO} + R_{BSGN}} < R_{GO}$$

Equation 4.6

We studied the effect of BSGN interfacing on the nature of majority charge carriers of the GO sheets by conducting gating studies on GO and GO-BSGN samples. Gating was performed at a source-drain voltage, $V_{DS} = 5$ V, and by measuring the change in conductivity with the gate voltage applied to the heavily doped silicon backgate (**Figure 4.5 b** bottom inset) under a 300 nm silica gate oxide. The surface charge density (n_o) induced upon application of a gate voltage (V_g) can be calculated as:

$$n_o = \frac{\epsilon_o \times \epsilon \times V_g}{d \times e}$$

Equation 4.7

where ϵ_o and ϵ are the relative permittivity of free space and silica respectively, e is the electron charge, and d is the thickness of the SiO₂ layer. GO exhibits a p-type semiconducting behavior, with a positive Dirac neutrality point located at $V_g = 18$ V (**Figure 4.5b** top inset). For the GO-BSGN sheet, the Dirac neutrality point is shifted toward large negative gate voltages, suggesting that the BSGNs inject electrons into the GO surface. The positive Dirac point of $V_o = 18$ V in the p-type GO suggests that at least 1.328×10^{12} holes cm⁻² in GO were paired with electrons during BSGN implantation ($V_g = V_o = 18$ V, $\epsilon = 4$, $\epsilon_o = 8.85 \times 10^{-12}$ F/m, $d = 300$ nm, and $e = 1.6 \times 10^{-19}$ C) to produce n-type GO-BSGN. The electron injection density is expected to be proportional to the GNP size and implantation density. Therefore, by controlling the implantation process, the carrier properties of the GO-BSGN can be tuned, thus opening avenues for fabricating graphene-based p-n junction devices with controllable electronic properties.

Similar to gold, silver nanostructures were also stabilized on GO via the microwave process. Microwaving silver salt (AgNO₃) in the presence of GO sheets results in the formation of GO-stabilized spherical and tadpole-shaped Ag NPs (Appendix C, Figures C.9 and C.10), suggesting the excellent adaptability of the MW method, making it a highly prospective tool for interfacing GO with diverse metal NPs

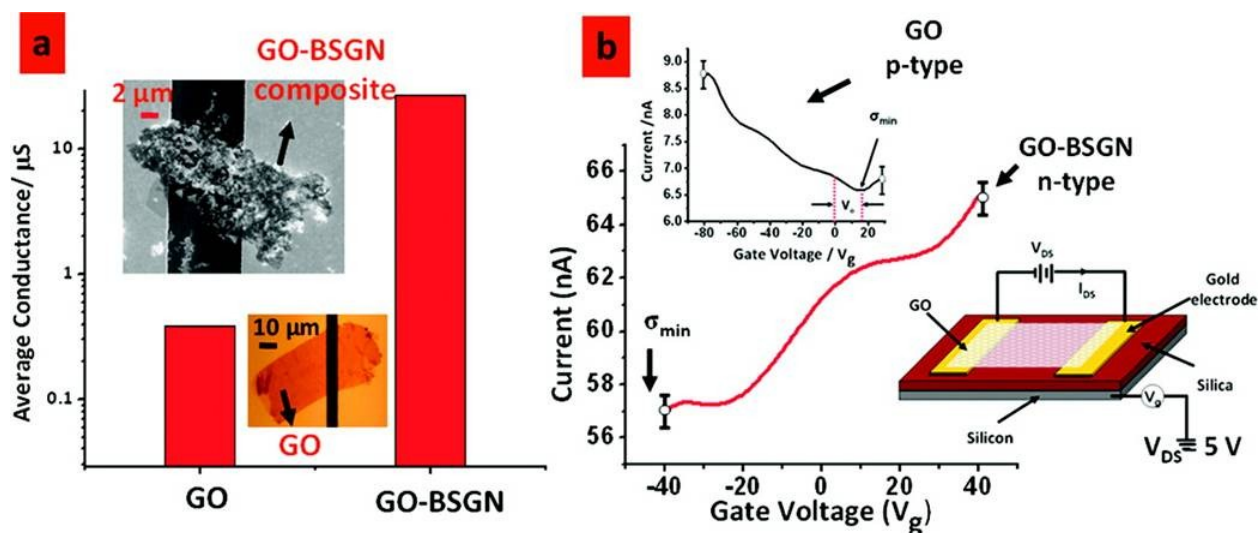


Figure 4.5 (a) BSGNs enhance the average conductance of GO sheets by an order of magnitude. The top inset shows the FESEM image of the surface-immobilized GO-BSGN composite, and the bottom inset shows the optical image of a GO sheet in between gold electrodes. (b) The effect of BSGNs on the nature of charge carriers in GO is determined by comparing the gating behaviour of GO and GO-BSGN at a constant source-drain voltage (V_{DS}) of 5 V. The top inset shows the gating behaviour of GO, which exhibits a p-type semiconducting behaviour; the Dirac neutrality point is situated at 18 V. In the presence of BSGNs, the Dirac neutrality point shift towards negative voltages, making GO-BSGN an n-type semiconductor. The bottom inset shows the schematic for the gating setup.

4.5 Summary

In summary, this work presents a potential solution to a major challenge in liquid-phase catalysis by enabling the synthesis of stable liquid dispersions of uncapped metal nanoparticles with enhanced density of accessible catalytic sites. This is achieved by the implantation of MW-nucleated NPs on the GO acting as a stabilization agent for GNPs. Remarkably, these naked BSGNs possess 258% higher density of catalytically active atomic sites, which enhance the catalytic reduction of p-nitro aniline 10-100 fold. Further, the BSGNs enhance the Raman signal of GO 3 fold and inject 1.328×10^{12} electrons into the p-type GO to make it n-type, thus enabling the manipulation of its carrier density. We envision that the results presented here will evolve the fields of liquid phase catalysis, graphene nanotechnology, and electronics, and this highly

versatile process will potentially produce next generation supported catalysts, graphene hybrids, optoelectronic devices, sensors, Raman multipliers, and molecular electronics.

4.6 References

- (1) Katsnelson, M. I.; Novoselov, K. S.; Geim, A. K. Chiral Tunnelling and the Klein Paradox in Graphene. *Nat. Phys.* 2006, 2, 620–625.
- (2) Novoselov, K. S.; Jiang, Z.; Zhang, Y.; Morozov, S. V.; Stormer, H. L.; Zeitler, U.; Maan, J. C.; Boebinger, G. S.; Kim, P.; Geim, A. K. Room-Temperature Quantum Hall Effect in Graphene. *Science* 2007, 315, 1379.
- (3) Wang, F.; Zhang, Y.; Tian, C.; Girit, C.; Zettl, A.; Crommie, M.; Shen, Y. R. Gate-Variable Optical Transitions in Graphene. *Science* 2008, 320, 206.
- (4) Blake, P.; Brimicombe, P. D.; Nair, R. R.; Booth, T. J.; Jiang, D.; Schedin, F.; Ponomarenko, L. A.; Morozov, S. V.; Gleeson, H. F.; Hill, E.W.; et al. Graphene-Based Liquid Crystal Device. *Nano Lett.* 2008, 8, 1704–1708.
- (5) Wright, A. R.; Xu, X. G.; Cao, J. C.; Zhang, C. Strong Nonlinear Optical Response of Graphene in the Terahertz Regime. *Appl. Phys. Lett.* 2009, 95, 072101.
- (6) Xu, X.; Gabor, N. M.; Alden, J. S.; van der Zande, A. M.; McEuen, P. L. Photo-Thermoelectric Effect at a Graphene Interface Junction. *Nano Lett.* 2010, 10, 562–566.
- (7) Lee, C.; Wei, X. D.; Kysar, J. W.; Hone, J. Measurement of the Elastic Properties and Intrinsic Strength of Monolayer Graphene. *Science* 2008, 321, 385–388.
- (8) Mohanty, N.; Berry, V. Graphene-Based Single-Bacterium Resolution Biodevice and DNA Transistor: Interfacing Graphene Derivatives with Nanoscale and Microscale Biocomponents. *Nano Lett.* 2008, 8, 4469–4476.
- (9) Lu, C. H.; Yang, H. H.; Zhu, C. L.; Chen, X.; Chen, G. N. A Graphene Platform for Sensing Biomolecules. *Angew. Chem., Int. Ed.* 2009, 48, 4785–4787.
- (10) Liu, Z.; Robinson, J. T.; Sun, X.; Dai, H. PEGylated Nanographene Oxide for Delivery of Water-Insoluble Cancer Drugs. *J. Am. Chem. Soc.* 2008, 130, 10876–10877.
- (11) Sundaram, R. S.; Gomez-Navarro, C.; Balasubramanian, K.; Burghard, M.; Kern, K. Electrochemical Modification of Graphene. *Adv. Mater.* 2008, 20, 3050–3053.

- (12) Wu, Z. S.; Pei, S.; Ren, W.; Tang, D.; Gao, L.; Liu, B.; Li, F.; Liu, C.; Cheng, H. M. Field Emission of Single-Layer Graphene Films Prepared by Electrophoretic Deposition. *Adv. Mater.* 2009, 21, 1756–1760.
- (13) Bunch, J. S.; Verbridge, S. S.; Alden, J. S.; van der Zande, A. M.; Parpia, J. M.; Craighead, H. G.; McEuen, P. L. Impermeable Atomic Membranes from Graphene Sheets. *Nano Lett.* 2008, 8, 2458–2462.
- (14) Ramanathan, T.; Abdala, A. A.; Stankovich, S.; Dikin, D. A.; Herrera-Alonso, M.; Piner, R. D.; Adamson, D. H.; Schniepp, H. C.; Chen, X.; Ruoff, R. S.; et al. Functionalized Graphene Sheets for Polymer Nanocomposites. *Nat. Nanotechnol.* 2008, 3, 327–331.
- (15) Stankovich, S.; Dikin, D. A.; Dommett, G. H. B.; Kohlhaas, K. M.; Zimney, E. J.; Stach, E. A.; Piner, R. D.; Nguyen, S. T.; Ruoff, R. S. Graphene-Based Composite Materials. *Nature* 2006, 442, 282–286.
- (16) Li, J.; Guo, S.; Zhai, Y.; Wang, E. Nafion-Graphene Nanocomposite Film As Enhanced Sensing Platform for Ultrasensitive Determination of Cadmium. *Electrochem. Commun.* 2009, 11, 1085–1088.
- (17) Fowler, J. D.; Allen, M. J.; Tung, V. C.; Yang, Y.; Kaner, R. B.; Weiller, B. H. Practical Chemical Sensors from Chemically Derived Graphene. *ACS Nano* 2009, 3, 301–306.
- (18) Williams, G.; Seger, B.; Kamat, P. V. TiO₂-Graphene Nanocomposites. UV-Assisted Photocatalytic Reduction of Graphene Oxide. *ACS Nano* 2008, 2, 1487–1491.
- (19) Jasuja, K.; Berry, V. Implantation and Growth of Dendritic Gold Nanostructures on Graphene Derivatives: Electrical Property Tailoring and Raman Enhancement. *ACS Nano* 2009, 3, 2358–2366.
- (20) Si, Y.; Samulski, E. T. Exfoliated Graphene Separated by Platinum Nanoparticles. *Chem. Mater.* 2008, 20, 6792–6797.
- (21) Wang, X.; Tabakman, S. M.; Dai, H. Atomic Layer Deposition of Metal Oxides on Pristine and Functionalized Graphene. *J. Am. Chem. Soc.* 2008, 130, 8152–8153.
- (22) Comotti, M.; la Pina, C.; Matarrese, R.; Rossi, M. The Catalytic Activity of “Naked” Gold Particles. *Angew. Chem., Int. Ed.* 2004, 43, 5812–5815.

- (23) Chen, M. S.; Goodman, D. W. The Structure of Catalytically Active Gold on Titania. *Science* 2004, 306, 252.
- (24) Majetich, G.; Hicks, R. Applications Of Microwave-Accelerated Organic Synthesis: Theory and Applications of Microwave Radiation. *Radiat. Phys. Chem.* 1995, 45, 567–579.
- (25) Landry, C. C.; Barron, A. R. Synthesis of Polycrystalline Chalcopyrite Semiconductors by Microwave Irradiation. *Science* 1993, 260, 1653–1655.
- (26) Lee, Y. T.; Choi, S. Y.; Lee, S. I.; Chung, Y. K.; Kang, T. J. Microwave-Assisted Synthesis of (6-Arene) Tricarbonylchromium Complexes. *Tetrahedron Lett.* 2006, 47, 6569–6572.
- (27) Tsuji, M.; Hashimoto, M.; Nishizawa, Y.; Tsuji, T. Synthesis of Gold Nanorods And Nanowires By a Microwave-Polyol Method. *Mater. Lett.* 2004, 58, 2326–2330.
- (28) Tu, W.; Liu, H. Rapid Synthesis of Nanoscale Colloidal Metal Clusters by Microwave Irradiation. *J. Mater. Chem.* 2000, 10, 2207–2211.
- (29) Liu, F. K.; Ker, C. J.; Chang, Y. C.; Ko, F. H.; Chu, T. C.; Dai, B. T. Microwave Heating for the Preparation of Nanometer Gold Particles. *Jpn. J. Appl. Phys.* 2003, 42, 4152–4158.
- (30) Pastoriza-Santos, I.; Liz-Marzan, L. M. Formation of PVPProtected Metal Nanoparticles in DMF. *Langmuir* 2002, 18, 2888–2894.
- (31) Fan, C.; Li, W.; Zhao, S.; Chen, J.; Li, X. Efficient One Pot Synthesis of Chitosan-Induced Gold Nanoparticles by Microwave Irradiation. *Mater. Lett.* 2008, 62, 3518–3520.
- (32) Tsuji, M.; Matsumoto, K.; Tsuji, T.; Kawazumi, H. Rapid Synthesis of Gold Nanostructures by a Microwave-Polyol Method with the Assistance of CnTAB (n=10, 12, 14, 16) or C16PC. *Mater. Lett.* 2005, 59, 3856–3860.
- (33) Wang, J.; Wang, Z. Rapid Synthesis of Hexagon-Shaped Gold Nanoplates by Microwave Assistant Method. *Mater. Lett.* 2007, 61, 4149–4151.
- (34) Dallinger, D.; Kappe, C. O. Microwave-Assisted Synthesis in Water as Solvent. *Chem. Rev* 2007, 107, 2563–2591.
- (35) Bi, Y.; Lu, G. Morphological Controlled Synthesis and Catalytic Activities of Gold Nanocrystals. *Mater. Lett.* 2008, 17-18, 2696–2699.

- (36) Chen, W.; Yan, L.; Bangal, P. R. Preparation of Graphene by the Rapid and Mild Thermal Reduction of Graphene Oxide Induced by Microwaves. *Carbon* 2010, 48, 1146–1152.
- (37) Murray, C. B.; Kagan, C. R.; Bawendi, M. G. Synthesis and Characterization of Monodisperse Nanocrystals and Close- Packed Nanocrystal Assemblies. *Annu. Rev. Mater. Sci.* 2000, 30, 545–610.
- (38) Gao, W.; Alemany, L. B.; Ci, L.; Ajayan, P. M. New Insights into the Structure and Reduction of Graphite Oxide. *Nat. Chem.* 2009, 1, 403–408.
- (39) Nittman, J.; Stanley, H. E. Tip Splitting Without Interfacial Tension and Dendritic Growth Patterns Arising from Molecular Anisotropy. *Nature* 1986, 321, 663–668.
- (40) Langer, J. S. Instabilities and Pattern Formation in Crystal Growth. *Rev. Mod. Phys.* 1980, 52, 1–28.
- (41) Cassagneau, T.; Fendler, J. H. Preparation and Layer-By-Layer Self-Assembly of Silver Nanoparticles Capped by Graphite Oxide Nanosheets. *J. Phys. Chem. B* 1999, 103, 1789–1793.
- (42) Saha, A.; Ranu, B. Highly Chemoselective Reduction of Aromatic Nitro Compounds by Copper Nanoparticles/Ammonium Formate. *J. Phys. Chem.* 2008, 73, 6867–6870.
- (43) Kundu, S.; Lau, S.; Liang, H. Shape-Controlled Catalysis by Cetyltrimethylammonium Bromide Terminated Gold Nanospheres, Nanorods, and Nanoprisms. *J. Phys. Chem. C* 2009, 113, 5150–5156.

5 Exfoliation of Boron Nitride

5.1 Overview

This chapter investigates a new chemical method to exfoliate ultrathin α -boron nitride sheets (UTBNSs) from their bulk 3-dimensional form and discusses the advantages over other currently available exfoliation methods. UTBNSs possess exclusive set of properties, including large band-gap, high optical-transparency, high mechanical strength, high thermal-conductivity, UV cathodoluminescence, and pronounced thermo chemical stability¹⁻⁸. However, exfoliating large α -BN layers in dispersions has remained a challenge due to high interlayer *lip-lip* cohesive-interaction and their chemically-resistant nature. Currently, exfoliation processes produce small sheets ($0.1 - 5 \mu\text{m}^2$) at low yields. Here we report on the protonation of α -BN lattice *via* treatment with chlorosulfonic acid that not only exfoliates ‘large’ UTBNSs (upto $10,000 \mu\text{m}^2$) at high yields ($\sim 23\%$), but also results in their covalent functionalization by introducing four forms of aminated N sites within the UTBNS-lattice: sp^2 -delocalized & sp^3 -quaternary protonation on internal N sites ($>\text{N}^+=$ and $>\text{NH}^+$), and pyridinic-like protonation on the edge N sites ($=\text{NH}^+$ and $-\text{NH}-$). The presence of these groups transform the chemically-passive BN sheets to their chemically-active form, which as demonstrated here, can be used as scaffolds for forming composites with gold nanoparticles and dye molecules. The UTBNS dispersion exhibits an optical band-gap of 5.74 eV, implying production of primarily monolayer UTBNSs; and a zeta potential of $\zeta = +36.25\text{mV}$ at $\text{pH}=6.1$ ($\zeta_{\text{max}} = +150 \text{ mV}$), confirming high dispersion-stability. We envision that these 2D nanomaterials with atomically-packed honeycomb lattice and high energy-gap will evolve next-generation applications in controlled-UV-emission, atomic-tunneling-barrier devices, ultrathin impermeable-membranes, and thermo-chemically-resistive transparent-coatings.

5.2 Introduction

Recent advances in the synthesis of ultrathin 2-D nanomaterials have provided access to quantum-relativistic electrical, physical and chemical phenomena, including massless Dirac fermions⁹, room-temperature quantum Hall effect¹⁰ and ambipolar field effects¹¹ in graphene;

and quantum confinement driven intense fluorescence¹² in MoS₂. While the synthesis of its structural isomorph, graphene^{13,14}, has been explored thoroughly, the synthesis strategies for UTBNs are currently at incipient stages, and routes to produce solvent-dispersible large-area sheets are being avidly sought¹⁵. The primary challenge in exfoliating UTBNs is the strong interlayer *lip-lip*^{16,17} interactions in α -BN that result from the partly ionic character of the B-N bond. The current techniques to achieve exfoliation involves ultrasonication of α -BN flakes in organic solvents/polymeric surfactants¹⁵ [like **(a)** dimethylformamide(DMF)¹⁸ (yield = 0.05 – 0.1 %, size ~ nanoscale), **(b)** 1,2 dichloroethane (DCE)¹⁹/DCE solution of poly(phenylenevinylene) polymer²⁰ (yield and concentration not reported, size $\approx 1 \mu\text{m}^2$), or **(c)** octadecylamine and amine-terminated Poly ethylene glycol²¹ (concentration = 0.5 – 1 mg/ml, yield = 10 – 20%, sheet size $\approx 200 \text{ nm}$)] that intercalate within the α -BN layers due to either a similarity in surface energy ($\gamma_{\text{polymer-BN}} \approx \gamma_{\text{BN-BN}}$) or Lewis-base complex formation with electron-deficient B atoms. This weakens the interlayer forces and thus exfoliates the sheets. Recently, exfoliation of UTBNs in isopropyl alcohol was also reported¹⁵ (yield $\approx 0.8\%$, concentration = 0.06 mg/ml, sheet size $\sim 1 \mu\text{m}^2$). The above mentioned routes produce small sheets ($\leq 1\text{-}2 \mu\text{m}^2$) and/or have a low yield. The main culprit for the small size is sonication, which induces tearing. Other CVD and micromechanical cleavage processes for fabricating BN monolayers generally do not produce solution dispersions. In this study, we protonate the α -BN lattice *via* chlorosulfonic acid (CA) treatment, which induces interlayer repulsion, resulting in spontaneous exfoliation of the stacked UTBNs to produce large-area UTBNs in significantly high yield ($\sim 23\%$) and concentrations ($> 0.7 \text{ mg/ml}$) (**Figure 5.1**). Subsequently, the UTBNs are transferred to aqueous solution to produce stable dispersions as explained in the Experimental Section.

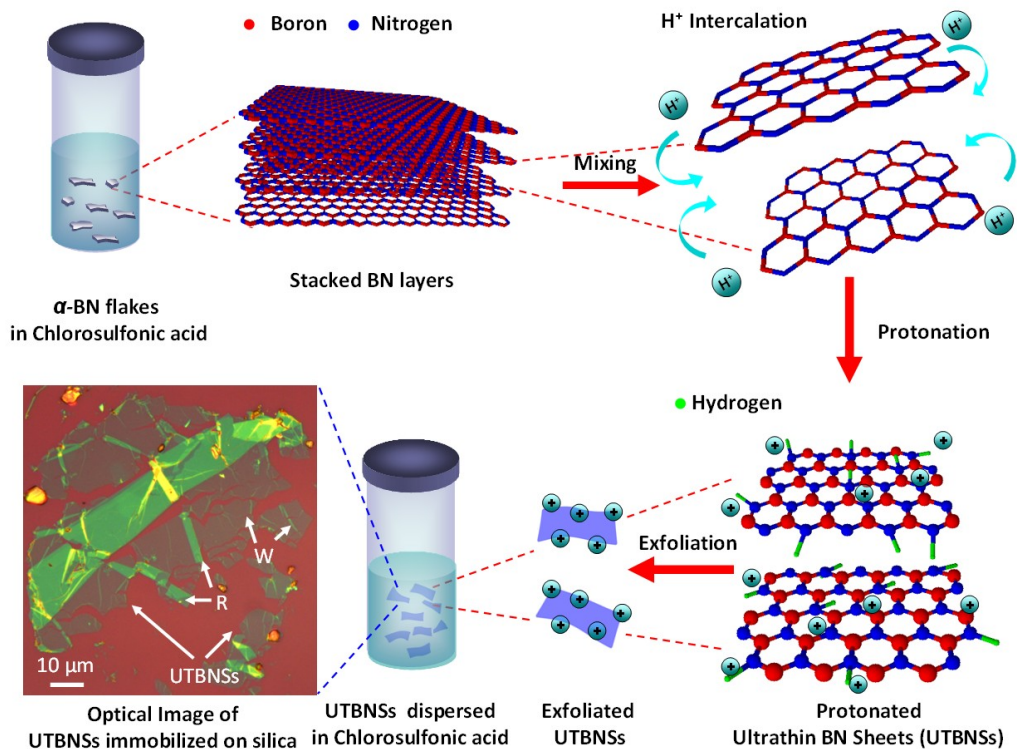


Figure 5.1 Chlorosulfonic Acid (CA) exfoliation of Ultrathin Boron Nitride Sheets (UTBNSs)

The AA' stacked α -BN sheets when suspended in CA undergo protonation at the N centre of the slightly polar B-N bonds which results in surface chemical modification of the intermittent layers. The presence of a high density of positive surface charges lead to intersheet repulsions that overcome the interlayer binding forces, resulting in layer-by-layer exfoliation of UTBNSs which remain suspended in CA due to electrostatic stabilization. Bottom left inset shows the optical image of UTBNSs on a silica substrate. The immobilized sheets exhibit surface wrinkles (labeled W) and raised regions (labeled R), which arise from the multiple-point electrostatic attachment.

5.3 Experimental section

5.3.1 Synthesis of UTBNSs

Bulk α -BN is procured in the form of (a) single crystals that obtained by scrapping high-purity hot-pressed boron nitride, grade HBC procured from Momentive Performance Materials,

and **(b)** a highly oriented pyrolytic boron nitride (HOPBN) . 10 ml of 97% pure CA was added to a glass vial with 50 mg of α -BN under the dry N₂ atmosphere of a glove-box. The α -BN and CA mixture was blended using a teflon coated magnetic stir bar for ~72 hrs at 1500 rpm, wherein a large fraction of the bulk α -BN undergoes exfoliation and the remainder settles down. This produces a stable dispersion of exfoliated UTBNSs which exhibits a pale white color due to distinct light scattering.

5.3.2 *Transfer to aqueous phase*

For further investigation outside the glove-box, the moisture-sensitive CA solution, containing the exfoliated UTBNSs, was diluted several folds (1:200) in an aqueous solution *via* a process of quenching. 500 ml of de-ionized (DI) water in a glass beaker was placed inside the glove-box and 2.5 ml of the UTBNSs-CA solution added drop-wise to the beaker to obtain the quenched solution. The quenched solution was then removed from the glove-box and allowed to stand for ~24 hours as the un-exfoliated α -BN flakes sediment to the bottom.

5.3.3 *XPS analysis*

Uniform Boron Nitride films with stacked UTBNS layers were formed on a polymeric membrane (Poly Tetra Fluoro Ethylene or polycarbonate) paper by vacuum filtration of the quenched suspensions (see Appendix D, Figure D.2). The XPS data was obtained from a Perkin–Elmer PHI 5400 electron spectrometer using achromatic AlK α radiation (1486.6 eV) under vacuum of 8.0×10^{-9} Torr. The XPS binding energies were measured with a precision of 0.1 eV and the analyzer pass energy was set to 17.9 eV, with a contact time of 50 ms. Before sample testing, the spectrometer was calibrated by setting the binding energies of Au 4f_{7/2} and Cu 2p_{3/2} to 84.0 and 932.7 eV, respectively and using C1s spectra at 285.0 eV as the reference. The samples were heated *in-vacuo* to a temperature of 400 °C for ~2hrs to remove any residues of CA and any atmospheric adsorbates.

5.3.4 FESEM Imaging and EDS

FESEM Images and EDS were obtained with a LEO field emission scanning electron microscope and FEI Nova Nano SEM 430. The UTBNSs were immobilized on silica substrates by surface pick-up technique (as explained in the Appendix D) and drop casting.

5.3.5 TEM Imaging and SAED studies

The TEM images and SAED pattern were obtained with a FEI Tecnai F20 XT Field Emission Transmission Electron Microscope and Philips CM 100 transmission electron microscope. For TEM sample preparation, 300 mesh size copper TEM specimen grids (Electron Microscopy Sciences) having a lacey carbon support film were used for picking up sheets from the surface of quenched solution.

5.3.6 Zeta Potential Measurement

Zeta potential is calculated from the Electrophoretic mobility obtained from light scattering measurements on aqueous UTBNS dispersions in a Zeta Plus Zeta Potential Analyzer (Brookhaven's Instrument Corporation). The pH of aqueous dispersion was adjusted using 0.1 M solution of sodium hydroxide. This instrument was also used for determining the size distribution by laser light scattering.

5.3.7 Synthesis of citrate capped gold nanoparticles (GNPs) and templating on UTBNSs

Citrate capped GNPs were synthesized by adding tri-sodium citrate to a solution of 1M HAuCl₄ and heating the mixture on a hot-plate for ~20 min until the solution color turns red. These GNPs are interfaced with UTBNSs in aqueous phase where they undergo an electrostatic self-assembly process.

5.4 Results and Discussion

While the CA's treatment of BN is a novel study, CA's strong protonating chemistry has been applied to solvate carbon nanotubes (CNTs)^{22,22-24} and exfoliate graphene²⁵. The route for dispersing UTBNSs in CA exhibits three significant strengths: **(a)** Produces large sheets by

precluding sonication: The high density of protonation enables spontaneous exfoliation without the assistance of sonication, which is known to fragment the sheets into smaller size. The method presented here produces sheets with lateral dimensions as large as $\sim 100\ \mu\text{m}$; **(b)** Enables chemical surface functionalization of UTBNSs: The UTBNS's lattice consists of protonated sp^2 and sp^3 N atoms ($>\text{N}^+=$ and $>\text{NH}^+$ respectively within lattice) and protonated pyridinic-like N atoms ($=\text{NH}^+$ and $>\text{NH}^+$ along the edges) [as shown ahead in the X-ray photoelectron spectroscopy (XPS) studies)], which are challenging to achieve on the inert BN surface. These active lattice functionalities can be leveraged for electrostatic interfacing and for tethering new chemical groups; and **(c)** Enables aqueous phase dispersion of UTBNSs: The highly charged lattice of UTBNSs results in their aqueous phase electrostatic stabilization without the need of surfactants.

The dispersion of UTBNSs in CA exhibits Tyndall Effect (distinct light scattering via suspended colloids), when exposed to a red laser beam (**Figure 5.2a**). The path of laser beam in UTBNS-CA dispersion is clearly discernible, in contrast to that in the bare CA solution. The dispersions remain stable for prolonged periods (> 4 months). Aqueous dispersions of UTBNSs were obtained by transferring the CA dispersed sheets to water ($\sim 1:200$ dilution, see SI section S02). Figure 2b shows the UV-visible absorption spectrum of the water- dispersed UTBNSs. The spectrum exhibits one sharp absorption peak at $\sim 198\ \text{nm}$, consistent with earlier studies. The otherwise featureless spectrum is explained by the extremely low optical coefficient of the UTBNSs reported earlier²¹. Figure 5.2b inset shows the Tauc's plot obtained from the absorbance spectrum; its linear regime is fitted (straight line, slope= 84.2°) and extrapolated to obtain the gap wavelength (λ_0) of $\sim 216\ \text{nm}$ and corresponding optical band-gap (E_g) of $5.74\ \text{eV}$. The sharp slope exhibited within the linear regime suggests the presence of an exclusive single crystalline phase in the aqueous solution²⁶.

Theoretical calculations predict $E_g = 6\ \text{eV}$ for a single atom thick α -BN sheet²⁷. The presence of layer-layer interactions can reduce E_g by widening the electronic band dispersion. 2-5 layer thick α -BN sheets exhibit a band-gap of $\sim 5.56\ \text{eV}$ ²⁸. We thus speculate that the UTBNSs, with $E_g = 5.74\ \text{eV}$, will be between 1 to 5 atoms thick. The observed decrease in band gap could

also be due to the presence of chemical functional groups (in which case the sheets will be thinner), but this needs to be confirmed.

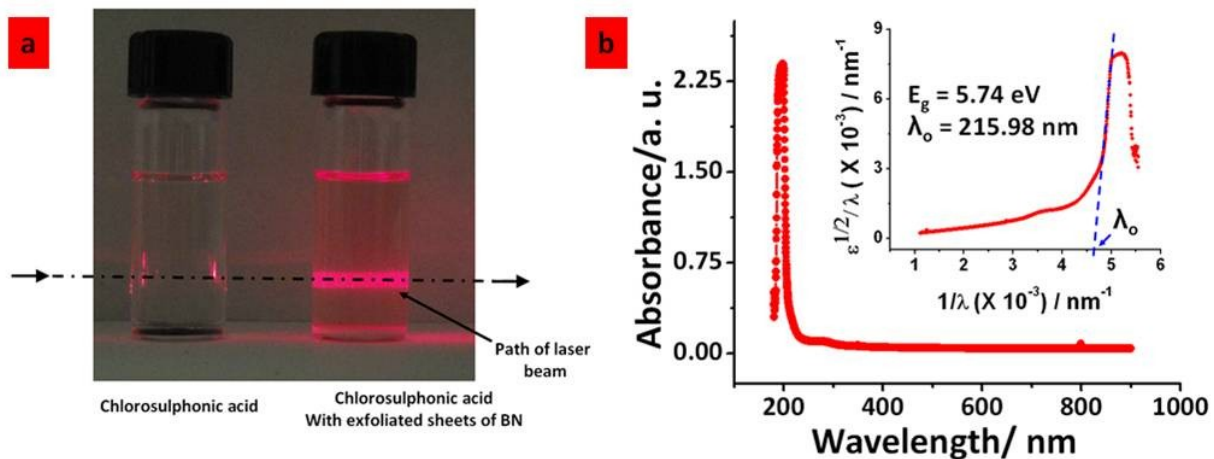


Figure 5.2 Optical Properties of UTBNSs and Band-gap determination a) Tyndall effect as observed in UTBNSs dispersed in a CA solution. The path of laser beam is clearly distinguishable in the CA solution containing UTBNSs as compared to the bare CA solution. b, Ultraviolet-visible absorption spectra of UTBNSs suspended in water at room temperature. The aqueous solution is obtained by transferring the CA containing exfoliated UTBNSs in water (as explained in Experimental section and Appendix section D.2). Inset shows the Tauc plot generated from the absorption spectra for UTBNSs. The linear regime is extrapolated to obtain gap wavelength $\lambda_0=216$ nm and corresponding optical band gap $E_g=5.74$ eV.

The chemical composition of UTBNSs was investigated by XPS scanning of BN flakes and UTBNS films. The UTBNS film was formed by vacuum filtration of the aqueous UTBNS suspensions (see Methods and Appendix section D.3 for detailed process). The central inset in **Figure 5.3** shows the cross-sectional FESEM image of an UTBNS film. The obtained spectra were analyzed for B1s and N1s core level peak-features. **Figure 5.3a** shows the XPS spectra for bulk α -BN flakes fitted with Gaussian distributions; the B1s and N1s peaks are located at 190.8eV and 398.4eV respectively, which is in accordance with the previously reported values of B1s and N1s peak position in conjugated BN systems [for example, the monolayer α -BN samples prepared by CVD on Cu substrates²⁸]. For the UTBNS films, the B1s and N1s spectra

exhibit primary peaks at 190.8 eV and 398.4 eV respectively. Additionally, secondary peaks appeared as shoulders at higher binding energies (**Figure 5.3b**).

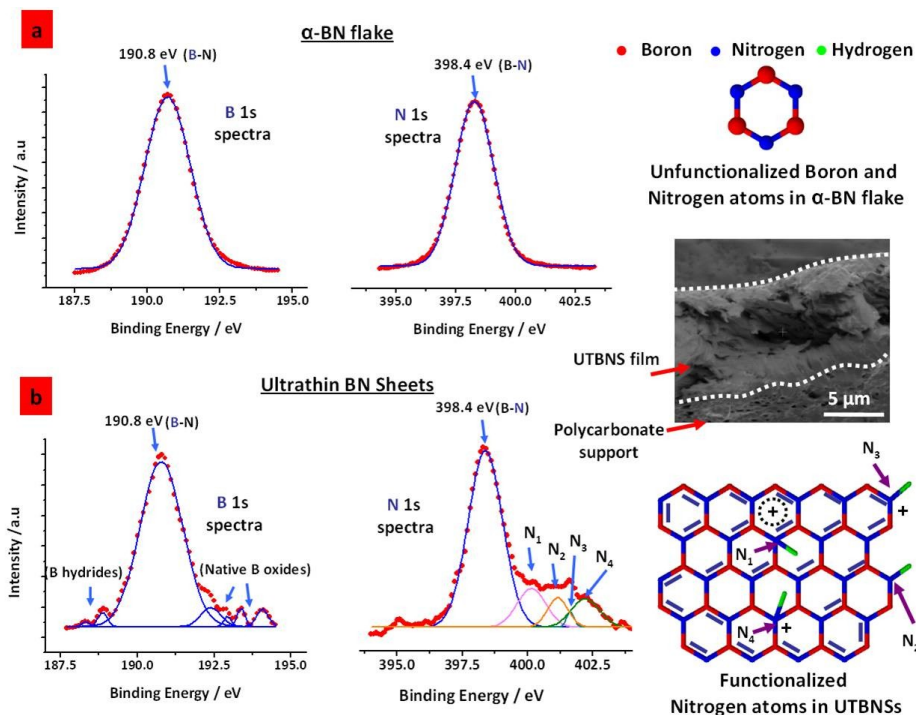


Figure 5.3 XPS studies to determine the chemical functionalization of UTBNSs a, B1s and N1s core level spectra from the XPS analysis of the α -BN flakes. The spectra fitted with Gaussian distributions exhibit peaks at 190.8eV and 398.4eV respectively, which correspond to the conjugated BN structures shown in the top right inset (=B- and =N-). b, B1s and N1s spectra of UTBNSs (obtained from an UTBNS film, cross-sectional FESEM image shown in middle inset) exhibit extended shoulders at higher binding energies in addition to the primary peaks at 190.8eV and 398.4eV respectively. The N1s spectra in the UTBNSs exhibits secondary shoulders at (1)400.1 eV, (2)401.1 eV, (3)401.6 eV and (4)402.2 eV attributed to N atoms protonated in four distinct manners as represented in the bottom right inset. This indicates functionalization of UTBNSs post CA treatment.

Deconvolution of the N1s spectrum using a Gaussian fit reveals the positions of these secondary peaks at: 400.1 eV, 401.1 eV, 401.6 eV and 402.2 eV. The shift of the peaks to higher binding energies indicates that, post CA treatment, the formal-charge on N becomes positive (attributed to its protonation). These peaks correspond to four distinct forms of N-protonations

on the lattice, as represented in **Figure 5.3b** insets: **(a)** The peak at 400.1 eV is attributed to protonation of sp^2 N atom, where the positive charge is delocalized over the conjugated hexagonal ring with preserved structural integrity (shown as N_1). This is similar to the protonation by sulfonic acid on the conjugated hexagonal carbon rings in CNTs²². **(b)** The peaks at 401.1 eV and 401.4 eV are attributed to the protonation of pyridinic-like N atoms (lying along the edges) present in milieu of un-conjugated and conjugated rings respectively (shown as N_2 and N_3), and **(c)** the peak at 402.2 eV is attributed to the direct protonation of quaternary N atom²⁹ in its sp^3 hybridized state (shown as N_4). This is similar to the binding energies reported for N atoms within cyclic rings^{29,30}.

The relative fractional contributions from the functional groups are: 12.7% (N_1), 7% (N_2), 1.3% (N_3) and 9.3% (N_4) (from the areas under respective peaks). Therefore, 22% of internal lattice N ($N_1 + N_4$) and 8.3 % edge N ($N_2 + N_3$) are protonated. The TEM images of several UTBNSs (Appendix D, Figure D.4) exhibit nanoscale perforations and crevices. The edges of these internal perforations, crevices along with the outermost sheet-edges and internal vacancy defects will also contribute the pyridinic-like dangling N atoms. The distribution of protonated N atoms was studied by labeling them with amine-reactive fluorescein isothiocyanate (FITC) dye (see Appendix D, section D.15). Under confocal microscope, fluorescence at 518 nm (emission maximum of FITC) from the functionalized UTBNS sheets on silica surface, confirmed the uniform distribution of protonated N centers on UTBNS lattice (**Figure 5.4a**).

The B1s spectrum also exhibits additional secondary peaks apart from the primary peak at 190.8 eV. The peaks located at ~ 193 eV correspond to the native boron-oxides, while the peak at ~ 188 eV corresponds to boron-hydride derivative³¹. However, the fraction of these B-derivatives on the lattice is less than the protonated Ns; attributed to the scant oxidation of edge B atoms by CA. Also, by multiple cycles of centrifuging and resuspending in water the concentration of more hydrophilic UTBNS with higher fraction of functionalized B and N atoms was increased (see Appendix D: Figure D.2). This lattice-protonation process is proposed to initiate in a fashion similar to the intercalation of nitric acid (NA) molecules within α -BN layers. Here, the CA molecules will enter the BN layers, increase the interlayer spacing, form charge transfer complexes by extracting electrons from the layers, and impart a high hole-density³². In

the presence of CA, a much higher degree of protonation is expected that would induce electrostatic repulsion between the protonated BN layers, sufficient to overcome the lip-lip attraction, resulting in layer-by-layer exfoliation of the UTBNSs.

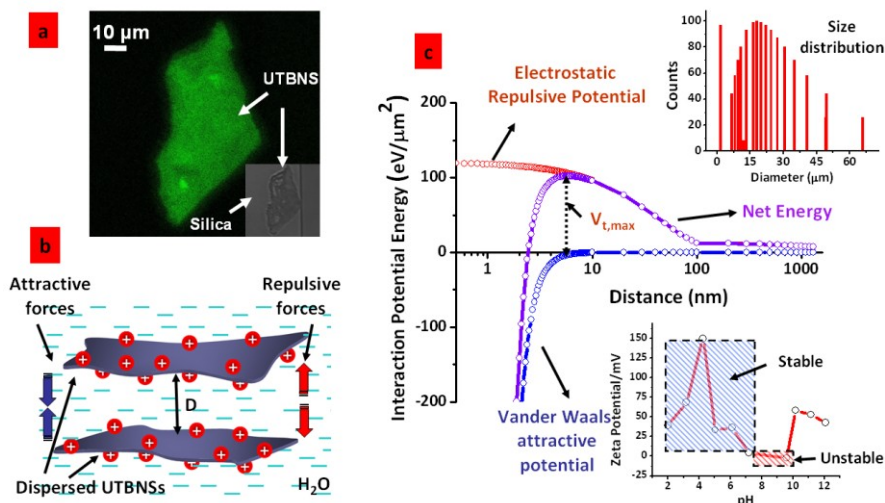


Figure 5.4 Presence of functionalized N centers on UTBNSs and stability of UTBNSs in aqueous phase. a, Confocal Image of a UTBNS covalently tagged with FITC molecules suggesting a uniform presence of functionalized N atoms on its surface. The bottom right inset shows the optical image of the corresponding UTBNS. b, UTBNSs, when dispersed in water exhibit positively charged surface due to the presence of protonated N atoms. This leads to their electrostatic stabilization enabling a colloidal formation. c, The net energy of water dispersed UTBNSs can be modeled using DLVO theory. The graph shows the net energy evaluated per unit surface area for an UTBNS exhibiting a zeta potential value $\zeta = +25$ mV. Top inset shows the size distribution of UTBNSs dispersed in water determined using laser light scattering. The average diameter of sheets is ~ 24.5 μm . Bottom inset shows the zeta-potential for UTBNSs dispersed in water as a function of the solution pH. The blue region ($\zeta > 2.4$ mV) denote pH regimes in which UTBNS dispersion is stable. The red region ($\zeta < 2.4$ mV) denote an instability in the colloidal dispersion [This analysis is for sheets with surface areas $> 1 \mu\text{m}^2$].

UTBNSs dispersed in aqueous phase are electrostatically stable due to their protonated lattice (**Figure 5.4b**), as confirmed by Zeta-potential (ζ , electrostatic potential at the sheet-water

interface) studies (**Figure 5.4c** bottom inset): ζ exhibits large positive values ($\zeta_{\text{max}} = +150$ mV) in the pH regime 2-9. The positive value of ζ confirms a positively charged surface. Further the pH dependence of ζ is consistent with the pH-dependent ionization of amine functional group. The UTBNS dispersion exhibits small negative ζ values for pH 9-10, which represents the isoelectric point regime for the UTBNSs. Beyond pH=10, ζ again assumes positive values, which is likely due to the adsorption of H^+ or Na^+ ions added to adjust the pH. The aqueous UTBNS-dispersion is modeled using the Derjaguin-Landau-Verwey-Overbeek (DLVO) theory. Here, the charged colloidal stabilization is analyzed by the interplay between electrostatic repulsive potential (V_R) and attractive van der Waal potential (V_A). We determined these potentials by considering a system of two adjacent UTBNSs interspaced with a separation D (**Figure 5.4b**, see Appendix D: section D.5):

The above values are used for estimating the net interaction energy of dispersed UTBNS ($V_{\text{net}} = V_R + V_A$) over a wide range of intersheet separations by using the sample $\zeta = 25$ mV (**Figure 5.4c**). The obtained V_{net} curve represents a stable system with distinct maximum (depicted as $V_{t,\text{max}}$), that represents the energy barrier obstructing coagulation of UTBNSs. A colloidal solution is considered to be reasonably stable if the height of $V_{t,\text{max}}$ is of the order of $\sim 25kT$ ($kT = 0.025$ eV, average kinetic energy of sheets at room temperature)^{33,34}. For a sheet with average area $1 \mu\text{m}^2$, $V_{t,\text{max}} = 102$ eV $\approx 4080kT$, and since most UTBNSs exhibit surface areas $\gg 1 \mu\text{m}^2$ (as shown in the size distribution, **Figure 4c top inset**), there exists a large potential barrier that will prevent lasting contact between two sheets in the aqueous UTBNS dispersion. Further, only sheets with a surface area $< 0.006 \mu\text{m}^2$ will tend to coagulate at room temperature. The net energy curve shows similar stable behavior for values of ζ different from 25 mV (see Appendix D: Figure D.7). Using the criteria for stability stated above, we calculated that a sheet with average area $1 \mu\text{m}^2$ is stable for all $\zeta > 2.4$ mV, below which $V_{t,\text{max}} < 25kT$. Thus the aqueous dispersions exhibit high-stability for most of the pH regime (shaded blue in **Figure 5.4c bottom inset**), except from pH 7.5-9.7 (shaded red, where $|\zeta| < 2.4$ mV).

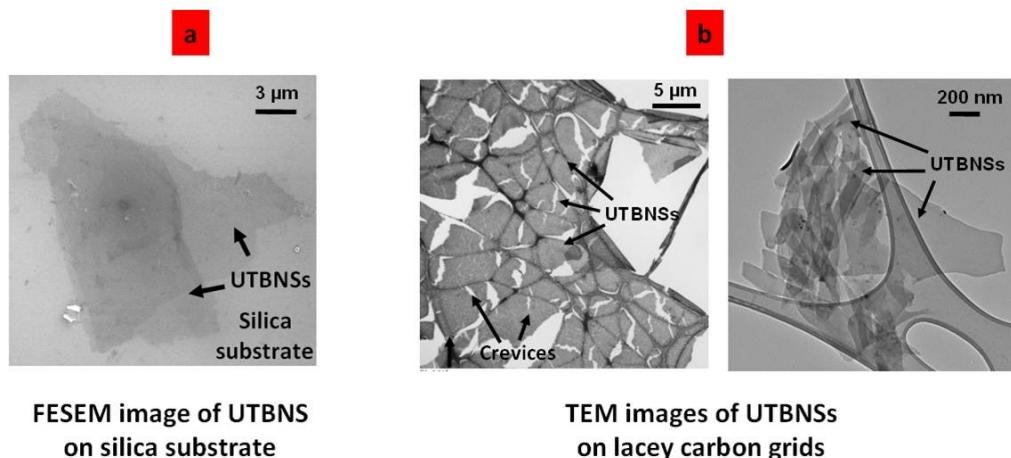


Figure 5.5 **Figure 5| Electron Microscopy Imaging of UTBNSs.** a, FESEM image of UTBNSs obtained from α -BN flakes and immobilized on 300 nm thick silica substrate. The absence of any wrinkled relief-features on the deposited sheet is attributed to electrostatically stretched UTBNS configuration within the aqueous dispersion. b, TEM image of large-sized and small-sized UTBNSs on lacey carbon grid. The larger sheets exhibit crevices on their surface which contribute to a high density of dangling bonds.

UTBNSs from aqueous suspension were immobilized on silica substrates or lacey carbon grids for visualization under optical microscope, field emission scanning electron microscope (FESEM) and transmission electron microscope (TEM) (see Experimental Section and Appendix D: sections D.7 through D.11). **Figure 5.5a** shows FESEM image of an UTBNS with lateral dimensions of $\sim 15\ \mu\text{m}$.

Several surface immobilized sheets do not exhibit visible wrinkles on their surface suggesting electrostatic stretching of the sheets in solutions. Some sheets do exhibit a scrolling of the edges. The maximum lateral dimension of UTBNSs was $\sim 100\ \mu\text{m}$. Some sheets also exhibit a perforated appearance (see Appendix D: Figure D.4), which is probably due to the chemical cleavage by strong CA during exfoliation. These localized edged structures bear pyridinic-like N atoms available for functionalization. The presence of these perforations is expected to increase the defect density and hence the reactivity of otherwise inert B-N pair³⁵.

Figure 5.5b shows the TEM images of UTBNSs immobilized on lacey carbon grids. The underlying lacey carbon grids are visible due to the electron-transparent nature of UTBNSs.

Figure 5.6a compares the Raman spectra of bulk α -BN crystal and UTBNS, obtained at room temperature using a 633 nm laser. The bulk α -BN crystal exhibits Raman peak at ~ 1366 cm^{-1} , which is the characteristic E_{2g} vibrational phonon mode of α -BN ³⁶⁻³⁸ (top left inset). The UTBNSs exhibit an extremely low intensity peak blue shifted to ~ 1384 cm^{-1} (the scale has been adjusted to clearly depict the peak). Since the E_{2g} peak intensity is directly proportional to the number of layers, a faint intensity suggests successful exfoliation from multi-layered crystal to

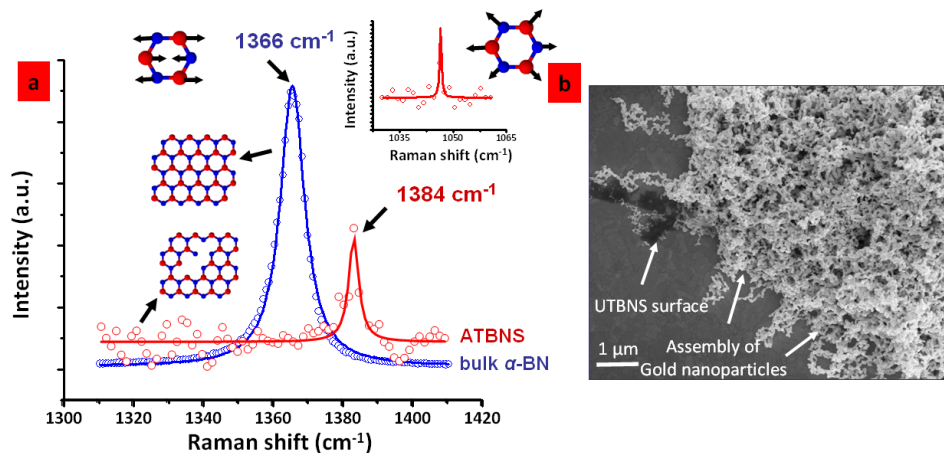


Figure 5.6 Raman spectroscopic study of UTBNSs and self-assembly of gold nanoparticles. a Raman spectrum of the UTBNS shown in panel a (red), compared with the Raman spectrum of α -BN flake (blue) from which it was exfoliated; exhibiting peaks at 1384 cm^{-1} and 1366 cm^{-1} respectively. The samples were excited by a 633 nm laser. These peaks correspond to the characteristic E_{2g} vibrational phonon mode of α -BN shown in top left inset. Top right inset shows the transverse phonon mode spectra ($\sim 1050 \text{ cm}^{-1}$) obtained from UTBNS representing the presence of sp^3 defect sites. The curves are fitted using Lorentzian distributions b, FESEM Image of an UTBNS templated with gold nanoparticles. Citrate capped gold nanoparticles (GNPs) can be templated on UTBNSs *via* a solution-phase electrostatic self-assembly process. The GNPs deposit uniformly on the sheet featuring a high surface coverage.

few layered sheet structure. The blue shift of $\sim 18\text{ cm}^{-1}$ is attributed to four different factors: **(a)** Reduced thickness: mono- and bi-layered UTBNSs exhibit $2\text{-}4\text{ cm}^{-1}$ up shifted E_{2g} peak,³⁹ **(b)** Intra-sheet compressive stress: the position of Raman modes depend on the stress-strain built up in the crystal structure⁴⁰, which can arise from the underlying substrate with nanoscale roughness, **(c)** Defects: isolated double bonds, such as those expected in the protonated lattice of UTBNSs, resonate at higher frequencies⁴¹⁻⁴³ (similar to the blue shift in graphene-oxide (GO) with respect to Graphene), and **(d)** Hole charges: This is analogous to the blue-shifts of the G peak in CNTs by 320 cm^{-1} for a unit hole charge on each C atom⁴⁴. The FWHM of the E_{2g} peak exhibits a low value of $\sim 2.05\text{ cm}^{-1}$. To the best of our knowledge, such a low peak-width has not been observed for BN and further studies are required to investigate the plausible causes. A decrease in the FWHM of analogous G peak in graphene has been shown to arise due to the presence of charged impurities/dopants^{45,46}.

We also leveraged the protonated sites on the UTBNSs for controlled nano-templating. Negatively charged citrate-capped gold-nanoparticles were electrostatically self-assembled on the positively-charged surface of ATBSNS. Here, the attachment takes place in aqueous media with UTBNSs mixed with the GNPs. The GNP-decorated-UTBNSs were immobilized on an amine-silanized silica substrate to obtain FESEM images (**Figure 5.6b**) (see also Appendix D: Figure D.13). The resultant GNP-attachment density is high (η_g =surface coverage index= 81%) (see Appendix D: Figure D.14). The presence of underlying BN is confirmed by EDS studies (Appendix D: Figure D.15).

5.5 Summary

In this study, we report on the CA based spontaneous exfoliation of layered α -BN at high yield to produce large, ultrathin BN sheets with optical band-gap of 5.74 eV . The exfoliated sheets are protonated with a high zeta-potential of $+150\text{ mV}$ at $\text{pH} = 4$, enabling stable aqueous dispersions without surfactants. The protonation sites are distributed on the internal and edge lattice points of the UTBNS. The UTBNSs were also shown to be excellent templates for designing hybrid nanoarchitectures. The ability to manipulate its lattice chemistry, plus their facile processability, will broaden the scope of UTBNS's applications^{18,47,47-52}. Some examples of

prospective UTBNS applications include lattice-matched-substrates for enhanced-graphene electronics, piezoelectric devices, drug-delivering agents, transistor-gate-barriers, polymeric composites with reinforced strength, luminescent nanomaterials, optoelectronic devices, protein-immobilized medical diagnostic devices, electrically insulating substrates, impermeable membranes, and graphene-interfaced devices.

5.6 References

1. Sugino, T.; Tai, T. Dielectric constant of boron nitride films synthesized by plasma-assisted chemical vapor deposition. *JAPANESE JOURNAL OF APPLIED PHYSICS PART 2 LETTERS* **2000**, 39 (11A), 1101-1104.
2. Kho, J. G.; Moon, K. T.; Kim, J. H.; Kim, D. P. Properties of boron nitride (B_xN_y) films produced by the spin-coating process of polyborazine. *Journal of the American Ceramic Society* **2000**, 83 (11), 2681-2683.
3. Li, C.; Bando, Y.; Zhi, C.; Huang, Y.; Golberg, D. Thickness-dependent bending modulus of hexagonal boron nitride nanosheets. *Nanotechnology* **2009**, 20, 385707.
4. Chen, Y.; Zou, J.; Campbell, S. J.; Le Caer, G. Boron nitride nanotubes: Pronounced resistance to oxidation. *Appl. Phys. Lett.* **2004**, 84, 2430.
5. Museur, L.; Kanaev, A. Near band-gap photoluminescence properties of hexagonal boron nitride. *Journal of Applied Physics* **2008**, 103 (10), 103520.
6. Museur, L.; Feldbach, E.; Kanaev, A. Defect-related photoluminescence of hexagonal boron nitride. *Phys. Rev. B* **2008**, 78 (15), 155204.
7. Watanabe, K.; Taniguchi, T.; Kanda, H. Direct-bandgap properties and evidence for ultraviolet lasing of hexagonal boron nitride single crystal. *Nature Materials* **2004**, 3 (6), 404-409.
8. Watanabe, K.; Taniguchi, T.; Niiyama, T.; Miya, K.; Taniguchi, M. Far ultraviolet plane-emission handheld device based on hexagonal boron nitride. *Nature Photonics* **2009**.
9. Novoselov, K. S.; Geim, A. K.; Morozov, S. V.; Jiang, D.; Katsnelson, M. I.; Grigorieva, I. V.; Dubonos, S. V.; Firsov, A. A. Two-dimensional gas of massless Dirac fermions in graphene. *Nature* **2005**, 438 (7065), 197-200.

10. Zhang, Y. B.; Tan, Y. W.; Stormer, H. L.; Kim, P. Experimental observation of the quantum Hall effect and Berry's phase in graphene. *Nature* **2005**, *438* (7065), 201-204.
11. Novoselov, K. S.; Geim, A. K.; Morozov, S. V.; Jiang, D.; Zhang, Y.; Dubonos, S. V.; Grigorieva, I. V.; Firsov, A. A. Electric field effect in atomically thin carbon films. *Science* **2004**, *306* (5296), 666-669.
12. Splendiani, A.; Sun, L.; Zhang, Y.; Li, T.; Kim, J.; Chim, C. Y.; Galli, G.; Wang, F. Emerging Photoluminescence in Monolayer MoS₂. *Nano Lett* **2010**, *10* (4), 1271-1275.
13. Park, S.; Ruoff, R. S. Chemical methods for the production of graphenes. *Nature Nanotechnology* **2009**, *4* (4), 217-224.
14. Reina, A.; Jia, X.; Ho, J.; Nezich, D.; Son, H.; Bulovic, V.; Dresselhaus, M. S.; Kong, J. Large area, few-layer graphene films on arbitrary substrates by chemical vapor deposition. *Nano Lett* **2009**, *9* (1), 30-35.
15. Coleman, J. N.; Lotya, M.; O'Gara, A.; Bergin, S. D.; King, P. J.; Khan, U.; Young, K.; Gaucher, A.; De, S.; Smith, R. J.; Shvets, I. V.; Arora, S. K.; Stanton, G.; Kim, H. Y.; Lee, K.; Kim, G. T.; Duesberg, G. S.; Hallam, T.; Boland, J. J.; Wang, J. J.; Donegan, J. F.; Grunlan, J. C.; Moriarty, G.; Shmeliov, A.; Nicholls, R. J.; Perkins, J. M.; Grieveson, E. M.; Theuwissen, K.; McComb, D. W.; Nellist, P. D.; Nicolosi, V. Two-Dimensional Nanosheets Produced by Liquid Exfoliation of Layered Materials. *Science* **2011**, *331* (6017), 568-571.
16. Blase, X.; De Vita, A.; Charlier, J. C.; Car, R. Frustration effects and microscopic growth mechanisms for BN nanotubes. *Phys. Rev. Lett.* **1998**, *80* (8), 1666-1669.
17. Golberg, D.; Bando, Y.; Huang, Y.; Terao, T.; Mitome, M.; Tang, C.; Zhi, C. Boron Nitride Nanotubes and Nanosheets. *Acs Nano*, 335-349.
18. Zhi, C.; Bando, Y.; Tang, C.; Kuwahara, H.; Golberg, D. Large-Scale Fabrication of Boron Nitride Nanosheets and Their Utilization in Polymeric Composites with Improved Thermal and Mechanical Properties. *Advanced Materials* **2009**, *21* (28), 2889-2893.
19. Warner, J. H.; Rummeli, M. H.; Bachmatiuk, A.; Buchner, B. Atomic Resolution Imaging and Topography of Boron Nitride Sheets Produced by Chemical Exfoliation. *Acs Nano* **2010**, *4* (3), 1299-1304.

20. Han, W. Q.; Wu, L.; Zhu, Y.; Watanabe, K.; Taniguchi, T. Structure of chemically derived mono-and few-atomic-layer boron nitride sheets. *Appl. Phys. Lett.* **2008**, *93*, 223103.
21. Lin, Y.; Williams, T. V.; Connell, J. W. Soluble, Exfoliated Hexagonal Boron Nitride Nanosheets. *The Journal of Physical Chemistry Letters* **2009**, *1* (1), 277-283.
22. Ramesh, S.; Ericson, L. M.; Davis, V. A.; Saini, R. K.; Kittrell, C.; Pasquali, M.; Billups, W. E.; Adams, W. W.; Hauge, R. H.; Smalley, R. E. Dissolution of pristine single walled carbon nanotubes in superacids by direct protonation. *J. Phys. Chem. B* **2004**, *108* (26), 8794-8798.
23. Parra-Vasquez, A. N. G.; Behabtu, N.; Green, M. J.; Pint, C. L.; Young, C. C.; Schmidt, J.; Kesselman, E.; Goyal, A.; Ajayan, P. M.; Cohen, Y. Spontaneous Dissolution of Ultralong Single-and Multiwalled Carbon Nanotubes. *Acs Nano*, 145-249.
24. Davis, V. A.; Parra-Vasquez, A. N. G.; Green, M. J.; Rai, P. K.; Behabtu, N.; Prieto, V.; Booker, R. D.; Schmidt, J.; Kesselman, E.; Zhou, W. True solutions of single-walled carbon nanotubes for assembly into macroscopic materials. *Nature Nanotechnology* **2009**, *4*, 830-834.
25. Behabtu, N.; Lomeda, J. R.; Green, M. J.; Higginbotham, A. L.; Sinitskii, A.; Kosynkin, D. V.; Tsentlovich, D.; Parra-Vasquez, A. N.; Schmidt, J.; Kesselman, E.; Cohen, Y.; Talmon, Y.; Tour, J. M.; Pasquali, M. Spontaneous high-concentration dispersions and liquid crystals of graphene. *Nature Nanotechnology* **2010**, *5* (6), 406-411.
26. Buchholz, D. B.; Liu, J.; Marks, T. J.; Zhang, M.; Chang, R. P. H. Control and Characterization of the Structural, Electrical, and Optical Properties of Amorphous ZincGêÆIndiumGêÆTin Oxide Thin Films. *ACS Applied Materials & Interfaces* **2009**, *1* (10), 2147-2153.
27. Blase, X.; Rubio, A.; Louie, S. G.; Cohen, M. L. Quasiparticle band structure of bulk hexagonal boron nitride and related systems. *Phys. Rev. B* **1995**, *51*(11), 6868.
28. Song, L.; Ci, L.; Lu, H.; Sorokin, P. B.; Jin, C.; Ni, J.; Kvashnin, A. G.; Kvashnin, D. G.; Lou, J.; Yakobson, B. I. Large Scale Growth and Characterization of Atomic Hexagonal Boron Nitride Layers. *Nano Letters*, 404-409.

29. Wang, Y.; Shao, Y.; Matson, D. W.; Li, J.; Lin, Y. Nitrogen-Doped Graphene and Its Application in Electrochemical Biosensing. *Acs Nano* **2010**, 4 (4), 1790-1798.
30. Stevens, J. S.; Byard, S. J.; Muryn, C. A.; Schroeder, S. L. M. Identification of Protonation State by XPS, Solid-State NMR, and DFT: Characterization of the Nature of a New Theophylline Complex by Experimental and Computational Methods. *The Journal of Physical Chemistry B* **2010**, 114 (44), 13961-13969.
31. Il'Inchik, E. A.; Volkov, V. V.; Mazalov, L. N. X-ray photoelectron spectroscopy of boron compounds. *Journal of Structural Chemistry* **2005**, 46 (3), 523-534.
32. Bardo, R. Reaction Mechanisms in Shocked, Intercalated Graphite and Boron Nitride. *J. Phys. IV France* **1995**, 05 (C4), C4-561.
33. Hiemenz, P. C.; Rajagopalan, R. *Principles of colloid and surface chemistry*; CRC: 1997.
34. Verwey, E. J. W.; Overbeek, J. T. G.; van Nes, K. *Theory of the stability of lyophobic colloids: the interaction of sol particles having an electric double layer*; Elsevier New York: 1948.
35. Lin, Y.; Williams, T. V.; Cao, W.; Elsayed-Ali, H. E.; Connell, J. W. Defect Functionalization of Hexagonal Boron Nitride Nanosheets. *The Journal of Physical Chemistry C* **2010**, 114 (41), 17434-17439.
36. Babich, I. L. Raman spectrum of hexagonal boron nitride. *Theoretical and Experimental Chemistry* **1974**, 8 (5), 594-595.
37. Geick, R.; Perry, C. H.; Rupprecht, G. Normal modes in hexagonal boron nitride. *Physical Review* **1966**, 146 (2), 543-547.
38. Arenal, R.; Ferrari, A. C.; Reich, S.; Wirtz, L.; Mevellec, J. Y.; Lefrant, S.; Rubio, A.; Loiseau, A. Raman spectroscopy of single-wall boron nitride nanotubes. *Nano Lett* **2006**, 6 (8), 1812-1816.
39. Gorbachev, R. V.; Riaz, I.; Nair, R. R.; Jalil, R.; Britnell, L.; Belle, B. D.; Hill, E. W.; Novoselov, K. S.; Watanabe, K.; Taniguchi, T.; Geim, A. K.; Blake, P. Hunting for Monolayer Boron Nitride: Optical and Raman Signatures. *Small* **2011**, 10.1002/sml.201001628.
40. Kuzuba, T.; Sato, Y.; Yamaoka, S.; Era, K. Raman-scattering study of high pressure effects on the anisotropy of force constants of hexagonal boron nitride. *Phys. Rev. B* **1978**, 18 (8), 4440.

41. Ferrari, A. C.; Robertson, J. Interpretation of Raman spectra of disordered and amorphous carbon. *Phys. Rev. B* **2000**, *61* (20), 14095.
42. Kudin, K. N.; Ozbas, B.; Schniepp, H. C.; Prud'homme, R. K.; Aksay, I. A.; Car, R. Raman spectra of graphite oxide and functionalized graphene sheets. *Nano Letters* **2008**, *8* (1), 36-41.
43. Ramesha, G. K.; Sampath, S. Electrochemical Reduction of Oriented Graphene Oxide Films: An in Situ Raman Spectroelectrochemical Study. *The Journal of Physical Chemistry C* **2009**, *113* (19), 7985-7989.
44. Sumanasekera, G. U.; Allen, J. L.; Fang, S. L.; Loper, A. L.; Rao, A. M.; Eklund, P. C. Electrochemical oxidation of single wall carbon nanotube bundles in sulfuric acid. *J. Phys. Chem. B* **1999**, *103* (21), 4292-4297.
45. Casiraghi, C.; Pisana, S.; Novoselov, K. S.; Geim, A. K.; Ferrari, A. C. Raman fingerprint of charged impurities in graphene. *Appl. Phys. Lett.* **2007**, *91* (23), 233108.
46. Das, A.; Pisana, S.; Chakraborty, B.; Piscanec, S.; Saha, S. K.; Waghmare, U. V.; Novoselov, K. S.; Krishnamurthy, H. R.; Geim, A. K.; Ferrari, A. C.; Sood, A. K. Monitoring dopants by Raman scattering in an electrochemically top-gated graphene transistor. *Nature Nanotechnology* **2008**, *3* (4), 210-215.
47. Dean, C. R.; Young, A. F.; Meric, I.; Lee, C.; Wang, L.; Sorgenfrei, S.; Watanabe, K.; Taniguchi, T.; Kim, P.; Shepard, K. L. Boron nitride substrates for high quality graphene electronics. *Arxiv preprint arXiv:1005.4917* **2010**.
48. Salehi-Khojin, A.; Jalili, N. Buckling of boron nitride nanotube reinforced piezoelectric polymeric composites subject to combined electro-thermo mechanical loadings. *Composites Science and Technology* **2008**, *68* (6), 1489-1501.
49. Ciofani, G.; Raffa, V.; Menciassi, A.; Cuschieri, A. Boron nitride nanotubes: an innovative tool for nanomedicine. *Nano Today* **2009**, *4* (1), 8-10.
50. Samanta, S. K.; Gomathi, A.; Bhattacharya, S.; Rao, C. N. R. Novel Nanocomposites Made of Boron Nitride Nanotubes and a Physical Gel. *Langmuir* **2010**.

51. Chen, X.; Wu, P.; Rousseas, M.; Okawa, D.; Gartner, Z.; Zettl, A.; Bertozzi, C. R. Boron nitride nanotubes are noncytotoxic and can be functionalized for interaction with proteins and cells. *Journal of the American Chemical Society* **2009**, *131* (3), 890-891.
52. Giovannetti, G.; Khomyakov, P. A.; Brocks, G.; Kelly, P. J.; van den Brink, J. Substrate-induced band gap in graphene on hexagonal boron nitride: Ab initio density functional calculations. *Phys. Rev. B* **2007**, *76* (7), 73103

6 Conclusion and Future Work

6.1 Summary of contributions

The research results presented in this thesis have contributed significantly towards advancing the current state of knowledge by providing unprecedented details on: the dynamics of nanoscale motion in polymer cross linked nanoparticle constructs; solution phase interfacing properties of chemically modified graphene sheets; and synthesis of ultrathin Boron Nitride sheets. These important advancements are briefly summarized in this section.

- **Ability to Incorporate nanoscale motion by applying macroscopic forces**

The polymer cross-linked assembly of GNPs examined in Chapter 2 displayed a nanoparticle matrix system which can undergo a controlled nanoscale motion under the effect of macroscopic forces. This is an important addition to the current capabilities of maneuvering the basic components at the nano dimension. Also the phenomenon of electron tunneling was applied to monitor this motion, which reasserts the immense capabilities that rest with nanoscale phenomena. Further, the spring-like nature of the GNP-polymer assembly opens up newer avenues to store energy at nano-scale. The ability to store compression energy in a molecular-device-architecture and to manipulate them by actuating junctions has the potential to power future molecular devices by stored molecular-energy and controlling the properties of nanocomponent based devices.

- **Solution phase interfacing capability of graphene**

When we initiated the study reported in Chapter 3 on building graphene-metal nanoparticle hybrids, graphene had exhibited a multitude of exceptional solid-state properties. There were, however, no reports on the ability of solution-dispersed graphene-chemical-derivatives (GCDs) to function as ‘swimming’ macromolecular ‘templates’ where their large surface’s active groups could be accessed for chemical/physical processes. Similarly, there were no reports on methods that can enable a facile interfacing of graphene with metal NPs. We established this science by

demonstrating that the oxy-functional moieties present on dispersed GO sheets can interface and nucleate in-situ synthesized GNPs.

- **Important insights into the structural, chemical and electronic properties of graphene-metal hybrids**

The attachment of metal nanostructures to graphene was theoretically being predicted to sensitively tailor graphene's electronic properties (band gap, carrier density, nature of charge carriers) and physico-chemical properties (chemical response). An accessibility to the graphene-metal nanoparticle hybrids enabled us to investigate and realize these effects and build correlations and theories which could relate the degree of functionalization with the nature of modifications introduced.

- **Applying the gold nanoparticle decorated graphene sheets for addressing pertinent challenges in liquid-phase catalysis**

The ability of chemically modified graphene sheets to nucleate metal nanoparticles was carried forward for achieving “uncapped”, highly-active, supported nanocatalysts dispersed in liquid phase. This was made possible by microwave-reduction and the stabilizing chemistry offered by graphene-oxide sheets as explained in Chapter 4. While the bare surface of these BSGNs enabled increased electro-catalytically active site-density, their implantation on GO can also be employed to control the electron-injection and tune its electrical properties. We also applied this modifiable approach to stabilize bare-surfaced silver-nanoparticles on GO sheets.

- **Synthesis of Ultrathin sheets of Boron Nitride**

Chapter 5 reported a novel chlorosulfonic acid (CA) based treatment route that resulted in protonation assisted layer-by-layer exfoliation of BN monolayers with highest reported yields till date. The as exfoliated sheets of BN monolayers exhibited extensively protonated nitrogen centers, which we utilized for chemically interfacing GNPs, demonstrating their ability to act as excellent nano-templates. These were the first time ever reported studies on chemical

functionalization of BN sheets and formation of their nano-constructs. This work has the potential to spur a worldwide research effort towards studying atomic thin sheets of BN.

In addition to these works, we have initiated two potential projects on graphene. The following sections present an overview of these projects.

6.2 Future work on detecting mechanical motion in a molecule using graphene-platform

In this section we present the preliminary studies on a potential graphene work that revisits the *quasi* quantum sensitivity of graphene and applies it to detect the mechanical motion taking place in azo-benzene molecules.

6.2.1 Introduction

Controlling and detecting the mechanics at molecular scale is of fundamental importance in realizing the next-generation molecular electromechanical systems. Nanoscale constructs with mechanically actuating molecules have been employed in the past for fabricating photomechanical switches, electromechanical switches and nano-mechanical assemblies. Several ‘molecular-electronic’ devices have utilized the phenomenon of reversible molecular-conformational change for fabricating electro-mechanical switches where the conformational change enables avenues for manipulating and controlling the electronic properties by introducing an additional degree of freedom at nano scale.

The single atom thick *quasi* planar sheets of graphene functions as an ultra sensitive electrical platform due to the high carrier density and the low-scattering, sp^2 bound-carbon lattice-structure. The single atom thickness with a high density of p-electrons on the surface makes graphene ultrasensitive to surface events which can either change the carrier density or produce scattering sites. A synergistic integration of the molecular mechanics with the sensitive electronics of graphene is a promising route for the development of molecular electromechanical systems.

We designed an azo-functionalized graphene device and investigated the effect of azo’s molecular-scale mechanics on the fundamental electrical properties of the base graphene by

characterizing of fermionic redistribution on graphene surface in response to sub-nano scale mechanical graphene-azo optoelectronic device. **Figure 6.1** shows the schematic of the Azo-derivatized GO device with the azo-group in their *trans* and *cis* states, and the corresponding electrical states in graphene. A *trans* to *cis* switching of the azo-group reduces the separation between two aromatic rings from 2.1 Å to 0.7 Å, which increases the proximity of the electron-rich benzene ring to the CMG surface. The isomerization-actuated mechanical-motion of the electron-rich benzene group of the azo molecule tethered to the graphene surface is expected to induce a change in the base conductivity due to the generation and reduction of charge carriers.

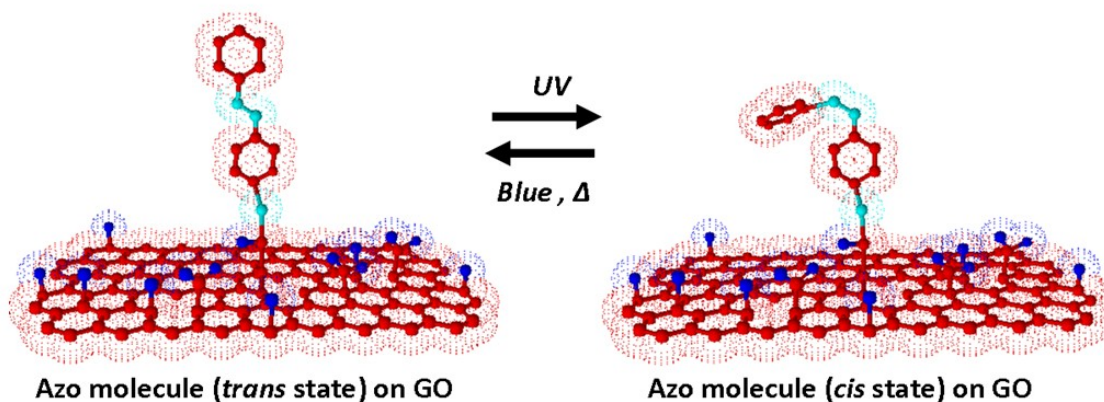


Figure 6.1 Schematic illustration of an amino azo-benzene molecule functionalized graphene sheet. The azo-benzene molecule can be reversibly switched between its *cis* and *trans* conformational states on irradiations with UV (365 nm) and blue (420 nm) lights. The conformational change is associated with a molecular motion of the electron rich benzene moiety bringing it closer to the Graphene base by a distance of $2.1 \text{ Å} - 0.7 \text{ Å} = 1.4 \text{ Å}$. The sensitive graphene base is utilized for electrically detecting this sub-nano scale molecular motion.

6.2.2 Experimental Section

The azo-functionalized graphene sheets were obtained by covalently binding the amine-derivatized azo-benzene molecules with the carboxylic functionalities present on Graphene-Oxide (GO) sheets that results in the formation of strong amide bonds. The GO sheets, obtained

by modified Hummer's method, are immobilized via electrostatic interactions on a heavily doped n-type silicon substrate with a 300 nm thick thermally grown silica layer with pre-fabricated gold electrodes. This GO coated chip is treated overnight with a 20 ml mixture of 5 % Amino azo-benzene hydrochloride containing 5 mg HATU (a coupling agent) and then thoroughly washed with methanol for 10 min. This results in a covalent grafting of azo-benzene molecules on GO sheets.

The azo-benzene molecules are reversibly switched between their *trans* to *cis* conformations by successive illuminations with UV-Blue light and the response of underlying graphene sheet is electrically measured as a change in its conductance across the gold electrodes. The electrical measurements are carried out under a steady nitrogen flow in a cryostat the temperature of which can be externally controlled.

6.2.3 Preliminary Results

Preliminary results demonstrate that an increased proximity of the electron cloud of the azo group's benzene ring in its *cis*-state increases the hole-concentration of the graphene-azo sheet that enhances the conductivity of GO sheet. A lower conductivity state is subsequently reached on switching off UV as the *cis*-azo molecules transiently revert back to their *trans* states. The fraction of *cis* molecules which revert to their *trans* state can also be regulated by temperature. More molecules retain the *cis* conformation enabling avenues to thermally regulate the memory of this opto electromechanical device. (Figure 6.2)

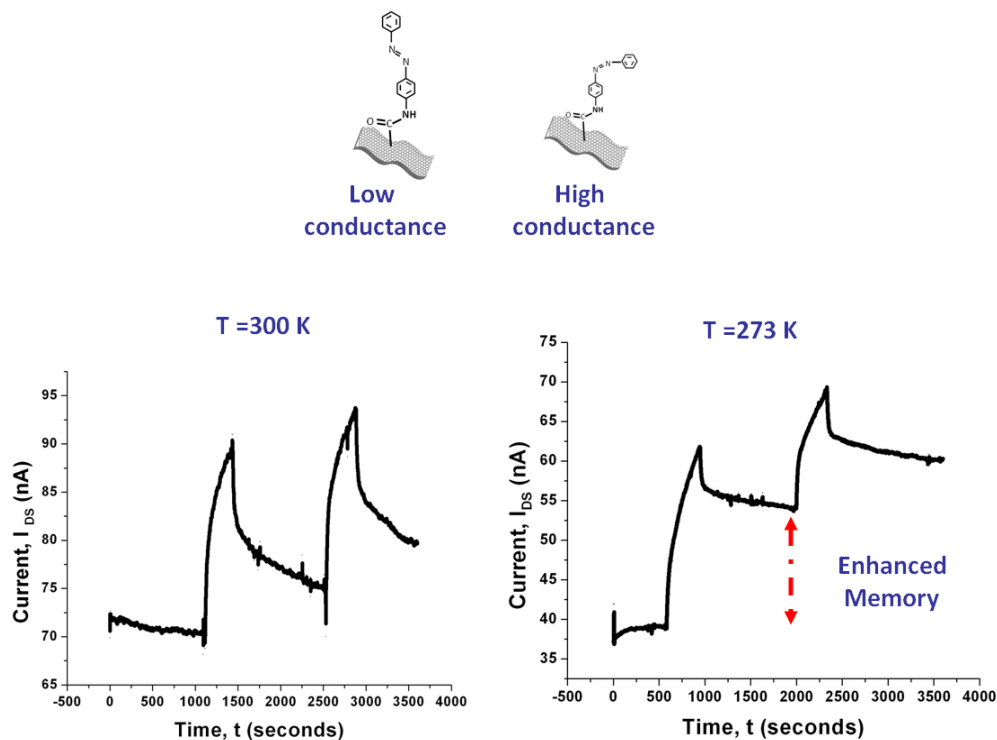


Figure 6.2 Controlled conductance switching in an azo-functionalized graphene device can be achieved by irradiations with UV and blue lights. A *trans* to *cis* isomerization of the azo molecule on UV application switches the azo-functionalized graphene to a higher conductive state that reverts close to its original state upon *cis* to *trans* isomerization. This electrical response of graphene is measured at temperatures of 273 K and 300 K. Temperature acts as an external factor to regulate the memory of this optoelectronic switch.

6.2.4 Intellectual Merit

This work combines the photo-induced molecular switching ability of azobenzene with the ultra sensitive electronic properties of graphene to fabricate a novel opto-electronic graphene device. The graphene interface is shown to efficiently detect the nanoscale motion on its surface associated with the conformational change of tethered molecules. This unique interface potentially enables an improved understanding of the photo switching kinetics and can lead to the realization of next generation optoelectronic and logic devices. Detailed ongoing

investigations are expected to yield more insights on the isomerization regulated conductance switching.

6.3 Future work on a novel scheme to non-invasively functionalize graphene

In this section we present our preliminary work on a novel functionalization scheme of graphene that promises to introduce interfaceable groups on pristine graphene without compromising the superior properties of graphene.

6.3.1 Introduction

The functionalization of graphene has been studied extensively by several research groups. However all of the proposed methods suffer from a severe limitation, post functionalization, the planar sp^2 carbons get converted to tetrahedral sp^3 carbons, which results in: (a) distortion in the planar structure of graphene that introduces scattering sites and reduced carrier mobility, and (b) loss of π electrons (associated with the sp^2 carbons) that drastically reduce the carrier density. There is an urgent need for a method that can enable functionalization of graphene and still retain its superior properties.

This project is aimed to methodically develop routes for synthesizing superior-quality graphene-metal conjugates by studying η^6 functionalization of epitaxial graphene with transition metal carbonyls. The term η^6 functionalization refers to a scheme of chemical modification which enables a co-ordinate binding of transition metal-carbonyls (Cr, Mn, Fe, Co, Ni) with polycyclic aromatic compounds such as graphene (**Figure 6.3**). This bond formation, which occurs *via* a transfer of electrons from arenes to the hybridized metal d-orbitals, is exceptionally unique, as the metal atoms effectively bind to the aromatic ring centers on graphene, rather than binding to the terminal carbon atoms.

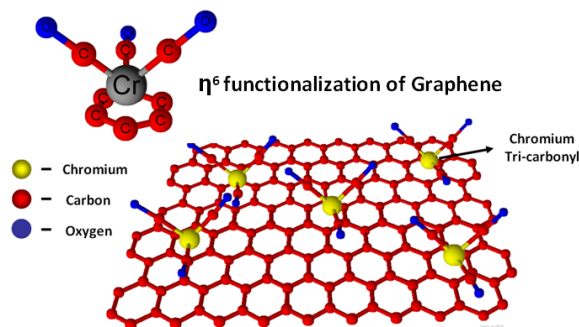


Figure 6.3 Chromium carbonyl functionalization of graphene *via* formation of metal-aromatic η^6 coordination bond.

The bonding orbitals (shaded red) contribute towards the σ interaction while the non bonding/ antibonding orbitals (shaded blue) can overlap with ligand orbitals of the correct symmetry to contribute towards π -interaction (**Figure 6.4**). Since arenes act as π -acceptor ligands, a transfer of electrons from metal to C non-bonding orbitals that increases the electron density at the C centers. This synergy between metal and arenes leads to a stronger binding than σ or π binding alone.

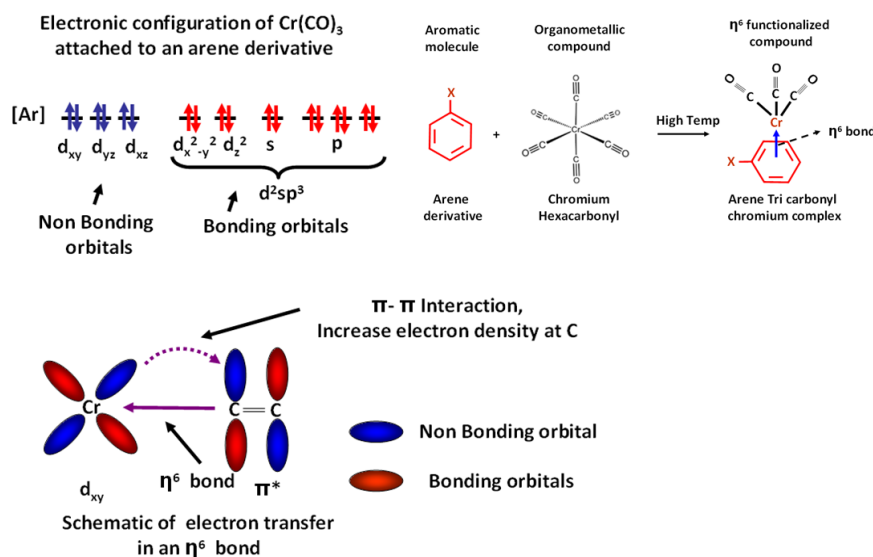


Figure 6.4 : Chromium carbonyl functionalization of an arene molecule *via* metal-aromatic η^6 coordination bond. Transfer of electrons in an bond formation and π - π Interactions among the non-bonding orbitals which increase the electron density at the arene center has an electron accepting tendency.

6.3.2 Experimental Section

We realized η^6 chemical modification of graphene on epitaxial graphene (EG) layers grown by a chemical vapor deposition process on Silica Carbide (SiC) wafers and Copper substrates (sized 5 mm X 5 mm). Briefly, the EG deposited substrate is exposed to a 20 ml solution of 45 mM Cr (CO)₆ in THF under moderate-temperature moderate pressure (50 °C) batch conditions for ~ 12 hrs in a that results in a grafting of chromium-tri carbonyl [Cr(CO)₃] groups on the 6-membered arene rings of EG yielding η^6 *graphene tri-carbonyl chromium complex*. This chemical functionalization is verified by X-ray Photoelectron and Raman spectroscopies.

6.3.3 Preliminary Results

The η^6 functionalization was confirmed by XPS spectra (Fi10), where (a) the Cr 2p spectra starts showing 2 new peaks at 587.7 eV and 578.4 eV; (b) the Cr 3p spectra starts showing a new peak at 45.4 eV; and (c) the C1s peak shifts from 285.9 eV to 286.4 eV). This confirms functionalization on graphene. Preliminary electrical studies suggest that post functionalization; the average conductance of graphene reduces by an order of magnitude while the carrier mobility increases by ~42.8%. Detailed investigation for these effects and determination of band-gap, nature of charge carriers are under way.

6.3.4 Intellectual merit

This novel scheme addresses a most pertinent challenge faced in functionalizing graphene. These functionalization techniques compromise the planar sp² hybridized state of C atoms converting these to tetrahedral sp³ C atoms. This disrupts the planar lattice structure of graphene introducing scattering sites which renders graphene devoid of its high carrier density and exceptional carrier mobility, the very properties which makes it special. The functionalization at the center of aromatic ring *via* η^6 bonding introduces chemical groups on graphene without converting the sp² hybridized state of C atoms and thus retaining planar structure. This ability of functionalizing graphene in a non-invasive manner will be immensely useful in developing and producing new nanotechnologies.

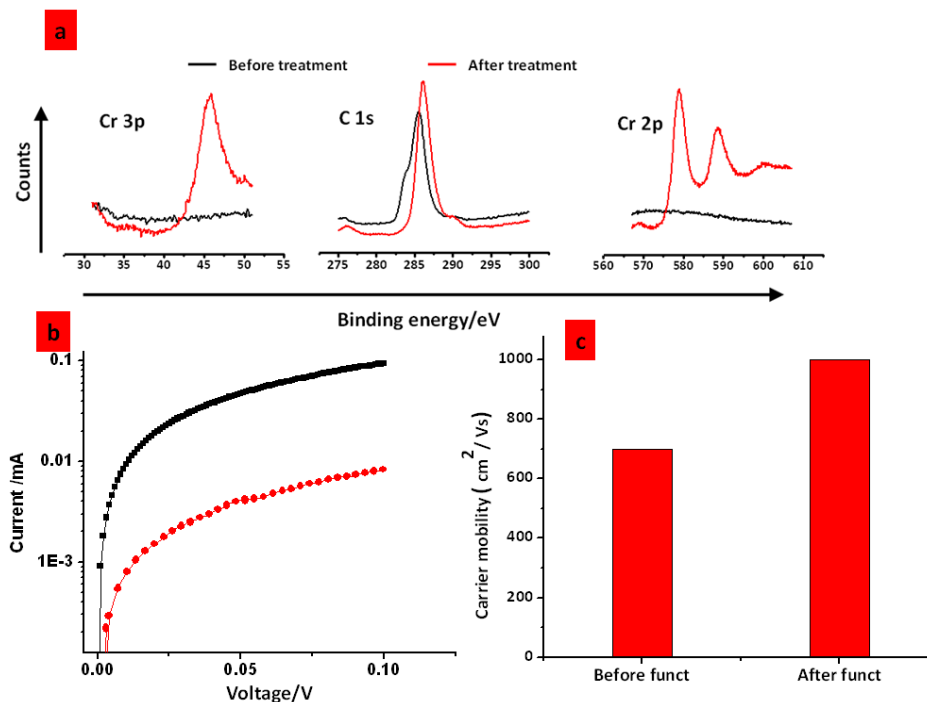


Figure 6.5 Preliminary Results (confirmation of bonding on graphene): (a) XPS analysis of pristine graphene sample before and after treatment with the chromium hexacarbonyl solution at a temperature of 80 °C and 2 atm. Functionalization of Cr(CO)₃ on graphene is evidenced by the appearance of 3 new peaks post treatment: 578.4 eV & 587.7 eV (Cr 2p spectra) and 45.4 eV (Cr 3p spectra). The formation of coordination bond between the metal atom and aromatic ring alters the electron density of the conjugated C atoms on graphene and is reflected in the C1s spectra in the form of a shift of 0.5 eV. (b) The average conductance of graphene decreases by an order of magnitude post functionalization, and (c) Average carrier mobility enhances by 42.8% post functionalization

Since η^6 functionalization of graphene constitute a new research area, the fundamental findings obtained from this systematic study will significantly support current research activities on graphene and greatly impact its future applications. The η^6 functionalization is self limiting in nature, as it only modifies a monolayer on graphene. The η^6 functionalization is self limiting in nature, as it only modifies a monolayer on graphene. Hence this functionalization

scheme will exhibit an improved control on surface modification, making it an excellent candidate **for realizing atomic-layer deposition** of gate-oxide on graphene. Further, since the η^6 bonds maintain and increase the aromaticity in benzene, these are expected to maintain or increase graphene's carrier density too.

6.4 Closing Remarks

In principle, the family of 2-D nanomaterials presents a gamut of perspectives that enable reexamination of older research problems and avenues of studying newer ones. The knowledge we have obtained in this work has significantly contributed to the evolving story on the science of 2-D nanosystems. The results presented here have inspired other researchers and they have improved and expanded upon the work we have developed. The scientific fields discussed here have been an extremely fruitful area of research and have expanded at a rapid pace. The 2-dimensional nanomaterial family discovered 6 years ago is no longer an unfamiliar territory today. While the science of graphene has developed the most; research on other members is still in embryonic stages and concerted research efforts are needed to uncover the large possibilities and continue to generate useful knowledge for realizing mainstream applications.

Appendix A Appendix for the work on reversibly compressible and stretchable spring-like polymeric junctions in between metal nanoparticles

A.1 Electrodes used in the study

Gold electrodes of 300 nm thickness were deposited on silica substrates (1 micron thick silica on 990 micron n-type silicon). The various electrode configurations used for measurement of conductivity change from electric field and centrifugation are shown in figure A.1. The most common parallel electrodes were 5 μm apart and ~ 7 mm long.

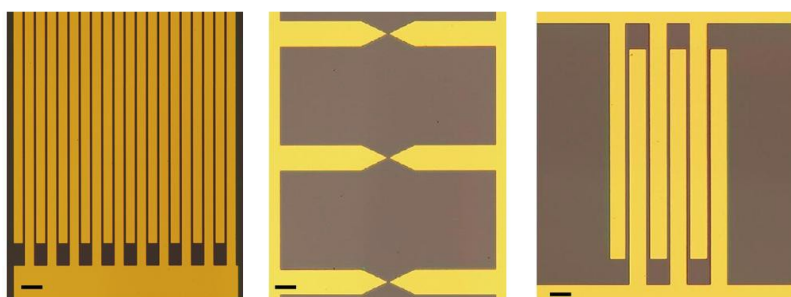


Figure A.1 Typical electrode configurations used in the conductivity measurements of nanoparticle-polyelectrolyte assembly (Scale bar = 50 μm)

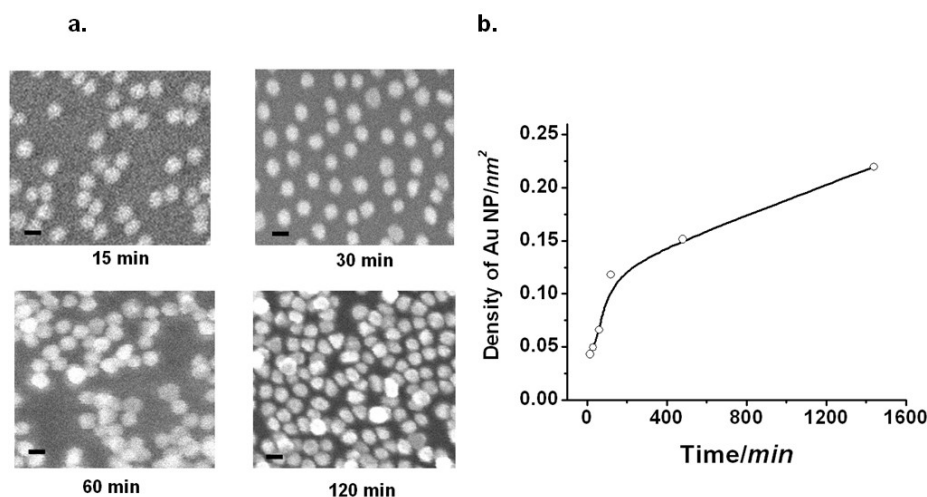


Figure A.2 Controlling the thickness of polymeric junctions. a, FESEM micrographs of 30 nm GNP deposited on ~ 50 nm thick cPAH film, shown for deposition times of 15 , 30 , 60, and 120 minutes. Conduction-percolation is achieved at 120 min. Scale bar = 25 nm. b, Plot showing the increase in the GNP density with increase in the GNP deposition-time.

A.2 Electron Transport Analysis

There are four modes of electron transportation through a nanoscale junction. These are (a) direct-tunneling, (b) Fowler-Nordheim tunneling, (c) thermionic emission and (d) hopping conduction. While electron tunneling modes ((a) and (b)) are independent of temperature, thermionic emission and electron hopping are temperature dependent. Since it has been shown earlier that the conductivity of nanoparticles in a similar device through polyteichoic acid changes with extremely low electron-transport activation energy of 1.71 meV, thermionic emission and electron hopping can be eliminated as transport mechanism. Further to differentiate between direct tunneling and Fowler-Nordheim tunneling, current voltage behavior of the sample can be analyzed. While the direct tunneling occurs for voltages smaller than the potential barrier (ϕ) or $eV < \phi$, Fowler-Nordheim tunneling occurs for voltages higher than the potential barrier ($eV > \phi$).

The probability of Fowler-Nordheim tunneling is proportional to:

$$J = V^2 \exp\left(-4 \frac{\sqrt{2m\phi}^{3/2}}{3eV\hbar} d\right), V > \phi/e \quad \text{Equation 6.1}$$

$$J = V \exp\left(-2 \frac{\sqrt{2m\phi}}{\hbar} d\right), V < \phi/e \quad \text{Equation 6.2}$$

Plotting the IV for the device (Figure A.3) and fitting the electron-tunneling equations shows that the Fowler-Nordheim equation does not fit the curve below 2.5 V, while the direct tunneling fits the curve on a larger scale. This suggests that the barrier height (ϕ) of the junctions is < 2.5 V (this process is similar to one used by Wang et al²). Further from Fowler-Nordheim equation fit for higher voltage range we find that the barrier height is 0.43 eV assuming an interparticle thickness of 2.7 nm³. Since the HOMO-LUMO gap of most of the polymers is between 6 to 9, the Fermi level of the metal junction therefore lies closer to either the HOMO or the LUMO level. Therefore, a more appropriate equation was found to be the Simmon's model^{4,5} which showed that for lower voltage range (0 to 1 V) the barrier height was 0.8335 eV for HP and 0.8156 eV for LP device. Since Simon model is best for voltages lower than the barrier height a voltage of 0.2 V was chosen for compression and stretch analysis by

$$\frac{J}{J_o} = \exp\left(-2 \frac{\sqrt{2m\phi}}{\hbar} \Delta d\right) \quad \text{Equation 6.3}$$

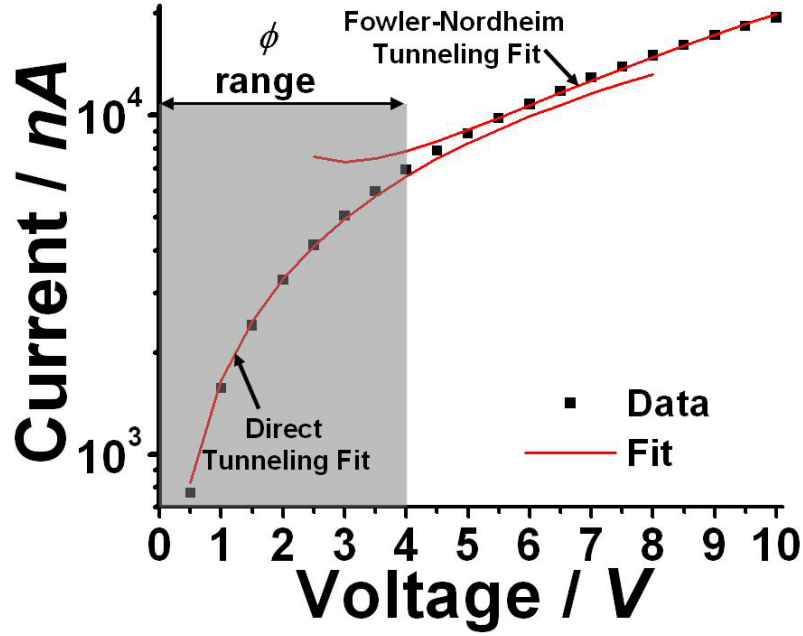


Figure A.3 The voltage current relationship of the sample with a series of polymeric junctions. Direct-tunneling and Fowler-Nordheim tunneling equation fits are shown. It can be seen that the Fowler-Nordheim tunneling equation fits the data only for $V > 4$ V. This implies that the electron-barrier ($\phi < 4$ eV).

A.3 Difference between the thickness of LP and HP devices

The conductivity data for the HP and LP device is shown in the figure A.4. It has already been established that the conduction for LP and HP devices follows Simmons model.

Simmons Model:

$$J = \left(\frac{e}{4\pi^2 \hbar d^2} \right) \left\{ \left(\phi - \frac{eV}{2} \right) \exp \left[-\frac{2(2m)^{0.5}}{\hbar} \left(\phi - \frac{eV}{2} \right)^{0.5} d \right] - \left(\phi + \frac{eV}{2} \right) \exp \left[-\frac{2(2m)^{0.5}}{\hbar} \left(\phi + \frac{eV}{2} \right)^{0.5} d \right] \right\}$$

Equation 6.4

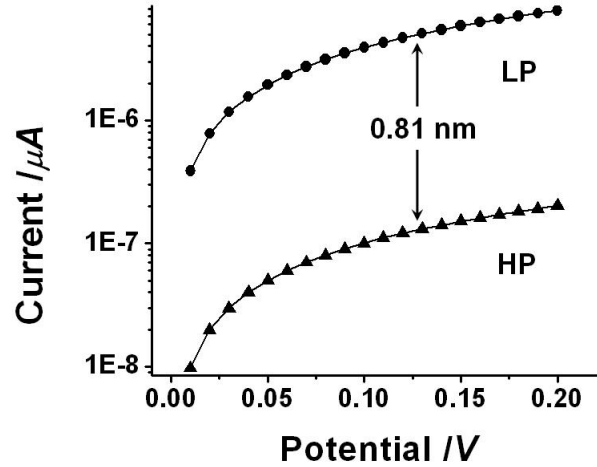


Figure A.4 Conductivities of HP and LP devices. The inter nanoparticle distance was controlled by varying the time of deposition of nanoparticles. Two kinds of devices are presented, namely HP and LP devices with deposition times of ~8 h and ~24 h to get higher and lower inter-GNP cPAH thickness, respectively, which in turn affects the native conductivity as shown. The difference in the inter particle distance for these devices can be calculated using the electron tunneling equation.

For high voltages:

$$J = \left(\frac{e}{4\pi^2 \hbar d^2} \right) \left\{ \left(\phi - \frac{eV}{2} \right) \exp \left[- \frac{2(2m)^{0.5}}{\hbar} \left(\phi - \frac{eV}{2} \right)^{0.5} d \right] \right\} \quad \text{Equation 6.5}$$

For low voltages:

$$J = \left(\frac{(2m\phi)^{0.5} e^2}{\hbar^2 d} \right) \left\{ V \exp \left[- \frac{2(2m)^{0.5}}{\hbar} (\phi)^{0.5} d \right] \right\} \quad \text{Equation 6.6}$$

This implies:

$$(J_1^2 / J_2) \propto \exp \left(- \frac{\sqrt{m\phi}}{\hbar} (4 - \sqrt{2})(d) \right) \quad \text{Equation 6.7}$$

where J_1 is the conductivity at low voltage and J_2 is the conductivity at high voltage. Using this formula and Figure A.4, we have:

$$\frac{(J_1^2 / J_2)_{HP}}{(J_1^2 / J_2)_{LP}} = \exp\left(-\frac{\sqrt{m\phi}}{\hbar}(4 - \sqrt{2})(d_{HP} - d_{LP})\right) \quad \text{Equation 6.8}$$

This gives the value of $(d_{HP} - d_{LP})$ of 0.81 nm.

A.4 Error in Calculating $d_{HP} - d_{LP}$ from different models:

Calculating the difference in thickness using either the Simmons model or the direct tunneling model at low biases when the mode of transport is not known gives the following difference in measurements:

Simmons Model:

$$\frac{1}{(4 - \sqrt{2})} \ln\left(\frac{(J_1^2 / J_2)}{(J_1^2 / J_2)_0}\right) = -\frac{\sqrt{m\phi}}{\hbar}(\Delta d_{Simmons}) \quad \text{Equation 6.9}$$

Direct Tunneling:

$$\frac{1}{(2\sqrt{2})} \ln\left(\frac{(J_1^2 / J_2)}{(J_1^2 / J_2)_0}\right) = -\frac{\sqrt{m\phi}}{\hbar}(\Delta d_{Direct_Tunneling}) \quad \text{Equation 6.10}$$

Therefore:

$$\frac{(\Delta d_{Direct_Tunneling} - \Delta d_{Simmons})}{\Delta d_{Simmons}} = \frac{\frac{1}{(2\sqrt{2})} - \frac{1}{(4 - \sqrt{2})}}{\frac{1}{(4 - \sqrt{2})}} = -8.58\% \quad \text{Equation 6.11}$$

However, since our calculations show that most of the junctions follow Simmons model (with triangular barrier) rather than direct tunneling, in our case this error is much lower than 8.58 % (~ 0.858 %).

A.5 Rate of compression

Upon application of an electric field, the polymeric junctions in LP and HP devices undergo compression resulting in an increase in the device conductivity. Moreover, the rate of compression was found to decrease with time indicating the presence of an opposing force from

the polymeric junction (Figure A.5). Characteristic to the spring motion, this opposing force gradually increases with time and at steady state, exactly counter balances the electric field induced force

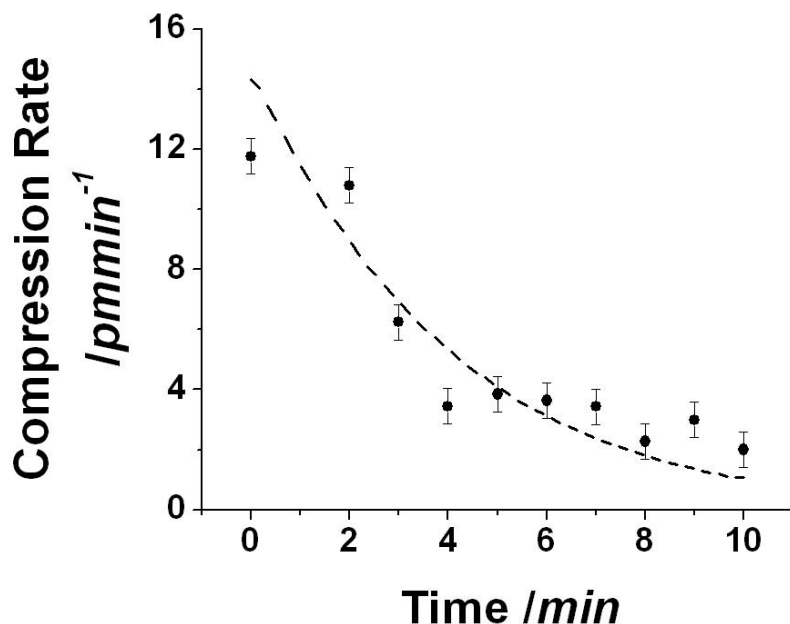


Figure A.5 Rate of polymeric-junction-compression. The rate of electric-field induced molecular compression in an HP device is found to decrease with the time of application. This indicates presence of an opposing force that increases with time, a characteristic of spring action.

A.6 Device characteristics:

The current versus voltage characteristics (Figure A.6) shows that there is no hysteresis or diodic behavior, hence eliminating any possibility of charge trapping.

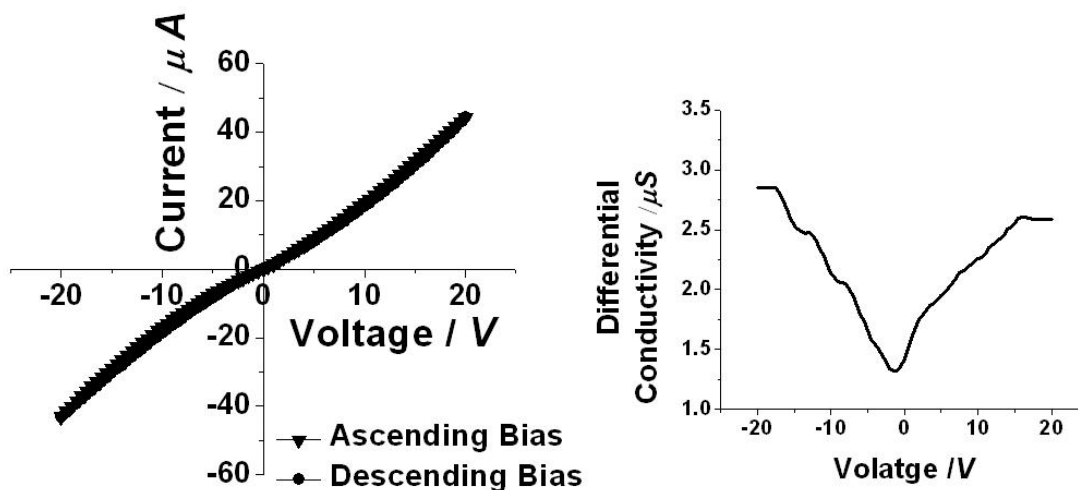


Figure A.6 IV Behavior at higher electric fields. The current-voltage response of an LP device is shown where the voltage is varied from -20 to + 20 V. There is no hysteresis or diodic behavior in IV indicating an absence of charge trapping or capacitive effects. The figure on the right shows the differential conductivity.

A.7 Relaxation of the polymeric junctions

On removal of the electric field, the compressed polymeric junctions relax back to their native uncompressed states by applying a recoil force, the magnitude of which depends on the initial thickness of the polymeric junction (which determines the equivalent spring constant) and the magnitude of induced compression. Figure A.7 shows the time dependent relaxation for an LP and an HP device.

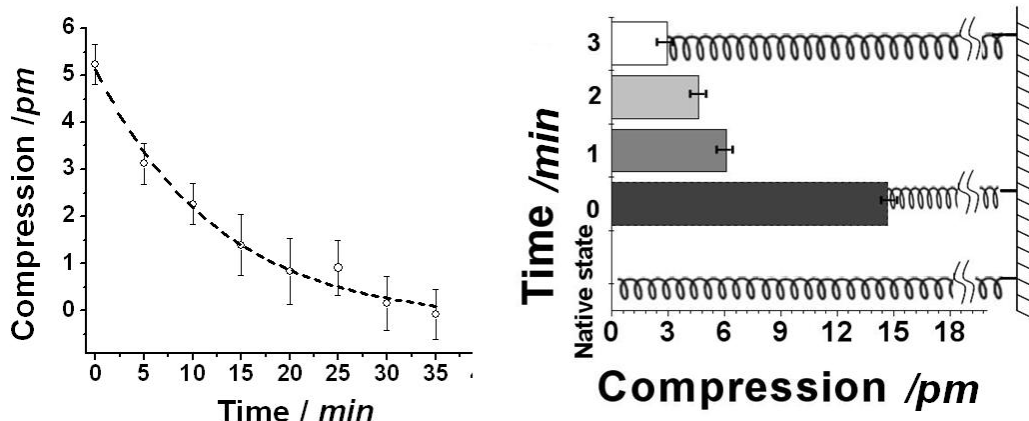


Figure A.7 Relaxation depends on the initial thickness of polymeric junctions in the device. The rate of relaxation was found to depend on the initial thickness of the polymeric junction and the compression induced by electric field.. An LP device compressed by ~5.2 pm relaxes back to its original state in ~35 min while an HP device compressed by ~15 pm quickly relaxes back to its original state within ~3 min. The relaxation dynamics (shown as data points) can be fitted with the relaxation equation explained in the following section

A.8 Compression/Stretching and Relaxation Dynamics

This many-nanoparticle system is complex due to **(a)** the integration of nanoparticles with one another leading to pushing/pulling of the whole film during stretching and compression, and **(b)** a number of electrostatic bonding present with viscous and elastic forces. A simple spring-in-a-viscous-media force-balance equation for the dynamics of compression, stretching and relaxation including inertial forces, external force fields from either electric-field or centrifugation, viscous forces and spring forces is:

a. External Forces:

Electric Field induced force

$$\frac{\delta^2}{\delta t^2} \Delta d \propto F_{\text{external}} - A \frac{\delta}{\delta t} \Delta d - k \Delta d \quad \text{Equation 6.12}$$

Centrifugal field induced force

$$\frac{\delta^2}{\delta t^2} \Delta d \propto A_0 F_C - A \frac{\delta}{\delta t} \Delta d - k \Delta d \quad \text{Equation 6.13}$$

b. Decompression or Relaxation

$$\frac{\delta^2}{\delta t^2} \Delta d \propto -A \frac{\delta}{\delta t} \Delta d - k \Delta d \quad \text{Equation 6.14}$$

where Δd is the instantaneous compression or stretching of the polymeric junction, F_E and F_c are the electric-field induced and centrifugal forces, A_0 is a constant, A is the coefficient of viscous force from the cPAH and k is the average spring constant. The value of the average spring constant for lateral application of force on a polyelectrolyte film⁶ is $2.76 \times 10^{-3} \text{ Nm}^{-1}$.

A.9 Importance of the c-PAH thickness in device response

The thickness of the cPAH layer which anchors the GNPs to the substrate, affects the restraining forces on the GNPs and thus determines the GNPs' mobility. As expected, the nanomechanical response of the system was found to be critically dependent on the thickness of the cPAH layer as shown in Figure A.8. In the devices presented in this report, a thin polyelectrolyte film under the nanoparticles acts as a cushion for the nanoparticles to move relatively freely with lesser restrain. This unrestrained motion also compensates for the collective compression of the junctions. For example, a compression of 0.10 nm of each junction will lead to a total compression of less than 7.5 nm per side across the electrodes. Since the polyelectrolyte cushion is at least 30 nm (50 nm (film) – 15 nm (or 20 nm) (nanoparticle)), this compensation can be easily achieved.

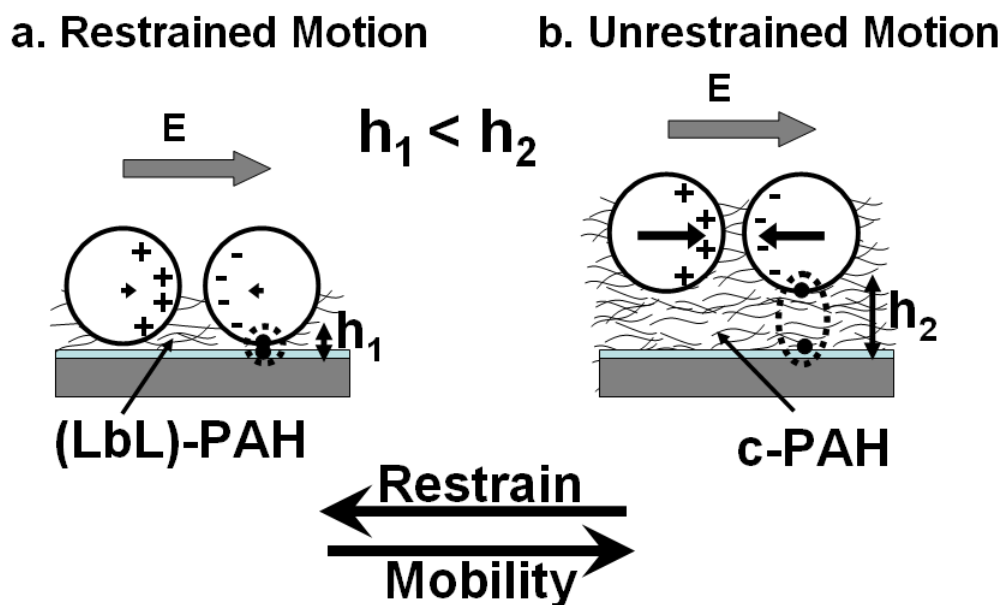


Figure A.8 Response of devices with different thickness of c-PAH: The nanomechanical response of the cPAH-junctions between GNPs is determined by the thickness of the cPAH layer. a. In a layer-by-layer assembled device, the GNPs are bound too close to the surface leading to a restrain on their mobility. b. A polyelectrolyte layer thickness of ~ 50 nm was found to be appropriate to reduce the restraining forces on GNPs, allowing them to exhibit relatively higher mobility and reversible compression.

A.10 Irreversible relocation of GNPs in a thick polyelectrolyte device

Devices fabricated with a thicker polyelectrolyte layer (>100 nm) exhibit an irreversible compression of the GNPs, which is attributed to permanent relocation of GNPs into the extra polyelectrolyte-network. In this case, the GNPs are expected to have mobility but after compression they do not relax back to their original state as shown in Figure A.9.

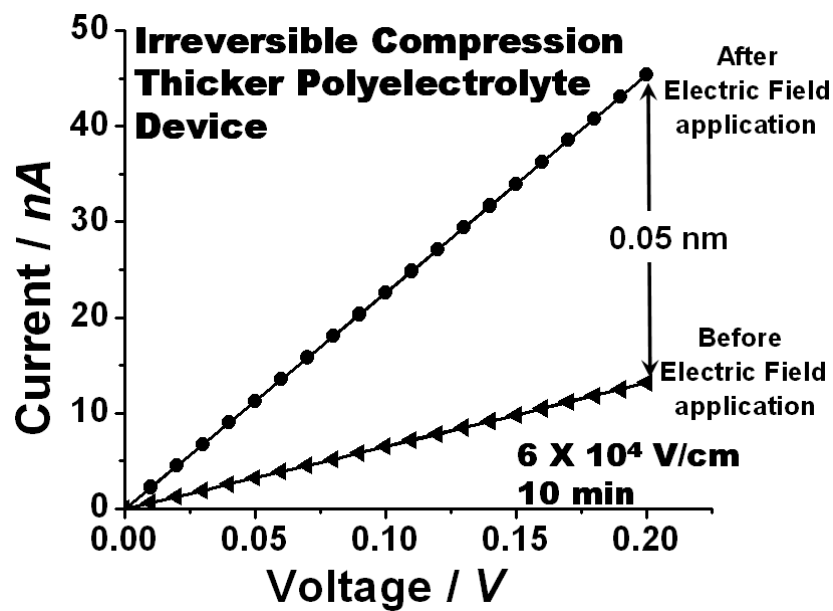


Figure A.9 A device fabricated with a thicker polyelectrolyte layer (>100 nm) exhibits an average irreversible-polymeric-junction-compression of ~0.05 nm. Electric field applied = 6×10^4 Vcm⁻¹ for 10 min.

A.11 Centrifugal Stretching of HP device

An HP device was studied under a centrifugal field of 90 g and the stretching was measured three times after 30 seconds centrifugation each.

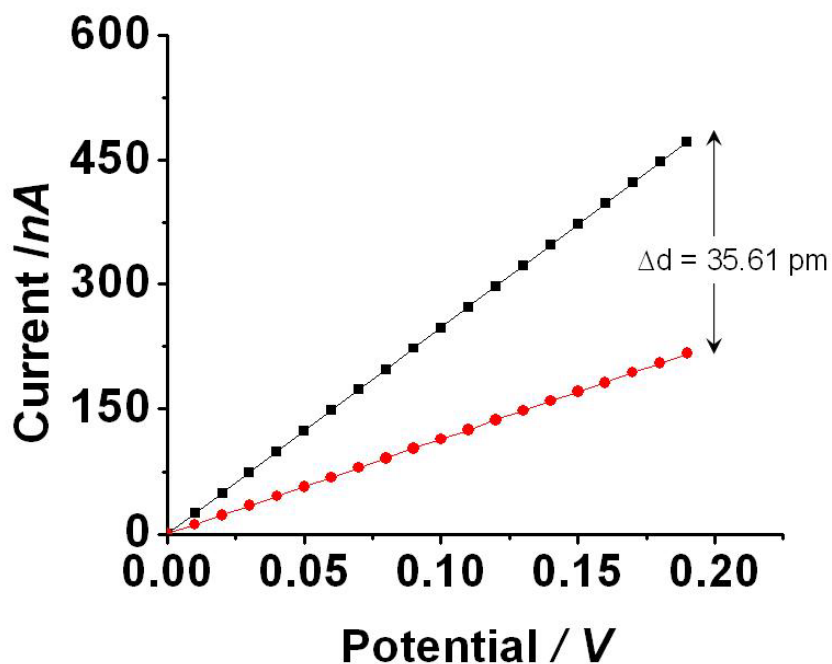


Figure A.10 The change in conductivity upon application of 90 g centrifugal field on an HP device gives a change in average junction thickness of 35.61 pm.

A.12 Gold nanoparticles used for device fabrication

The polymeric junctions were fabricated by incorporating c-PAH molecules within arrays of gold nanoparticles. The gold nanoparticles used in this fabrication were purchased from British Biocell International(EM GC 30, $\sim 2 \times 10^{11}$ particles/ml). The average nanoparticles size is ~ 30 nm as characterized by the UV-VIS Spectroscopy measurement (Figure A.11) which shows a peak at ~ 520 nm.

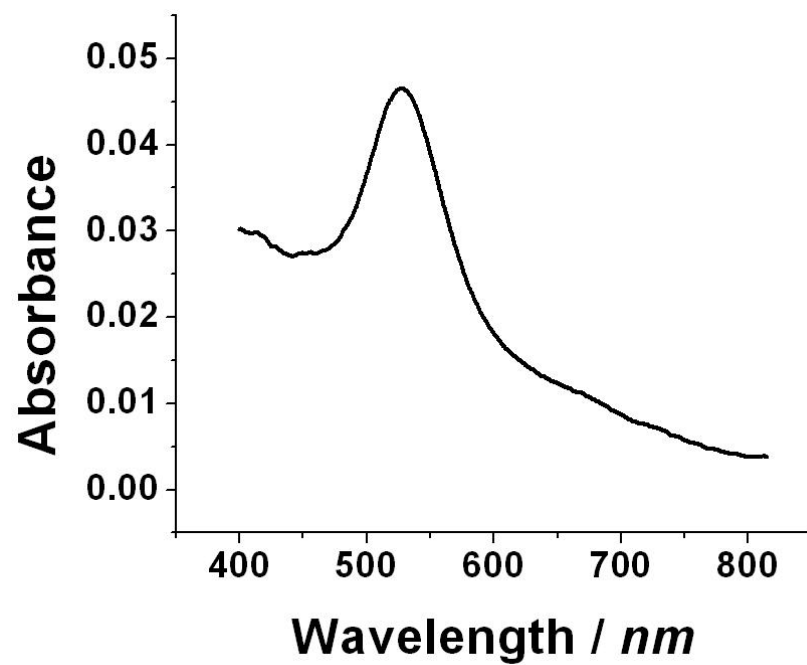


Figure A.11 UV-VIS Spectra for 30 nm Gold nanoparticles.

Appendix B. Appendix for the work on implantation and growth of dendritic gold nanostructures on graphene derivatives

B.1 Materials

Amino propyltriethoxy silane was purchased from Gelest. Gold chloride trihydrate ($\text{HAuCl}_4 \cdot 3\text{H}_2\text{O}$), graphite flakes, nitric acid, sulfuric acid, potassium permanganate and hydrogen peroxide were purchased from Fisher Scientific. Hydroxyl amine (50 % solution in water) was purchased from Sigma Aldrich. The aqueous solutions were prepared in Deionized (DI) water obtained by a Millipore Milli-Q membrane filtration system.

B.2 Preparation of Graphene oxide

5 grams of Mesh 7 - graphite flakes were mixed with 33 ml of 68% nitric acid + 200 ml of 96% sulfuric acid and stirred continuously for 40 minutes in an ice bath. 30 grams of potassium permanganate was then added into the solution, while the temperature was slowly increased to 40°C, and kept at 40°C for 30 minutes. Subsequently, the excess potassium permanganate was removed by treatment with 10% hydrogen peroxide. Finally, the GO sheets were obtained by centrifuging this solution at 15,000 rpm for 30 minutes followed by repeated washing with DI water. The sample was then dialyzed (MWCO 2000D) for 24 hours and the subsequently stored as a suspension in DI water at room temperature.

B.3 Immobilizing the GO-SFGN hybrids

The GO sheets functionalized with SFGNs were immobilized via electrostatic interactions on a heavily doped n-type silicon substrate with a 300 nm thick thermally grown silica layer. Briefly the silicon substrate, cleaned with organic solvents (acetone, isopropanol and ethanol) is first exposed to oxygen plasma (100 W, 2 mbar, 2 min) followed by treatment with 3-Amino Propyl triethoxy silane (1% in ethanol, 10 min), The substrate is then baked at 120°C for

4 min that makes the silica surface positively charged due to the presence of amine groups on its surface. This amine-functionalized substrate is then momentarily exposed to the synthetic mixture of GO-SFGNs (an aqueous dispersion of GO, hydroxyl amine and gold salt). The substrate is then subsequently washed 3 times with Deionized (DI) water that facilitates selective electrostatic deposition of GO-SFGN hybrids on silica surface. Figure B.1 shows FESEM image of such an immobilized GO-SFGN hybrid. The FESEM data was obtained with a Leo Field Emission Scanning Electron microscope operated at 10-15 KV.

B.4 Presence of characteristic wrinkles associated with GO-SFGN hybrids

SFGN formation takes place on both sides of a GO sheet in solution which is evidenced by a difference in the observed intensity of SFGNs in FESEM images as shown in Figure B.2. The SFGNs which are darker are present on the rear face of the immobilized GO sheet, which shields the SFGNs during imaging, while the SFGNs which are brighter are present on the front face of GO sheet. The presence of SFGNs on rear surface of GO results in the formation of wrinkles as it immobilizes on a silica substrate. The wrinkles are formed as the rear SFGNs raise and stretch the GO sheets above the silica surface creating a deformation. This is consistent with the fact that wrinkles are only associated with darker SFGNs as shown in Figure B.2

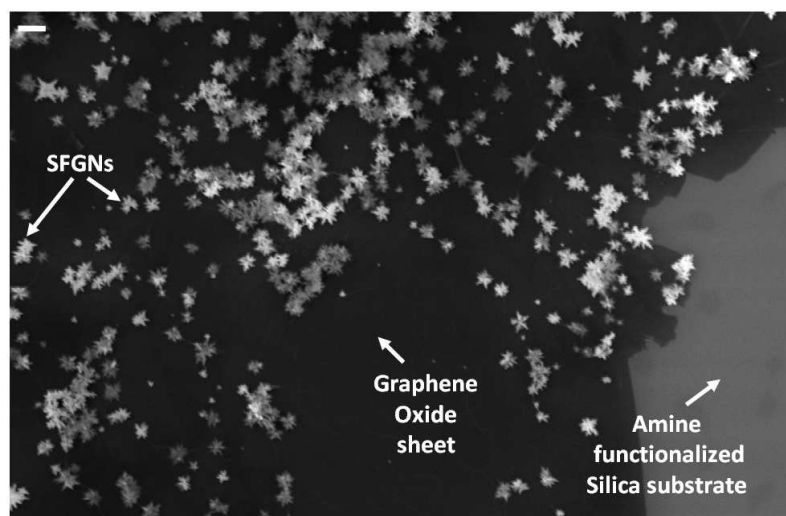


Figure B.1 Snow-flake shaped nanostructures of gold (SFGNs) templated on the sheets of Graphene-oxide (GO) immobilized on an amine functionalized substrate. Scale bar = 500 nm

B.5 Structural Parameters of the SFGNs

As shown in Fig 3.1b (central panel), the SFGNs were analyzed for their characteristic structural parameters namely number of primary branches (N_p), their average length (L_p), their average width (W_p) and the range displayed for the angle of emergence (Θ_e). The TEM Images were obtained with a Philips CM 100 transmission electron microscope operated at 100 kV. The GO-SFGN hybrids were deposited from solution on to 300 mesh size copper TEM specimen grids (Electron Microscopy Sciences) having a carbon support film. Table B1 list these parameters for SFGNs with 4, 5, 6 and 7 primary branches. The average

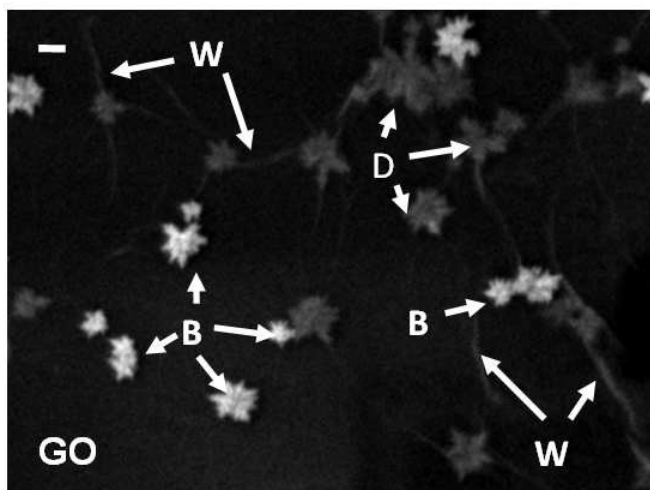


Figure B.2 The formation of SFGNs takes place on both sides of a GO sheet in solution as is evident from a difference in the observed intensity of SFGNs. The SFGNs which are darker (labeled as D) are present on the rear surface of GO sheet facing the silica substrate while the brighter SFGNs (labeled as B) are present on the upward facing surface of the immobilized GO sheet. The darker SFGNs are found to be associated with characteristic wrinkles (labeled as W) on the surface of GO sheet. Scale bar = 500 nm length of primary branches lies in the range of 419 nm-550 nm while the average width lies in the range of 211 nm-267 nm.

B.6 Topographic analysis SFGNs

Figure B.3 shows the AFM cross sectional analysis for neighboring SFGNs on the GO sheet. The height of the SFGNs was found to lie in the range of ~45 nm-55 nm while their width is ~ 500 nm. The AFM image also shows the presence of wrinkles on the GO surface which are associated with the SFGNs.

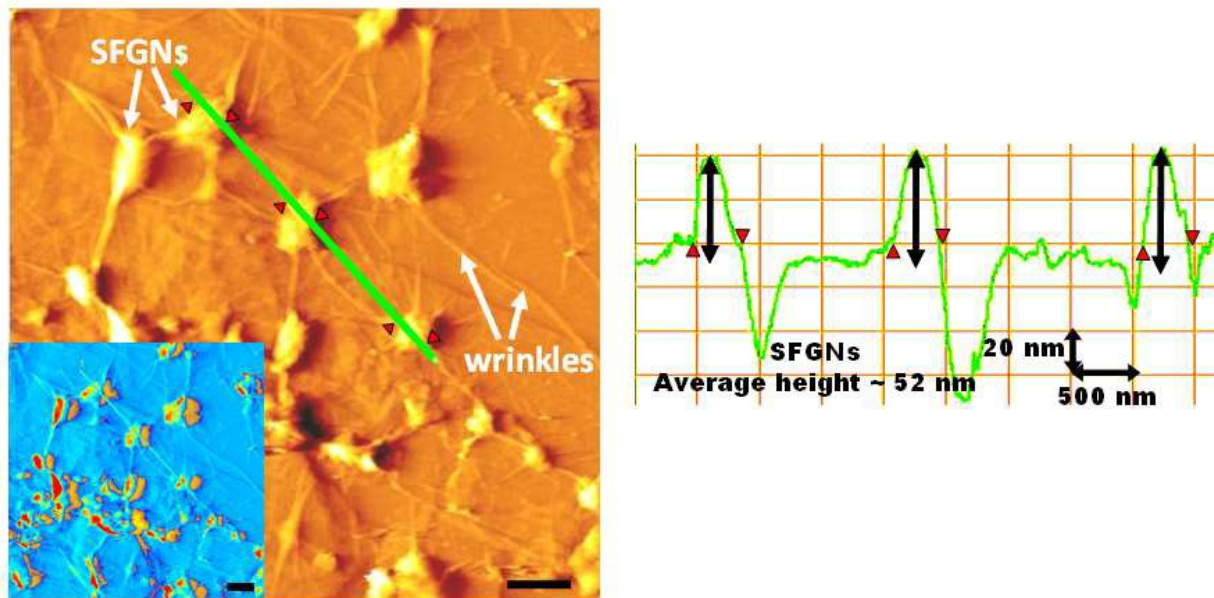
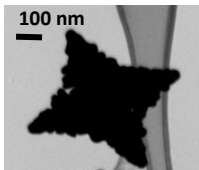
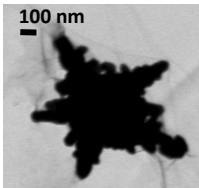
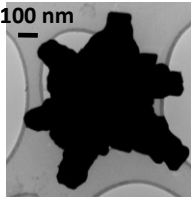
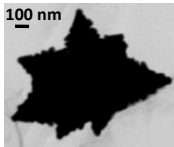


Figure B.3 Atomic Force Microscopy Scan for SFGNs templated on GO and their cross sectional analysis. The height of the SFGNs on this GO sheet was found to lie in the range of ~45 nm- 55 nm as shown in the adjacent line scan. The wrinkles associated with the SFGNs are clearly seen on the GO surface. Scale bar = 500 nm Bottom inset shows a lesser magnified version of the main image with a modified contrast to improve the appearance of original image. Scale bars = 500 nm

Table 1 Structural Parameters (number of primary branches, their average length, average width and the angle of emergence range) shown for different SFGNs

	TEM Image of the SFGNs	Number of Primary branches (N_p)	Average length of Primary branch (L_p)	Average width of the Primary Branch (W_p)	Range displayed for Emergence angle (Θ_e)
1.		4	475.3 nm	266.9 nm	$\sim 63^\circ - 87^\circ$
2.		5	419.8 nm	211.9 nm	$\sim 54^\circ - 90^\circ$
3.		6	511.2 nm	239.2 nm	$\sim 72^\circ - 84^\circ$
4.		7	550.9 nm	235.1 nm	$\sim 40^\circ - 89^\circ$

B.7 Seed mediated formation via sodium borohydride reduction of gold salt

In the synthesis of gold nanostructures on GO sheets, hydroxyl amine first reduces the gold salt to form seeds and then enable a seeding growth which results in the formation of SFGNs. In order to enable formation of seeds which do not undergo seeding growth, hydroxyl-amine was replaced by sodium borohydride in presence of sodium citrate. 0.6 ml of a freshly prepared ice-cold solution of 0.1 M NaBH₄ was added to a 20 ml solution of 0.275 mM HAuCl₄ and 0.250 mM sodium citrate, followed by addition of 100µl of graphene oxide (GO) suspension (80 mM carboxylic acid, quantified by titration). This results in the formation of small seeds on GO sheets as shown in Figure B.4. These seeds exhibit spherical morphologies with a size range of 5-10 nm.

B.8 Calculation example of determining mass flux rate of gold

The average mass flux rate (ϕ_{avg}) of gold for the formation of SFGNs on a GO sheet can be estimated as

$$\phi_{avg} = \frac{A_s \times t_o \times \rho}{A_p \times T} \quad \text{Equation B.1}$$

where A_s is the horizontal surface area of SFGN, t_o is its thickness, ρ is the density of gold (19.3 g/cm³), A_p is the lateral/perimetric surface area and T is the average time required for the formation of SFGN. For $N_p = 5$, these parameters are calculated for a symmetric structure in terms of average length of primary branch (L_p) and average width of primary branch (W_p) :

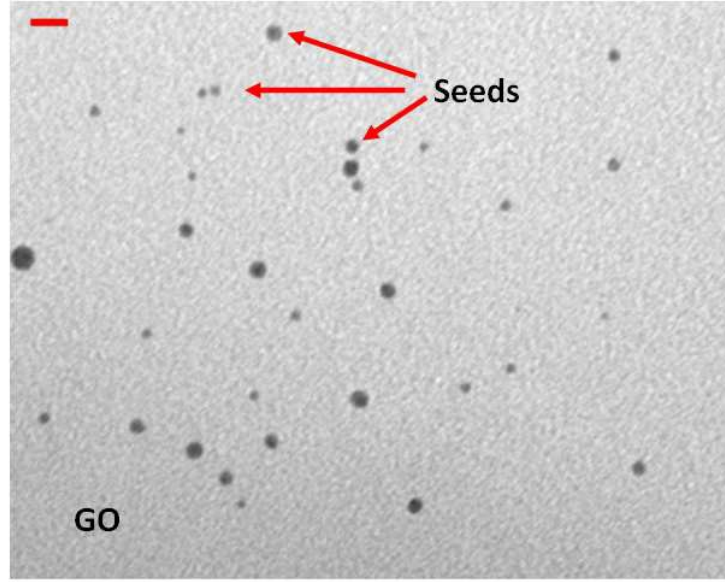


Figure B.4 TEM Image for gold seeds on GO synthesized by sodium borohydride reduction of gold salt in presence of sodium citrate and GO. Scale bar = 10 nm

$$A_s \approx 5 \times 0.5 \times W_p \times (L_p - 0.5 \times W_p \times \tan 36^\circ) + 5 \times 0.5 \times W_p \times \tan 36^\circ \times 0.5 \times W_p$$

Equation B.2

$$A_p \approx 5 \times 2 \times \left[(L_p - 0.5 \times W_p \times \tan 36^\circ)^2 + (0.5 \times W_p)^2 \right]^{0.5} \times t$$

Equation B.3

The time T required for the formation of SFGN is ~1 h. From Table B.1, the mean values of L_p and W_p was calculated to be ~485 nm and ~239 nm respectively. The average thickness of SFGNs (t) is assumed to be 45 nm from Figure B.3 (although this term cancels out in calculation). Using these estimates, the average rate of gold influx on the surface of GO sheet is calculated to be $0.1346 \text{ g cm}^{-2}\text{h}^{-1}$.

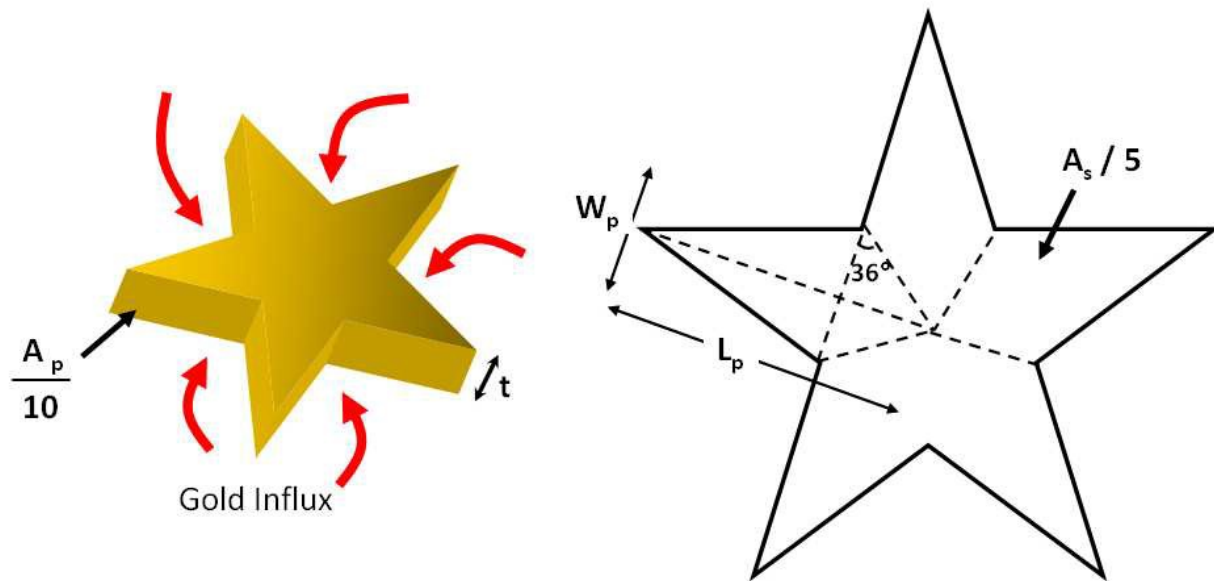


Figure B.5 Schematic that is used for estimating the average mass flux rate for the horizontal growth of SFGN. The lateral and horizontal surface area of a regular SFGN (N_p) is found in terms of L_p and W_p as shown.

B.9 Surface coverage of GO sheets by SFGNs

The surface density of SFGNs on GO was moderate at room temperatures and high at higher temperatures as explained in the main text. Figure B.7 shows the FESEM images of a GO sheet which was templated with GNS at $\sim 70^\circ\text{C}$ resulting in a very high density of deposition of gold nanostructures.

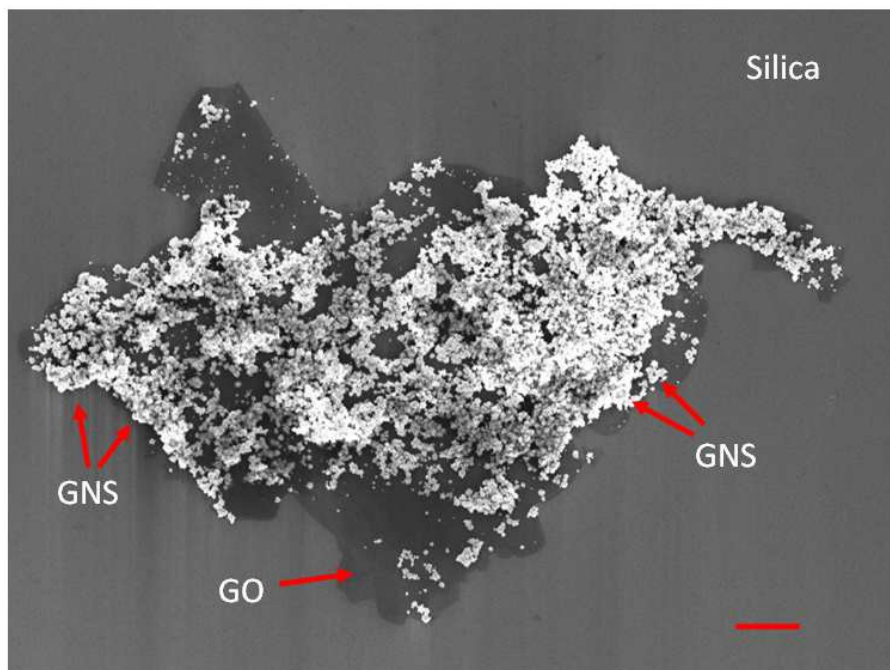


Figure B.6 FESEM image of a GO sheet exhibiting high surface coverage densities of gold nanostructures (GNS) on GO with high selectivity for a synthesis temperature of $\sim 70^{\circ}\text{C}$. Scale bar = $5\ \mu\text{m}$

B.10 Surface enhanced Raman spectra for GO sheets densely coated with gold nanostructures

The GO sheets that were densely coated with Gold nanostructures (synthesized at 75°C) were compared with SFGNs (coated at moderate density, synthesized at 25°C) for the Raman spectra enhancement factors. While the enhancement factor for GO-SFGN (25°C) was $\sim 250\%$, the enhancement factors for GO-GNS (75°C) was found to be $\sim 800\%$. The increased enhancement factors can be attributed to the high density of gold nano structures templated at high temperature.

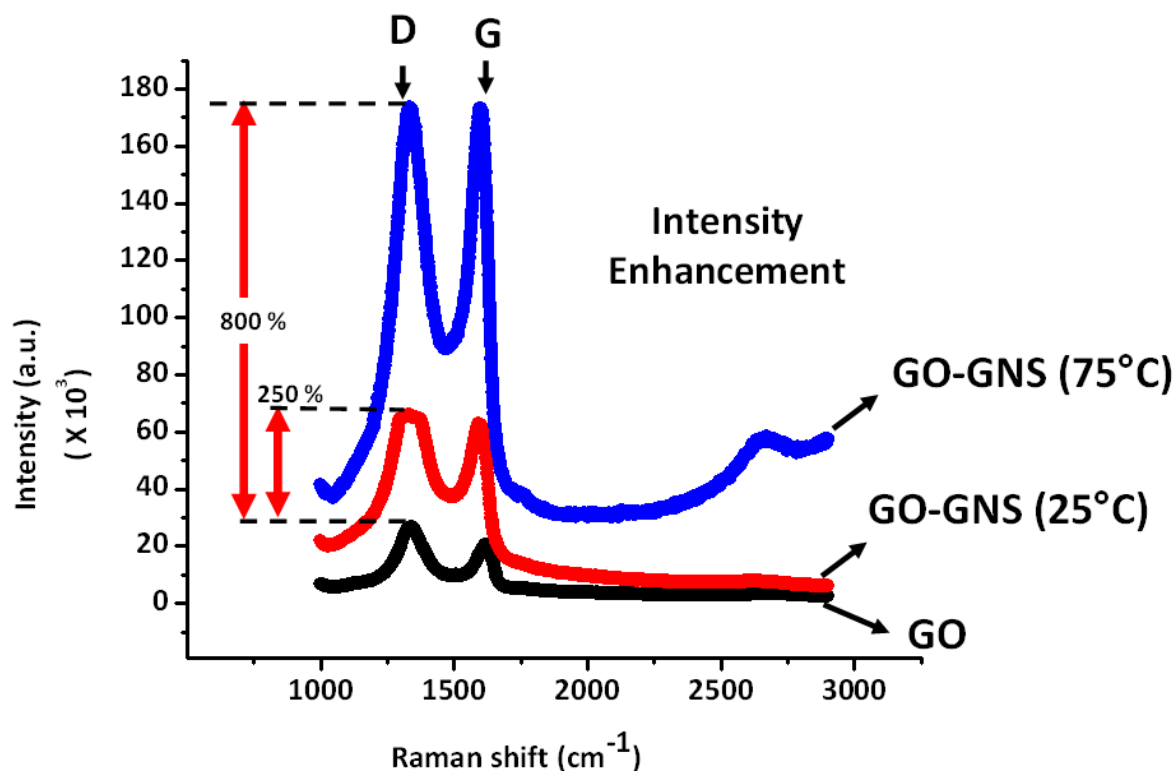


Figure B.7 Raman spectra for GO, GO-SFGN (25°C) and GO-Gold nanostructures (75°C) **Gold hybrid**. The enhancement factors for GO-GNS (synthesized at 75°C) was greater (~800 %) than the enhancement factor for GO-SFGNs synthesized at 25°C (~250 %) which can be attributed to the higher density of nanostructures that get templated at higher temperature.

B.11 Shape dependence of SFGNs on the gold ion concentration

The dendritic morphology of SFGNs was found to sensitively depend on the concentration of Au ions that are available for seeding growth. A higher concentration of gold salt (2X and 4X, X=0.275 mM) resulted in a more pronounced *secondary branching* and in some cases instances of *ternary branching* as shown in Figure B.8.

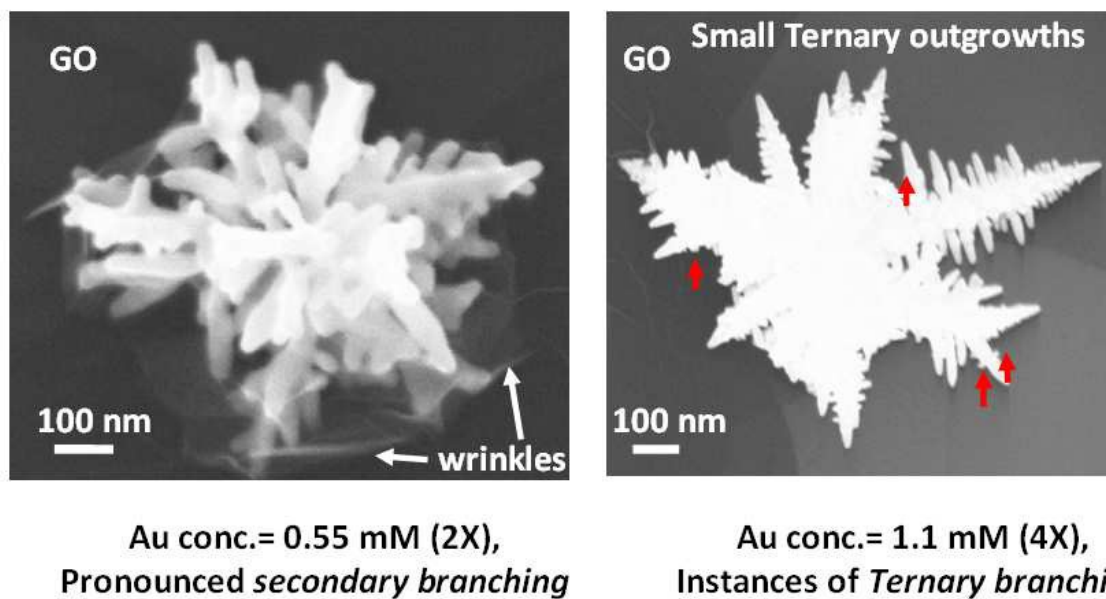


Figure B.8 FESEM images of SFGNs that were synthesized at higher gold concentration exhibited a more pronounced growth of secondary branches. In some cases, the secondary branches further differentiate to emanate ternary branches (labeled by red arrows). Scale bar = 100 nm

B.12 Selected Area Electron Diffraction (SAED) patterns for SFGNs with incompletely formed secondary branches

The SAED patterns were obtained with a Philips CM 100 transmission electron microscope operated at 100 kV. The GO-SFGN hybrids were deposited from solution on to 300 mesh size copper TEM specimen grids (Electron Microscopy Sciences) having a carbon support film. Most of the SFGNs exhibited a pronounced secondary branching and displayed mixed diffraction patterns. There was a small fraction of SFGNs with either reduced or no secondary branches. SAED patterns for such SFGNs ($N_p=5$ and $N_p=6$) are as shown in Fig B.9. The SAED still exhibits mixed patterns but at a lower scale as compared to a completely formed SFGN (Figure 3.5d). The incidence of defects in these SFGNs is found to be lesser which suggests that the crystalline defects primarily arise during the particle incorporation as more particles get added to the seed nuclei.

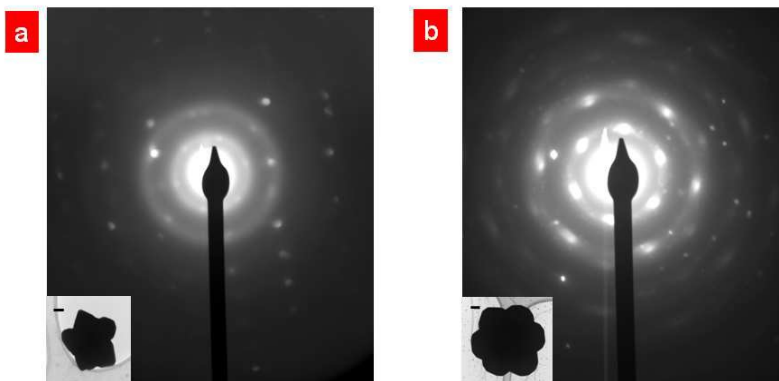


Figure B.9 SFGNs with Selected Area Electron Diffraction pattern for SFGNs with incompletely formed secondary branches (as shown in the insets) suggest that the incidence of defects in such particles is smaller as compared to a SFGN with completely formed secondary branches. Such an observation indicates that the defects are introduced as the SFGN gets formed progressively. Scale bar = 100 nm

B.13 Electrical Studies

The electrical measurements for determining the effect of hydrazine reduction on GO and GO-SFGN hybrids, were taken at room temperature, under a steady nitrogen environment, using a Keithley 2612 Dual-Channel System Source Meter connected to a computer via a GPIB/IEEE-488 interface card. The temperature studies for determining the band-gap and Schottky barrier height were carried out in a Janes cryostat the temperature of which can be externally controlled by a Lake Shore 331 Temperature Controller.

B.14 Sample calculations for determining the band-gap (E_g) and Schottky barrier height (SBH) using the temperature-dependent electrical studies

For an intrinsic semiconductor, the conductivity varies with temperature as $\sigma_i = B(T) \exp(-E_g/2k_B T)$ where E_g is the semiconductor band gap, $B(T)$ is weakly dependent on the temperature and k_B is the Boltzmann constant. Hence, the band gap can be obtained by measuring the slope of the curve obtained by plotting conductivity as a function of inverse

temperature in a semi-logarithmic plot. Figure B.8 shows the temperature dependent current-voltage behavior of a GO-SFGN device. Inset shows the semi-logarithmic plot of average conductivity against inverse temperature for this device. The slope m of this curve is given by $-E_g/2k_B$. Hence $E_g = -2 \times m \times k_B$. For GO-SFGN, $m = -1090$ and $E_g = 174$ meV. For G-SFGN, $m = -953.8$, hence $E_g = 156$ meV.

The electrical properties of GO-SFGN and G-SFGN were modeled by assuming several back-to-back Schottky contacts within these hybrids. At forward bias V , the current density through these Schottky Contacts is described by the following equation:

$$I = A^* \times a \times T^2 \times \exp\left(\frac{-q(\phi_B - V)}{k_B T}\right) \quad \text{Equation B.4}$$

where A^* is the modified Richardson constant, where A^* is the modified Richardson constant, a is the cross sectional area, ϕ_B is the Schottky barrier height (SBH), k_B is the Boltzmann constant and T is the absolute temperature. We can calculate mean value for SBH by assuming that it is independent of temperature. A plot of $\ln(I/T^2)$ versus $1/T$ at a forward bias V_1 can be used for determining the slope m_1 which is given by:

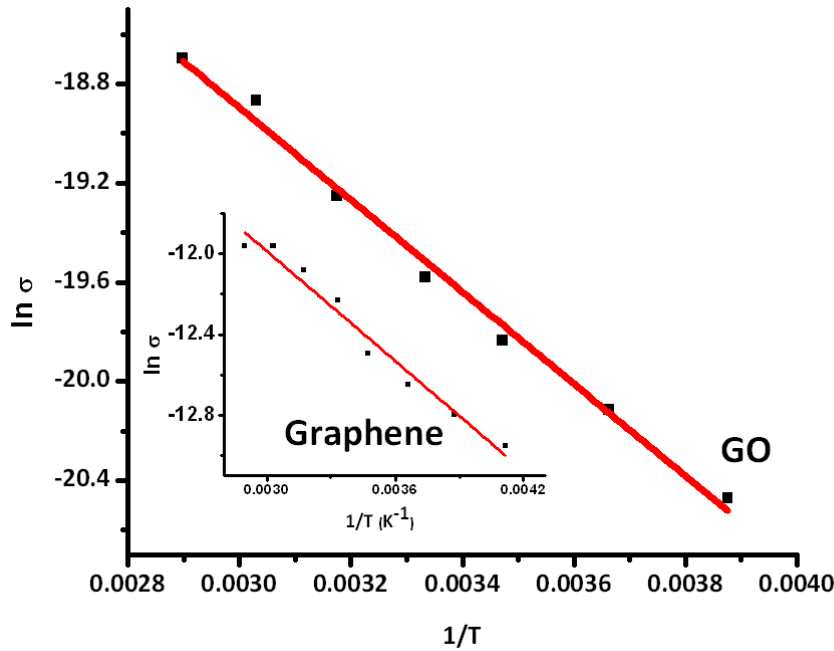


Figure B.10 Determining the energy band gap for GO and G using the temperature studies.

$$m_1 = \left(\frac{-q(\phi_B - V_1)}{k_B} \right) \quad \text{Equation B.5}$$

Similarly, for a forward bias V_2 the slope m_2 can be determined as

$$m_2 = \left(\frac{-q(\phi_B - V_2)}{k_B} \right) \quad \text{Equation B.6}$$

The SBH can then be obtained from two preceding equations as :

$$\phi_B = \left(\frac{-k_B(V_2 m_1 - V_1 m_2)}{q} \right) \quad \text{Equation B.7}$$

For G-SFGN hybrid, $V_1=0.05$ V, $V_2=0.1$ V, $m_1=-413.17$ and $m_2=-373.46$ are used to get SBH as 38.98 meV.

B.15 Variable Range Hopping as a possible mechanism of carrier transport in the Graphene devices

The experimental data for the conductivities of GO, G and GO-SFGN was found to be excellently represented by the hopping fit conduction mechanism as is shown by the linear fits of currents against $T^{-1/3}$ as shown in Figure B.11.

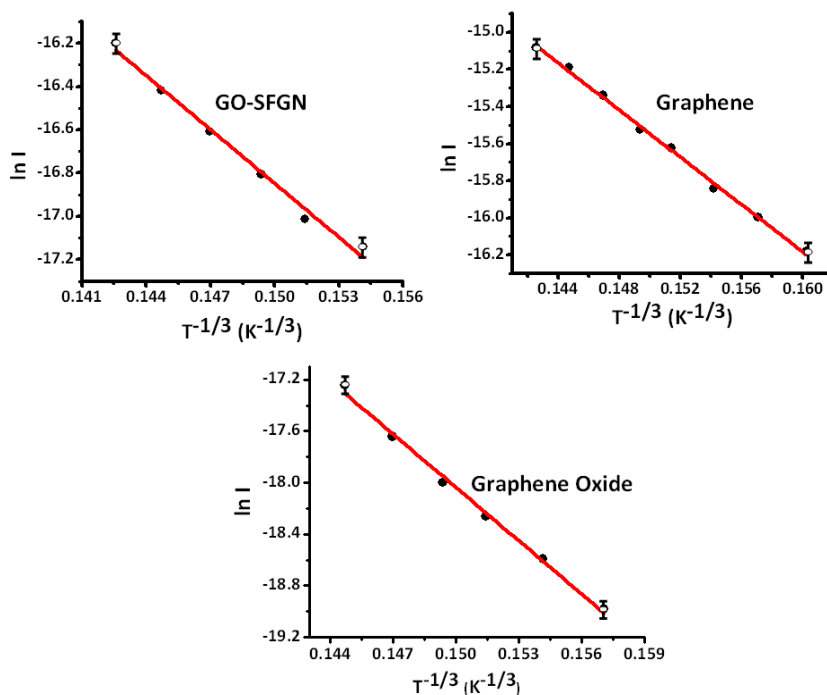


Figure B.11 Variable Range Hopping fits for the conductivities of GO, G and GO-SFGN.

B.16 Energy dispersive X-ray spectroscopy for GO-SFGN hybrid

EDS data was obtained with a Leo Field Emission Scanning Electron microscope operated at 10-15 KV.

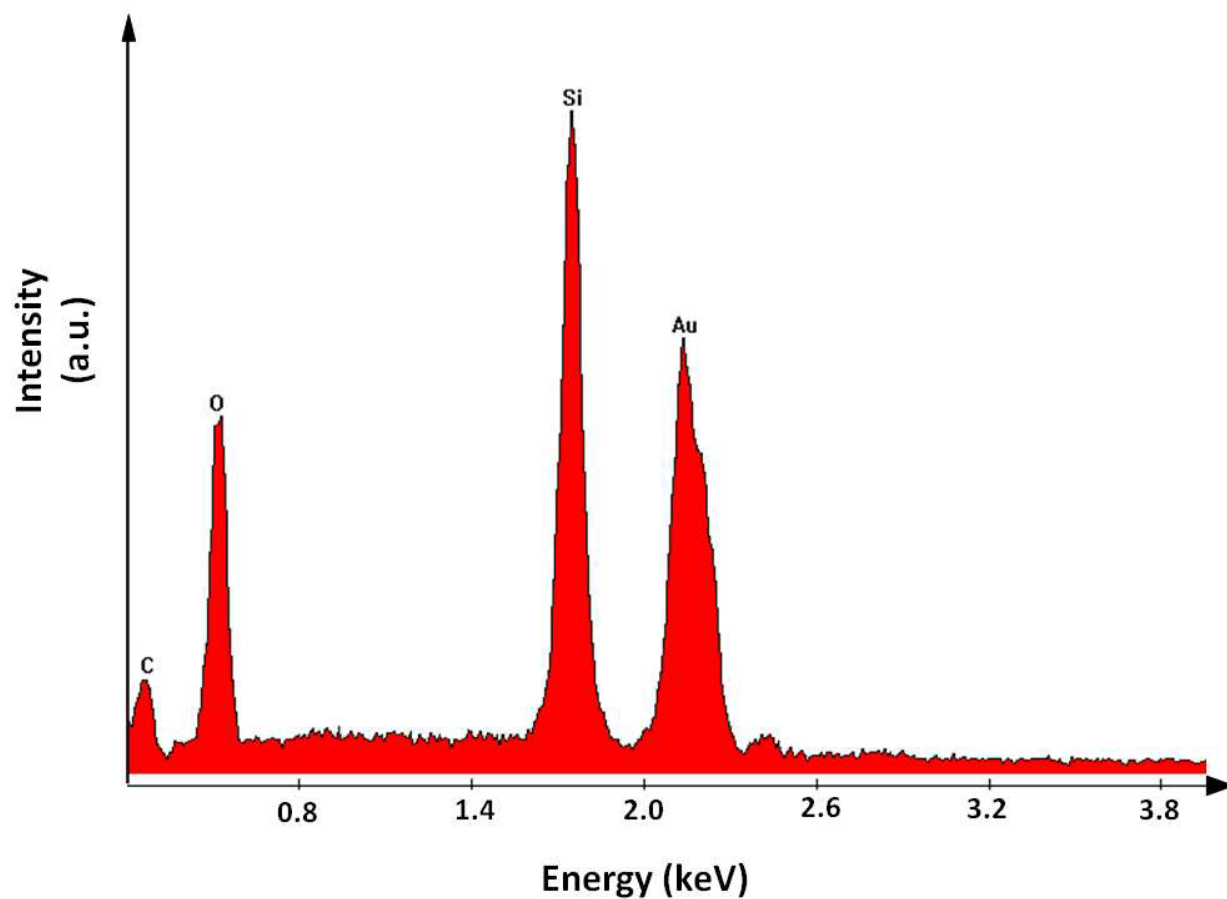


Figure B.12 Energy Dispersive X-ray spectroscopy (EDS) analysis of the GO-SFGN nanocomposite shows the spectrum obtained from a SFGN templated on a GO sheet consisting of different peaks for gold (from the SFGNs), silicon & oxygen (from the silica substrate) and carbon (from the graphene)

Appendix C Appendix for the work on microwave assisted growth of nanoparticles on graphene

C.1 Materials

Amino propyl triethoxy silane was purchased from Gelest. Gold chloride trihydrate ($\text{HAuCl}_4 \cdot 3\text{H}_2\text{O}$), graphite flakes, p-Nitro aniline, sodium borohydride, nitric acid, sulfuric acid, potassium permanganate and hydrogen peroxide were purchased from Fisher Scientific. The aqueous solutions were prepared in Deionized (DI) water obtained by a Millipore Milli-Q membrane filtration system.

C.2 Preparation of bare surfaced gold nanostructures templated on GO sheets

The GO-BSGN nanocomposite was synthesized by MW exposure (1.05 kW, 2450 MHz) on an aqueous solution of GO (100 μl , 20 mM carboxylic acid quantified by titration) and gold salt $\text{HAuCl}_4 \cdot 3\text{H}_2\text{O}$ (10 ml, 0.275 mM) for a time interval between 60s and 300s with intermittent cooling after every 10 s. The mixture is allowed to stand for ~24 h that result in the formation of BSGNs with triangular, hexagonal and dendritic morphologies, which either assemble on or get wrapped with the GO sheets depending on the MW exposure time.

C.3 Surface immobilization of the GO-BSGN hybrids

The GO sheets functionalized with BSGNs were immobilized via electrostatic interactions on a heavily doped n-type silicon substrate with a 300 nm thick thermally grown silica layer. Briefly the silicon substrate, cleaned with organic solvents (acetone, isopropanol and ethanol) is first exposed to oxygen plasma (100 W, 2 mbar, 2 min) followed by treatment with 3-Amino Propyl triethoxy silane (1% in ethanol, 10 min), The substrate is then baked at 120°C for 4 min that makes the silica surface positively charged due to the presence of amine groups on its surface. This amine-functionalized substrate is then momentarily exposed to the synthetic

mixture of GO-BSGNs. The substrate is then subsequently washed 3 times with Deionized (DI) water that facilitates selective electrostatic deposition of GO-BSGN hybrids on silica surface. Figure C.1 shows FESEM image of the GO-BSGN hybrid that was immobilized using this method. The FESEM data was obtained with a Leo Field Emission Scanning Electron microscope operated at 10-15 KV.

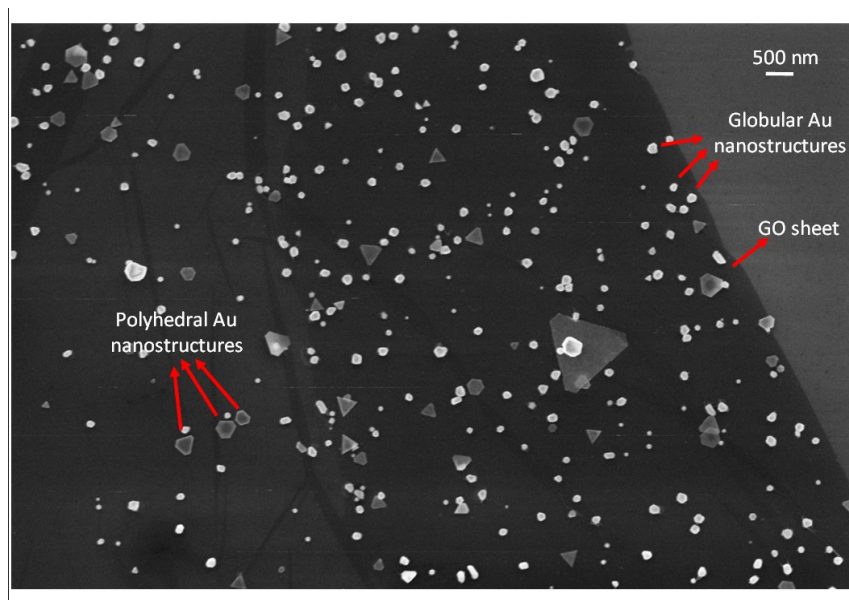


Figure C.1 A MW induced BSGN decorated GO sheet immobilized on an amine silanized substrate exhibiting a highly specific dispersion BSGNs with polyhedral and globular morphologies.

C.4 Formation of characteristic wrinkles on GO-BSGN surface

Wrinkles are formed on the GO sheets as they are immobilized on surface due to the raising and stretching of the sheets at spots where the BSGNs are attached as shown in Figure C.2.

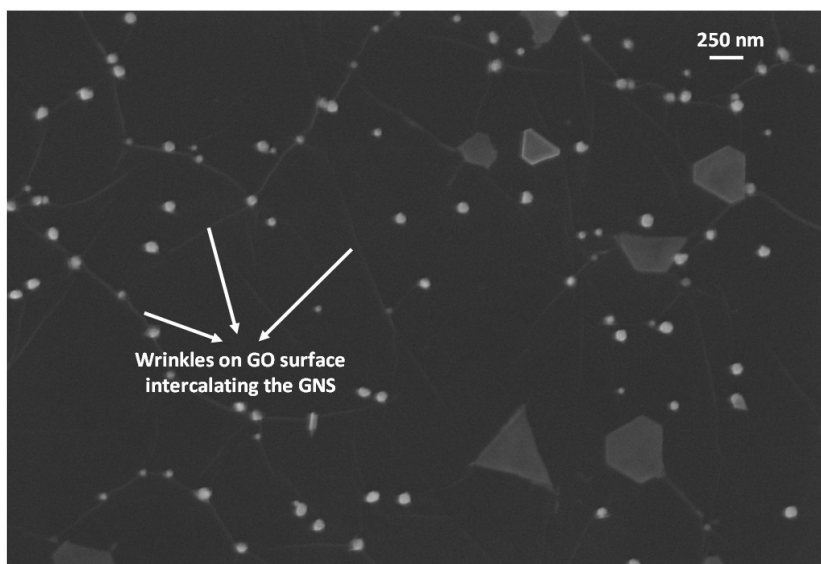


Figure C.2 Formation of characteristic wrinkles on the GO sheet surface induced by the presence of BSGNs present on the rear surface of GO sheet

C.5 Selected Area Electron Diffraction patterns for BSGNs and Ag nanostructures

The SAED patterns were obtained with a Philips CM 100 transmission electron microscope operated at 100 kV. The GO-AGN and the GO-Ag hybrids were deposited from solution on to 300 mesh size copper TEM specimen grids (Electron Microscopy Sciences) having a carbon support film. The diffraction patterns suggest a mono crystalline nature of the BSGNs and the Ag nanoparticles.

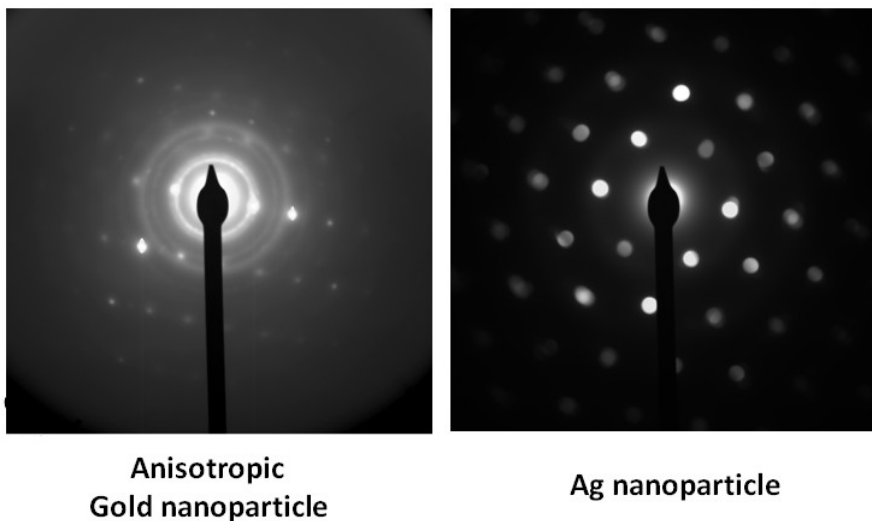


Figure C.3 Selected Area Electron Diffraction Patterns of BSGNs and Ag nanoparticles suggest the mono crystalline nature of these nanostructures

C.6 Surface coverage of GO sheets by BSGNs

It was observed that the dispersion density of BSGNs on GO sheets can be enhanced by increasing the incubation period of GO sheets in the microwaved gold salt solution which provides a greater time for the gold nuclei to interact with the charged moieties on GO surface resulting in a very high density of deposition of AGNs. Figure C.4 shows GO sheets that were incubated for ~72h in the microwaved Au salt solution before surface immobilization, exhibiting a high surface density of BSGNs.

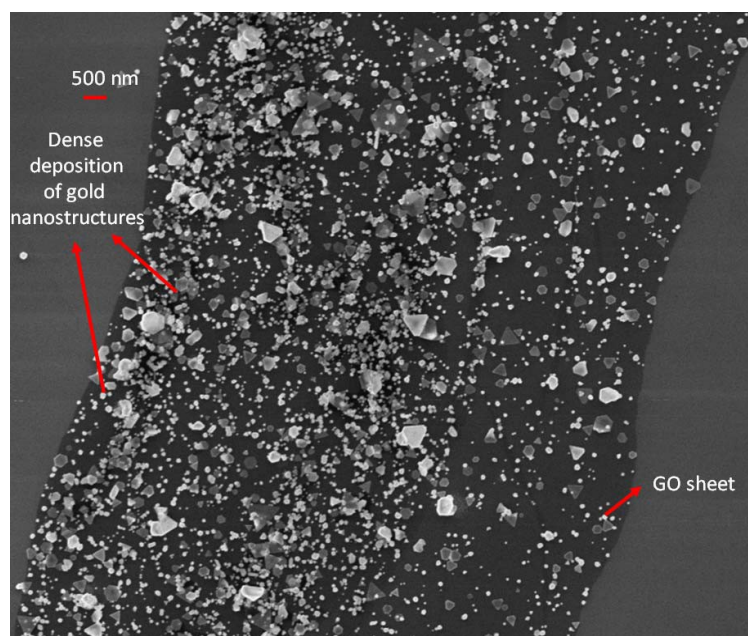
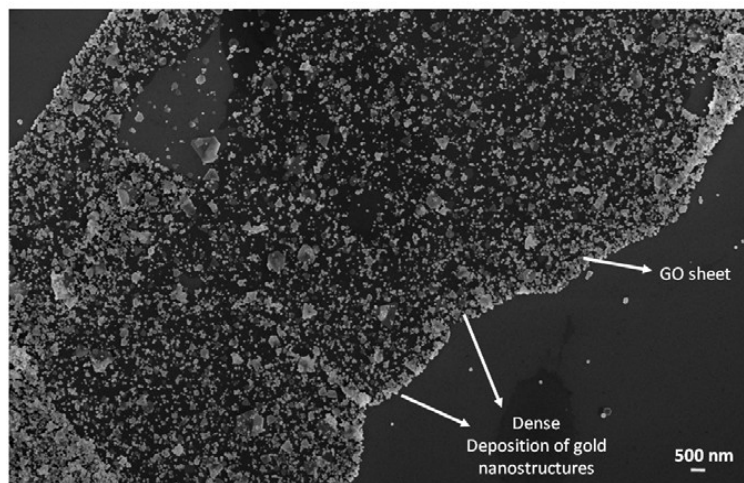


Figure C.4 GO sheets immobilized on an amine silanized silica substrate exhibiting a high surface coverage index for the BSGNs deposited on it by MW. This GO sheet was allowed to interact with MW exposed gold salt solution for ~72 h.

C.7 Formation of dendritic BSGNs templated on GO sheets

By decreasing the ambient temperature of the solution of GO and Gold salt during the MW exposure, some dendritic shaped Gold nanostructures are formed which template with high density on the GO sheets (Figure C.5)

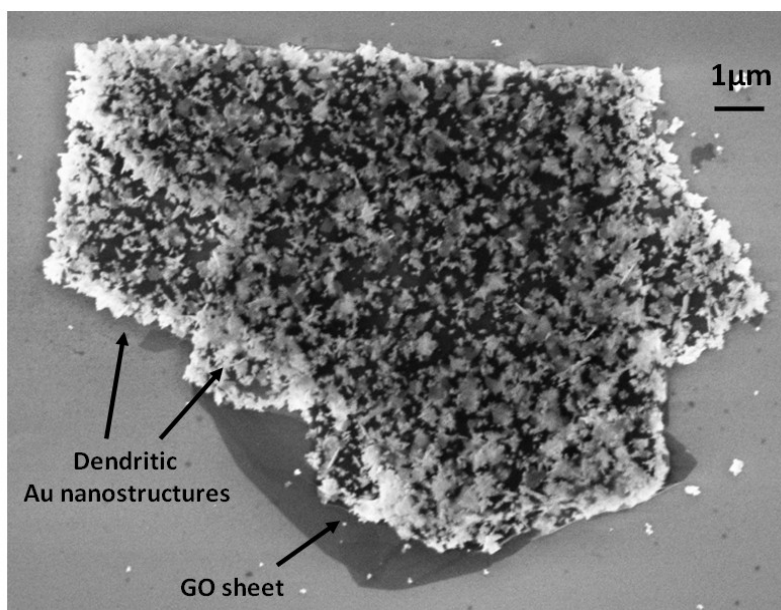


Figure C.5 GO sheet covered with a high density of dendritic gold nanoparticles that were synthesized by increasing the MW exposure time to the solution of GO and gold salt.

C.8 Formation of dendritic BSGNs encapsulated with GO sheets

Besides templating on GO sheets, some of the dendritic and polyhedral nanoparticles also get encapsulated with the GO sheets as shown in Figure C.6

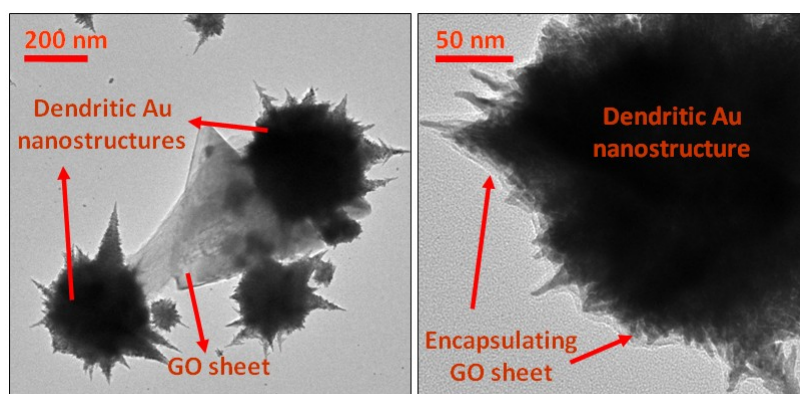


Figure C.6 Isolated dendritic shaped gold nanoparticles encapsulated/wrapped within GO sheets

C.9 Determining the catalytic activity of BSGNs stabilized on GO

The catalytic activity is determined by monitoring the course of NaBH_4 induced reduction of 4-Nitro aniline that is catalyzed in the presence of gold nanoparticles stabilized on GO. A complete reduction is indicated by the disappearance in the absorption band at 380 nm that takes ~6 min and ~ 9 min by gold seeds stabilized on GO and citrate capped GNPs respectively.

C.10 Electrical Measurements

The BSGN decorated GO sheets were immobilized on a n++ silica substrate with pre-fabricated gold electrodes. All electrical measurements were taken at room temperature, under a steady nitrogen environment, using a Keithley 2612 Dual-Channel System Source Meter connected to a computer via a GPIB/IEEE-488 interface card. The gating experiments were carried out in a Janis cryostat maintained under vacuum.

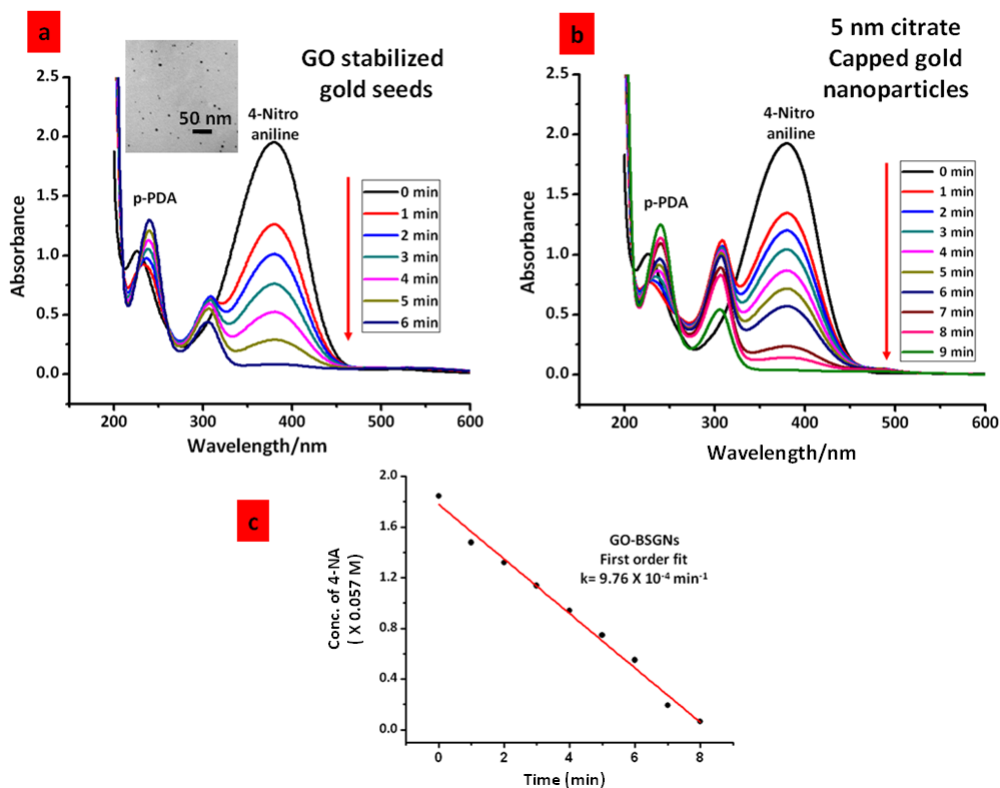


Figure C.7 Gold seeds stabilized on graphene oxide are compared for their catalytic activity with the 5 nm citrate capped gold nanoparticles by comparing the gold nanoparticle catalyzed NaBH_4 induced reduction of 4-Nitro aniline. The reaction times are evaluated by monitoring the successive decrease of the band at 380 nm for 4-NA and the corresponding increase in the band at 238 nm for *p*-phenylene diamine. (a) Complete reduction of 4-NA in the presence of 5-20 nm gold seeds stabilized on GO (left inset) takes 6 min as compared to (b) 5 nm citrate capped gold nanoparticles where it takes 9 min for the complete reduction. The first order reaction rate for the reaction catalyzed by GO-BSGNs obtained by an exponential fit comes out to be $9.76 \times 10^{-4} \text{ min}^{-1}$.

C.11 Formation of Microwave assisted silver nanoparticles on GO sheets

It was found that microwaving silver salt in the presence of GO sheets results in the formation of Ag nanoparticles stabilized by the GO sheets. Briefly, 10 ml aqueous solution of 0.275 mM AgNO_3 and 100 μl of 20mM GO was microwaved for 2 min and the solution was allowed to sit for ~24 hrs. Silver nanoparticles with spherical and characteristic tadpole shapes

were found to be templated on the GO sheets with a moderate coverage density (Figures C.8,C.9). This makes *MW* a useful tool for facile fabrication with diverse metal NPs on GO sheets. More research is required to study the factors that govern the formation of spherical and tadpole shapes

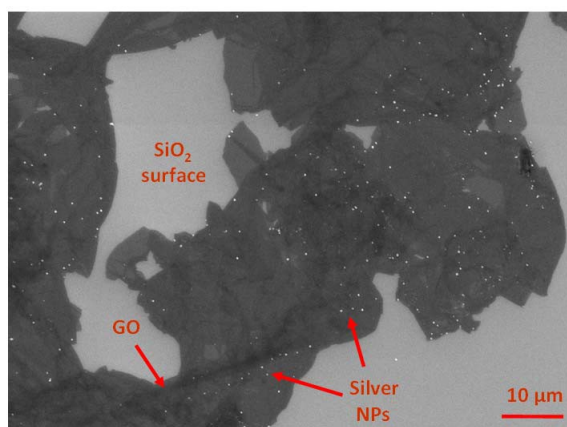


Figure C.8 GO-Ag nanocomposite immobilized on an amine silanized silica substrate. The GO-Ag nanocomposite was synthesized in a similar manner using *MW* as the inducing agent for NP synthesis.

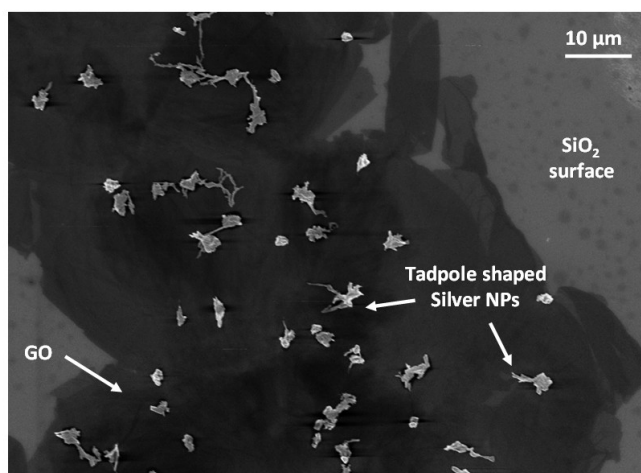


Figure C.9 GO-Ag nanocomposite in which the Ag nanoparticles exhibit a characteristic tadpole-shaped morphology with a central core structure emanating a tail/shoot like elongation.

C.12 Structural parameters and shape distribution of the BSGNs

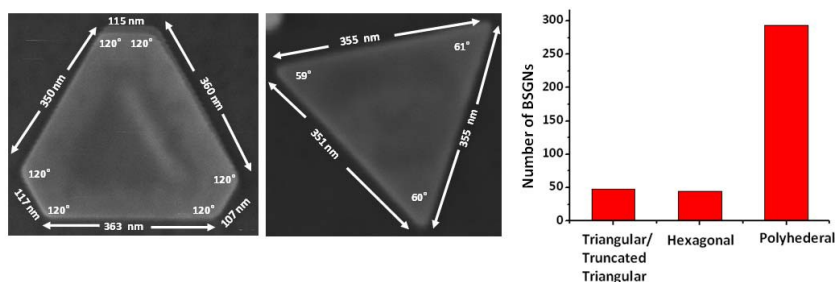


Figure C.10 Structural parameters (side length, vertex angle) for the triangular and the truncated triangular BSGNs. Bar graph shows the shape distribution of the BSGNs

C.13 EDS analysis for the GO-BSGNs immobilized on silica substrate

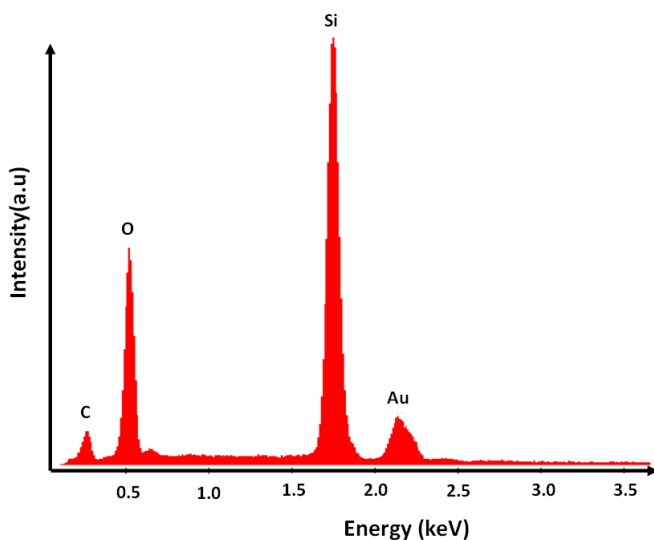


Figure C.11 Energy Dispersive X-ray spectroscopy (EDS) analysis of the GO-BSGN nanocomposite shows the spectrum obtained from BSGNs templated on a GO sheet consisting of different peaks for gold (from the AGNs), silicon & oxygen (from the silica substrate) and carbon (from the graphene)

Appendix D Appendix for the work on synthesizing ultra thin sheets of Boron Nitride using chlorosulfonic acid

D.1 Exfoliation of hexagonal-Boron Nitride (α -BN)

Chlorosulfonic acid (CA, 97% purity) was used for exfoliating atomic thick Boron Nitride Sheets (UTBNSs) from bulk α -BN. The bulk α -BN was obtained from two sources: (a) single crystals produced by scrapping high-purity hot-pressed Boron Nitride, grade HBC purchased from Momentive performance materials, and (b) a Highly Oriented Pyrolytic Block (HOPB). 50 mg of bulk α -BN was weighed in a glass vial and placed inside a glove-box maintained under standard, dry N_2 atmosphere conditions for carrying out the process of exfoliation. 10 ml of Chlorosulfonic Acid (CA) was added to the glass vial and the α -BN-CA assembly was blended using a Teflon coated magnetic stir bar on a magnetic stirrer for ~72 hrs at ~1500rpm. CA leads to an intercalation assisted protonation of bulk α -BN layers that result in the exfoliation of atomic thin (2-5 layers) BN Sheets. In a CA environment, the intermediate α -BN layers undergo protonation and functionalization (as discussed in the XPS studies, Figure 5.3) which results in their exfoliation to form UTBNSs. This is also indicated by a pale white color of the CA solution containing dispersed UTBNSs (Figure D.1).

D.2 Transfer to aqueous phase

For further investigation outside the glove-box, the moisture-sensitive CA solution, containing the exfoliated UTBNSs, was diluted several folds (1:200) in an aqueous solution via a process of quenching. 500 ml of de-ionized (DI) water in a glass beaker was placed inside the glove-box and 2.5 ml of the UTBNSs-CA solution was added drop-wise to the beaker to obtain the quenched solution. The quenched solution was then removed from the glove-box and allowed to stand for ~24 hours to let the un-exfoliated α -BN flakes sediment to the bottom. Some white floating legions were found to rise to the water surface. These likely are clusters of exfoliated sheets hydrophobic in nature.

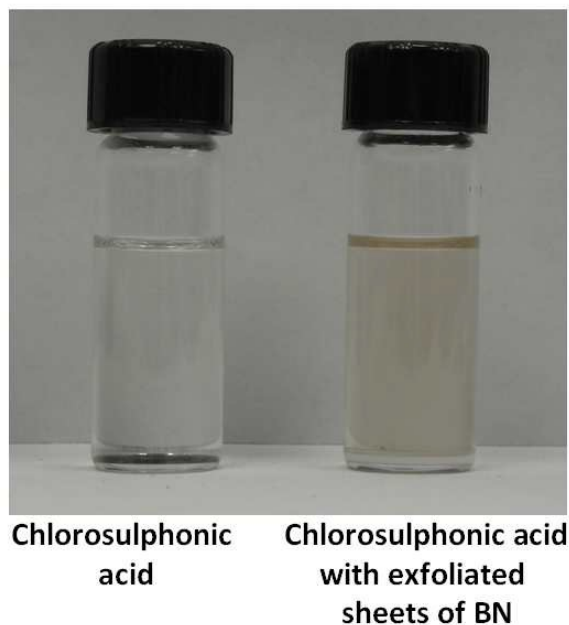


Figure D.1 Optical Light scattering as exhibited by the CA solution with dispersed sheets of Boron Nitride giving the CA-UTBNSs solution a pale white color.

D.3 Preparation of the UTBNS film for XPS

Uniform UTBNS films (stacked layers of UTBNSs) were formed on a polymeric (Poly Tetra Fluoro Ethylene or Polycarbonate) membrane by vacuum filtration of the quenched suspensions through it. (Figure D.2a). A Buchner funnel was placed on a Buchner flask, which was connected to a vacuum source with rubber tubing. The polymeric membrane filter was then placed inside the Buchner funnel and the quenched solution containing UTBNSs was gently poured onto the filter to allow for filtration. An average vacuum filtration process takes ~72 hrs. Following the filtration of UTBNSs, the polymeric membrane was gently lifted off the Buchner funnel and heated in an oven at ~200 °C for ~30 minutes to remove any residues and used for XPS studies. The film sample on filter paper was also heated in-vacuo within the XPS instrument to a temperature of 400 °C for ~2hrs to minimize any residues of CA and atmospheric adsorbates. The XPS results shown in Chapter 5, Figure 5.3 are obtained on a film prepared by aforementioned method.

To minimize the influence of CA residues, another UTBNS film was fabricated that uses the washed UTBNS solution in place of quenched UTBNS solution. The washed UTBNSs were

prepared by centrifuging the quenched suspensions at 13000 rpm for 60 minutes, followed by decanting the top phase and re-suspending the centrifuged sheets in water. This process was repeated 3 times to obtain UTBNS solution with lesser CA residues. Figure D.2b shows the B1s and N1s spectra from the film prepared by filtering the washed UTBNSs. These exhibit a higher relative fraction of functionalized B and N atoms. The XPS data was obtained from a Perkin–Elmer PHI 5400 electron spectrometer using achromatic AlK α radiation (1486.6 eV) under vacuum of 8.0×10^{-9} Torr. The XPS binding energies were measured with a precision of 0.1 eV and the analyzer pass energy was set to 17.9 eV, with a contact time of 50 ms. Before sample testing, the spectrometer was calibrated by setting the binding energies of Au 4f $_{7/2}$ and Cu 2p $_{3/2}$ to 84.0 eV and 932.7 eV, respectively.

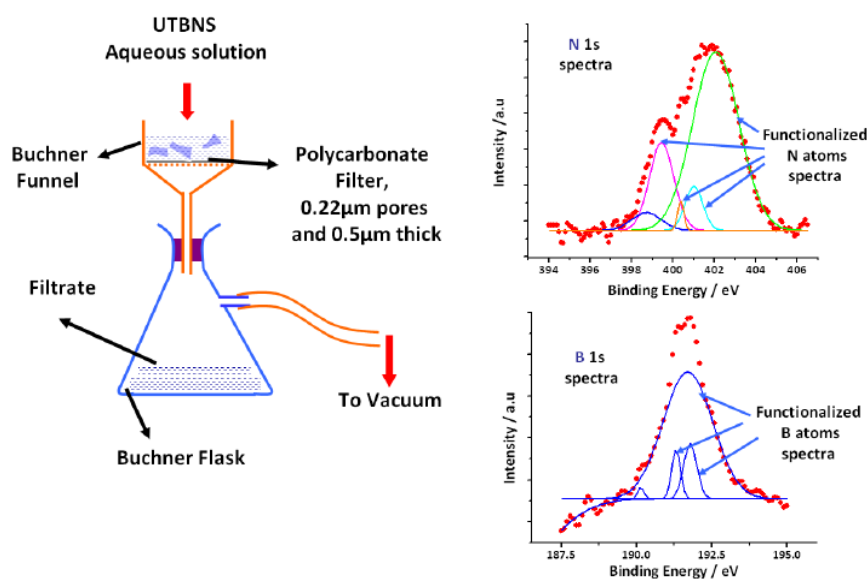


Figure D.2 (a) Experimental set-up for the formation of thin UTBNS film via vacuum filtration on a polymeric membrane substrate. (b) B1s and N1s spectra of an UTBNS film formed by filtering a washed solution of UTBNSs. The washed solution was prepared by repeatedly (3X) centrifuging and re suspending the centrifuged sheets in aqueous suspension to minimize the presence of CA residues. These sheets exhibit a much higher percentage of functional groups as compared to the sheets obtained by direct filtration of quenched suspensions.

D.4 Calculating the fraction of dangling N atoms on a UTBNS exhibiting surface perforations

Let the surface area of sheet under consideration be $S \text{ nm}^2$ and the perimeter of perforations be $P \text{ nm}$. The perimeter is calculated by summing the peripheries of each perforation present within the sheet (shown as dashed lines in panel b). The line density of N atoms (σ_N) along the edge of an UTBNS (assuming zigzag edge) can be given as (see panel a):

$$\sigma_N = \frac{1}{0.251} \text{ N atom/nm} \quad \text{Equation D.1}$$

Hence the total number of N atoms on edges (N_E) can be given by:

$$N_E = \sigma_N \times P = \frac{P}{0.251} \quad \text{Equation D.2}$$

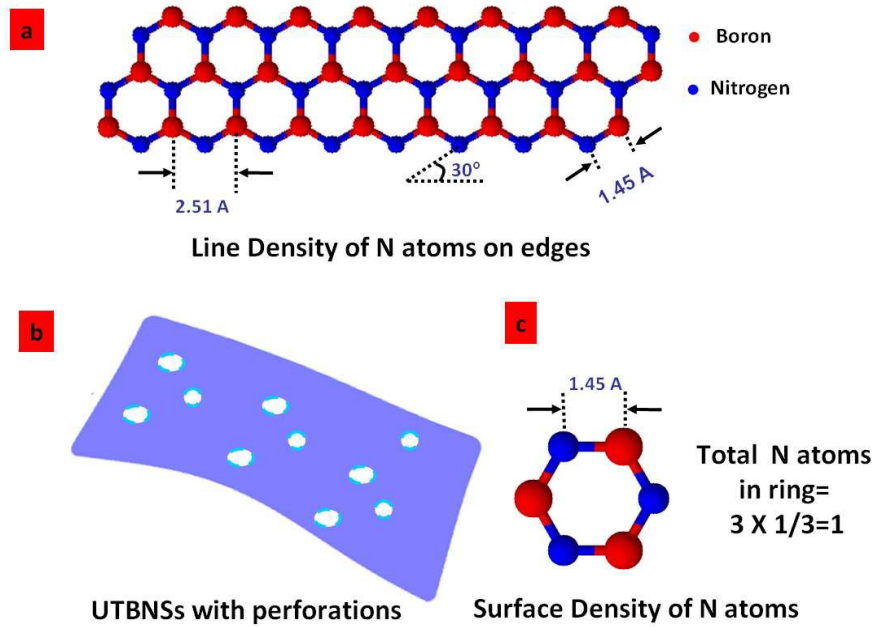


Figure D.3 (a) Zigzag edge of a BN sheet that is assumed for calculating the line density of N atoms. (b) Schematic of an UTBNS with internal perforations. The dashed line on perforations indicates their periphery which contributes the dangling N atoms. (c) Hexagonal BN ring for calculating the surface density of N atoms on a BN sheet.

Since a BN ring has 3 N atoms, each of which is shared by two neighboring BN rings, the total contribution of N atoms from a ring is $3 \times 1/3 = 1$ (see panel c). Thus the surface density of N atoms (ρ_N) present on a UTBNS can be given as

$$\rho_N = \frac{1}{A} \text{ N atom/ nm}^2 \quad \text{Equation D.3}$$

where A is the surface area of a BN ring given by

$$A = \frac{3\sqrt{3} \times 0.145^2}{2} \text{ nm}^2 \quad \text{Equation D.4}$$

$$\rho_N = \frac{1}{0.054} \text{ N atom/nm}^2 \quad \text{Equation D.5}$$

Thus the total number of N atoms (N_s) on a sheet with surface area S are

$$N_s = \frac{S}{0.054} \text{ N atoms} \quad \text{Equation D.6}$$

Thus the fraction f of N atoms in an UTBNS that are present along the edges of perforations is:

$$f = \frac{N_E}{N_E + N_s} \approx \frac{N_E}{N_s} = \frac{\frac{P}{0.251}}{\frac{S}{0.054}} \quad \text{Equation D.7}$$

For an average sheet with diameter D, the fraction of overall dangling N atoms (including the ones at sheet boundaries) can be given by:

$$f_{\text{overall}} = \frac{(\sigma_N \times \pi D) + (f \times \rho_N \times \pi D^2 / 4)}{\rho_N \times \pi D^2 / 4} = f + \frac{4\sigma_N}{\rho_N \times D} \quad \text{Equation D.8}$$

The parameters P and S are calculated for the sub-sections of an UTBNS, the TEM images of which are shown in Figure D.4. For sub-section shown in panel a, P=56323.2 nm and S=25 X 10⁶ nm² are obtained using Image J software. Thus f comes out to be

$$f = \frac{\frac{P}{0.251}}{\frac{S}{0.054}} = 0.048\%$$

Equation D.9

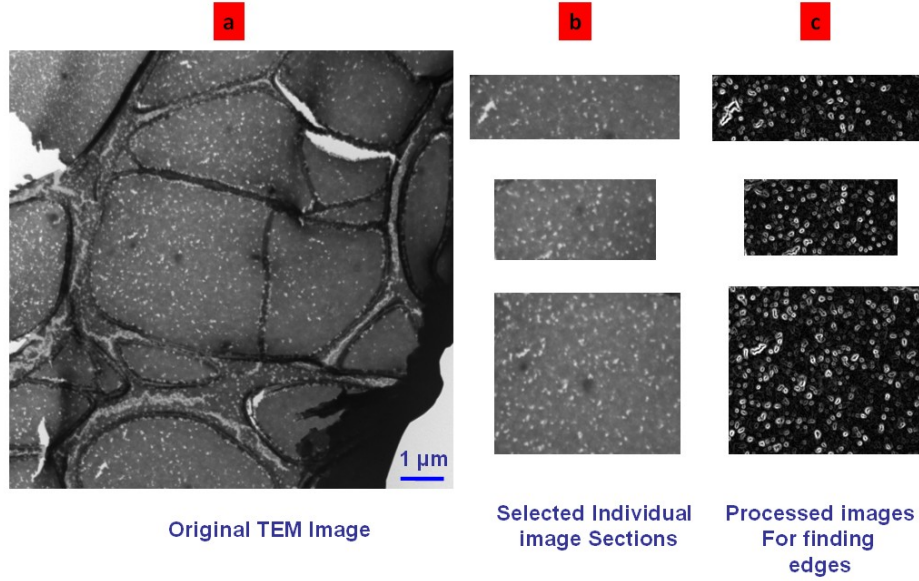


Figure D.4 (a) TEM image of an UTBNS with perforations (b) Sub-sections of the TEM image that were analyzed for estimating the density of edges contributed from perforations present on surface. (c) Processed images that are used for calculating the perimeter of perforations (highlighted white) and the surface area (shaded black).

Considering the average diameter of sheet to be $10 \mu\text{m}$, f_{overall} can be calculated to be:

$$f_{\text{overall}} = f + \frac{4\sigma_N}{\rho_N \times D} = 0.057\%$$

Equation D.10

D.5 Obtaining the expressions for attractive and repulsive potentials for evaluating the DLVO model

Repulsive Potential: The repulsive potential is determined in accordance with the Gouy-Chapman theory², where the UTBNSs suspended in solution can be represented by two parallel plates distanced such that their electrical double layers interact and influence each other as shown in Figure D.5. If the pressure acting on the volume element perpendicular to the surface

of sheet is P_o and that acting perpendicular to the surface centered in between sheets is $P_{D/2}$, then the repulsive Force (F_R) acting per unit area of sheets can be written as

$$F_R = P_{D/2} - P_o \quad \text{Equation D.11}$$

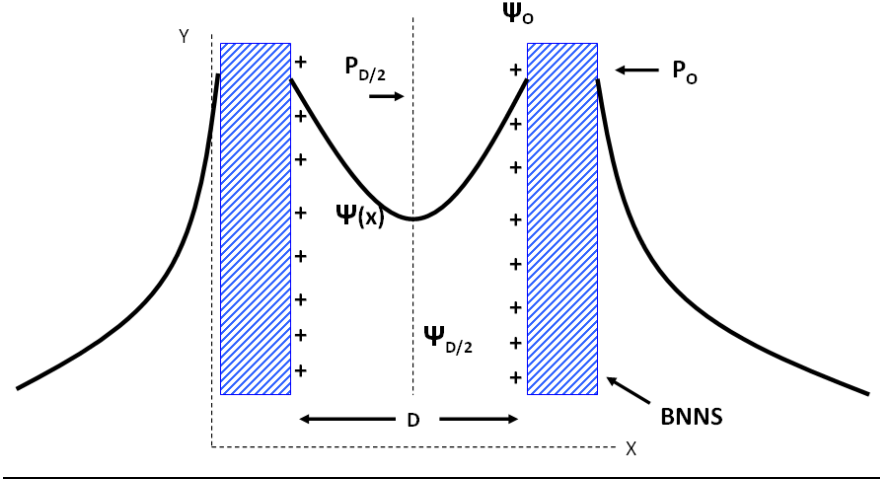


Figure D.5 Determining the Electrostatic Repulsive potential between two UTBNSs using Gouy-Chapman theory

Next consider the net force acting per unit area along x-axis on a volume element lying in between the sheets. It is given by the sum of Pressure force (F_p) and electrical force (F_{el}).

$$F_p = \frac{\partial P}{\partial x} \quad \text{Equation D.12}$$

$$F_{el} = \rho^* \times \frac{\partial \psi}{\partial x} \quad \text{Equation D.13}$$

where ρ^* is the charge density of system and ψ denotes the electric potential at a point in between the sheets. Under equilibrium,

$$F_p + F_{el} = 0 \quad \text{Equation D.14}$$

$$\frac{dP}{dx} + \rho^* \times \frac{d\psi}{dx} = 0 \quad \text{Equation D.15}$$

This gives

$$dP = \rho^* d\psi \quad \text{Equation D.16}$$

The charge density ρ^* is related to the ion concentration as (using the Boltzmann equation)

$$\rho^* = eN_0 \left[\exp\left(\frac{-e\psi}{kT}\right) - \exp\left(\frac{e\psi}{kT}\right) \right] \quad \text{Equation D.17}$$

where N_0 is the number of charges present per unit volume of solution. An estimate of N_0 within the electrical bilayer formed around UTBNs suspended in aqueous solution is obtained is section D.6.

Substituting ρ^* gives

$$dP = 2eN_0 \sinh\left(\frac{e\psi}{kT}\right) d\psi \quad \text{Equation D.18}$$

This can be integrated to obtain a difference in the pressures:

$$F_R = P_{D/2} - P_o = 2kTN_0 \left[\cosh\left(\frac{e\psi_{D/2}}{kT}\right) - 1 \right] \quad \text{Equation D.19}$$

Where $\psi_{D/2}$ denotes the electric potential at the central point in between the sheets. Using the Gouy-Chapman expression for the variation of potential within the double layer,

$$\psi_{D/2} = \frac{8kT\chi_0}{e} \exp(-\kappa D/2) \quad \text{Equation D.20}$$

where,

$$\chi_0 = \frac{\exp(e\psi_0/2kT) - 1}{\exp(e\psi_0/2kT) + 1} \quad \text{Equation D.21}$$

$$\kappa^{-1} = \sqrt{\frac{\epsilon_r \epsilon_o kT}{2e^2 N_o}} \quad \text{Equation D.22}$$

This gives

$$F_R = 64kTN_0\chi_0^2 \exp(-\kappa D) \quad \text{Equation D.23}$$

Since

$$F_R = \frac{\partial V_r}{\partial D} \quad \text{Equation D.24}$$

where V_r is the repulsive potential per unit area experienced by sheets

$$V_r = \frac{64kTN_0\chi_0^2}{\kappa} \exp(-\kappa D) \quad \text{Equation D.25}$$

Attractive Potential: The expression for attractive van der Waals potential (V_{att}) is obtained in a similar way as has been derived in Reference 1¹ which obtained V_{att} for two parallel graphene sheets (surfactant-stabilized) by considering the London inter atomic potential. We are restating their calculation here for a clearer understanding in context of Boron Nitride Sheets. The van der waal energy of interaction between an atom placed at a distance D from the sheet and the sheet atoms in the differential ring element (as shown in Figure D.6a) is given by

$$dV_a = \frac{-C \times \rho \times 2\pi \times x dx}{(x^2 + D^2)^3} \quad \text{Equation D.26}$$

Thus the interaction energy between the atom and the entire sheet can be given by integrating this expression over the sheet area.

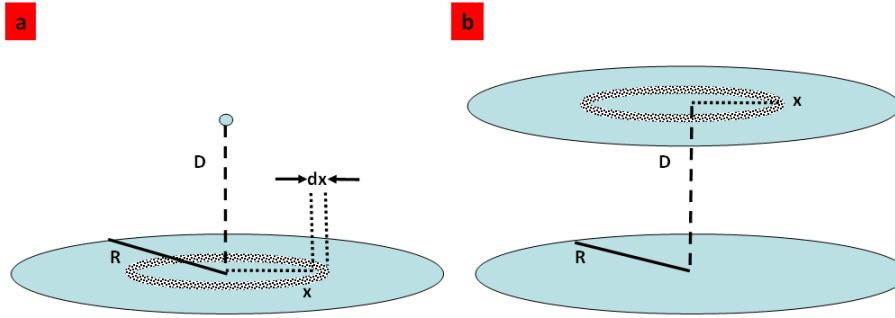


Figure D.6 Calculating the van der waal attractive potential between UTBNs

$$V = -C \times \rho \times 2\pi \int_{x=0}^{x=\infty} \frac{x dx}{(x^2 + D^2)^3} = \frac{-C\rho\pi}{2D^4} \quad \text{Equation D.27}$$

Extending this result for a pair of sheets placed parallel to each other, the potential energy between a sheet and the sheet atoms in the differential ring element (as shown in Figure D.6b) is thus given by

$$dV_s = \frac{-\pi C \rho}{2D^4} \times \rho \times 2\pi x dx \quad \text{Equation D.28}$$

And hence the interaction energy between two sheets separated by a distance D is obtained by integrating the above expression

$$V_{att} = \frac{-C \times \rho^2 \times \pi^2}{D^4} \int_{x=0}^{x=R} x dx = \frac{-C \rho^2 R^2 \pi^2}{2D^4} = \frac{-C \rho^2 S \pi}{2D^4} \quad \text{Equation D.29}$$

where $S=\pi R^2$ is the surface area of a sheet.

The value for $\rho^2 C$ is estimated by knowing the value of surface energy (γ) of BN. This is the energy required to separate the two intermittent sheets from their minimum separation do. Thus by definition (using the above expression)

$$V_{att}(for D = d_o) = \gamma = \frac{-C \rho^2 S \pi}{2d_o^4} \quad \text{Equation D.30}$$

$$C \rho^2 = \frac{2\gamma d_o^4 S \pi}{S \pi} \quad \text{Equation D.31}$$

$$V_A = \frac{-S d_o^4 \gamma}{D^4} \quad \text{Equation D.32}$$

For BN, $d_o=0.33$ nm and $\gamma=55.38$ mJ/m² is used to obtain the expression of V_A per unit area for different values of D . Figure D.7 shows the net interaction energy of UTBNSs modeled for values of ζ ranging from 1mV to 25 mV.

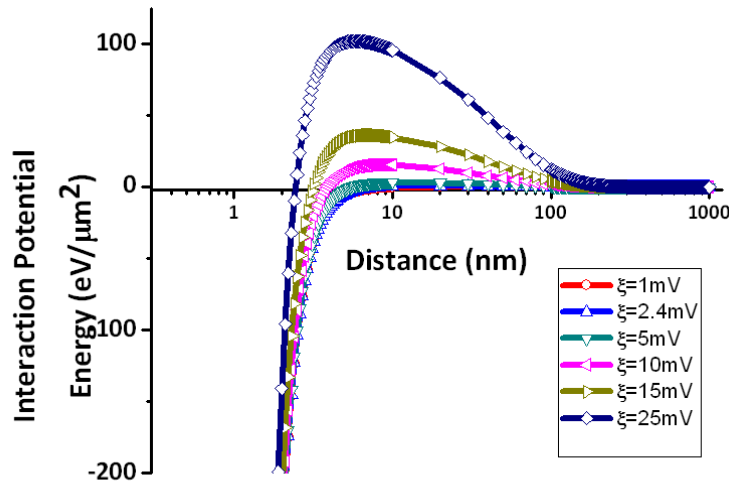


Figure D.7 The net energy curves for dispersed UTBNSs for values of ζ ranging from 1mV to 50 mV.

D.6 Calculating the charge density per unit volume of the aqueous UTBNS dispersion for evaluating the DLVO model

N_o denotes the concentration of unit charges of counter ions present per unit volume of the solution within the electrical bilayer formed between two adjacent UTBNSs. Assuming charge neutrality in the space confined within UTBNSs, the number of counter ions should be equal to the number of charges present on UTBNS surface (N_s). We thus obtain an estimate for the charges present of UTBNS surface UTBNS solution. If N = Total number of UTBNSs present per unit volume of solution, and n_o =Total number of unit charges present on the solvent exposed surface of a dispersed UTBNS, then:

$$N_o = N_s = N \times n_o \quad \text{Equation D.33}$$

We first obtain an estimate for N . Let the average lateral cross sectional area of the dispersed UTBNSs be S , the average number of layers be t and the weight per unit area of UTBNS be m_o , then for a concentration C (weight per unit volume) of UTBNSs, the total number of UTBNSs per unit volume (N) can be given as

$$N = \frac{C}{S \times m_o \times t} \quad \text{Equation D.34}$$

Since the contribution of an N atom and a B atom in the hexagonal BN ring is 1/3, each BN ring contributes 1N atom and 1B atom. If the surface area of a BN ring is A , the weight per unit area (m_o) can be given by:

$$m_o = \frac{(MW_{Boron} + MW_{Nitrogen})}{N_A} \times \frac{1}{A} \quad \text{Equation D.35}$$

where $MW_{Boron} = 11$ and $MW_{Nitrogen} = 14$ and N_A = Avogadro's constant.

Next we obtain an estimate of n_o . The electrostatic interaction is contributed by the protonated N atoms present on the surface of UTBNSs that undergo ionization on dispersion in water. The total number of N atoms (N_N) on a single atom thick UTBNS with surface area S , can be given by:

$$N_N = \frac{S}{A} \quad \text{Equation D.36}$$

If f denotes the fraction of N atoms that have undergone protonation ($-NH_2$, $-NH^+$ and $-NH_3^+$), then the number of protonated N atoms (N'_P) on a surface of UTBNS are:

$$N'_P = \frac{f \times S}{A} \quad \text{Equation D.37}$$

Since the lateral dimensions of a UTBNS is much higher than its thickness, we assume that the primary electrostatic interaction takes place only at the flat layers exposed to solution (top and bottom) via the formation of electrical bilayer. Hence the total number of protonated N atoms available for solvent interaction (N_P) in a UTBNS with any number of layer can be given by

$$N_P = 2 \times N' = \frac{2 \times f \times S}{A} \quad \text{Equation D.38}$$

And this should be equal to the number of unit charges present on the external surface of a UTBNS

$$N_P = n_o = \frac{2 \times f \times S}{A} \quad \text{Equation D.39}$$

Substituting the values of N and n_o gives

$$\Rightarrow N_o = N \times n_o \quad \text{Equation D.40}$$

$$\Rightarrow N_o = \frac{C}{S \times \frac{(MW_{Boron} + MW_{Nitrogen})}{N_A} \times \frac{1}{A} \times t} \times \frac{2 \times f \times S}{A} \quad \text{Equation D.41}$$

$$\Rightarrow N_o = \frac{C \times f \times N_A}{(MW_{Boron} + MW_{Nitrogen})} \times \frac{2}{t} \quad \text{Equation D.42}$$

For $C=0.01\text{mg/ml}$, $f=0.303$, (as obtained from the XPS studies) and $t=5$, N_o comes to be 2.92×10^{22} unit charges/ m^3 .

D.7 Immobilization of UTBNSs

For optical, electron microscopic and Raman Spectroscopic investigations, the UTBNSs were immobilized from the quenched solution on silica wafers (300 nm SiO_2 grown on a Si substrate) by either surface-pick up technique or by utilizing hydrophobic interactions. Each silica wafer was thoroughly cleaned with organic solvents (acetone, isopropanol, and ethanol purchased from Sigma-Aldrich) and then treated with O_2 plasma using a version 5 FEMTO Plasma System [Diener Electronics]. In the surface-pick up technique, the cleansed wafer was dipped under the surface of the quenched UTBNS-CA solution and slowly drawn out (at an angle of 45° or less with the surface of the solution), in close proximity to visible sheets floating

on the solution surface. The sheets were then allowed to settle on the wafer for ~3-6 minutes, followed by a gentle wash with DI water and successive air-dry. This results in a low-density deposition of UTBNSs on the wafer. The wafer is kept in the oven at ~200° C for ~2hrs to enable a firm anchoring of sheets on surface. Higher density of immobilized sheets was achieved by using an octadecyl-amine silanized hydrophobic silica surface. The un-functionalized BN regions within UTBNSs should be hydrophobic in nature and hence enable a denser deposition of UTBNSs from solution.

D.8 Optical Imaging

Optical microscopy imaging was carried out with an Olympus BX41 microscope and Olympus DP71 microscope digital camera. Figure D.8 show optical images of UTBNSs deposited on silicon substrate with a top grown 300nm thick silica layer. It has been recently shown that UTBNSs possess optimum visibility on a 90nm thick silica background and their visibility increases with an increase in the number of layers. Thus these images which we were able to visualize on 300 nm thick silica are most likely few-atoms thick.

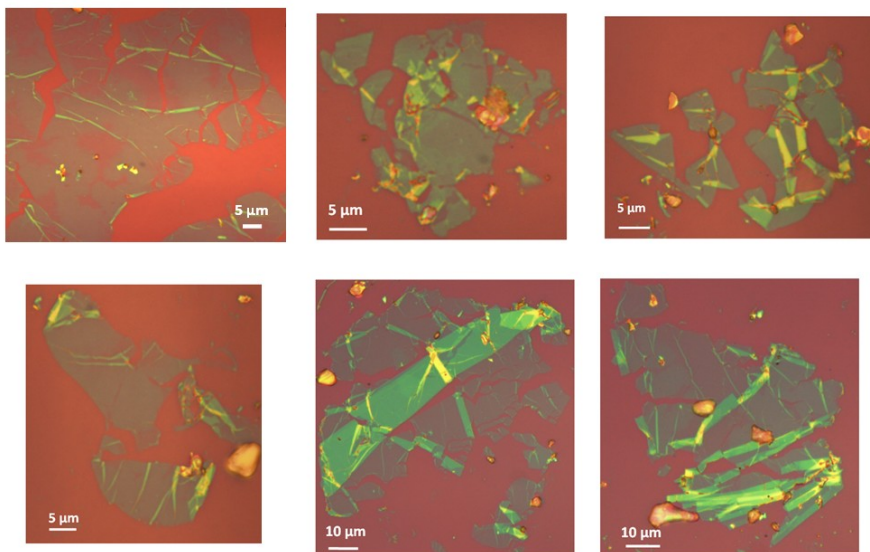


Figure D.8 Optical images of UTBNSs immobilized on silica substrate by drop-casting and electrostatic interactions with a silanized surface. The sheets exhibit micron scale large surface areas.

D.9 Obtaining UTBNSs from pyrolytic BN sample

CA exfoliation was also carried on Highly oriented Pyrolytic α -BN block to obtain exfoliated sheets. Figure D.9 shows the optical and FESEM image of UTBNSs obtained from the pyrolytic sample

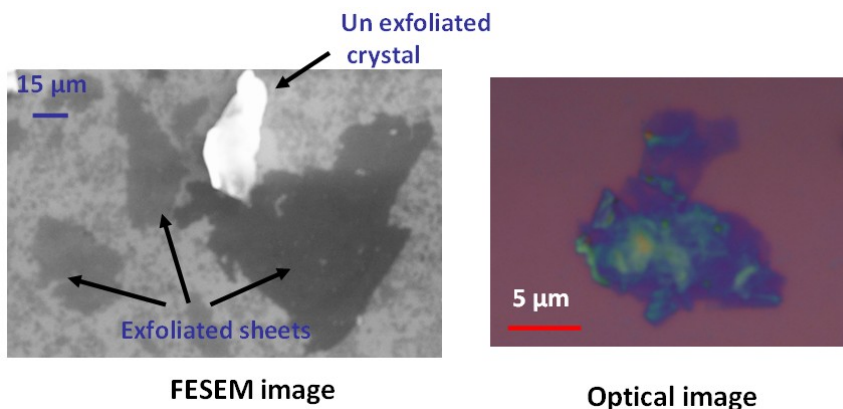


Figure D.9 FESEM and optical images of UTBNSs immobilized on silica substrate by surface-pick up technique. These sheets were obtained from the pyrolytic α -BN sample.

D.10 FESEM Imaging

FESEM Images were obtained with a Leo field emission scanning electron microscope operated at ~15-25 kV. Some of the sheets exhibit perforations uniformly distributed over their surface. These appear as spots with a brighter average intensity than their milieu (Figure D.10, left panel). These are the background silica signals and hence are brighter than their milieu of UTBNSs which absorb a fraction of the imaging electrons from their background before they reach the detector and hence result in a faintly darker appearance. The perforations could be formed due to the harsh chemical nature of CA and are expected to have a high density of edges possessing several primary and quaternary amine functional groups. By analyzing these perforations in a TEM image (as shown before in section D.3), we calculated the fraction of edge atoms contributed by these perforations to the total atoms present in a sheet.

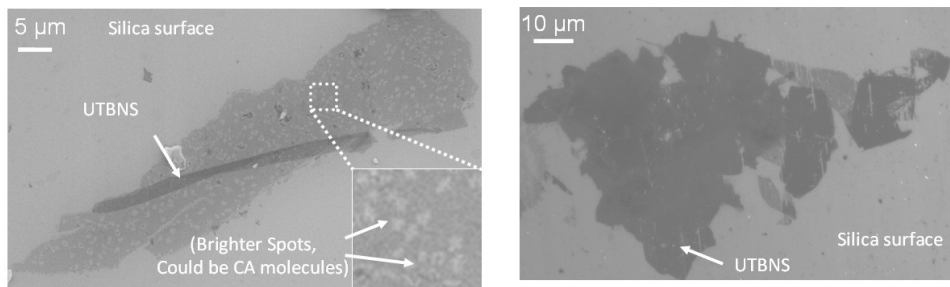


Figure D.10 FESEM images of UTBNSSs immobilized on silica substrate by surface-pick up technique. The UTBNSS shown in left panel exhibits brighter spots on their surface which could be because of the presence of CA molecules on its surface.

D.11 TEM Imaging and SAED

The TEM samples were prepared by surface-pick up technique. 300 mesh size copper TEM specimen grids (Electron Microscopy Sciences) having a lacey carbon support film were used for picking up sheets from the surface of

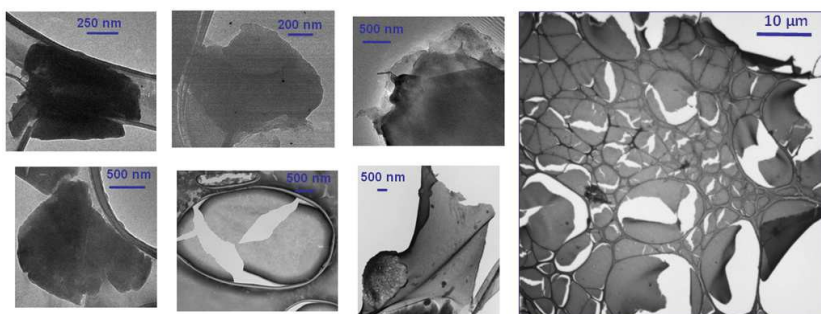


Figure D.11 TEM images of UTBNSSs immobilized on lacey-carbon Copper TEM grids.

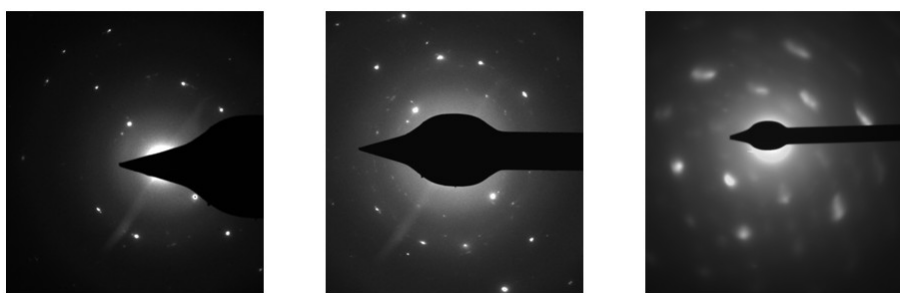


Figure D.12 SAED patterns of UTBNSSs immobilized on lacey-carbon Copper TEM grids. The regular patterns suggest the presence of a crystalline behavior.

quenched solution. The TEM grids were then placed in a drop of water to remove any CA residues and the excess water dried using a Whatman filter paper. The washing step with water is repeated again to eliminate the residues as much as possible. The TEM images and SAED pattern were obtained with a FEI Tecnai F20 XT Field Emission Transmission Electron Microscope and Philips CM 100 transmission electron microscope. Figure D.11 and D.12 show an ensemble of TEM images and SAED patterns obtained for UTBNSs.

D.12 Raman Spectroscopic measurement

UTBNSs and α -BN powder were analyzed for Raman spectroscopy to obtain detailed structural insights. The UTBNSs were immobilized on silica surface by surface-pick up technique and α -BN powder was firmly adhered to silica substrate manually by hard-pressing. The Raman spectra were recorded from 300-1800 cm^{-1} on a Horiba Jobin Yvon LabRAM ARAMIS Raman Spectrometer with a red He-Ne laser ($\lambda=632.8$ nm, laser power <5 mW, spot size $\approx 1 \mu\text{m}^2$), which was parked at various locations on and around a α -BN sheet away from the chip edge, to avoid edge effects. The Spectrometer specifications include a 200-mm confocal pinhole, 150-mm-wide entrance slit, 600 gr mm^{-1} grating, and 100x objective Olympus lens.

D.13 Forming gold nanoparticle conjugates of UTBNSs

Citrate capped GNPs were self-assembled on the surface of UTBNSs via electrostatic attractions in solution.

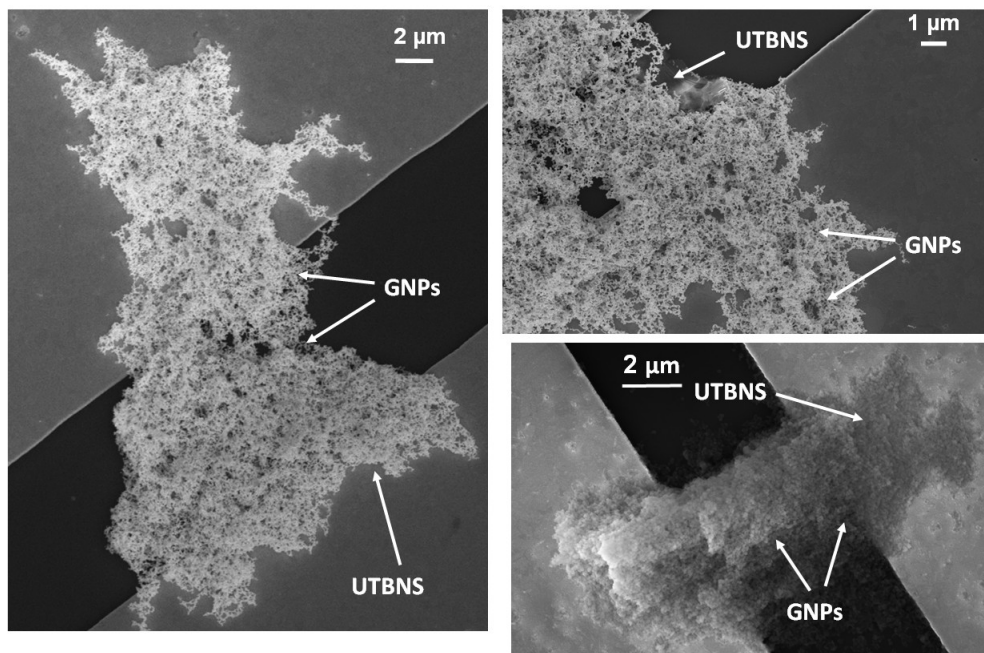


Figure D.13 FESEM images of UTBNSs templated with citrate capped GNPs. The sheets exhibit a high surface density of GNPs.

D.14 Calculating the surface coverage index of GNPs templated on UTBNSs

Image J is used to analyze the density of GNPs templated on UTBNSs. Figure D.14 shows the image from the section of an UTBNS sheet decorated with GNPs. Image J is used to process this image for quantitative estimation of the darker background (corresponding to UTBNS, shaded as red in the processed image) to obtain the surface coverage index η , fraction of UTBNS surface occupied with GNPs. η is calculated to be equal to 0.81.

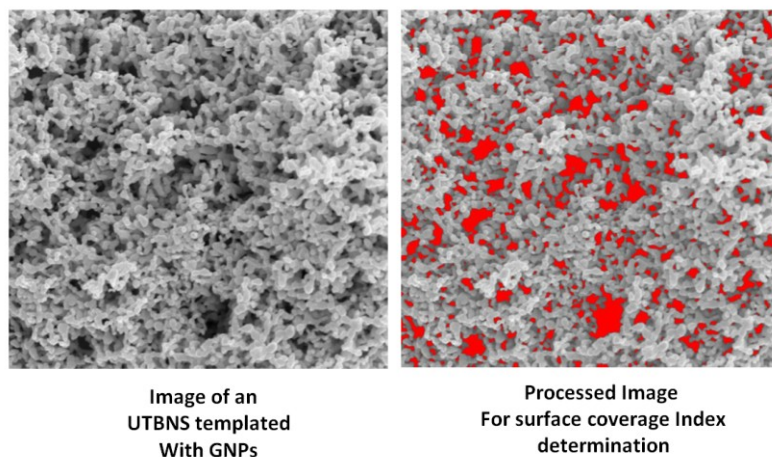


Figure D.14 Determining the surface coverage index of GNPs self-assembled on UTBNS

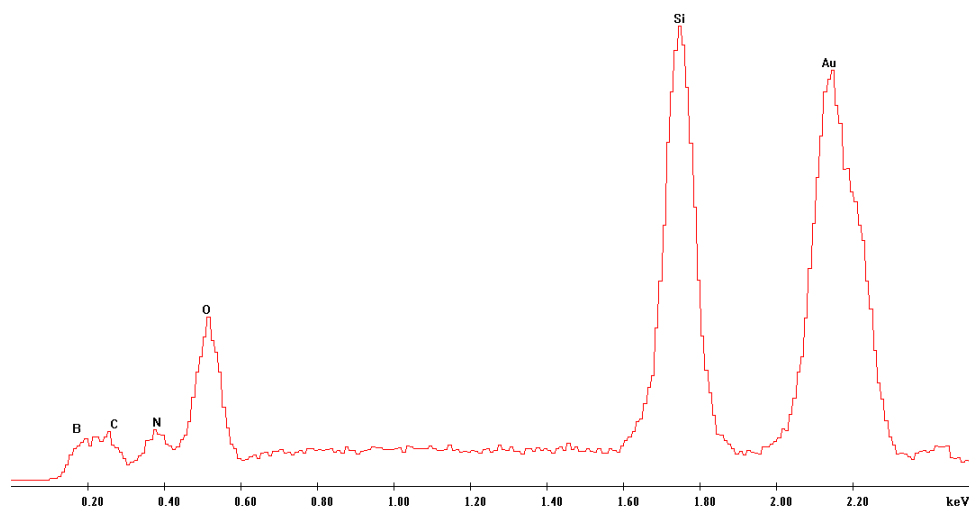


Figure D.15 EDS of a UTBNS decorated with citrate capped gold nanoparticles showing signatures of B, N and Au. The spectrum also shows Si and O signatures from the underlying silica surface

D.15 Preparing samples for Confocal microscopy

Confocal studies were conducted using a Zeiss LSM 5 PASCAL Laser Scanning Confocal Microscope on UTBNS samples immobilized *via* electrostatic interactions on O₂ plasma treated silica wafers. Fluorescein Isothiocyanate (FITC) obtained from Sigma-Aldrich was used for labeling the N functionalities present on the immobilized sheets *via* covalent attachment. Briefly, 5 mg of FITC was dissolved in 20 ml of 0.1 M Phosphate Buffered Saline together with 5 ml of HATU (*O*-(7-azabenzotriazole-1-yl)-*N,N,N,N'*-tetramethyluronium hexafluorophosphate,

an amide-coupling reagent). The silica chip with immobilized UTBNs was incubated in this solution under dark conditions at room temperature for ~8hrs. Since the protonated N atoms are present only on the sheets and not on the surrounding silica surface, the dye molecules selectively tether to the sheets. The physically adsorbed FITC molecules were removed by repeated washing (5x) and air-drying with 0.1 M Phosphate Buffered Saline solution. The positive control sample was prepared by incubating an amine-silanized silica chip with the FITC solution. Amine silanization was achieved by incubating the plasma cleaned silica surface to a 1% solution of amine-propyl tri-ethoxy silane in ethanol for 20 min, followed by repeated (3X) with ethanol and air-drying. A negative control sample was prepared by incubating a bare silica surface (O_2 plasma treated) to the FITC solution.

Appendix E Personal Publication List

The following is a list of publications that Kabeer Jasuja has co-authored during his career at Kansas State University:

1. Kabeer Jasuja, Arthur Thompson, and Vikas Berry, "Reversibly Compressible and Stretchable 'Spring-like' Polymeric Nano-Junctions between Metal Nanoparticles," **Small**, 4, 2181-2886, 2008
2. Kabeer Jasuja and Vikas Berry, "Implantation and Growth of Dendritic Gold Nanostructures on Graphene Derivatives: Electrical-Property-Tailoring and Raman-Enhancement," **ACS-Nano**, 3 (8), 2358-2366, 2009
3. Kabeer Jasuja, Joshua Linn, Steven Melton, and Vikas Berry, "Microwave- Reduced Uncapped Metal Nanoparticles on Graphene: Tuning Catalytic, Electrical and Raman Properties", **Journal of Physical Chemistry Letters**, 1, 1853-1860, 2010
4. Kabeer Jasuja and Vikas Berry, "Incorporating Azo-group-functionalized Molecular Junctions between Metal Nanoparticles to produce High-rectification-memory Nanodevices," **MRS proceedings**, 2008